Inductively Coupled Electromechanics Utilizing a Nonlinear Cavity

"Fishing for a Macroscopic Cat-State"

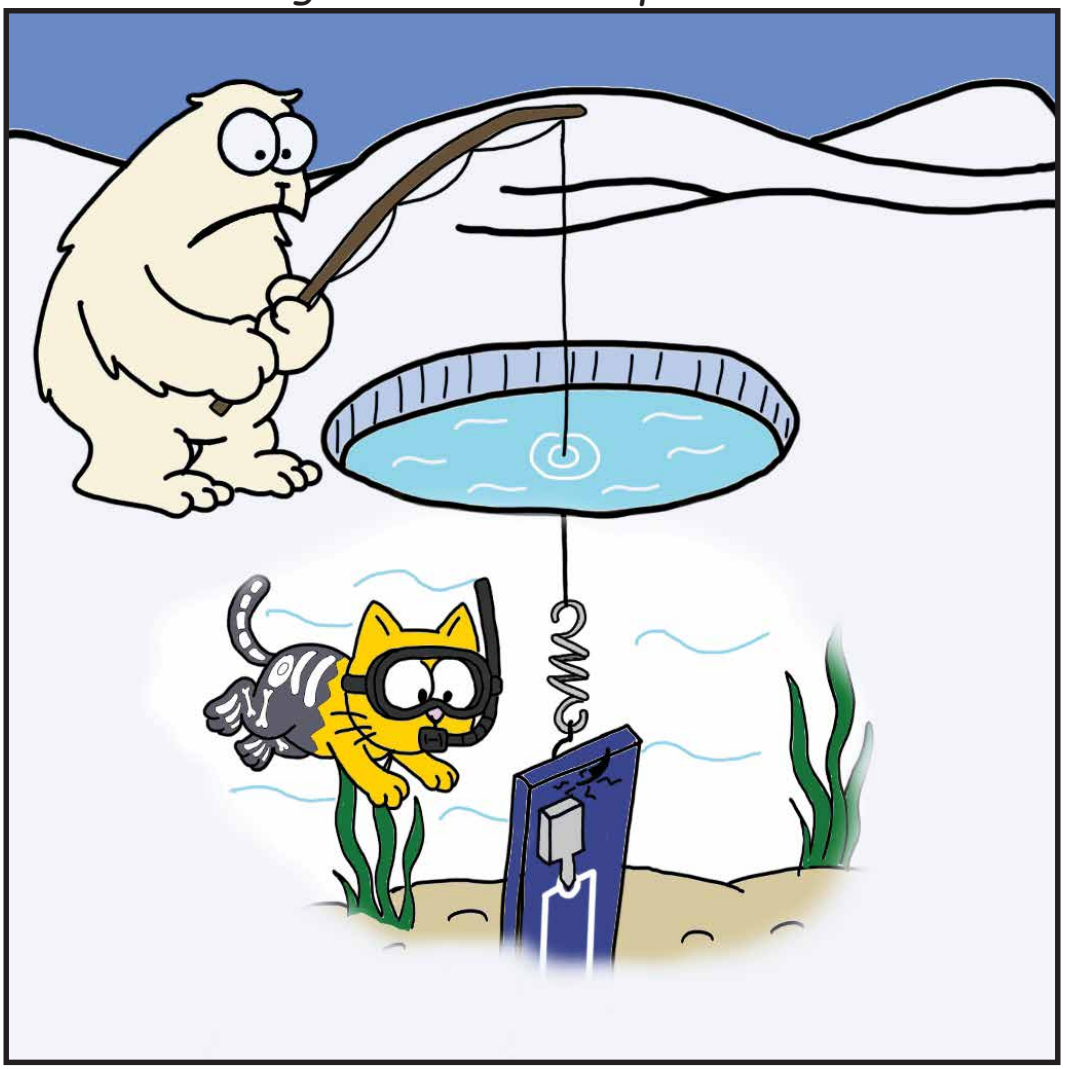

Lukas Deeg

universität innsbruck

Inductively Coupled Electromechanics Utilizing a Nonlinear Cavity

Lukas Felix Deeg, 12043042
Innsbruck, November 2025

Dissertation

submitted to the Faculty of Mathematics, Computer Science and Physics of the University of Innsbruck in partial fulfillment of the requirements for the academic degree

Doctor of Philosophy

Doctor of Philosophy – Doctoral Program in Physics
Main Supervisor: Univ. Prof. Dr. Gerhard Kirchmair
Institute of Experimental Physics
Co-supervisor: Univ. Prof. Dr. Tracy Northup
Institute of Experimental Physics
Faculty of Mathematics, Computer Science and Physics

Contents

Abstract

This thesis extends the development of a nonlinear inductively coupled magnetomechanical system, where a magnetically modified mechanical cantilever interacts with a microwave SQUID-cavity. Based upon the experimental setup realized in previous works demonstrating high coupling strength and efficient backaction cooling [1–4], this work aims to increase the reproducibility in sample preparation, experimental stability; and to extend the regimes the system is operated at. With a newly designed mounting stage, we increased the control and reproducibility of our flip-chip design. By implementing a passive vibration isolation stage based on an elastic pendulum, an effective decoupling from vibrational noise is achieved. With this, continuous operation of the system with the cryostat pulse tube active and measurements at high coupling strengths became possible. Using this improved setup, detailed backaction cooling measurements were performed across a wide range of coupling strengths, reaching a 500 fold compression from the thermal occupation. The results extend the observation made on the enhanced cooling capability arising from the nonlinear cavity in the unresolved sideband regime. Furthermore, we deliberately drive the nonlinear cavity beyond its bifurcation to observe backaction cooling in this regime, in excellent agreement with theory predictions [5]. Despite these advances, ground-state cooling remains inaccessible due to the fundamental sideband-unresolved limitation. To overcome this, the thesis follows up on a theoretical proposal [6] and experimentally explores a hybridization scheme of the magnetomechanical system with a high-quality auxiliary cavity. Presenting two experimental approaches, first proof-of-principle measurements are presented. This scheme may be particularly relevant for achieving ground-state cooling in systems with large and low-frequency mechanical resonators.

Kurzfassung

Diese Arbeit erweitert die Entwicklung eines nichtlinearen, induktiv gekoppelten magnetomechanischen Systems, bei dem ein magnetisch modifizierter mechanischer Cantilever mit einer mikrowellenbasierten SQUID-Kavität wechselwirkt. Aufbauend auf der in früheren Arbeiten realisierten experimentellen Plattform, in der bereits hohe Kopplungsstärken und effizientes „Backaction-Cooling“ demonstriert wurden [1–4], zielt diese Arbeit darauf ab, die Reproduzierbarkeit der Probenpräparation, die experimentelle Stabilität sowie den Betriebsbereich des Systems zu erweitern. Mit einer neu entwickelten Montagevorrichtung konnte die Kontrolle und Reproduzierbarkeit des Flip-Chip-Designs verbessert werden. Durch die Implementierung einer passiven Vibrationsisolierung auf Basis eines elastischen Pendels wurde eine effektive Entkopplung von (externen) Vibrationen erreicht. Dadurch ist ein kontinuierlicher Betrieb des Systems bei aktivem Pulsröhrenkühler sowie Messungen bei hohen Kopplungsstärken möglich. Mit diesem verbesserten Aufbau konnten detaillierte „Backaction-Cooling“-Messungen über einen weiten Bereich von Kopplungsstärken durchgeführt werden, wobei eine etwa 500-fache Reduktion der thermischen Besetzungszahl erreicht wurde. Die Ergebnisse erweitern die Beobachtung der verbesserten Kühlleistung, die aus der Nichtlinearität der Mikrowellen-Kavität im Seitband-unaufgelösten Regime resultiert. Darüber hinaus wurde „Backaction-Cooling“ jenseits der Bifurkation der Kavität in guter Übereinstimmung mit theoretischen Vorhersagen beobachtet, wodurch das zuvor untersuchte nichtlineare Regime erweitert wird [5]. Trotz dieser Fortschritte bleibt ein Kühlen bis in den Grundzustand aufgrund der fundamentalen Einschränkung im unaufgelösten Seitband-Regime unerreichbar. Um dieses Limit zu überwinden, wird in dieser Arbeit ein in [6] vorgeschlagenes Hybridisierungskonzept experimentell untersucht, bei dem das magnetomechanische System mit einem zusätzlichen Mikrowellenresonator hoher Güte gekoppelt wird. Zwei experimentelle Ansätze werden vorgestellt, mit denen erste grundlegende Messungen demonstriert werden konnten. Dieses Konzept könnte insbesondere für die Realisierung von Grundzustandskühlung in Systemen mit großen und niederfrequenten mechanischen Resonatoren von besonderer Relevanz sein.

CHAPTER 1

Introduction

Our perception of reality, and the intuition we build from it in our everyday experience, follows the laws of classical physics formulated by Isaac Newton. When we examine a diving board, for example, we understand how it behaves under various external conditions. We know that we can simultaneously assign a well-defined momentum and precise position to the center of mass of the board in space at any time. This means the board can be bent upward, downward, or remain at rest, and its trajectory in space and time can be predicted deterministically knowing external/internal forces. Furthermore, in the absence of an external force and initialized at rest, the board remains at rest, with no deflection or movement. When an external force is applied, such as by jumping on it, the board can bend by an arbitrary amplitude corresponding to a continuous range of energies we can impart to the system.

However, in the early 20^{th} century, physicists discovered that the behavior of electrons and atoms contradicted our classical intuition and could not be explained within the classical framework. This realization led to the formulation of a radical new theory – *quantum mechanics* – describing processes in terms of probabilities rather than deterministic trajectories governed by its *wavefunction* introduced by Erwin Schrödinger [7]. For the center of mass of our diving board example, if we imagine it behaves in a quantum manner, this theory implies fundamental changes in its behavior. Without looking at it (a measurement of its position), we can only give a probability distribution of where to find it. A peculiar consequence of this is a phenomenon called *superposition*, which allows the board to be physically in two places at the same time, for instance, being deflected simultaneously upwards and downwards. Only upon looking, thus conducting a measurement, does the board acquire a definite position in space, a process referred to as the collapse of its wavefunction. Moreover, even if we measured the precise position of the board, we cannot simultaneously know its momentum with arbitrary precision, according to the Heisenberg uncertainty principle [8]. This directly implies that the board can never be truly at rest. Even in its *ground state* (the quantum equivalence of the board being at rest), the uncertainty principle has to be satisfied, resulting in a motion of the board referred to as the *zero-point motion*. An external force can still deflect the board by an arbitrary amplitude, but

contrary to energy continuity of the classical case, the board can only occupy discrete/quantized energy levels or superpositions thereof – the higher the energy level, the larger the deflection amplitude.

Despite this counter-intuitive behavior – sparking remarks from renowned scientists such as Richard Feynman's *"I think that I can safely say that nobody understands quantum mechanics"* or Roger Penrose's *"quantum mechanics makes absolutely no sense"* – quantum mechanics is the most precise and best tested physical theory we have. Until today it holds itself up in experimental test spanning a large range of scales: from the interference of electrons [9], atoms [10], and larger molecules such as fullerenes [11] and 2000-atom complexes [12], to macroscopic currents in superconducting devices [13–16]; this last was even awarded the Nobel Prize in Physics in 2025.

This naturally raises the question of why we do not observe such quantum effects in our everyday experience. Theoretically, there is no size or mass limit on quantum systems. However, quantum states are fragile, and macroscopic systems are never perfectly isolated. Their constant interaction with the environment – collisions with air molecules, radiation, and other sources of noise – rapidly destroys any quantum state, resulting in the collapse of its wavefunction into a classical state – a process known as decoherence [17]. Furthermore, the thermal energy at ambient temperatures vastly exceeds the quantum energy scales and thus renders quantum signatures effectively unobservable. This becomes especially challenging for massive objects, as the amplitude of the zero-point motion decreases with mass, making the observation of quantum effects progressively more difficult to detect experimentally. As a result, the behavior of everyday objects appears smooth and deterministic, giving rise to the classical world we experience.

Despite these challenges, experiments exploring quantum mechanics with increasingly massive objects enable us to tackle some of the most fundamental questions in physics. For instance, they allow for testing deviations from standard quantum theory predicted in so-called collapse models [18–20]. Including stochastic and nonlinear modifications to the Schrödinger equation, these models predict the collapse of the wavefunction into a distinct state at rates scaling with the size and mass of the quantum object. Furthermore, possessing non-negligible mass, macroscopic objects allow us to investigate the interplay between quantum mechanics and gravity [21, 22]. This would pave the way to a theory unifying quantum mechanics and general relativity, which are the widely accepted models in the microscopic and macroscopic regimes, respectively.

To extend quantum experiments to systems containing billions of atoms requires a macroscopic object sufficiently isolated from its environment, that can be controlled to exceptional precision. The field of optomechanics and the more recent field of electromechanics offer a versatile platform to address these challenges. Here, the interaction between the electromagnetic mode of a cavity and the mechanical mode of a resonator can be studied by coupling the electromagnetic field of the cavity to the displacement of a mechanical resonator via radiation pressure. If the strength of the coupling quantified by the *single-photon coupling strength* exceeds both the cavity and resonator loss rates, we enter the so-called *single-photon strong-coupling* regime. This enables controllable swaps of quantum states between the two modes and generating nonclassical mechanical states due to the intrinsic nonlinear nature of the interaction [23]. However, this quantum state transfer only works under the premise that the electromagnetic and mechanical modes are initilized in a known state – which mostly means their respective ground states.

In recent years, technical advances – particularly in electromechanical platforms based on superconducting circuits – have greatly reduced the requirements to reach the strong single-photon coupling regime. On the one hand, mechanical resonators now routinely achieve sublime

quality factors up to $Q \sim 10^9$ corresponding to loss rates in the sub-Hertz regime and lifetimes close to or even exceeding 1 ms [24–28]. On the other hand, planar microwave cavities demonstrate quality factors in the range of $Q \sim 10^6$ and loss rates on the order of $10 - 100$ kHz [29–31]. As sources of non-classical quantum states, superconducting qubits have reached lifetimes progressively approaching the millisecond regime [32, 33].

Additionally to its ability to answer fundamental physics questions by creating macroscopic quantum states, the field of optomechancis and electromechanics offer a variaty of technical applications. With quantum controll over mechanical systems and high mechanical quality factors corresponding to long coherence times, optomechanical systems could harness the mechanical resonator as a quantum memory within the field of quantum information science [34]. Furthermore, as the mechanical elements can be effectively coupled to photons of different wavelengths – e.g., optical and microwave photons – they provide a well suited platform to realize coherent quantum transducers that bridge optical and superconducting quantum technologies [34–37]. Lastly, as optomechanical systems rely on their ability to detect the mechanical mode down to its zero-point motion, they inherently function as exceptionally precise force and acceleration sensors, making them highly attractive for applications in metrology [38, 39]. Furthermore, by preparing the mechanical mode in a nonclassical quantum state – such as a superposition or an entangled state – their sensitivity can be further enhanced [40].

To realize the coupling between the mechanical resonator and the superconducting circuit, one typically exploits a mechanically compliant element that modulates either the circuit's capacitance or its inductance. With the former and most common approach today, the position dependent capacitance is implemented by relying on either a drum, membrane or bulk acoustic wave resonantor representing one side of the capacitor electrode [25, 28, 41]. With this approach significant milestones could be achieved by many groups: ground state cooling of the mechanical mode [28, 42], reaching the photon-enhanced ultra-strong coupling regime [43], entanglement of two mechanical resonators [44] and the stabilization of nonclassical states in the mechanical mode [45, 46]. Despite these achievements, the coupling strength achievable using the capacitive approach is fundamentally limited. This is because the coupling strength scales inversely with the electrode separation, but there is an engineering limit for the distance of the capacitive plates given by Casimir/van der Waals-induced forces which cause the plates to collapse. With values around ~ 100 Hz the single-photon coupling strength achievable is typically several orders of magnitude smaller than the cavity loss rates. This has made the single-photon strong-coupling regime inaccessible until now [47].

This limitation led to the rise in popularity of the inductive coupling approach. These typically rely on a *Superconducting Quantum Interference Device* (SQUID) – an extremely magnetic-flux-sensitive inductor – incorporated into the microwave circuit to mediate the coupling to a mechanical element. For these systems, the coupling can be realized in two ways: either the mechanically compliant element modulates the SQUID area threaded by a magnetic field [48, 49] or the mechanical mode actively changes the magnetic field [3, 50]. By reaching coupling strengths exceeding 10 kHz [3, 51], these inductively coupled systems began to outperform the capacitive approach with respect to the achievable coupling strengths. However, the single-photon strong-coupling regime remains experimentally out of reach to date, as inductive coupling introduces additional challenges that must first be overcome.

Building on a theoretical proposal [52], an inductively coupled electromechanical system was developed in our group prior to the start of my PhD. The device consists of a micrometer-scale, commercial atomic-force-microscopy *cantilever* (essentially a miniature diving board) inductively coupled via an attached magnetic particle to a superconducting microwave SQUID-cavity.

Within this platform, my colleagues demonstrated photon-enhanced strong coupling between the mechanical and electromagnetic modes, as well as cooling of the mechanical resonator [3, 4]. Even though large coupling strength up to 8 kHz have been demonstrated, it remains 3 orders of magnitude lower than the cavity linewidth preventing to reach the single photon-strong coupling regime. Nevertheless, the achieved coupling when enhanced by a pump is sufficient to transfer a quantum state into the mechancis using a quantum source (e.g. a qubit). However, the necessity to initialize the mechanics in a known state (ground state) remains, where backaction cooling provides an efficient way to achieve this. My thesis aimed towards these goals by further characterizing and deepening our understanding of the system by exploring new operational regimes. Additionally, efforts were made to mechanically isolate the mechanical mode from its vibration-rich environment and to improve the reproducibility of the sample preparation process. Towards the end of my PhD, we began augmenting the existing setup with an auxiliary high-Q cavity with the goal to achieve ground state cooling of the mechanics, following a theoretical proposal by Liu et al. [6]. Over the course of my PhD, I contributed to three journal articles [4, 5, 53].

1.1 Overview of the thesis

The thesis starts with a theoretical description of our system developed in collaboration with Nicolás Díaz Naufal and Prof. Anja Metelmann (KIT). By using the general theoretical framework of optomechanics [23] and extending it by allowing for an intrinsically nonlinear cavity [53], we derive the behavior of the cavity and mechanical mode under the optomechanical coupling and cover the necessary processes to discuss our experimental results.

In the next chapter, we focus on the theoretical background of superconducting circuit theory to explain the working principle of a SQUID in our system. Starting with the description of *LC-circuits*, the basic equations of superconductivity are worked out, which finally allows us to describe the working principle of a SQUID. The chapter is concluded by presenting simulation results on the behavior of a SQUID-cavity with and without a magnetic cantilever, and upon changing internal and external parameters.

Next, the experimental setup is presented. The chapter starts with a general description of a dilution cryostat used to reach the millikelvin temperatures at which superconducting circuits are operated. We further describe our implementation of a vibration isolation setup by suspending the experiment by an elastic pendulum setup. There, we assess the degree of isolation achieved and discuss thermalization challenges that arise from this approach. We continue with the microwave platform, covering the cavity fabrication process, the 3D-waveguide used for measurements, and the characterization methods used. Next, the microwave wiring of the experiment is presented. The chapter ends with an introduction to the mechanical cantilever. We explain how to experimentally detect its fundamental motional mode and discuss the sample preparation process, presenting several samples. For a complete description of the mechanical platform, we include the magnetic characterization of the magnetic particles used, which was performed by Prof. A. Ney (University of Linz).

The main experimental results are discussed in Chapter 5. First, we cover the behavior of the SQUID-cavity and changes which occur upon mounting the magnetic cantilever, focusing on the flux tunability and intrinsic cavity nonlinearity. Subsequently, to demonstrate the improvement in system stability using the suspension setup, we determine the coupling strength by detecting the mechanical mode while avoiding backaction. Lastly, we present measurements of backaction on the mechanical mode, which show good overall agreement with the theoretical model developed. We first investigate how varying the coupling strength affects the mechanical

cooling achieved, and then demonstrate controlled backaction as the system enters the bistable regime of the cavity.

With the outstanding challenge to reach the ground state despite our system residing in the unresolved sideband regime, we provide an outlook on our existing platform in the final chapter. Here, we present an approach to increase the cooling capability of our system by hybridizing it with an auxiliary cavity. We begin with a basic theoretical description of the augmented system and present a proof-of-principle measurement. This is followed by a discussion of design choices based on simulation results and by the presentation of first experimental results. The chapter concludes with an outlook on possible future directions for this approach.

1.2 Work not covered

During my PhD, I had the privilege to be part of the doctoral program Atom, Lights and Molecules (DK-Alm), allowing me to conduct three research stays in different experimental groups. These projects are beyond the scope of this thesis, but I would still like to mention them.

For two months, I visited the group of Prof. Witlef Wieczorek at the University of Chalmers (Göteborg, Sweden) on their project of magnetic levitation of superconducting microparticles [54]. There, I learned about the experimental and fabricational challenges of the setup, used my knowledge to help with the implementation of a new suspension setup, and contributed to the evaluation of their first set of flux-tunable microwave cavities.

For the next stay, I joined the group of Prof. Yiwen Chu at the ETH (Zürich, Switzerland) for four months, working on their experimental platform that couples high-overtone bulk acoustic wave resonators to transmon superconducting circuits [55, 56]. By providing a superconducting fluxhose built in our own group [57], we replaced the single-frequency transmon previously used in the experiment with a flux-tunable version. This modification enabled access to a larger number of mechanical modes. During my stay, I integrated this new setup and developed an automated evaluation routine to characterize the lifetime and dephasing rates of more than 100 modes in a single acoustic resonator.

My last stay was in the group of Prof. Hans Hübl at the WMI (München, Germany) for a month. They realized an inductive coupling by suspending the arms of a SQUID integrated into a microwave cavity, which leads to an effective SQUID area modulated by a mechanical motion [48, 58]. During my stay, we developed a new chip design aimed at higher microwave quality factors, implemented magnetic shielding of their experiment, and provided an additional method to characterize the nonlinearity of their microwave mode.

CHAPTER 2

Cavity Optomechanics

The goal of this chapter is to introduce optomechanics - the interaction between a photonic cavity and a mechanical resonator. In contrast to common literature assuming a linear cavity, we will focus throughout this chapter on the effects of an intrinsic Kerr nonlinear cavity on the dynamics of the optomechanical system by comparing it to the linear case.

We begin by presenting the canonical description of optomechanics and derive its Hamiltonian formulation. Building on this, we analyze the system dynamics within a linearized description, focusing on the behavior of the cavity mode. The resulting cavity response provides insight into the system's dynamics, particularly the emergence of backaction effects. We focus on how this backaction interaction is used to cool the mechanical mode, discussing the relevant limits and emphasizing the beneficial effects introduced by the presence of cavity nonlinearity.

The theory developed in this chapter is based on our collaborative work with Nicolás Díaz Naufal and Prof. Anja Metelmann. Therefore, all derivations and equations are drawn from our work [53], unless otherwise noted. For a broader overview on linear optomechanics and optomechanics in general, the reader is referred to [23].

2.1 Hamiltonian Formulation

The textbook realization of an optomechanical system - the optical *Fabry–Pérot* cavity - is depicted in Fig. 2.1. The two mirrors define an optical cavity that supports a confined photonic mode with its resonance frequency ω_c depending on the cavity length. For completeness, a nonlinear Kerr-medium is added to the cavity, as we will focus on effects arising from such an element within an optomechanical system. Furthermore, one mirror is attached to a mechanical spring with frequency ω_m, allowing it to modify the cavity length. Photons inside the cavity, introduced by an external driving field (e.g. a laser), exert a radiation pressure force on the mirror, displacing the spring. This gives rise to a parametric interaction between the modes, as the mechanical displacement modifies the cavity frequency.

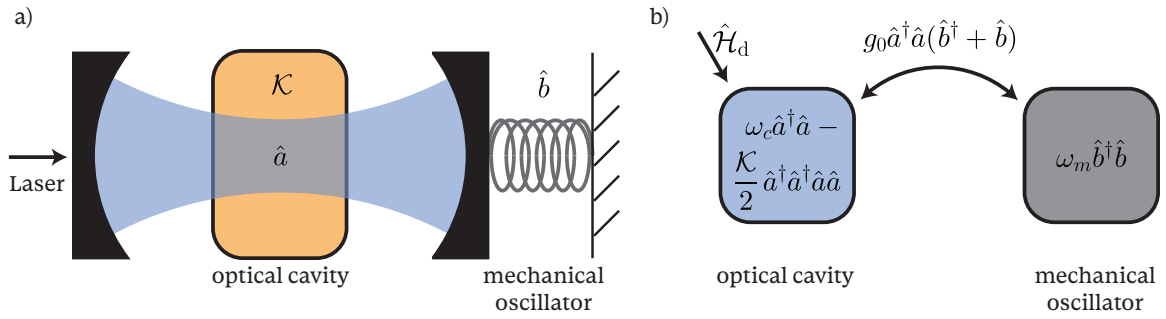

Fig. 2.1 **a)** Schematic of the optomechanical setup with an intrinsic nonlinearity. An optical cavity incorporating a nonlinear Kerr-medium with one movable mirror is connected to a mechanical resonator, allowing the oscillation of the mechanical element to change the optical resonance frequency. **b)** Schematic representation of the Hamiltonian in this optomechanical setup.

The uncoupled optical and mechanical system is described by the Hamiltonian (see Fig. 2.1)

$$\hat{\mathcal{H}}_0/\hbar = \omega_\mathrm{c}\hat{a}^\dagger\hat{a} - \frac{\mathcal{K}}{2}\hat{a}^\dagger\hat{a}^\dagger\hat{a}\hat{a} + \omega_\mathrm{m}\hat{b}^\dagger\hat{b}, \tag{2.1}$$

with the reduced Planck constant $\hbar$, the cavity frequency ω_c, the mechanical resonance frequency ω_m and the annihilation and creation operators of the cavity (mechanics) $\hat{a}\,(\hat{b})$ and $\hat{a}^\dagger\,(\hat{b}^\dagger)$, respectively. The Kerr-constant given by $\mathcal{K}$ represents the lowest order nonlinearity of the cavity and is considered to be $\mathcal{K} > 0$. As we will see later in this work, this leads to a photon-number-dependent frequency shift.[1]
The interaction between the two systems is given by the change in cavity length and thus frequency ω_c upon displacing the mechanical element by $\hat{x}$. This coupling can therefore be derived by expressing the cavity frequency as a function of the mechanical displacement as

$$\omega_\mathrm{c}(\hat{x}) = \omega_\mathrm{c} + \hat{x}\frac{\partial\omega_\mathrm{c}}{\partial\hat{x}} + \ldots \approx \omega_\mathrm{c} + \frac{\hat{x}}{x_\mathrm{zpm}}g_0. \tag{2.2}$$

Here we define $g_0 = x_\mathrm{zpm}\frac{\partial\omega_\mathrm{c}}{\partial\hat{x}}$ as the optomechanical single-photon coupling strength and introduce the *zero-point motion* x_zpm of the mechanical mode as

$$x_\mathrm{zpm} = \sqrt{\frac{\hbar}{2m_\mathrm{eff}\omega_\mathrm{m}}}, \tag{2.3}$$

with the effective mass of the mechanical resonator m_eff. The zero-point motion of a resonator is the amplitude of residual quantum fluctuation of its position in the ground state. As x_zpm

[1] The complete term corresponding to the nonlinearity in the Hamiltonian reads as

$$\frac{\mathcal{K}}{12}(\hat{a}^\dagger+\hat{a})^4 = \frac{\mathcal{K}}{12}(\hat{a}^{\dagger4}+\hat{a}^4) + \frac{\mathcal{K}}{3}(\hat{a}^{\dagger3}\hat{a}+\hat{a}^\dagger\hat{a}^3) + \frac{\mathcal{K}}{2}(\hat{a}^{\dagger2}+\hat{a}^2) + \frac{\mathcal{K}}{2}\hat{a}^\dagger\hat{a}^\dagger\hat{a}\hat{a} + \mathcal{K}\hat{a}^\dagger\hat{a} + \frac{\mathcal{K}}{4},$$

where we used the commutator $[\hat{a},\hat{a}^\dagger] = 1$. We neglect all the unbalanced terms in $\hat{a}^\dagger$ and $\hat{a}$ in the rotating wave approximation [53]. The quartic term $\hat{a}^\dagger\hat{a}^\dagger\hat{a}\hat{a}$ represents the photon-number-dependent frequency shift, whereas the $\hat{a}^\dagger\hat{a}$ term, representing a small constant frequency offset, and the third term, being a constant, is usually omitted.

decreases for heavier mechanical objects, one has to increase the frequency sensitivity $\partial\omega_c/\partial\hat{x}$ to maintain a strong g_0. The ability to exceed state-of-the-art values for g_0 [23], is one of the benefits of the system discussed within the frame of this work (see chapter 3.4.1). Replacing the position operator by $\hat{x} = x_{\mathrm{zpm}}(\hat{b}^\dagger + \hat{b})$ the cavity frequency becomes

$$\omega_c(\hat{x})\hat{a}^\dagger\hat{a} \approx (\omega_c + \frac{\hat{x}}{x_{\mathrm{zpm}}}g_0)\hat{a}^\dagger\hat{a} = \omega_c\hat{a}^\dagger\hat{a} + g_0\hat{a}^\dagger\hat{a}(\hat{b}^\dagger + \hat{b}). \tag{2.4}$$

The last term in Eq. (2.4) represents the interaction Hamiltonian $\hat{\mathcal{H}}_{\mathrm{int}}$ between the optical and mechanical modes. A displacement of the mechanical resonator - whose mode amplitude scales as $x_{\mathrm{amp}} = 2x_{\mathrm{zpm}}\sqrt{\bar{n}_{\mathrm{m}}}$ with mechanical occupation $\bar{n}_{\mathrm{m}}$ - modulates the cavity frequency ω_c via the coupling strength g_0. Therefore, detecting the optomechanically induced cavity frequency shift provides a direct means to deduce the amplitude of the mechanical motion and thus occupation of the mode through the cavity's response. Furthermore, this interaction enacts an additional force on the mechanical resonator, allowing for the control of the mechanical motion by cavity photons. This radiation pressure force can be written as

$$\hat{F}/\hbar = \frac{\partial\hat{\mathcal{H}}_{\mathrm{int}}/\hbar}{\partial\hat{x}} = \frac{g_0}{x_{\mathrm{zpm}}}\hat{a}^\dagger\hat{a}. \tag{2.5}$$

To enhance the force acting on the mechanics, either a larger coupling strength g_0 or an increased intracavity $\hat{a}^\dagger\hat{a}$ field is necessary.

To obtain the complete system Hamiltonian, we introduce an external drive with frequency ω_{d} and amplitude α_{d}. The corresponding drive Hamiltonian is given by $\hat{\mathcal{H}}_{\mathrm{d}}(t)/\hbar = \alpha_{\mathrm{d}}e^{-i\omega_{\mathrm{d}}t} + \textbf{h.c.}$ (with h.c. being the Hermitian conjugate). We derive the time-independent Hamiltonian by moving to a frame rotating with the drive frequency.[1] This results in

$$\hat{\mathcal{H}}/\hbar = -\Delta\hat{a}^\dagger\hat{a} - \frac{\mathcal{K}}{2}\hat{a}^\dagger\hat{a}^\dagger\hat{a}\hat{a} + \omega_{\mathrm{m}}\hat{b}^\dagger\hat{b} + g_0\hat{a}^\dagger\hat{a}(\hat{b} + \hat{b}^\dagger) + \hat{\mathcal{H}}_{\mathrm{d}}, \tag{2.6}$$

with $\Delta = \omega_d - \omega_c$ the drive (ω_d) - cavity (ω_c) detuning and $\hat{\mathcal{H}}_{\mathrm{d}} = \alpha_d\hat{a}^\dagger + \mathrm{h.c.}$ the time independent external drive.

2.1.1 Linearized Hamiltonian

To study the implications of the radiation pressure effects derived in chapter 2.1 on the cavity and mechanical mode in the presence of a cavity drive, it is useful to switch to the *linearized* approximation of cavity optomechanics. For this approximation to hold, we need a strong, coherent drive of the cavity. Since the single photon coupling strength g_0 in optomechanical systems is typically smaller than the cavity decay rate, such that a strong coherent drive is used to enhance the phonon-photon interaction. In the presence of such a strong drive (leading to a high intracavity photon number), the intracavity field can be described as a combination of an average coherent amplitude $\langle\hat{a}\rangle = \bar{\alpha}$ and a fluctuation term $\delta\hat{a}$

$$\hat{a} \to \bar{\alpha} + \delta\hat{a}. \tag{2.7}$$

[1] The change to this framework is typically valid as the optical frequency ω_c is large compared to other system parameters. The Hamiltonian is then derived by the unitary transformation

$$\hat{\mathcal{H}}' = \hat{U}\hat{\mathcal{H}}\hat{U} - \hat{A}$$

with $\hat{A} = \omega_{\mathrm{d}}\hat{a}^\dagger\hat{a}$, the unitary matrix $\hat{U} = e^{-i\hat{A}t}$ and the Hamiltonian $\hat{\mathcal{H}} = \hat{\mathcal{H}}_0 + \hat{\mathcal{H}}_{\mathrm{int}}$.

By applying this displacement transformation, the equations of motion become linear (hence the term linearized approximation), where we find the Hamiltonian in Eq. (2.6) to be

$$\hat{\mathcal{H}}_{\mathrm{lin}}/\hbar \approx -(\Delta + 2\bar{n}_{\mathrm{c}}\mathcal{K})\delta\hat{a}^{\dagger}\delta\hat{a} - \frac{1}{2}\bar{n}_{\mathrm{c}}\mathcal{K}(\delta\hat{a}^{\dagger}\delta\hat{a}^{\dagger} + \delta\hat{a}\delta\hat{a}) + \omega_{\mathrm{m}}\hat{b}^{\dagger}\hat{b} + \hat{\mathcal{H}}_{\mathrm{int}}^{\mathrm{lin}}/\hbar. \tag{2.8}$$

Here we correlate the mean cavity amplitude to the mean intracavity photon number $|\bar{\alpha}| = \sqrt{\bar{n}_c}$ by assuming $\bar{\alpha} \in \mathbb{R}$. The second term corresponds to single-mode squeezing, whose effects will be further discussed in section 2.3. The interaction Hamiltonian can be written as

$$\hat{\mathcal{H}}_{\mathrm{int}}^{\mathrm{lin}}/\hbar = g_0\bar{n}_{\mathrm{c}}(\hat{b}^{\dagger} + \hat{b}) + g_0\sqrt{\bar{n}_{\mathrm{c}}}(\delta\hat{a} + \delta\hat{a}^{\dagger})(\hat{b}^{\dagger} + \hat{b}) + g_0\delta\hat{a}^{\dagger}\delta\hat{a}(\hat{b}^{\dagger} + \hat{b}). \tag{2.9}$$

The first term in Eq. (2.9) represents the effect of an average radiation pressure force $\bar{F}/\hbar = \bar{n}_c g_0/x_{\mathrm{zpm}}$ enacting a static displacement on the mechanics $\delta\bar{x} = \bar{F}/m_{\mathrm{eff}}\omega_{\mathrm{m}}^2$ and leading to a frequency shift $\delta\omega_{\mathrm{c}} = g_0\delta\bar{x}/x_{\mathrm{zpm}}$. This term can be omitted after a proper transformation of the mechanical origin and cavity frequency. The second term represents the quadrature-quadrature coupling between the two modes, which is amplified by the coherent cavity amplitude $\sqrt{\bar{n}_{\mathrm{c}}}$. Since the last term is small in comparison, we can neglect it. Thus, the interaction Hamiltonian reads as

$$\hat{\mathcal{H}}_{\mathrm{int}}^{\mathrm{lin}}/\hbar \approx g_0\sqrt{\bar{n}_{\mathrm{c}}}(\delta\hat{a}^{\dagger} + \delta\hat{a})(\hat{b}^{\dagger} + \hat{b}). \tag{2.10}$$

From the linearized Hamiltonian, the enhancement of the coupling strength with cavity photons becomes evident, and we introduce the photon-enhanced coupling as

$$g = g_0\sqrt{\bar{n}_{\mathrm{c}}}. \tag{2.11}$$

2.2 Semiclassical Cavity Dynamics

The dynamics of the cavity in an optomechanical system can be obtained by utilizing standard *input-output* theory [59] and is described by the equation

$$\frac{d}{dt}\hat{a} = -i[\hat{a}, \hat{\mathcal{H}}] - \frac{\kappa_{\mathrm{l}}}{2}\hat{a} - \sqrt{\kappa_{\mathrm{c}}}\hat{a}_{\mathrm{in}}. \tag{2.12}$$

Here, the loaded or total linewidth $\kappa_{\mathrm{l}} = \kappa_{\mathrm{c}} + \kappa_{\mathrm{i}}$ is introduced as the sum of an intrinsic loss rate κ_{i} and a coupling rate κ_{c} to an input photon field $\hat{a}_{\mathrm{in}}$ resulting in an input photon number rate $\bar{n}_{\mathrm{in}}$. The system dynamics are derived by introducing the mechanical position and momentum quadratures

$$\hat{q} = \frac{\hat{b}^{\dagger} + \hat{b}}{\sqrt{2}}\ ,\ \hat{p} = i\frac{\hat{b}^{\dagger} - \hat{b}}{\sqrt{2}}, \tag{2.13}$$

and analyzing the system in the *semiclassical* limit $\alpha(t) := \langle\hat{a}(t)\rangle$ and $q(t) := \langle\hat{q}(t)\rangle$ for sufficiently large photon and phonon numbers. With that Eq. 2.12 results in

$$\frac{d}{dt}\alpha = \left(i\Delta - \frac{\kappa_{\mathrm{l}}}{2}\right)\alpha - i\sqrt{2}g_0 q\alpha + i\mathcal{K}|\alpha|^2\alpha - \sqrt{\kappa_{\mathrm{c}}}\alpha_{\mathrm{in}} \tag{2.14}$$

for the cavity dynamics. Using the same formalism for the mechanical quadratures, the dynamics of the mechanical mode results in

$$\begin{aligned}\frac{d}{dt}q &= \omega_{\mathrm{m}}p - \frac{\Gamma_{\mathrm{m}}}{2}q \\ \frac{d}{dt}p &= -\omega_{\mathrm{m}}q - \frac{\Gamma_{\mathrm{m}}}{2}p - \sqrt{2}g_0|\alpha|^2,\end{aligned} \tag{2.15}$$

where we introduced the mechanical decay rate Γ_{m}. For now, the noise operator $\hat{b}_{\mathrm{in}}$ is neglected in Eq. (2.15), which represents the coupling to a bath at temperature T leading to a thermal phonon occupation $\bar{n}_{\mathrm{m}}^{T}$ given by the Bose-Einstein distribution $\bar{n}_{\mathrm{m}}^{T} = [\exp\{-\hbar\omega_m/k_{\mathrm{B}}T\} - 1]^{-1}$. From Eq. (2.14) we can identify the term $-\sqrt{2}g_0 q$ as the mechanically induced cavity frequency shift and the radiation pressure force on the mechanics as $-\sqrt{2}g_0|\alpha|^2$ in Eq. (2.15).
For weak coupling strengths, the mechanical displacement weakly modifies the optical mode, and thus the mechanical position Eq. (2.15) can be solved in the long time limit, leading to the steady state position

$$q_{\mathrm{st}} = -\frac{\sqrt{2}g_0\omega_{\mathrm{m}}|\alpha|^2}{\omega_{\mathrm{m}}^2 + \Gamma_{\mathrm{m}}^2/4}. \tag{2.16}$$

Inserting this solution into the Eq. (2.14) we derive the classical cavity amplitude

$$\frac{d}{dt}\alpha = \left(i\Delta - \frac{\kappa_{\mathrm{l}}}{2}\right)\alpha + i(\mathcal{K} + \mathcal{K}_{\mathrm{m}})|\alpha|^2\alpha - \sqrt{\kappa_{\mathrm{c}}}\alpha_{\mathrm{in}}, \tag{2.17}$$

with the optomechanical induced nonlinearity - mechanical Kerr - $\mathcal{K}_{\mathrm{m}}$ given by

$$\mathcal{K}_{\mathrm{m}} = \frac{2g_0^2\omega_{\mathrm{m}}}{\omega_{\mathrm{m}}^2 + \Gamma_{\mathrm{m}}^2/4}, \tag{2.18}$$

Multiplying the steady state solution ($\frac{d}{dt}\alpha = 0$) of Eq. (2.17) with its complex conjugate, we obtain the cubic equation describing the circulating intracavity photon number

$$\bar{n}_{\mathrm{c}}\left[(\Delta + \mathcal{K}_{\mathrm{eff}}\bar{n}_{\mathrm{c}})^2 + \frac{\kappa_{\mathrm{l}}^2}{4}\right] = \kappa_{\mathrm{c}}\bar{n}_{\mathrm{in}}, \tag{2.19}$$

with $\bar{n}_{\mathrm{c}} = |\alpha|^2$, $\bar{n}_{\mathrm{in}} = |\alpha_{\mathrm{in}}|^2$ and $\mathcal{K}_{\mathrm{eff}} = \mathcal{K} + \mathcal{K}_{\mathrm{m}}$. In Fig. 2.2a), the intracavity photon number for different drive strengths is depicted. With increasing $\bar{n}_{\mathrm{in}}$ and therefore larger $\bar{n}_{\mathrm{c}}$, the nonlinear cavity starts to deviate from the typical Lorentzian lineshape of a linear cavity by shifting its resonance to lower frequencies for $\mathcal{K} > 0$. The effective resonance frequency corresponding to the maximum intracavity photon number of Eq. (2.19) with respect to Δ shifts as

$$\omega_{\mathrm{c}}(\bar{n}_{\mathrm{c}}) = \omega_{\mathrm{c}}(0) - \mathcal{K}\bar{n}_{\mathrm{c}}. \tag{2.20}$$

For sweeping the drive from negative to positive detunings, this results in an increasingly steep response towards the highest intracavity photon number, followed by a shallow decrease. The solution of Eq. (2.17) remains single-valued until a critical drive strength $\bar{n}_{\mathrm{in,bi}}$. Upon exceeding $\bar{n}_{\mathrm{in,bi}}$, the cavity response becomes bistable with two stable solutions - a low and high photon number branch - and an unstable one. The frequency range over which bistability is observed broadens upon further increasing the input power.

To derive the drive strength at which bistability occurs, we evaluate Eq. (2.17) at the point where the slope of the intracavity photon number with respect input power diverge. This is

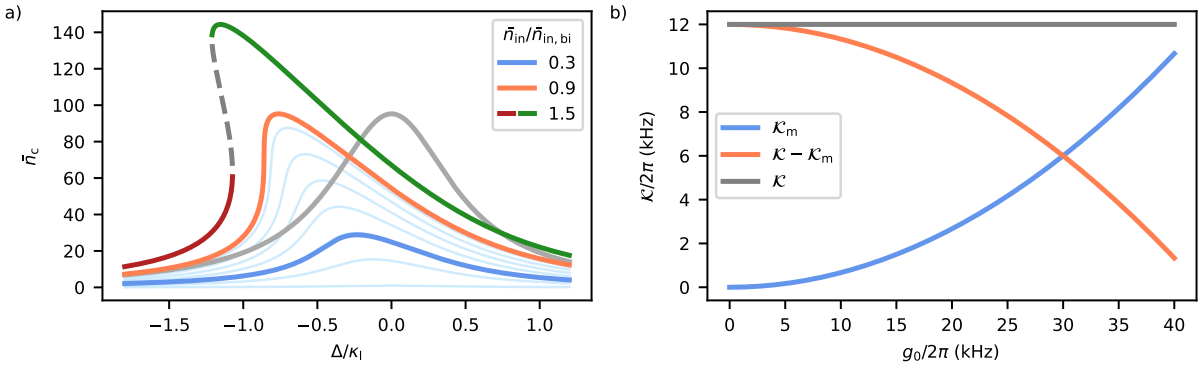

Fig. 2.2 **a)** Intracavity photon number for different drive strengths as a function of the drive detuning. For drive strength $\bar{n}_{in}/\bar{n}_{in,bi} > 1$ a bistable regime occurs with two stable solutions (red, green) and an unstable one (dashed). The gray curve corresponds to $\bar{n}_{in}/\bar{n}_{in,bi} = 0.9$ for a linear ($\mathcal{K} = 0$), but otherwise identical cavity. **b)** Comparison of the mechanical Kerr to intrinsic Kerr typically observed in the course of this thesis. Parameters used are $\kappa_l/2\pi = \kappa_c/2\pi = 1.5\,\mathrm{MHz}$, $\omega_m/2\pi = 300\,\mathrm{kHz}$, $\Gamma_m/2\pi = 0.5\,\mathrm{Hz}$ and $\mathcal{K}/2\pi = 12\,\mathrm{kHz}$.

equivalent to the point where $d\bar{n}_{in}/d\bar{n}_c = 0$. Assuming additionally that the cavity response remains continuous ($d^2\bar{n}_{in}/d\bar{n}_c^2 = 0$) at the bifurcation one can derive

$$\Delta_{bi} = -\frac{\sqrt{3}\kappa_l}{2} \quad , \quad \bar{n}_{bi} = \frac{\kappa_l}{\sqrt{3}\mathcal{K}_{eff}}. \tag{2.21}$$

Here, we obtained first the detuning Δ_{bi} at which bistability arises along with the corresponding intracavity photon number $\bar{n}_{bi}$. Substituting Eq. (2.21) into Eq. (2.17) yields the critical input photon number rate at the onset of bistability

$$\bar{n}_{in,bi} = \frac{\kappa_l}{\kappa_c}\frac{\kappa_l^2}{3\sqrt{3}\mathcal{K}_{eff}}. \tag{2.22}$$

In contrast to the theoretical work [53], we distinguish between the total loss rate and the coupling rate to allow for intrinsic losses taking into account experimental imperfections. Thus, the critical input power differs from their derivation by a factor κ_l/κ_c.

Notably, even an intrinsically linear cavity exhibits nonlinear behavior due to the optomechanical interaction with increasing g_0 (Eq. (2.18)). Up to typical coupling strengths of $g_0 < 5\,\mathrm{kHz}$ [3], this added nonlinearity is generally small compared to intrinsic nonlinearities observed throughout this thesis, as shown in Fig. 2.2b). Therefore, in the following chapters, we approximate $\mathcal{K}_{eff} \approx \mathcal{K}$.

2.3 Cavity Backaction

For optomechanical systems with mechanical frequencies from $\sim$ Hz to $\sim$ MHz, the mechanical mode remains in a thermally highly excited state due to the coupling to a thermal bath even at low temperatures down to $\sim 100\,\mathrm{mK}$. Following the Bose-Einstein distribution, the mechanical

occupation can be given as

$$\bar{n}_{\mathrm{m}}^{\mathrm{th}} = \frac{1}{e^{\hbar\omega_{\mathrm{m}}/k_{\mathrm{B}}T} - 1} \approx \frac{k_{\mathrm{B}}T}{\hbar\omega_{\mathrm{m}}}, \tag{2.23}$$

with the Boltzmann constant k_{B} and the bath temperature T. This results in an approximately linear temperature dependence for sufficiently low temperatures. To observe quantum phenomena, additional cooling is required to bring the mechanical mode to its motional ground state. Over the last decade, this goal was achieved through various approaches. For example, the mechanical mode was actively cooled by detecting its motion via the optomechanical interaction and applying a feedback scheme [60–62]. This is especially effective in systems where the cavity reacts much faster than the mechanical frequency ($\kappa_{\mathrm{l}} \gg \omega_{\mathrm{m}}$), making it a useful tool in highly unresolved systems. For more resolved systems ($\kappa_{\mathrm{l}} \leq \omega_{\mathrm{m}}$), this approach is not feasible. There, sideband or backaction cooling can be used, which utilizes radiation-pressure force from the cavity discussed in section 2.1.1. With this approach, the ground state was reached in several systems operating in the resolved regime [42, 63–65]. However, it remains challenging to use sideband cooling in systems with increasingly larger mechanical objects, which places them within the unresolved regime. In the following sections, we will discuss the effects of this scheme on the mechanics for systems in the unresolved regime and how an intrinsic Kerr-nonlinear cavity benefits the cooling capability. The changes occurring for the resolved regime are later discussed in section 2.3.4

2.3.1 Optomechanical damping and spring effect

To study the effects of the optomechanical interaction on the mechanical oscillator, we use the linearized Hamiltonian in Eq. (2.8), which allows an analytical description of the dynamics. We derive the dissipative dynamics of the fluctuations via the quantum Langevin equation as

$$\frac{d}{dt}\vec{\hat{A}} = \mathbf{M}\vec{\hat{A}} - \mathbf{K}\vec{\hat{A}}_{\mathrm{in}}, \tag{2.24}$$

with the mode operators $\vec{\hat{A}} = [\delta\hat{a}, \delta\hat{a}^\dagger, \hat{b}, \hat{b}^\dagger]^T$, the system input noise vector $\vec{\hat{A}}_{\mathrm{in}} = [\delta\hat{a}_{\mathrm{in}}, \delta\hat{a}_{\mathrm{in}}^\dagger, \hat{b}_{\mathrm{in}}, \hat{b}_{\mathrm{in}}^\dagger]^T$ combined with the decay rate matrix $\mathbf{K} = \mathrm{diag}(\sqrt{\kappa_{\mathrm{c}}}, \sqrt{\kappa_{\mathrm{c}}}, \sqrt{\Gamma_{\mathrm{m}}}, \sqrt{\Gamma_{\mathrm{m}}})$ and the dynamical matrix as

$$\mathbf{M} = \begin{bmatrix} i\tilde{\Delta} - \frac{\kappa_{\mathrm{l}}}{2} & i\mathcal{K}\bar{n}_{\mathrm{c}} & -ig & -ig \\ -i\mathcal{K}\bar{n}_{\mathrm{c}} & -i\tilde{\Delta} - \frac{\kappa_{\mathrm{l}}}{2} & ig & ig \\ -ig & -ig & -i\omega_{\mathrm{m}} - \frac{\Gamma_{\mathrm{m}}}{2} & 0 \\ ig & ig & 0 & i\omega_{\mathrm{m}} - \frac{\Gamma_{\mathrm{m}}}{2} \end{bmatrix}, \tag{2.25}$$

where we introduce the effective detuning $\tilde{\Delta} = \Delta + 2\bar{n}_{\mathrm{c}}\mathcal{K}$ and $g = g_0\sqrt{\bar{n}_c}$. The off-diagonal terms $\pm i\mathcal{K}\bar{n}_{\mathrm{c}}$ are a result of the single mode squeezing term in Eq. (2.8). Using the Fourier transformation defined by $\hat{\mathcal{F}}[\omega] = \int_{-\infty}^{\infty} dt e^{i\omega t}\hat{\mathcal{F}}[t]$ this set of equations can be solved for the mechanical mode $\hat{b}, \hat{b}^\dagger$ by moving to the frequency domain

$$\begin{bmatrix} \chi_{\mathrm{m}}^{-1}[\omega] - i\Sigma_{\mathrm{c}}[\omega] & -i\Sigma_{\mathrm{c}}[\omega] \\ i\Sigma_{\mathrm{c}}[\omega] & \chi_{\mathrm{m}}^{*-1}[-\omega] + i\Sigma_{\mathrm{c}}[\omega] \end{bmatrix} \begin{bmatrix} \hat{b}[\omega] \\ \hat{b}^\dagger[\omega] \end{bmatrix} = -\sqrt{\Gamma_m} \begin{bmatrix} \hat{b'}_{\mathrm{in}}[\omega] \\ \hat{b'}_{\mathrm{in}}^\dagger[\omega] \end{bmatrix}, \tag{2.26}$$

with the modified noise operator $\hat{b}'_{\mathrm{in}}$[1] and the mechanical susceptibility $\chi_{\mathrm{m}}^{-1}[\omega] = -i(\omega - \omega_{\mathrm{m}}) + \Gamma_{\mathrm{m}}/2$ which characterizes the response of the mechanics to external forces. From Eq. (2.26) it follows that the optomechanical interaction influences the coherent dynamics of the mechanical mode by altering its susceptibility with the cavity self-energy

$$\Sigma_{\mathrm{c}}[\omega] = 2\bar{n}_{\mathrm{c}} g_0^2 \frac{\bar{n}_{\mathrm{c}}\mathcal{K} - \tilde{\Delta}}{\tilde{\Delta}^2 - (\bar{n}_{\mathrm{c}}\mathcal{K})^2 + (\kappa_{\mathrm{c}}/2 - i\omega)^2}, \tag{2.27}$$

acting as an additional force on the mechanics. Within the weak coupling limit $\kappa_{\mathrm{l}} \gg g_0$ this additional force has the form of

$$\Sigma_{\mathrm{c}}[\omega] = -\delta\omega_{\mathrm{m}}[\omega] + \frac{i}{2}\Gamma_{\mathrm{OM}}[\omega], \tag{2.28}$$

where the first term corresponds to a mechanical frequency shift and the second term to optomechanical damping. Within the high-Q approximation ($\Gamma_{\mathrm{m}} \ll \omega_{\mathrm{m}}$), it is sufficient to evaluate the self-energy at the mechanical frequency as $\Sigma_{\mathrm{c}}[\omega] \approx \Sigma_{\mathrm{c}}[\omega_{\mathrm{m}}]$.

Optomechanical damping: In the weak coupling regime and high-Q approximation, one can evaluate Eq. (2.28) at $\omega = \omega_{\mathrm{m}}$ to get the optomechanical induced damping

$$\Gamma_{\mathrm{OM}} = 2\,\mathrm{Im}\{\Sigma_{\mathrm{c}}[\omega_{\mathrm{m}}]\} = 4g_0^2\bar{n}_{\mathrm{c}}\kappa_{\mathrm{l}} \frac{(\bar{n}_{\mathrm{c}}\mathcal{K} - \tilde{\Delta})\omega_{\mathrm{m}}}{\left[\tilde{\Delta}^2 - \omega_{\mathrm{m}}^2 + \frac{\kappa_{\mathrm{l}}^2}{4} - (\bar{n}_{\mathrm{c}}\mathcal{K})^2\right]^2 + \kappa_l^2\omega_{\mathrm{m}}^2}, \tag{2.29}$$

for an intrinsic nonlinear cavity. Assuming a linear cavity by $\mathcal{K} = 0$ this reduces to the commonly known equation from [23]

$$\Gamma_{\mathrm{OM}}|_{\mathcal{K}=0} = g_0^2\bar{n}_{\mathrm{c}}\left(\frac{\kappa_{\mathrm{l}}}{(\Delta + \omega_{\mathrm{m}})^2 + \kappa_{\mathrm{l}}^2/4} - \frac{\kappa_{\mathrm{l}}}{(\Delta - \omega_{\mathrm{m}})^2 + \kappa_{\mathrm{l}}^2/4}\right), \tag{2.30}$$

for the optomechanical damping. Together with its natural linewidth, the effective mechanical damping is given by

$$\Gamma_{\mathrm{m,eff}} = \Gamma_m + \Gamma_{\mathrm{OM}}. \tag{2.31}$$

As we see from Eq. (2.30) and also depicted in Fig. 2.3 for the linear case, a red-detuned drive $\Delta < 0$ results in $\Gamma_{\mathrm{OM}} > 0$, inducing extra damping and therefore cooling the mechanical mode. On the contrary, for a blue-detuned drive $\Delta > 0$, the mechanical mode is amplified (heated) due to an effective reduction of the damping rate $\Gamma_{\mathrm{OM}} < 0$. Regardless of the input power considered, the detuning corresponding to the maximum cooling/heating is constant and found at $\Delta = \mp\kappa_{\mathrm{l}}/4$ (see Fig. 2.3) for the unresolved sideband regime. In literature the optimal detuning is usually

[1] The modification of the noise operator is due to the radiation pressure force and can be explicitly written as

$$\hat{b}'_{\mathrm{in}}[\omega] = \hat{b}_{\mathrm{in}}[\omega] - i\sqrt{\frac{1}{\Gamma_{\mathrm{m}}}}\hat{F}[\omega],$$

with the radiation pressure given by

$$\hat{F}[\omega] = -g\sqrt{\kappa_{\mathrm{l}}}\left(\chi_{\mathrm{c}}[\omega]\delta\hat{a}_{\mathrm{in}}[\omega] + \chi_{\mathrm{c}}^{*}[-\omega]\delta\hat{a}_{\mathrm{in}}^{\dagger}[\omega]\right),$$

where we introduce the cavity susceptibilty $\chi_{\mathrm{c}}^{-1}[\omega] = -i(\omega - \omega_{\mathrm{c}}) + \kappa_{\mathrm{l}}/2$.

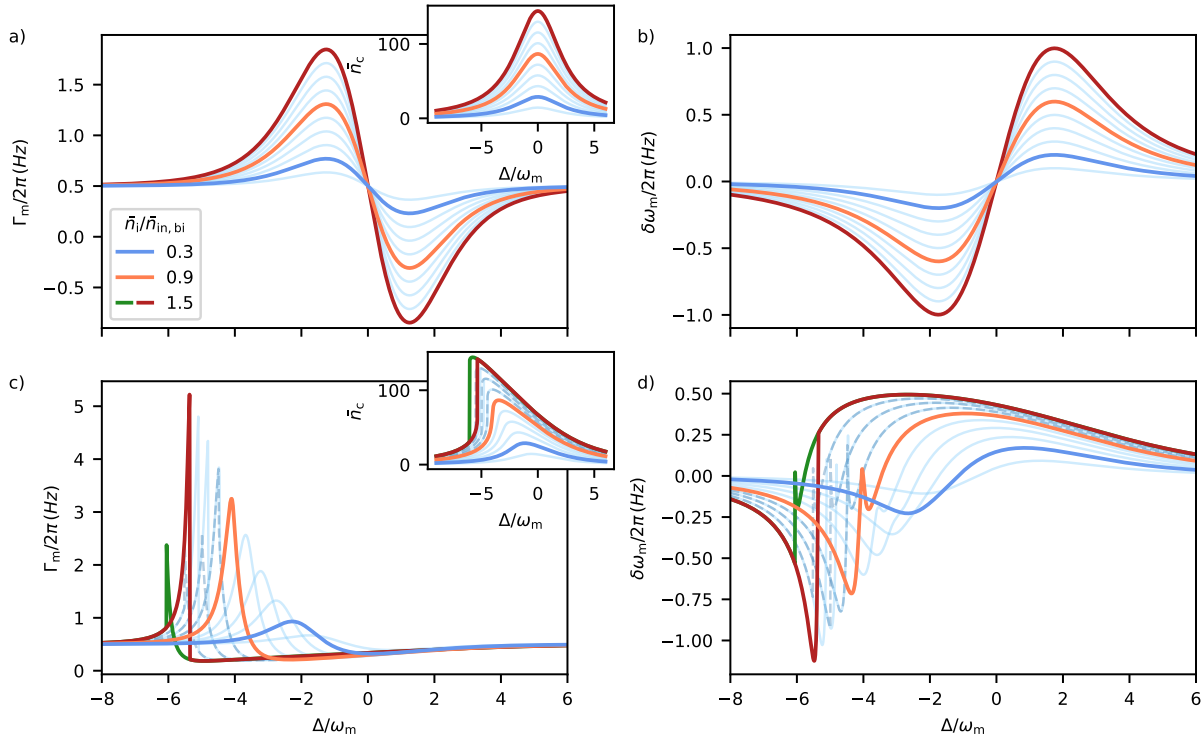

Fig. 2.3 Optical damping and optical spring effect against detuning for a linear cavity **a)-b)** and for a nonlinear cavity **c)-d)** for different pump strengths. Insets show the intracavity photon number for both cases. The solid red/green line and dashed blue line represent the solutions of the low/high photon number branch in the bistable regime of the nonlinear cavity. Parameters used are $\kappa_l/2\pi = \kappa_c/2\pi = 1.5\,\mathrm{MHz}$, $\omega_m/2\pi = 300\,\mathrm{kHz}$, $\Gamma_m/2\pi = 0.5\,\mathrm{Hz}$, $g_0/2\pi = 100\,\mathrm{Hz}$ and $\mathcal{K}/2\pi = 12\,\mathrm{kHz}$.

given as $\Delta = \mp\kappa_l/2$, which is the case for a constant intracavity photon number instead of a constant drive strength.

The effects of the nonlinearity on Γ_{OM} at the same input powers are visualized in Fig. 2.3 in comparison to the linear case. Due to $\mathcal{K}$ an increase in damping is observed further red-detuned from the bare cavity and over a narrower frequency range. In contrast, the anti-damping already occurs at red-detunings and extends over a larger frequency range. Furthermore, the overall induced optical damping is significantly enhanced for the nonlinear case, whereas the anti-damping is reduced, following the corresponding slopes in $\bar{n}_c$. These effects increase with drive power until close to bifurcation - orange trace in Fig. 2.3. After bifurcation two different regimes can be observed depending on the photon number branch. In comparison to the high photon number branch (green curve), the low photon number branch (red curve) features a larger additional damping. Both show an abrupt change right at the detuning, where the photon number jumps from one to the other branch. However, the range of detunings with optical damping subsequently narrows upon increasing the input power further, which makes it experimentally challenging to access.

Optical spring effect: In the weak coupling regime, the mechanical frequency shift, also called the optical spring effect, is derived as:

$$\delta\omega_{\mathrm{m}} = -\,\mathrm{Re}\{\Sigma_{\mathrm{c}}[\omega_{\mathrm{m}}]\} = -2g_0^2\bar{n}_{\mathrm{c}}\frac{(\bar{n}_{\mathrm{c}}\mathcal{K}-\tilde{\Delta})\left[\tilde{\Delta}^2-\omega_{\mathrm{m}}^2+\frac{\kappa_{\mathrm{l}}^2}{4}-(\bar{n}_{\mathrm{c}}\mathcal{K})^2\right]}{\left[\tilde{\Delta}^2-\omega_{\mathrm{m}}^2+\frac{\kappa_{\mathrm{l}}^2}{4}-(\bar{n}_{\mathrm{c}}\mathcal{K})^2\right]^2+\kappa_l^2\omega_{\mathrm{m}}^2} \tag{2.32}$$

Putting $\mathcal{K}=0$ one retrieves the equation for the linear spring effect as

$$\delta\omega_{\mathrm{m}}|_{\mathcal{K}=0} = g_0^2\bar{n}_{\mathrm{c}}\left(\frac{\Delta+\omega_{\mathrm{m}}}{(\Delta+\omega_{\mathrm{m}})^2+\kappa_{\mathrm{l}}^2/4}+\frac{\Delta-\omega_{\mathrm{m}}}{(\Delta-\omega_{\mathrm{m}})^2+\kappa_{\mathrm{l}}^2/4}\right). \tag{2.33}$$

In a linear system for a red detuned drive $\Delta<0$, this results in a spring-softening, meaning the mechanical frequency will decrease $\delta\omega_{\mathrm{m}}<0$. Whereas for a blue detuned drive $\Delta>0$, the interaction leads to a spring-hardening, causing the mechanical frequency to increase $\delta\omega_{\mathrm{m}}>0$. Here in the unresolved regime, the largest obtained spring softening/hardening aligns with the highest damping/anti-damping.
The influence of the nonlinearity on the spring effect is qualitatively similar to the one discussed for the optomechanical damping and is visualized in Fig. 2.3. However, the increasingly steep slope in $\bar{n}_{\mathrm{c}}$ close to bifurcation (orange curve) leads to a distinct feature not observed in the optical damping. Aligning with the largest damping rate the frequency shift drops towards zero, such that maximum damping does not correspond to the highest spring hardening anymore. This resembles qualitatively the backaction behavior observed in the resolved regime (see section 2.3.4).

2.3.2 Average mechanical occupation

We consider the conventional scattering framework to gain an intuitive understanding of the occupation of the mechanical mode in the presence of backaction. Within this picture, we assume that photons from an input drive can be scattered to lower/higher frequencies by creating/absorbing a mechanical phonon, causing it to heat up or cool down. Frequency up-scattering is called anti-Stokes process at a rate Γ_-, whereas its counterpart —frequency down-scattering —is referred to as Stokes process at rate Γ_+. To obtain a qualitative insight into the rates at which these processes occur, it is helpful to examine three distinct cases for the drive detuning. We start from the linearized interaction Hamiltonian in Eq. (2.10) and move to the interaction frame for both cavity and mechanics, which results in

$$\begin{aligned}\hat{\mathcal{H}}_{\mathrm{int}}^{\prime\mathrm{lin}} &= e^{i\hat{\mathcal{H}}_0^{\mathrm{lin}}}\hat{\mathcal{H}}_{\mathrm{int}}^{\mathrm{lin}}e^{-i\hat{\mathcal{H}}_0^{\mathrm{lin}}}\\ &= \hbar g\left(\delta\hat{a}\hat{b}e^{id_-t}+\delta\hat{a}^\dagger\hat{b}^\dagger e^{-id_-t}\right)+\left(\delta\hat{a}\hat{b}^\dagger e^{id_+t}+\delta\hat{a}^\dagger\hat{b}e^{-id_+t}\right),\end{aligned} \tag{2.34}$$

with $d_\pm=\Delta\pm\omega_{\mathrm{m}}$. In what follows, we neglect fast-rotating components within the rotating wave approximation and assume for simplicity $\mathcal{K}=0$.

- $\Delta\approx-\omega_{\mathrm{m}}$: This is called the *beamsplitter* interaction.

$$\hat{\mathcal{H}}_{\mathrm{int}}^{\prime\mathrm{lin}}/\hbar \approx g(\delta\hat{a}^\dagger\hat{b}+\delta\hat{a}\hat{b}^\dagger) \tag{2.35}$$

  Being red-detuned, only the exchange between excitations of the two modes is resonant. However, due to the cavity mode shape the anti-Stokes process is resonant with the cavity,

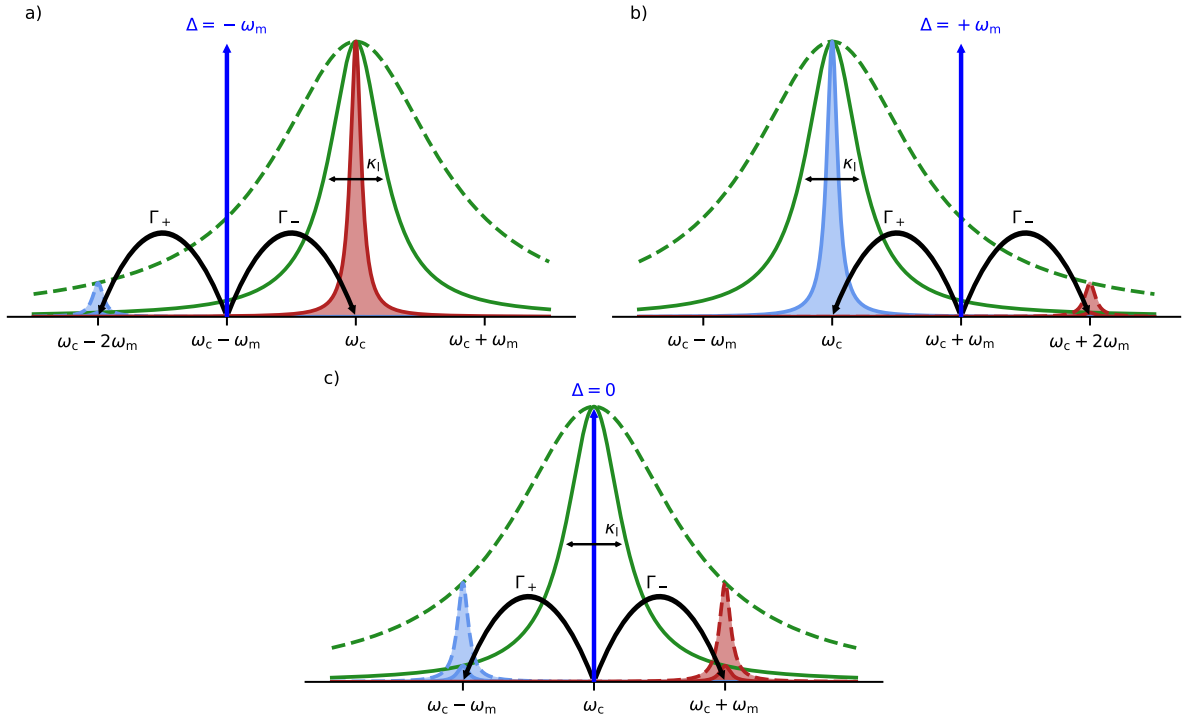

Fig. 2.4 Qualitative illustration of the three driving schemes discussed for the linearized Hamiltonian $\hat{\mathcal{H}}_{\text{int}}^{\prime\text{lin}}$. To emphasize the difference between the resolved and unresolved sideband regime, the cavity mode is shown via the photon number spectrum for both cases as the solid and dashed green lines, respectively. The influence of the cavity mode shape on the anti-Stokes (rate Γ_- (red)) and Stokes (rate Γ_+ (blue)) processes is visualized by their respective amplitudes. **a)** *beam-splitter* interaction with the drive red-detuned, allowing the cooling of the mechanical mode. **b)** *two-mode-squeezing* interaction with the drive blue detuned, creating correlated phonon-photon pairs, effectively exciting the mechanics. **c)** On resonance driving allows for the detection of the mechanical mode while avoiding backaction.

whereas its counterpart - the Stokes process - is suppressed due to the cavity mode shape in Fig. 2.4a). By continuously driving, this interaction can be effectively used to cool the mechanical mode.

- $\Delta \approx 0$:

$$\hat{\mathcal{H}}_{\text{int}}^{\prime\text{lin}}/\hbar \approx g(\delta\hat{a}^\dagger + \delta\hat{a})(\hat{b}^\dagger + \hat{b}) \tag{2.36}$$

Probed on resonance in Fig. 2.4c), the mechanical motion $(\hat{b}^\dagger + \hat{b})$ is imprinted on the phase quadrature, allowing us to detect the mechanical mode. Simultaneously, we avoid any backaction as Stokes and anti-Stokes processes cancel each other.

- $\Delta \approx +\omega_{\text{m}}$: Being blue detuned results in the so called *two-mode-squeezing* interaction:

$$\hat{\mathcal{H}}_{\text{int}}^{\prime\text{lin}}/\hbar \approx g(\delta\hat{a}^\dagger\hat{b}^\dagger + \delta\hat{a}\hat{b}) \tag{2.37}$$

Here, only the creation/annihilation of a phonon-photon pair with high correlations is resonant. Contrary to the beamsplitter interaction, being blue-detuned, the cavity mode shape leads to a suppression of Γ_- in comparison to Γ_+. This leads to an accumulation of excitation in both modes, effectively causing the mechanical mode to heat.

Fig. 2.4 illustrates the effect of the three different driving schemes. For both detuned cases in Fig. 2.4a) and 2.4b), it is evident that the cavity mode shape creates an imbalance between the Stokes and anti-Stokes processes. In the resolved case due to $\kappa_\mathrm{l} \ll \omega_\mathrm{m}$, this leads to very efficient control of the mechanical mode since the off-resonant process is completely suppressed. However, for the sideband unresolved regime $\kappa_\mathrm{l} \gg \omega_\mathrm{m}$ the imbalance is reduced, resulting in less efficient control. Nevertheless, cooling and heating of the mechanics remains possible in this regime. However, the cooling is limited due to the presence of the unwanted heating process. In the case of resonant driving illustrated in Fig. 2.4c), for both regimes Γ_- and Γ_+ are in balance, allowing backaction evading detection of the mechanical mode.

To quantify the cooling possible, we calculate the resulting mechanical mode occupation from the rates at which the Stokes and anti-Stokes processes occur. By applying Fermi's golden rule to the radiation pressure force $\hat{\mathcal{H}}_\mathrm{int} = \hat{F}\hat{x}$ the Stokes and anti-Stokes rates in the regime of weak coupling $\kappa_\mathrm{l} \gg g_0$ are given by

$$\Gamma_\pm = \frac{x_\mathrm{zpf}^2}{\hbar^2} S_{FF}(\omega = \mp\omega_\mathrm{m}) = g_0^2 S_{nn}(\omega = \mp\omega_\mathrm{m}), \tag{2.38}$$

with the force spectral density defined as $S_{FF}(\omega) = \int_{-\infty}^{+\infty} dt e^{i\omega t}\langle \hat{F}(t)\hat{F}(0)\rangle$. Due to the OM interaction, the force spectral density is directly related to the photon number spectrum S_nn, which can be written as

$$\begin{aligned} S_\mathrm{nn}[\omega] &= \int_{-\infty}^{\infty} dt\, e^{i\omega t}\, \langle (\hat{a}^\dagger\hat{a})(t)(\hat{a}^\dagger\hat{a})(0)\rangle \\ &= \bar{n}_\mathrm{c}\kappa_\mathrm{l} \frac{\left(-\tilde{\Delta} + \omega + \bar{n}_\mathrm{c}\mathcal{K}\right)^2 + \frac{\kappa_\mathrm{l}^2}{4}}{\left[\tilde{\Delta}^2 - \omega^2 + \frac{\kappa_\mathrm{l}^2}{4} - (\bar{n}_\mathrm{c}\mathcal{K})^2\right]^2 + \kappa^2\omega^2}. \end{aligned} \tag{2.39}$$

The optically induced linewidth takes the form

$$\Gamma_\mathrm{OM} = \Gamma_- - \Gamma_+ \quad \Rightarrow \quad \Gamma_\mathrm{m,eff} = \Gamma_\mathrm{m} + \Gamma_\mathrm{OM}. \tag{2.40}$$

Evaluating Eq. (2.39) for a single detuning at $\omega = \mp\omega_\mathrm{m}$ to get $\Gamma_\pm$, respectively, results in the same expression for Γ_OM as derived in Eq. (2.29).

Within the constraints of $\Gamma_\mathrm{m} \ll g \ll \kappa_\mathrm{l}, \omega_\mathrm{m}$, the steady-state phonon occupation under backaction can be expressed as [1]

$$\bar{n}_\mathrm{m} = \bar{n}_\mathrm{m}^\mathrm{th} \frac{\Gamma_\mathrm{m}}{\Gamma_- - \Gamma_+ + \Gamma_\mathrm{m}} + \frac{\Gamma_+}{\Gamma_- - \Gamma_+ + \Gamma_\mathrm{m}}. \tag{2.41}$$

[1] If these constraints do not hold, the mechanical occupation is given by

$$\bar{n}_\mathrm{m} = \int S_\mathrm{bb}[\omega]\frac{d\omega}{2\pi} = \int \langle b^\dagger[\omega] b[\omega]\rangle \frac{d\omega}{2\pi},$$

where the correlator can be obtained by the dynamics in Eq. (2.26).

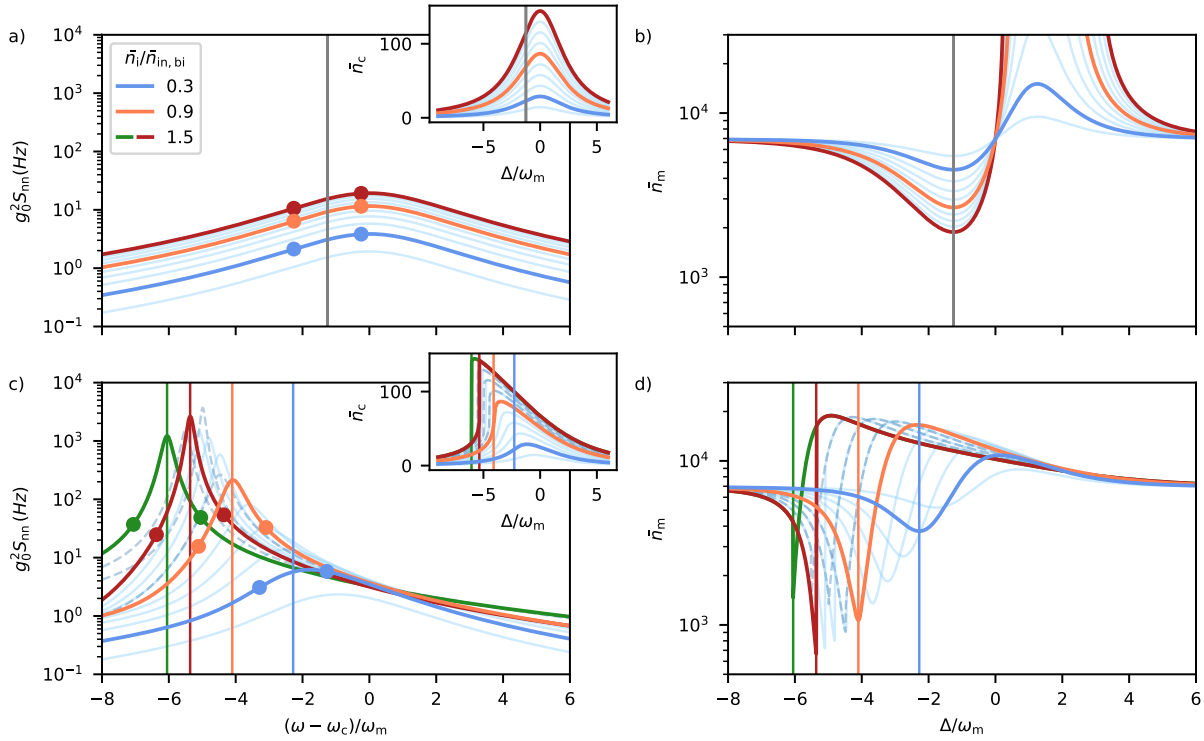

Fig. 2.5 Photon number spectrum for best cooling and phonon occupation for a linear **a)-b)** and for a nonlinear cavity **c)-d)** against drive detuning for different drive strengths. Insets show the intracavity photon number for both cases. For detuning associated with the best cooling (vertical lines) the corresponding anti-Stokes and Stokes rates are marked as dots in the photon number spectra at $\pm\omega_m$ from the drive. Parameters used are $\kappa_l/2\pi = \kappa_c/2\pi = 1.5\,\mathrm{MHz}$, $\omega_m/2\pi = 300\,\mathrm{kHz}$, $\Gamma_m/2\pi = 0.5\,\mathrm{Hz}$, $g_0/2\pi = 100\,\mathrm{Hz}$ and $\mathcal{K}/2\pi = 12\,\mathrm{kHz}$.

The first term represents the modified coupling rate to the bath resulting from the optomechanical interaction, which causes a change in the mechanical occupation. The second term corresponds to unwanted backaction heating, setting an overall limit to the achievable cooling, further discussed in section 2.3.3.

In Fig. 2.5, a cooling traces (phonon occupation numbers as a function of drive detuning) for a linear and a nonlinear system are depicted for various powers. We calculate the imbalance in Γ_-/Γ_+ from $S_{nn}[\omega]$ for each drive detuning and track the resulting phonon occupation. For each input power, the photon number spectrum $S_{nn}[\omega]$ corresponding to the drive detuning (vertical lines) associated with the minimal obtained phonon number is shown. The Stokes processes are indicated by the dots detuned by $\pm\omega_m$ from the drive.
In the linear case, $S_{nn}[\omega]$ has a Lorentzian shape and is symmetric around the resonance of the undriven system. This shape leads to an imbalance in Γ_-/Γ_+ such that for red detunings ($\Delta < 0$), cooling, and for blue detunings ($\Delta > 0$), heating, is observed. Since $S_{nn}[\omega]$ is symmetric around the resonance frequency, the imbalance and the corresponding backaction on the mechanics remain symmetric. As the shape of $S_{nn}[\omega]$ is independent of the drive strength, best cooling consistently occurs at $\Delta_{opt} = -\kappa_l/2$ for a given input power, with the phonon number decreasing as the power increases.

On the contrary, for a nonlinear system ($\mathcal{K} > 0$) in the presence of a strong drive, $S_{\mathrm{nn}}[\omega]$ develops an asymmetric shape accompanied by a shift of its resonance frequency. Both the asymmetry and frequency shift become more pronounced with increasing drive power (blue to orange trace in Fig. 2.5), causing the detuning for best cooling to move further to lower frequencies. Simultaneously, the range of detunings correlated to cooling subsequently narrows with increasing power. However, the increasing asymmetric shape of $S_{\mathrm{nn}}[\omega]$ enhances the imbalance in the Stokes processes, which leads to a more efficient cooling with overall lower phonon occupation compared to the linear case.
Upon exceeding the bistable input power $\bar{n}_{\mathrm{in,bi}}$ given in Eq. (2.22), $\bar{n}_{\mathrm{c}}$ and thus $S_{\mathrm{nn}}[\omega]$ splits into the low and high photon number branch within a certain frequency range corresponding to the red and green curves in Fig. 2.5. Within the bistable regime, an abrupt change in the rates can be observed right at the detuning where the photon number jumps from one to the other branch. A drive close to these detunings leads to a suppression of Γ_+ compared to Γ_-. Thus, a rapid increase in the cooling capability within the proximity of the switching is obtained in Fig. 2.5. However, to observe backaction in the bistable regime, it is crucial to be sufficiently close to these detunings. This makes cooling beyond bifurcation of the cavity susceptible to resonance frequency fluctuations, which can cause the cavity to switch branches, nullifying the observed backaction. Therefore, it is important to establish an experimental setup well isolated from external noise sources, like flux or vibrational noise, to avoid those switching events.

To emphasize the enhanced cooling capability due to the Kerr-nonlinearity Fig. 2.6 compares the minimal obtained phonon number $\bar{n}_{\mathrm{m}}$ at optimal detuning Δ_{opt} by increasing the input power, along with the corresponding intracavity photon number $\bar{n}_{\mathrm{c}}$, mechanical linewidth Γ_{m} and frequency shift $\delta\omega_{\mathrm{m}}$ for a linear and nonlinear cavity.
For a linear cavity, the shape of $S_{\mathrm{nn}}[\omega]$ is unaffected by the input power and thus the optimal detuning for cooling remains at $\Delta_{\mathrm{opt}} = -\kappa_{\mathrm{l}}/2$ (see inset Fig. 2.6a). This leads to a linear increase of $\bar{n}_{\mathrm{c}}$ with power at Δ_{opt}, resulting in a steadily decreasing phonon occupation. Due to the linear dependence on $\bar{n}_{\mathrm{c}}$ (Eq. (2.30)/(2.33)), Γ_{m} and $\delta\omega_{\mathrm{m}}$ follow a linear power dependence.
Comparing this to the nonlinear case, due to the power dependence of $S_{\mathrm{nn}}[\omega]$ the optimal detuning Δ_{opt} shifts following the steepest slope in $\bar{n}_{\mathrm{c}}$, which results in a nontrivial power dependence of the depicted parameters. Nevertheless, the higher cooling capability is evident as for the nonlinear cavity lower phonon occupations (e.g. a factor of ~ 3 at $\bar{n}_{\mathrm{in,bi}} = 1$) and corresponding higher Γ_{m} are observed for the same input power compared to the linear case. As discussed in section 2.3.1, an inflection point occurs for $\delta\omega_{\mathrm{m}}$ such that the highest spring softening occurs at a different detuning from that for best cooling. At $\bar{n}_{\mathrm{in,bi}} = 1$ we observe $\delta\omega_{\mathrm{m}} = 0$, which resembles cooling in the sideband-resolved regime. Even though increasing power beyond bistability leads to a further decrease in $\bar{n}_{\mathrm{m}}$ in the low photon number branch, the cooling feature becomes experimentally harder to access as it occurs in a narrow range of detunings.

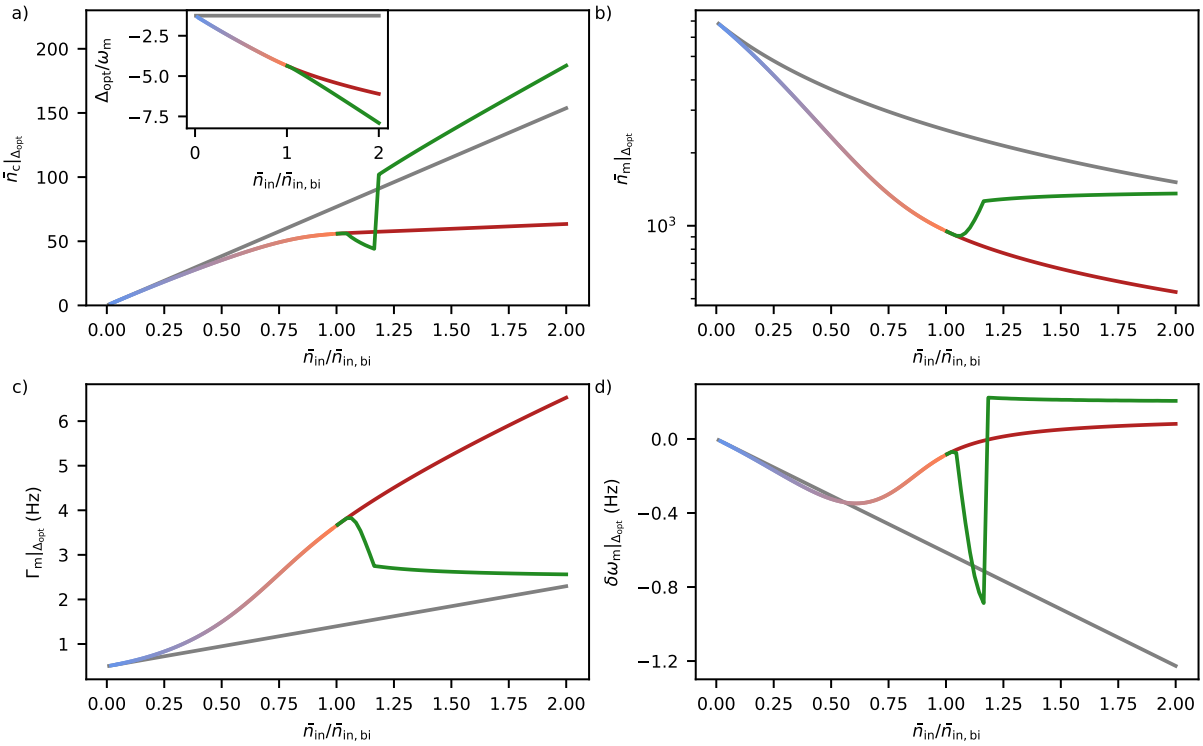

Fig. 2.6 Evaluated at optimal detuning Δ_{opt} (inset): **a)** Intracavity photon number $\bar{n}_{\mathrm{c}}$, **b)** minimal phonon occupation $\bar{n}_{\mathrm{m}}$ and mechanical **c)** linewidth Γ_{m} and **d)** frequency shift $\delta\omega_{\mathrm{m}}$ against input power for a linear cavity (grey) and a nonlinear cavity before (blue-orange) and after bistability for the low and high photon number branch (red and green). The input power for both cases is set normalized to $\bar{n}_{\mathrm{in}}/\bar{n}_{\mathrm{in,bi}}$ of the nonlinear cavity. Parameters used are $\kappa_{\mathrm{l}}/2\pi = \kappa_{\mathrm{c}}/2\pi = 1.5\,\mathrm{MHz}$, $\omega_{\mathrm{m}}/2\pi = 300\,\mathrm{kHz}$, $\Gamma_{\mathrm{m}}/2\pi = 0.5\,\mathrm{Hz}$, $g_0/2\pi = 100\,\mathrm{Hz}$ and $\mathcal{K}/2\pi = 12\,\mathrm{kHz}$.

2.3.3 Lowest phonon number

Within the scheme of backaction cooling, the lowest achievable phonon occupation is fundamentally limited by residual backaction heating originating from the cavity due to the coherent drive combined with Stokes processes. This *backaction limit* directly follows from Eq. 2.41 by assuming the mechanical mode is perfectly decoupled from the bath $\Gamma_{\mathrm{m}} = 0$ resulting in:

$$\bar{n}_{\mathrm{m}}^{\mathrm{min}} = \frac{\Gamma_+}{\Gamma_- - \Gamma_+} = \frac{1}{4}\frac{\left(-\tilde{\Delta} - \omega_{\mathrm{m}} + \bar{n}_{\mathrm{c}}\mathcal{K}\right) + \frac{\kappa_{\mathrm{l}}^2}{4}}{(-\tilde{\Delta} + \bar{n}_{\mathrm{c}}\mathcal{K})\omega_{\mathrm{m}}} \tag{2.42}$$

This expression reveals that the cooling limit is independent of the optomechanical coupling strength g_0, and instead is governed by the so-called *resolved sideband parameter* $\omega_{\mathrm{m}}/\kappa_{\mathrm{l}}$. In the unresolved limit $\omega_{\mathrm{m}}/\kappa_{\mathrm{l}} \ll 1$ the unwanted backaction prevents ground state cooling:

$$\bar{n}_{\mathrm{m}}^{\mathrm{min}} = \frac{\kappa_{\mathrm{l}}}{4\omega_{\mathrm{m}}} > 1 \tag{2.43}$$

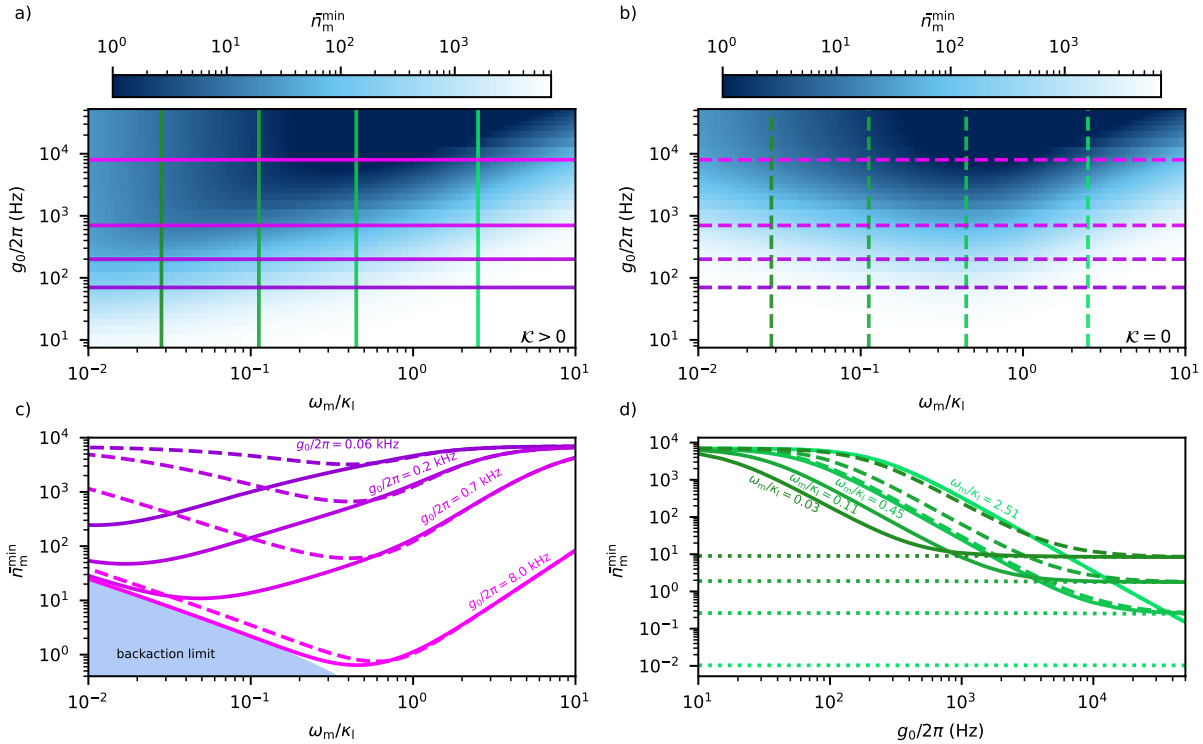

Fig. 2.7 Minimal phonon occupation versus resolved sideband parameter ω_m/κ_l and single photon coupling strength g_0 for **a)** a nonlinear and **b)** linear cavity. Colored lines correspond to linecuts with respect to ω_m/κ_l and g_0 displayed in **c)** and **d)**. Solid lines for $\mathcal{K} \neq 0$ and dashed lines for $\mathcal{K} = 0$. Backaction limit in **c)** shown as the colored area and in **d)** as dotted lines. Parameters used are $\omega_m/2\pi = 300\,\mathrm{kHz}$, $\Gamma_m/2\pi = 0.5\,\mathrm{Hz}$, $\mathcal{K}/2\pi = 12\,\mathrm{kHz}$ and $\bar{n}_{in}/\bar{n}_{in,bi} = 0.99$.

On the contrary, for the resolved regime $\omega_m/\kappa_l \gg 1$, the backaction heating process is suppressed such that ground state cooling is possible:

$$\bar{n}_m^{min} = \left(\frac{\kappa_l}{4\omega_m}\right)^2 < 1 \tag{2.44}$$

Fig. 2.7 depicts the dependence of the minimal phonon occupation on the coupling strength g_0 and the resolved sideband parameter ω_m/κ_l for a nonlinear and linear cavity. For each set of parameters, both systems are driven with the same input power corresponding to $\bar{n}_{in}/\bar{n}_{in,bi} = 0.99$ right before bistability to harness the increased cooling capability for the $\mathcal{K} \neq 0$ case. Comparing the colormaps depicted in Fig. 2.7a) and b) shows that in the nonlinear case, the cooling capability is improved, which is evident by the increased dark blue area indicating good cooling. This improvement is further illustrated by the linecuts along the ω_m/κ_l-axis (Fig. 2.7c). For $\omega_m/\kappa_l < 1$, the nonlinear cavity enhances cooling, where the enhancement is most pronounced at weaker coupling rates, whereas for higher coupling rates the effect diminishes as the system approaches the backaction limit. As the system becomes resolved $\omega_m/\kappa_l > 1$ the cooling remains unaffected by $\mathcal{K}$, as the optimal detuning $\Delta_{opt} = -\omega_m$ for cooling does not directly populate the cavity anymore. The linecuts along the g_0-axis (Fig. 2.7d) emphasize the improvement in cooling capability due to the $\mathcal{K}$ in the unresolved regime. For systems deeply in the unresolved regime, the backaction limit is reached for significantly smaller g_0 compared to a linear system.

However, the system is still backaction limited Eq. (2.42) and the improvement in cooling due to $\mathcal{K}$ decreases towards the resolved regime.

It is important to note that the input power is set to $\bar{n}_{\mathrm{in}}/\bar{n}_{\mathrm{in,bi}} = 0.99$. On the one hand, in Fig. 2.7c) this results in an effective increase in cooling at low $\omega_{\mathrm{m}}/\kappa_{\mathrm{l}}$ and weak coupling strength g_0 since the applied input power is larger ($\bar{n}_{\mathrm{in,bi}} \propto \kappa_{\mathrm{l}}^2$). The resulting larger input powers lead to higher $\bar{n}_{\mathrm{c}}$ and therefore lead to better cooling as the photon-enhanced coupling strengths g is increased. On the other hand, we observe a less efficient cooling for $\omega_{\mathrm{m}}/\kappa_{\mathrm{l}} > 1$ as the input power is not optimized but fixed. In the resolved regime, better cooling would be achievable by increasing $\bar{n}_{\mathrm{in,bi}}$, which also holds for the resolved trace in Fig. 2.7d).

2.3.4 Resolved sideband regime

As illustrated in Fig. 2.7, a nonlinearity does not influence the lowest attainable phonon number when in the resolved sideband regime. Therefore, this section considers an optomechanical system in the resolved regime with $\mathcal{K} = 0$ for simplicity.

As qualitatively shown in Fig. 2.4 a system residing in the resolved regime allows for effective cooling as the heating process is suppressed for red-detunings by the cavity mode shape. Best cooling is observed at $\Delta_{\mathrm{opt}} = -\omega_{\mathrm{m}} > \kappa_{\mathrm{l}}$, where the anti-Stokes process is resonant with the cavity. However, to maintain a high $g = g_0\sqrt{\bar{n}_{\mathrm{c}}}$ with the now off-resonant drive, high input powers are necessary to reach the ground state.
The changes in the backaction for a system advancing towards the resolved regime are depicted in Fig. 2.8 for a constant input drive (corresponding to $\bar{n}_{\mathrm{c}}|_{\Delta=0} = 40$) and for a constant intracavity photon number of $\bar{n}_{\mathrm{c}} = 40$. For both cases a shift of the optimal detuning from $\Delta_{\mathrm{opt}} = -\kappa_{\mathrm{l}}/2$ to $\Delta_{\mathrm{opt}} = -\omega_{\mathrm{m}}$ is observed. However, regarding the first case, the constant input power leads to a varying intracavity photon number with detuning. Thus, the best cooling is not observed for the highest $\omega_{\mathrm{m}}/\kappa_{\mathrm{l}}$, but for the semi-resolved regime around $\omega_{\mathrm{m}}/\kappa_{\mathrm{l}} \approx 0.5$, optimizing intracavity photon number and suppression of the backaction heating. Whereas for constant intracavity photon number, the best cooling is obtained for the highest $\omega_{\mathrm{m}}/\kappa_{\mathrm{l}}$ at $\Delta_{\mathrm{opt}} = -\omega_{\mathrm{m}}$. For both cases, the linewidth Γ_{m} aligns with respective cooling and heating features. However, the largest spring softening $\delta\omega_{\mathrm{m}}$ starts to deviate from the detuning corresponding to the best cooling as the resolved sideband parameter $\omega_{\mathrm{m}}/\kappa_{\mathrm{l}}$ increases. For the semi-resolved regime the spring effect vanishes around $\Delta = 0$, further evolving for larger $\omega_{\mathrm{m}}/\kappa_{\mathrm{l}}$ until the detuning at which $\delta\omega_{\mathrm{m}} = 0$ coincides with that for best cooling. For the plots in which the photon number is held constant, this feature is accompanied by a steep spring softening for $\Delta < -\omega_{\mathrm{m}}$ and hardening for $\Delta > -\omega_{\mathrm{m}}$.

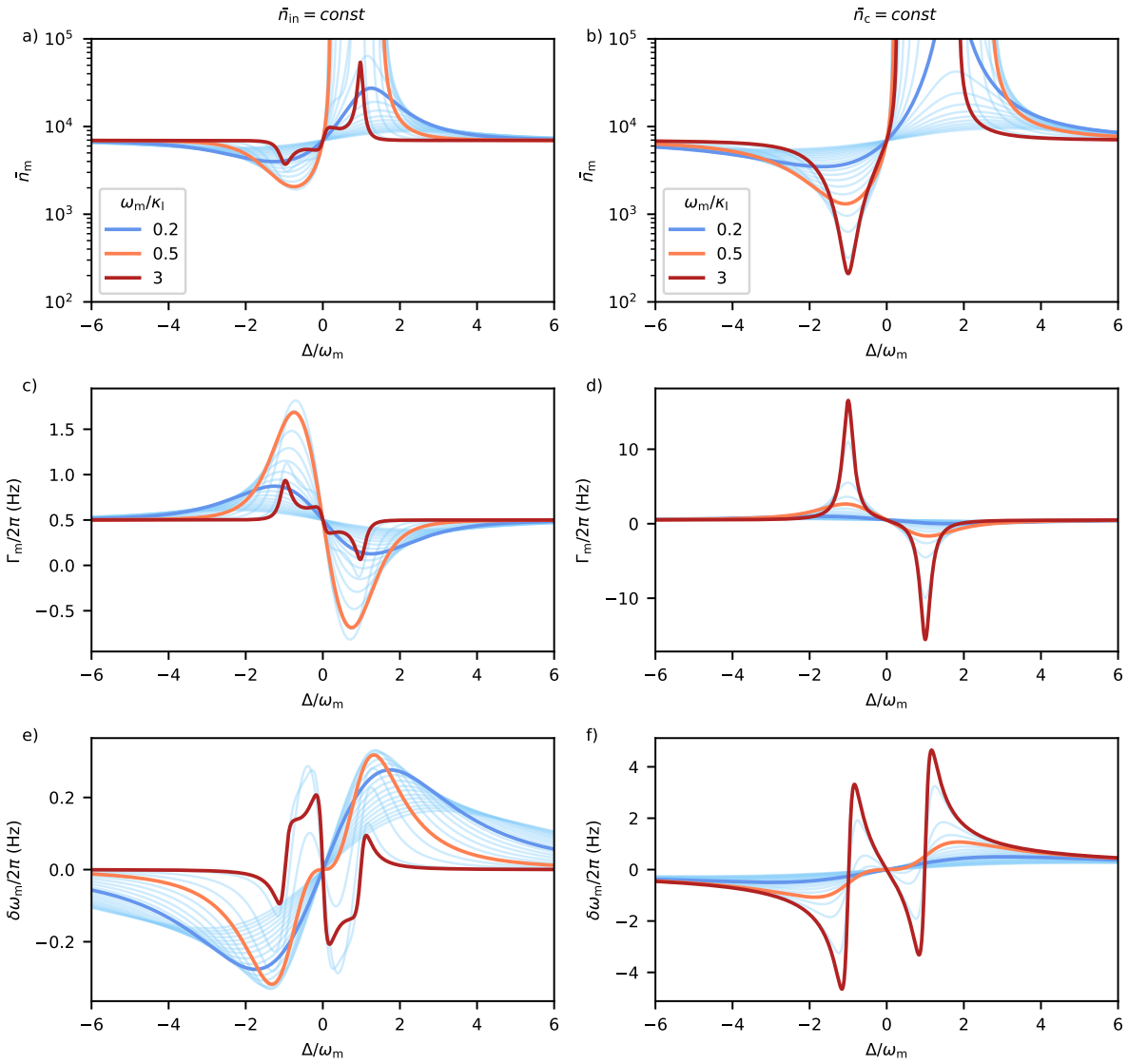

Fig. 2.8 Backaction on the mechanical mode as a function of the resolved sideband parameter ω_m/κ_l for a constant drive set to $\bar{n}_c|_{\Delta=0} = 40$ (**a,c,e**) and for a constant intracavity photon number of $\bar{n}_c = 40$ (**b,d,f**). Parameters used are $\omega_m/2\pi = 300\,\mathrm{kHz}$, $\Gamma_m/2\pi = 0.5\,\mathrm{Hz}$ and $g_0/2\pi = 100\,\mathrm{Hz}$.

CHAPTER 3

Superconducting microwave cavities

Since we use the toolbox of superconducting circuits in this work to realize an inductive coupling between a magnetically modified mechanical resonator and a microwave cavity, this chapter introduces the field of superconducting circuitry. First, we introduce LC-circuits as the building blocks of superconducting circuits. We cover the fundamentals of superconductivity and explain the working principle of the Josephson Junction (JJ), a key nonlinear element in these circuits. Subsequently, we introduce the Superconducting Quantum Interference Device (SQUID), which is based on the JJ and functions as a magnetic field-sensitive element. With these building blocks, we develop the concept of a flux-tunable resonator by introducing a SQUID into an LC-circuit and finally review the inductive coupling mechanism used in this thesis between the mechanical cantilever and such a SQUID-microwave cavity.

3.1 *LC*-circuits

LC-circuits form the basis of a wide range of electronic components, including filters, detectors, and information processing in quantum technologies. Their key properties, such as resonance frequency and spectral response, can be precisely engineered. In this thesis, the electromagnetic mode in the optical cavity introduced in section 2.1 is replace by that of such an LC-circuit with a resonance frequency in the microwave regime. This microwave cavity can be described by the circuit illustrated in 3.1a), consisting of an inductor L in parallel with a capacitor C. Furthermore, intrinsic loss mechanisms can be modeled as an additional resistive element R, which does not influence the resonance frequency of the cavity in case of weak damping but leads to a finite linewidth κ_i.

Hamiltonian Derivation: In the following, we will cover the key points in the derivation of the Hamiltonian for an LC-circuit, assuming no internal losses $R = 0$. For a full description, we recommend the following manuscript by U. Vool and M. Devoret [66].

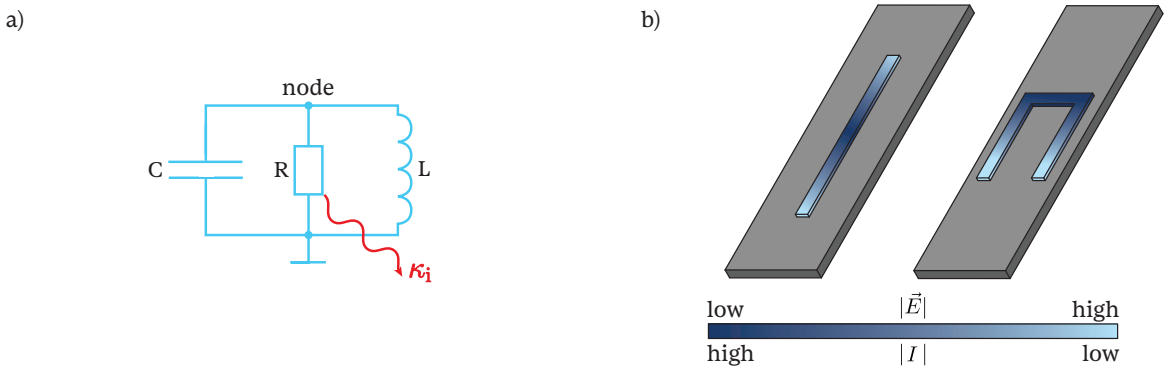

Fig. 3.1 **a)** Circuit representation of an LC-circuit, consisting of an inductor L and a capacitor C, connected in parallel. Intrinsic losses, occurring at a rate κ_i, are modeled by an additional resistor R. **b)** Two realizations - straight and U-shaped for a more compact design - of $\lambda/2$-microstrip resonators functioning as an LC-resonator. The electrical field $|\vec{E}|$ is maximal at the ends with a node at the center, whereas the current $|I|$ exhibits an antinode at the center.

We start by introducing the branch fluxes and charges

$$\begin{aligned} \Phi_b(t) &= \int_{-\infty}^{t} u_b(t')dt' \\ Q_b(t) &= \int_{-\infty}^{t} i_b(t')dt', \end{aligned} \tag{3.1}$$

by using the individual branch current i_b and voltage u_b. The energies of the respective components are given by

$$E_\mathrm{L} = \frac{1}{2L}\delta\Phi^2 \tag{3.2}$$

$$E_\mathrm{C} = \frac{1}{2C}\delta Q^2, \tag{3.3}$$

with $\delta\Phi$ (δQ) the node flux (charge) difference over the inductor (capacitor). With this, we derive the full Hamiltonian for $\Phi_0, Q_0 = 0$ at the ground node as

$$\mathcal{H} = \frac{Q^2}{2C} + \frac{\Phi^2}{2L}, \tag{3.4}$$

with the magnetic flux Φ in the inductor and charge Q on the capacitor. Quantization of this Hamiltonian is achieved by introducing the corresponding quantum operators $\hat{\Phi}, \hat{Q}$, which have to fulfill the commutator relation $[\hat{\Phi}, \hat{Q}] = i\hbar$. Further, we write these operators in terms of the creation and annihilation operators $\hat{a}^\dagger$ and $\hat{a}$ as

$$\begin{aligned} \hat{\Phi} &= \sqrt{\frac{\hbar Z_0}{2}}(\hat{a} + \hat{a}^\dagger) \\ \hat{Q} &= \sqrt{\frac{\hbar}{2Z_0}} i(\hat{a} - \hat{a}^\dagger), \end{aligned} \tag{3.5}$$

with the characteristic circuit impedance $Z_0 = \sqrt{L/C}$. Using the commutator relation $[\hat{a}, \hat{a}^\dagger] = 1$ and plugging Eq. (3.5) into Eq. (3.4), the quantized Hamiltonian reads

$$\hat{\mathcal{H}}/\hbar = \omega_\mathrm{c}(\hat{a}^\dagger a + \frac{1}{2}) \tag{3.6}$$

where the resonance frequency is given by $\omega_\mathrm{c} = \sqrt{1/LC}$.
As we assumed a lossless circuit, the resulting eigenstates lead to infinitely sharp energy levels spaced by $\hbar\omega_\mathrm{c}$.

Microstrip $\lambda/2$-cavities: One of the simplest distributed element realization of a LC-circuit is a half-wave ($\lambda/2$) cavity as illustrated in Fig. 3.1b). A strip of conducting material is patterned onto a dielectric substrate, such as silicon or sapphire. Even though the theoretical description of such a cavity is more complex, we can describe it by modeling each infinitesimal segment of the strip as an inductance and capacitance (transmission line model [67]). Each of its modes can be effectively described by an LC-circuit with a corresponding value for the inductance and capacitor. Due to open boundary conditions at both ends, the fundamental mode is the $\lambda/2$-mode with length $l = \lambda/2$. Also considering higher-order modes that fulfill the boundary conditions, the resonance frequency ω_c for the k-th mode is given by

$$\omega_{\mathrm{c,k}} = (k+1)2\pi\frac{v_0}{2l}, \tag{3.7}$$

with the speed of light v_0 in the transmission line. For the fundamental mode $k = 0$, the resulting electrical field $|\vec{E}|$ and current $|I|$ distributions are color-encoded in Fig. 3.1b). Whereas $|\vec{E}|$ exhibits a node at the center of the strip, the current shows an antinode at this location. Deviations from the straight stripline geometry — such as adopting a meandered or U-shaped design — can be exploited to achieve a more compact structure. Such modifications typically result in shifts in the resonance frequency ω_c, caused by changes in the effective capacitance.

Loss mechanisms: For actual circuits such as microstrip $\lambda/2$-cavities, the assumption of $R = 0$ does not hold anymore. Any external coupling to an environment κ_c and various internal loss channels κ_i result in a finite total or loaded linewidth $\kappa_\mathrm{l} = \kappa_\mathrm{c} + \kappa_\mathrm{i}$ of the energy levels. A common way to compare losses for different samples is by the quality factor Q_l defined as

$$Q_\mathrm{l} = \omega_\mathrm{c}\frac{\text{energy stored}}{\text{energy lossrate}} = \omega_\mathrm{c}RC = \frac{\omega_\mathrm{c}}{\kappa_\mathrm{l}}. \tag{3.8}$$

The external coupling κ_c is typically a design parameter and can be varied over a few orders of magnitude as required. However, the internal loss rate κ_i arises from a variety of mechanisms. One main mechanism is conductive loss within the cavity material, which can be mitigated by using superconducting materials such as niobium or aluminum below their critical temperature (see section 3.2). Besides reducing conductive loss for superconductors, another benefit of the low temperatures necessary – typically below 1 K – is that the microwave-cavities are brought to or close to their ground state. However, even at these temperatures, high magnetic fields can lead to conductive losses due to a reduction of the Cooper pair density and the creation of flux vortices [68, 69]. To diminish conductive losses in the substrate, high resistive silicon or sapphire wafers are used in the fabrication to ensure high quality factors. Any conductive material in close vicinity to areas of high $|\vec{E}|$ (e.g. copper from the surroundings) leads to the induction of eddy currents, adding to the total loss of the cavity [70].

Another common loss channel are two-level-systems (TLS). These TLSs reside at the substrate surface, within fabrication residues such as photoresist or any other amorphous oxide layer formed on the stripline material [71–74]. By coupling to the cavity mode, they add to the intrinsic loss rate.

3.2 Superconductivity and Josephson Junctions

This section covers only the elements of superconductivity necessary to describe processes displayed in the experiment and is mainly based on the references [75] and [76]. For a broader and complete overview, the reader is referred to these manuscripts.

3.2.1 Superconductivity

Superconductivity is a material property exhibited by materials that have no electrical resistance and expel magnetic fields from their volume (the Meißner-Ochsenfeld effect) below a specific critical temperature T_c. The origin of these effects is explained by an atomic lattice mediate attractive force between two electrons, causing them to form *Cooper pairs*. Forming a bosonic ensemble of spin 1 particles, these pairs condense into a coherent state across the superconductor with an energy gap of $\mathcal{G} = 1.76 k_\mathrm{B} T_\mathrm{c}$. This prevents the pairs from scattering with the atomic lattice, which is the primary cause of electrical resistance in normal conducting materials. Within the BCS-theory (named after J. Bardeen, L. Cooper, and J. R. Schrieffer), the collective ground state of the condensate is described by a single macroscopic matter wavefunction

$$\Psi(\vec{r},t) = \sqrt{\bar{n}_\mathrm{s}(\vec{r},t)} e^{i\theta(\vec{r},t)}, \tag{3.9}$$

with the phase $\theta(r,t)$ and the Cooper pair density $\bar{n}_\mathrm{s}(r,t)$ as a function of position $\vec{r}$ and time t. Being an inherently quantum effect, the Cooper pairs obey the Schrödinger equation for charged particles in an electromagnetic field. By plugging Eq. (3.9) into the Schrödinger equation, we derive the supercurrent density $\vec{J}_\mathrm{s}$

$$\Lambda \vec{J}_\mathrm{s}(r,t) = -\vec{A}(r,t) + \frac{\hbar}{2e} \nabla\theta(\vec{r},t), \tag{3.10}$$

with the London parameter $\Lambda = m_\mathrm{e}/2\bar{n}_\mathrm{s}e^2$ and the vector potential $\vec{A}(\vec{r},t)$[1]. This shows that a supercurrent can be created by either an electric field or a phase gradient across the superconductor.

Meißner-Ochsenfeld effect: Taking the curl of Eq. (3.10) and utilizing the Maxwell equation $\nabla \times B = \mu_0 \vec{J}_\mathrm{s}$ in combination with vector identities yields

$$\nabla^2 \vec{B} = \frac{1}{\lambda_\mathrm{L}^2} \vec{B}. \tag{3.11}$$

This implies that inside a superconductor, a magnetic field decays exponentially over a characteristic decay length given by the London penetration depth $\lambda_\mathrm{L} = \sqrt{m_\mathrm{e}/2\mu_0\bar{n}_\mathrm{s}e^2}$. For common superconductors such as niobium and aluminum, values around $\lambda_\mathrm{L}^\mathrm{Nb} \approx 85\,\mathrm{nm}$ and $\lambda_\mathrm{L}^\mathrm{Al} \approx 50\,\mathrm{nm}$ are found for the bulk material [76]. For thin films, these values vary with the thickness. Reapplying Maxwell's equations, we obtain that the supercurrent also decays exponentially towards its center. E.g. for a superconductor in the xy-plane and an external field $\vec{B} = B\vec{e}_\mathrm{x}$ it follows that $\vec{B}_\mathrm{x}(z) = B_0 e^{-z\lambda_\mathrm{L}}$ and $J_\mathrm{s,y} = J_\mathrm{y,0} e^{-z/\lambda_\mathrm{L}}$.

[1] The Vector potential $\vec{A}(\vec{r},t)$ is related to the magnetic field by $\nabla \times \vec{A} = \vec{B}$ and the electric field by $\vec{E} = -\frac{\partial \vec{A}}{\partial t} - \nabla\phi$ with ϕ being the scalar electric potential.

Types of superconductors: To expel the magnetic field, screening currents are formed on the surface. Above a critical field B_c, the energy required to create sufficiently high screening currents would exceed the gap energy of the condensate $\mathcal{G}$. At this point, we differentiate between two types of superconductors:

- **Type 1 superconductors** expel magnetic fields until the critical field B_c is reached. Beyond B_c they transition to their normal (nonsuperconducting) state and magnetic fields can penetrate them again. For bulk aluminum, a type 1 superconductor, the critical magnetic field is around 10.5 mT.
- **Type 2 superconductors** behave similiar to type 1 until a first critical field $B_{\mathrm{c},1}$, upon which it becomes energetically favorable to form vortices. These vortices exhibit a normal conducting core, allowing the magnetic field to pass through the superconductor. Further increasing the field, the number of vortices continues to rise until a second critical field is reached at which superconductivity breaks down. For Niobium, a type 2 superconductor, the first and second critical fields are typically 150 mT and 300 mT, respectively [76].

In the case of superconducting LC-circuits, the presence of magnetic fields even below B_c is associated with a reduction of the quality factor [68, 69]. Breaking of Cooper pairs, interaction of vortices with the microwave field [77], or trapped flux at defects create additional dissipative channels due to the presence of normal conducting electrons.

Flux-Quantization: Integrating Eq. (3.10) around a closed contour C within the superconductor enclosing a surface S, we find

$$\frac{\hbar}{2e}\oint_C \nabla\theta(\vec{r},t)d\vec{l} = \oint_C (\Lambda\vec{J}_s)d\vec{l} + \int_S \vec{B}d\vec{s} = \oint_C (\Lambda\vec{J}_s)d\vec{l} + \Phi = n\Phi_0. \tag{3.12}$$

Here we used the requirement that the macroscopic wavefunction is well defined up to an integer of 2π in the phase $\theta(\vec{r},t) = \theta_0(\vec{r},t) + 2n\pi$. This implies, that the flux Φ enclosed within C is an integer multiple of the *flux quantum*

$$\Phi_0 = h/2e, \tag{3.13}$$

as we can take the contour integral within the bulk, where we find $\vec{J}_\mathrm{s} = 0$. Within a simply connected region, all the magnetic field is expelled, leading to $n = 0$, whereas for a contour including nonsuperconducting regions like vortices or rings, we find that the flux threading a loop is quantized by $\Phi = n\Phi_0$.

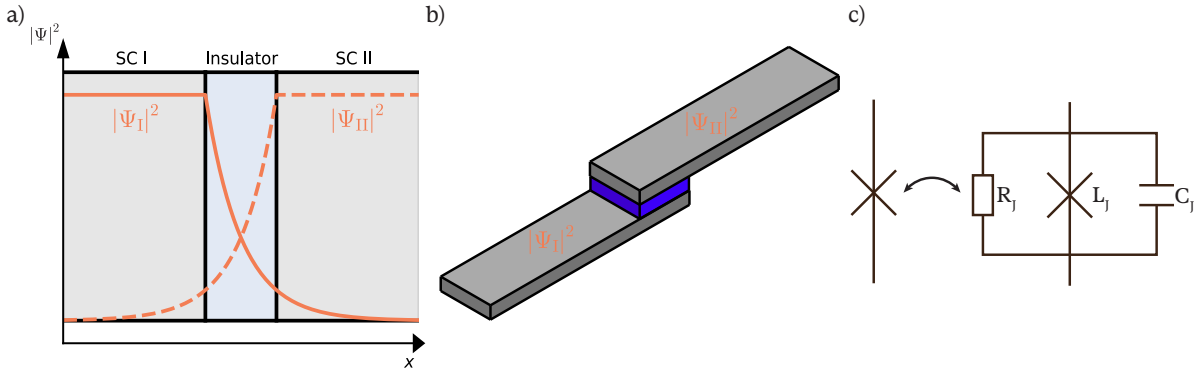

Fig. 3.2 **a)** Schematic representation of the Josephson Junction with the overlap of the macroscopic wavefunction Ψ. **b)** Sketch of a Josephson Junction, two superconducting layers are separated by an insulator. **c)** Circuit representation of the ideal Josephson junction and complete depiction within the RCSJ model including junction resistance R_J, capacitance C_J, and inductance L_J.

3.2.2 Josephson junctions

Josephson junctions, first postulated by B. D. Josephson in 1962 [78], consist of two superconductors separated by a thin insulating barrier, as illustrated in Fig. 3.2. The macroscopic wavefunctions describing the Cooper pairs in each superconductor extend slightly into the insulating region, which acts as a potential barrier. This spatial overlap enables the quantum mechanical tunneling of Cooper pairs across the junction, leading to a supercurrent whose amplitude depends on both the geometry of the junction – the barrier thickness and effective area – and on the materials used.

Josephson-equations: The current I and voltage V across the JJ are given by the first and second Josephson equations

$$I = I_\mathrm{c} \sin(\delta) \tag{3.14a}$$

$$\dot{\delta} = \frac{2\pi}{\Phi_0} V. \tag{3.14b}$$

Here, $\delta = \theta_2 - \theta_1$ is the phase difference of the superconducting wavefunction across the junction and I_c the critical current. I_c corresponds to the current at which superconductivity breaks down and the junction becomes normal conducting.

Josephson-inductance: Furthermore, the JJ behaves as a nonlinear inductive element; this becomes evident by taking the time derivative of Eq. (3.14a) and substituting $\dot{\delta}$ in Eq. (3.14b). After which, we derive

$$V = L_\mathrm{J}(\delta)\dot{I} = \frac{L_{\mathrm{J},0}}{\cos(\delta)}\dot{I} \tag{3.15}$$

where we introduce the Josephson inductance as

$$L_{\mathrm{J}0} = \frac{\Phi_0}{2\pi I_\mathrm{c}}. \tag{3.16}$$

As the total junction inductance L_J depends on the current I, the characteristic inductance of the JJ is nonlinear. To get an explicit form of the inductance, we use the branch flux $\Phi_b(t) = \int_{-\infty}^{t} V(t')dt'$ across the JJ. This allows us to rewrite the current relation as

$$I(t) = I_\mathrm{c} \sin\left(\frac{2\pi}{\Phi_0}\Phi_\mathrm{b}(t)\right). \tag{3.17}$$

Using the general definition that current is related to the branch flux via the inductance, we derive the explicit equation for the Josephson inductance to be

$$L_\mathrm{J} = \frac{\Phi_\mathrm{b}(t)}{I(t)} = \frac{\Phi_0}{2\pi}\frac{\arcsin\left(I/I_\mathrm{c}\right)}{I} \approx L_{\mathrm{J}0}\left[1 + \frac{1}{6}\left(\frac{I}{I_\mathrm{c}}\right)^2\right]. \tag{3.18}$$

To lowest order, L_J increases quadratically with current, until the applied current exceeds I_c.

RCSJ-model: To describe the dynamics of the JJ in the presence of a transport current I, we work within the *Resistively and Capacitively Shunted Junction* (RCSJ) model. Here, we assume that a resistive element R_J and a capacitance C_J are in parallel to the ideal junction, as shown in 3.2b). R_J corresponds to a normal conductive channel across the junction, and C_J arises due to the proximity of the junction electrode representing a classical conductor. The total current across is then given by

$$I_\mathrm{c}\sin\left(\delta\right) + \frac{V}{R_\mathrm{J}} + C_\mathrm{J}\dot{V} = I. \tag{3.19}$$

As long as the applied current does not exceed the critical current $I < I_\mathrm{c}$ and $T \ll T_\mathrm{c}$, the JJ remains superconducting and the quasiparticle density small. Therefore, we can completely neglect the normal conducting channel assigned to the resistive element R_J as it is shorted by the JJ. With that, we rewrite the current using the Josephson equations and obtain

$$\frac{\ddot{\delta}}{\omega_\mathrm{pl}^2} = j - \sin\left(\delta\right) = -E_\mathrm{J}\frac{\partial E_\mathrm{pot}}{\partial \delta}, \tag{3.20}$$

where we introduce the plasma frequency $\omega_\mathrm{pl} = \sqrt{2\pi I_\mathrm{c}/\Phi_0 C_\mathrm{J}} = 1/\sqrt{L_\mathrm{J}C_\mathrm{J}}$, the Josephson energy $E_\mathrm{J} = \frac{\Phi_0}{2\pi}I_\mathrm{c}$ and the normalized current $j = I/I_\mathrm{c}$. This resembles the equation of a phase particle of mass $m_\mathrm{eff} = \Phi_0/2\pi C_\mathrm{J}$ in the potential landscape of E_pot [79]. For a more intuitive insight into its dynamics, we solve Eq. (3.20) and derive

$$E_\mathrm{pot}(\delta)/E_\mathrm{J} = (1 - \cos\left(\delta\right)) - j\delta, \tag{3.21}$$

resembling a tilted washboard potential. The first term corresponds to the periodic junction energy, and the second term is a generalized force on the particle due to the applied current. For $j = 0$, the particle remains within one of the minima of E_pot. Applying a current tilts the potential, allowing the particle to roll down the potential landscape as soon as $|I| > I_\mathrm{c}$. Any resistance within the system corresponds to the particle's friction.

Josephson Junctions in a magnetic field: As we couple our mechanical resonator inductively to the LC-cavity by utilizing a strong permanent magnet (as presented in section 3.4), it is important to discuss the behavior of a JJ in presence of an inplane magnetic field $\vec{B} = B_\mathrm{y}$ as illustrated in Fig. 3.3a). As the magnetic field decays exponentially with λ_L in the superconducting electrodes, the effective barrier thickness is given by $t_\mathrm{B} = d + 2\lambda_\mathrm{L}$ for a junction electrode

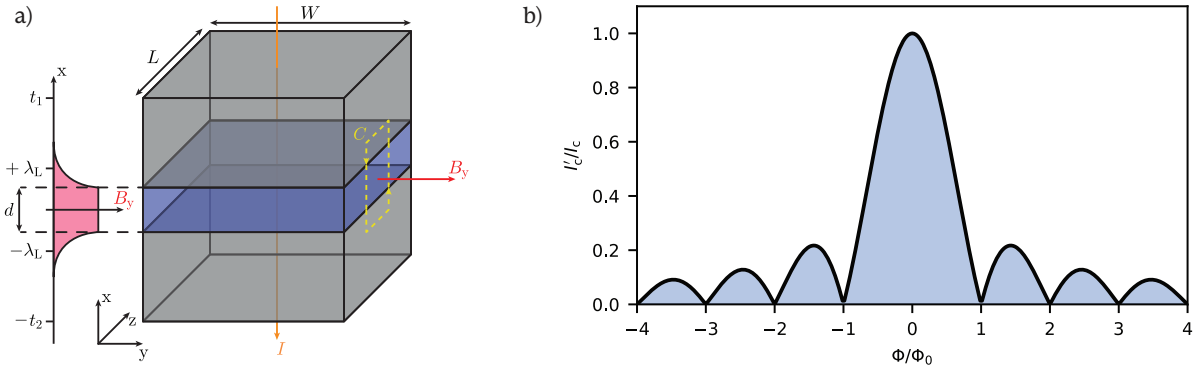

Fig. 3.3 **a)** Schematic illustration of a JJ (blue barrier, grey electrodes) with an applied magnetic field along the y-axis and current I along the x-axis. Dimension of the electrodes are given by the length L, width W and thicknesses t_1 and t_2. The axis on the left visualizes the surface penetration of the magnetic field by λ_L, adding to the effective barrier thickness d (Picture modified from [76]). **b)** Fraunhofer pattern for the effective critical current of the JJ caused by an in-plane magnetic field with Φ being the flux enclosed by the junction cross section.

separation of d. Using Eq. (3.10) and the fact that the phase change along a closed contour C is given by $\oint_C \nabla\theta = 2\pi n$ (due to the wavefunction being well defined and single valued), the supercurrent density across the JJ can be expressed as

$$J_s(z) = J_c \sin(kz + \phi_0), \tag{3.22}$$

with $k = \frac{2\pi}{\Phi_0} t_B B_y$ and a homogenous distribution of the critical Josphson current density J_c. To take a phase differenz at $z = 0$ into account we add the integration constant ϕ_0. Applying an in-plane magnetic field leads to a sinusoidally varying J_s along the z-direction, with period $\Delta z = 2\pi/k = \Phi_0/t_B B_y$. With the periodicity and the magnetic thickness, we see that the total flux within a period is given by $\Phi = t_B \Delta z B_y = \Phi_0$.
The overall current through the junction can be calculated by the integral $\int\int J_s(z) dy dz$ over the junction area. Inserting Eq. (3.22) and the boundary condition that J_c is homogeneous within and zero outside the junction boundaries, one finds that the effective critical Josephson current is given by the Fraunhofer diffraction pattern

$$I'_c = I_c \left| \frac{\sin(\pi\Phi/\Phi_0)}{(\pi\Phi/\Phi_0)} \right|, \tag{3.23}$$

where $\Phi = B_y t_B L$ is the total flux through the junction barrier as depicted in Fig. 3.3b).
As a final note, we have to take into account that each electrode will expel magnetic fields from its interior. Using symmetry arguments, half of the expelled field from each electrode should be focused towards the junction, increasing the effective junction area $A_{eff} = L(t_1 + t_2)/2$ over which the junction picks up the magnetic flux. This flux can be given to the first order by

$$\Phi = B_y A_{eff}. \tag{3.24}$$

3.2.3 DC-SQUID

Two JJs combined in parallel within a loop form a device known as a *Direct Current Superconducting QUantum Interference Device* (DC-SQUID, or SQUID) as depicted in Fig. 3.4. As we

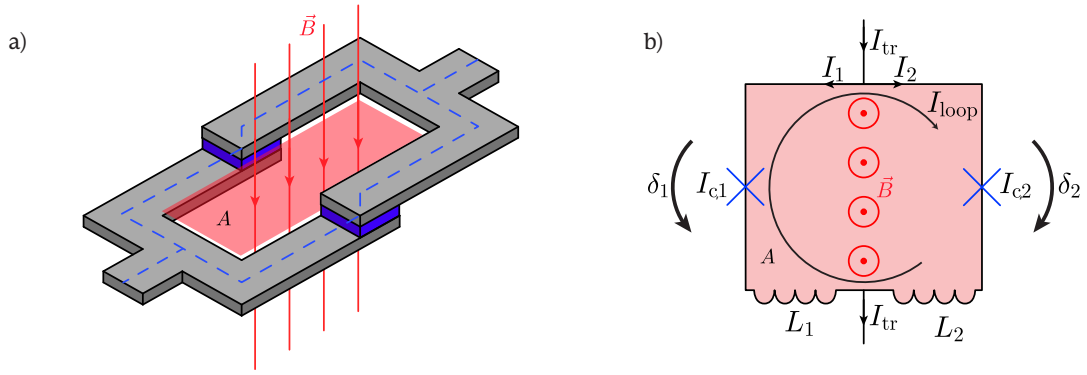

Fig. 3.4 **a)** Illustration of DC-SQUID consisting of two JJs in parallel. A magnetic field $\vec{B}$ penetrating the loop area A creates a periodically tunable critical current due to flux quantization. **b)** Circuit of the squid loop showing the individual junctions and linear inductances of each SQUID arm with a transport current I_{tr} and loop current I_{loop}.

demonstrate in this chapter, a SQUID exhibits a high magnetic sensitivity, making it ideal to mediate the inductive coupling between our magnetic cantilever and our microwave cavity.

SQUID-currents: Using Kirchhoff's law, we obtain the normalized transport current through the SQUID as

$$\begin{aligned} j_{tr} &= \frac{I_{tr}}{I_c} = \frac{1}{I_c}(I_1 + I_2) \\ &= (1-\alpha)\sin(\delta_1) + (1+\alpha)\sin(\delta_2) \\ &= 2\sin(\delta_+)\cos(\delta_-) + 2\alpha\cos(\delta_+)\sin(\delta_-), \end{aligned} \tag{3.25}$$

with the new phases $2\delta_+ = \delta_2 + \delta_1$ and $2\delta_- = \delta_2 - \delta_1$ and the asymmetry in critical current α such that $I_{c,i} = (1 \mp \alpha)I_c$. This can be further simplified to

$$\begin{aligned} j_{tr} &= i_{sq}\sin\left(\delta_+ + \tan^{-1}(\alpha\tan(\delta_-))\right), \\ i_{sq} &= \frac{I_{sq}}{I_c} = 2|\cos(\delta_-)|\sqrt{1+\alpha^2\tan^2(\delta_-)}, \end{aligned} \tag{3.26}$$

by introducing the normalized squid critical current i_{sq}. Comparing this to Eq. (3.14a), we see that the SQUID can be viewed as a single JJ with a tunable critical current that depends on δ_-.

We now use the fact that the SQUID encloses a nonsuperconducting area A, hence the flux $\Phi = B \cdot A$ within the loop has to be quantized according to Eq. (3.12). By taking a contour integral deep within the superconductor where $\vec{J}_s = 0$ and utilizing Eq. (3.10), we derive

$$\delta_- = \frac{\delta_2 - \delta_1}{2} = \frac{\pi\Phi}{\Phi_0} + \pi n \tag{3.27}$$

correlating the phase difference δ_- to the total flux Φ threading the loop. Returning to Eq. (3.26), we see from the above equation that the critical current exhibits a magnetic flux dependence $i_{sq} \propto |\cos(\pi\Phi/\Phi_0)|$. By applying an external magnetic field, we can tune the critical

current with a periodicity of Φ_0. This field dependence of the critical current makes the SQUID one of the most sensitive magnetometer known [75] and thus an ideal candidate for our inductive coupling scheme.

When an external flux Φ_{ext} is applied to the SQUID, one has to take screening effects within the SQUID-loop itself into account which adds to the total flux Φ. As a direct consequence of the flux quantization, a loop current builds up to ensure the quantization condition for any applied magnetic field. The loop current is given by

$$\begin{aligned} j_{\text{loop}} &= \frac{I_{\text{loop}}}{I_{\text{c}}} = \frac{1}{I_{\text{c}}}\frac{I_1 - I_2}{2} \\ &= -\cos(\delta_+)\sin(\delta_-) - \alpha\sin(\delta_+)\cos(\delta_-). \end{aligned} \tag{3.28}$$

Due to its geometric inductance L_{loop} shown in Fig. 3.4b), any circulating current I_{loop} adds to the total flux by a self-induced flux. For completeness, we account for an asymmetry in the SQUID-arms using a factor η, such that $L_i = (1 \pm \eta)L_{\text{loop}}/2$ for the individual linear inductances of each arm. This asymmetry results in an additional flux term due to the imbalance in flux created by a transport current across the SQUID. The total flux threading the SQUID loop adds up to

$$\Phi = \Phi_{\text{ext}} + L_{\text{loop}} I_{\text{loop}} - \eta L_{\text{loop}} I_{\text{tr}}/2 \tag{3.29}$$

At this point, it makes sense to introduce the screening parameter

$$\beta_{\text{L}} = \frac{2L_{\text{loop}} I_{\text{c}}}{\Phi_0}. \tag{3.30}$$

Rewriting the total flux in terms of β_{L} we get

$$\frac{\Phi}{\Phi_0} = \frac{\Phi_{\text{ext}}}{\Phi_0} + \frac{\beta_{\text{L}}}{2} j_{\text{loop}} - \frac{1}{4}\eta\beta_{\text{L}} j_{\text{tr}}. \tag{3.31}$$

To get an intuitive picture, we simplify the situation by assuming $I_{\text{tr}} = 0$ and $\alpha = 0$. For this case, we get $\delta_+ = 0$ and accordingly derive that $j_{\text{loop}} = \pm\sin(\pi\Phi/\Phi_0)$ accounting for positive and negative integers in Eq. (3.27). Together with Eq. (3.31) this leads to

$$\frac{\Phi}{\Phi_0} = \frac{\Phi_{\text{ext}}}{\Phi_0} \mp \frac{\beta_{\text{L}}}{2}\sin\left(\frac{\pi\Phi}{\Phi_0}\right). \tag{3.32}$$

We see that for $\beta_{\text{L}} > 0$ there exist two solutions to fulfill the flux quantization, either by creating a clockwise or anticlockwise current. The resulting self-induced flux either counters or adds to the external flux, which we will see leads to a hysteretic behavior of the SQUID critical current, as studied in section 3.3.2.1 upon sweeping the external flux.

SQUID-inductance: Similar to the inductance of a single JJ, one can attribute an inductance to the SQUID

$$\begin{aligned} L_{\text{sq}} &= \frac{\Phi_0}{2\pi}\frac{\arcsin(I_{\text{tr}}/I_{\text{sq}})}{I_{\text{tr}}} \\ &\approx L_{\text{sq0}}\left[1 + \frac{1}{6}\left(\frac{j_{\text{tr}}}{i_{\text{sq}}}\right)^2\right] \\ &= L_{\text{sq0}}\left[1 + \frac{1}{6}\sin^2\left(\delta_+ + \tan^{-1}(\alpha\tan\delta_-)\right)\right] \end{aligned} \tag{3.33}$$

From this, we see that the SQUID inductance features a nonlinearity similar to that of a single junction. The inductance of a SQUID is tunable with a magnetic flux due to the flux dependence of the critical current $I_{\mathrm{sq}}(\Phi)$. In Eq. (3.33), we introduce the inductance in the absence of an applied transport current as

$$L_{\mathrm{sq0}} \approx \frac{L_{\mathrm{J0}}}{2|\cos(\delta_-)|\sqrt{1+\alpha^2\tan^2(\delta_-)}}. \tag{3.34}$$

SQUID-potential: To determine which solution the SQUID adopts among the possibilities arising from the flux quantization in Eq. (3.31), it is useful to describe the tuning behavior by following the phase particle in the resulting potential landscape of the SQUID. We start similarly to the case of a single JJ described in Eq. (3.21) by using Kirchhoff's law for transport and loop current, and derive

$$\frac{\ddot{\delta}_i}{\omega_{\mathrm{pl},i}^2} = -(1\mp\alpha)\sin(\delta_i) + \frac{1}{2}j_{\mathrm{tr}} \pm j_{\mathrm{loop}}(\delta_1,\delta_2) = -\frac{1}{E_{\mathrm{J}}}\frac{\partial E_{\mathrm{pot}}}{\partial \delta_i}. \tag{3.35}$$

To get the SQUID-potential landscape, we sum Eq. (3.35) for each JJ $i = 1,2$ and swap to the variables δ_- and δ_+. Rewriting j_{loop} in terms of δ_- and Φ_{ext} according to Eq. (3.31), the SQUID potential is given by

$$\begin{aligned}\frac{E_{\mathrm{pot}}(\delta_+,\delta_-)}{2E_{\mathrm{J}}} &= 1-\cos(\delta_+)\cos(\delta_-)+\alpha\sin(\delta_+)\sin(\delta_-)\\ &\quad -\frac{j_{\mathrm{tr}}}{2}\delta_+ + \frac{j_{\mathrm{tr}}}{2}\eta\delta_- + \frac{1}{\pi\beta_L}\left(\delta_- - \pi\frac{\Phi_{\mathrm{ext}}}{\Phi_0}\right)^2.\end{aligned} \tag{3.36}$$

Fig. 3.5 depicts the potential landscape for different SQUID configurations at a fixed $\Phi_{\mathrm{ext}}/\Phi_0 = 0.35$. The two JJs in parallel lead to an overall periodic potential landscape in δ_+ and δ_- direction, with an additional quadratic potential in δ_- due to flux quantization. The minimum of this quadratic term aligns with $\delta_- = \Phi_{\mathrm{ext}}/\Phi_0$ and the corresponding parabola gets broader with increasing β_{L}. Hence, the particle can reside in a minimum of the total potential with $\Phi \neq \Phi_{\mathrm{ext}}$ – a result of the linear loop inductance and the corresponding shielding currents. Changing the external flux causes the particle to move along the δ_- direction with the δ_+ coordinate remaining constant. A finite transport current will primarily cause the potential to tilt along δ_+. In case of an asymmetry in geometric inductance η without a transport current the potential is identical to a symmetric SQUID, whereas an applied transport current results in an additional tilt along the δ_--direction. This leads to a shift of the obtained minima as indicated in Fig. 3.5b). For a system with a critical current asymmetry α, tuning the external flux will also move the particle along the δ_+ direction, and a non-zero transport current will now also move it along δ_-.

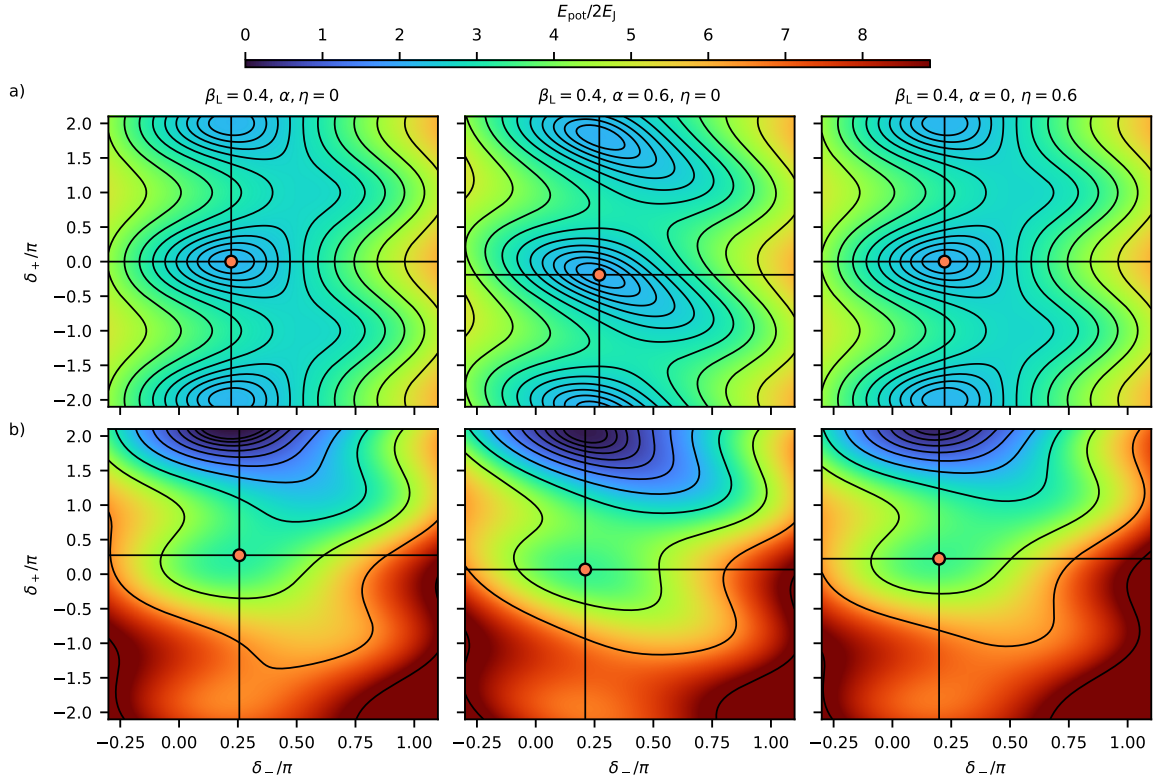

Fig. 3.5 Potential landscape of a SQUID at $\Phi_{ext}/\Phi_0 = 0.35$ considering three distinct cases for **a)** $j_{tr} = 0$ and **b)** $j_{tr} = 1$: a symmetric SQUID with $[\beta_L, \alpha, \eta] = [0.4, 0, 0]$ (column 1), and two asymmetric SQUIDs with $[\beta_L, \alpha, \eta] = [0.4, 0.6, 0]$ (column 2) and $[\beta_L, \alpha, \eta] = [0.4, 0, 0.6]$ (column 3). The circles and crosshairs indicate the positions of the local minimum to emphasize the changes originating from the different sets of parameters.

3.3 SQUID-Cavity

By incorporating a SQUID into a $\lambda/2$ stripline cavity as introduced in section 3.1, we obtain a cavity with a flux-tunable resonance frequency operating in the microwave regime. Such a flux-tunable cavity forms the core component of the optomechanical system discussed in this thesis, where the photon mode resides within the LC-cavity and the flux sensitivity of the SQUID mediates the coupling to the phonon mode of a magnetic cantilever. First, we discuss the tunability of such a SQUID-cavity, followed by its tuning behavior with applied flux or transport current. For that, we trace the trajectory of the phase particle within the SQUID potential defined in Eq. (3.36) for different sets of parameters. Then, we introduce a qualitative explanation of the coupling mechanism to the mechanical component and discuss changes in the SQUID potential landscape caused by the motion of the magnetic particle.

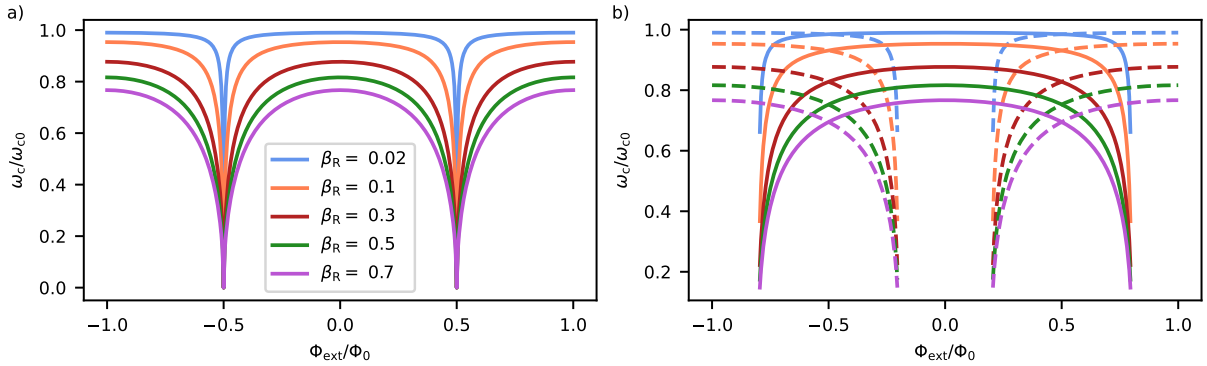

Fig. 3.6 Influence of β_R on the resonance frequency of a flux tunable cavity with external applied flux Φ_{ext}/Φ_0. We assume $j_{tr} = 0, \alpha = 0, \eta = 0$: **a)** Non-hysteretic tuning behavior with $\beta_L = 0$. **b)** All possible solutions of $\omega_c(\Phi)$ corresponding to clockwise and counterclockwise j_{loop} (solid/dashed) for $\beta_L = 0.6$.

3.3.1 Tunability and Nonlinearity

When a SQUID is incorporated into an LC-cavity, the SQUID inductance adds to the linear inductance of the cavity such that the resonance frequency is given by

$$\begin{aligned}\omega_c &= \frac{1}{\sqrt{C(L+L_{sq})}} \\ &= \frac{\omega_{c0}}{\sqrt{1+L_{sq}(I)/L}} \\ &\approx \frac{\omega_{c0}}{\sqrt{1+\frac{\beta_R}{|\cos(\delta_-)|\sqrt{1+\alpha^2\tan^2(\delta_-)}}}}.\end{aligned} \tag{3.37}$$

Here, we introduce the bare cavity frequency $\omega_{c0} = 1/\sqrt{LC}$ and the SQUID participation ratio $\beta_R = L_{J0}/2L$. The last line of Eq. (3.37) is valid for small transport currents across the SQUID. Furthermore, the SQUID participation results in a reduction of the cavity frequency from ω_{c0} even in the absence of any flux threading the SQUID loop

$$\omega_c(\Phi = 0) = \frac{\omega_{c0}}{\sqrt{1+\beta_R}}. \tag{3.38}$$

Fig. 3.6 shows the behavior of the SQUID-cavity resonance frequency as a function of an external flux threading the SQUID for different values of β_R. To emphasize the influence of the screening parameter β_L, the flux tuning of the SQUID resonator in the absence of β_L is displayed in Fig. 3.6a). In Fig. 3.6b), the solutions for both clockwise and anticlockwise j_{loop} are displayed upon tuning the flux for $\beta_L = 0.6$. Comparing the two cases, it is evident that the screening leads to a significant broadening of the respective lobes such that the edges of the lobes now occur at $\pm 0.8\,\Phi_0$. We also see that they overlap for a range of fluxes around $\pm 0.5\,\Phi_0$, allowing for two different possible solutions at every flux value in this range. In contrast, in the absence of screening, each lobe spans from -0.5 Φ_0 to 0.5 Φ_0 and only a single solution exists for each flux value. For dominating linear inductance, we see that the cavity frequency is largely unaffected by the SQUID until close to the edge of a lobe, where it exhibits a large resonance frequency change with flux and thus a high flux sensitivity. With increasing SQUID inductance (larger

β_R), the cavity tunes less abruptly, accompanied by a reduction of the sweet spot frequency. Thus, within the experiment, for good control of the frequency tuning, a β_R of around 10% is desirable.
In addition to the flux tuning, the SQUID introduces an intrinsic nonlinearity to the cavity. This is evident by considering driving the cavity with increasing power, which results in an AC-current increasing in amplitude. The current dependence of $L_{sq}(I)$ results in a shift of the cavity resonance frequency. As the AC-current-amplitude directly relates to the excitations of the cavity mode, the SQUID-cavity Hamiltonian can be described up to lowest order in nonlinearity by the Kerr-Hamiltonian introduced in Eq. (2.1). As derived in [80], one can relate the associated $\mathcal{K}$ constant of such resonators to the SQUID parameters as

$$\mathcal{K} = \left(\frac{2\pi}{\Phi_0}\right)^2 \frac{1}{8} \frac{\beta_R/\cos(\delta_-)}{(1+\beta_R/\cos(\delta_-))^4} \hbar\omega_{c0}^2 L. \tag{3.39}$$

As $\delta_- \propto \pi\Phi/\Phi_0$ this also implies that by flux tuning the SQUID-cavity to lower frequencies, the $\mathcal{K}$ of the cavity increases as

$$\mathcal{K} \propto \frac{\beta_R^3}{\cos^3(\pi\Phi/\Phi_0)}, \tag{3.40}$$

for a small SQUID participation $\beta_R \ll 1$ [80].

3.3.2 Particle Position in the SQUID Potential

Even for the simplified case considered in Fig. 3.6, it can not be determined which of the possible solutions the system will follow upon changing the external flux for $\beta_L \neq 0$. To reproduce tuning behaviors for more complex scenarios, we track the momentary particle position in the SQUID potential while varying the applied flux or transport current similar to the approach in [81]. This allows us to distinguish between possible solutions and capture the steady-state dynamics, thereby reproducing the actual tuning behavior.

We start with an initial potential and place the particle in a minimum. We then sweep the tuning parameter (applied flux or transport current) in small steps and calculate the resulting new potential. For this potential, we then locate all possible minima and search for the shortest path to the previous particle position (which no longer corresponds to a minimum) shown in Fig. 3.7a). As long as there are no potential barrier along this path, the particle can travel along it to the new minimum, and we adjust its current position to the new one as illustrated in Fig. 3.7b). To take noise sources into account such as thermal noise or flux noise σ without additing another step to the simulation, we allow the particle to overcome certain potential barrier heights ΔE_{pot}. This allows the particle to escape the current local minimum to an energetically more favourable one. Due to the periodicity of the SQUID-potential, we encounter several minima, some of which are equivalent (e.g. the two red indicated minima in Fig. 3.7a). As they lead to the same tuning behavior, we randomly pick either one of them.

3.3.2.1 Simulation of flux tuning

To fully simulate the flux tuning behavior of the SQUID-cavity, we sweep the applied external flux in both positive and negative directions to capture any hysteresis effects. Furthermore, we assume only weak driving of the cavity, allowing us to neglect j_{tr} and consequently any possible loop inductance asymmetry η as it is only relevant for $j_{tr} \neq 0$. By tracking the phase particle

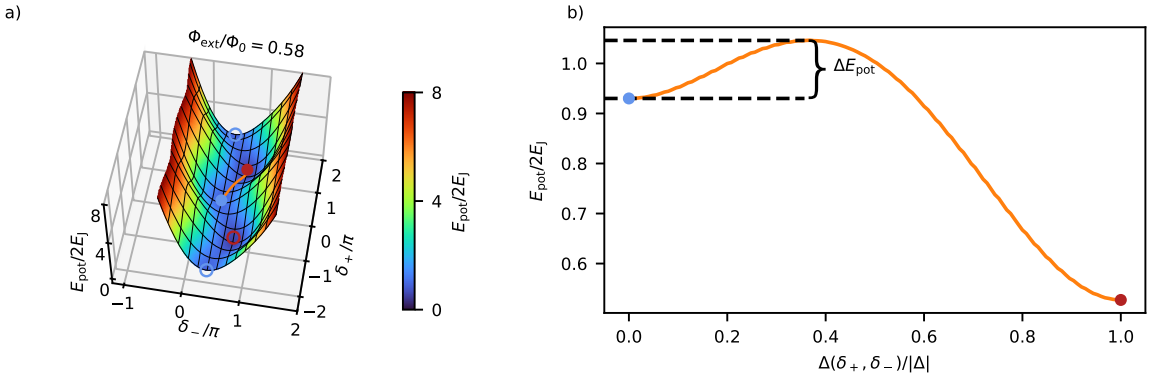

Fig. 3.7 **a)** SQUID potential for an applied magnetic field of $\Phi_{\text{ext}}/\Phi_0 = 0.58$. The current particle position is indicated as the filled blue sphere, and potential minima are indicated in red/blue for the two set of solutions. The filled red sphere corresponds to the new position of the particle. **b)** Potential energy along the path to the next minima. Due to noise σ, we allow the particle to overcome certain potential barrier heights ΔE_{pot}. Parameters used: $\beta_{\text{L}} = 0.4, \alpha = 0, \eta = 0, \beta_{\text{R}} = 0.1, j_{\text{tr}} = 0$

position (δ_+, δ_-), we calculate the corresponding changes in ω_{c} using Eq. (3.37), Φ/Φ_0 using Eq. (3.31), and circulating current $I_{\text{loop}}/I_{\text{c}}$ using Eq. (3.28).

In Fig. 3.8a-f), the potential landscape of the SQUID is shown for sweeping the applied flux Φ_{ext}/Φ_0 in positive and negative directions (color blue and red). For the particle position at each flux point, the resulting frequency of the SQUID-cavity ω_c, loop flux Φ/Φ_0, and circulating current $I_{\text{loop}}/I_{\text{c}}$ are shown in Fig. 3.8g-i). At $\Phi_{\text{ext}}/\Phi_0 = 0$, in order to fulfil flux quantization, equivalent minima are found along $\delta_- = 0$ and even multiples of π along δ_+. Upon sweeping the external flux, the particle follows the minima in δ_- direction at a constant δ_+. However, beyond a certain external flux value, additional minima corresponding to an opposite loop current appear at odd multiples of π in δ_+ with a slight offset in δ_- to the even ones. Further increasing the flux, the loop current approaches I_{c}, such that the new minima at odd δ_+ become energetically favorable. Therefore, the particle jumps, leading to a discrete step in Φ/Φ_0 and a flip of the sign of $I_{\text{loop}}/I_{\text{c}}$. For even higher flux, the set of initial minima at even π vanishes. A different set of solutions is observed when the external flux is tuned in the opposite direction. Since there is a range of flux values where we find minima for even and odd δ_+, the particle position at these fluxes depends on its previous states. The position of the particle in this range of fluxes is hysteretic, as is visible in Fig. 3.8 c) and d).

These simulations are carried out for various values of the screening parameter β_{L}, the current asymmetry α, and the noise term σ, and the results are displayed in Fig. 3.9. To allow easier comparison of the effects of individual parameters, we always use the same set of parameters (given in the figure caption) and vary only one parameter at a time.

Changing β_L, we effectively vary the curvature of the parabolic term in the SQUID-potential Eq. (3.36). For larger β_{L}, the flux range with minima accessible to the particle at even and odd

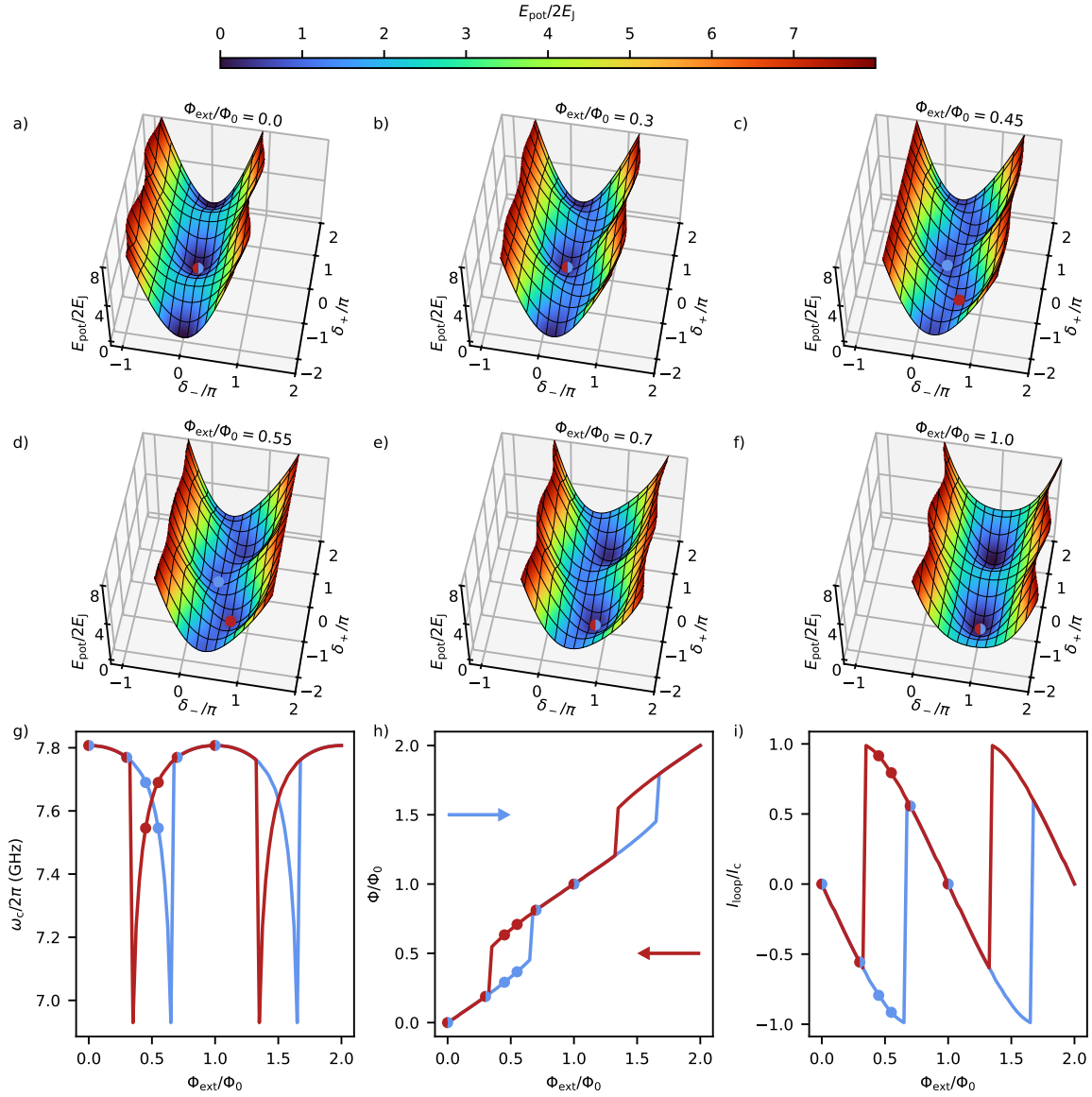

Fig. 3.8 **a-f)** Potential landscape of a SQUID for different external flux bias points against δ_-, δ_+. The minimum occupied by the particle for that particular value of flux while increasing (decreasing) is marked by a blue (red) sphere, respectively. **g-i)** Tuning behavior of the resonance frequency $\omega_c/2\pi$, loop flux Φ/Φ_0 and loop current I_{loop}/I_c against external applied flux. Sweep direction corresponding to the arrows in **h)**. Parameters used: $\beta_L = 0.4, \alpha = 0, \eta = 0, \sigma/E_J = 0.005, \beta_R = 0.1, j_{tr} = 0$

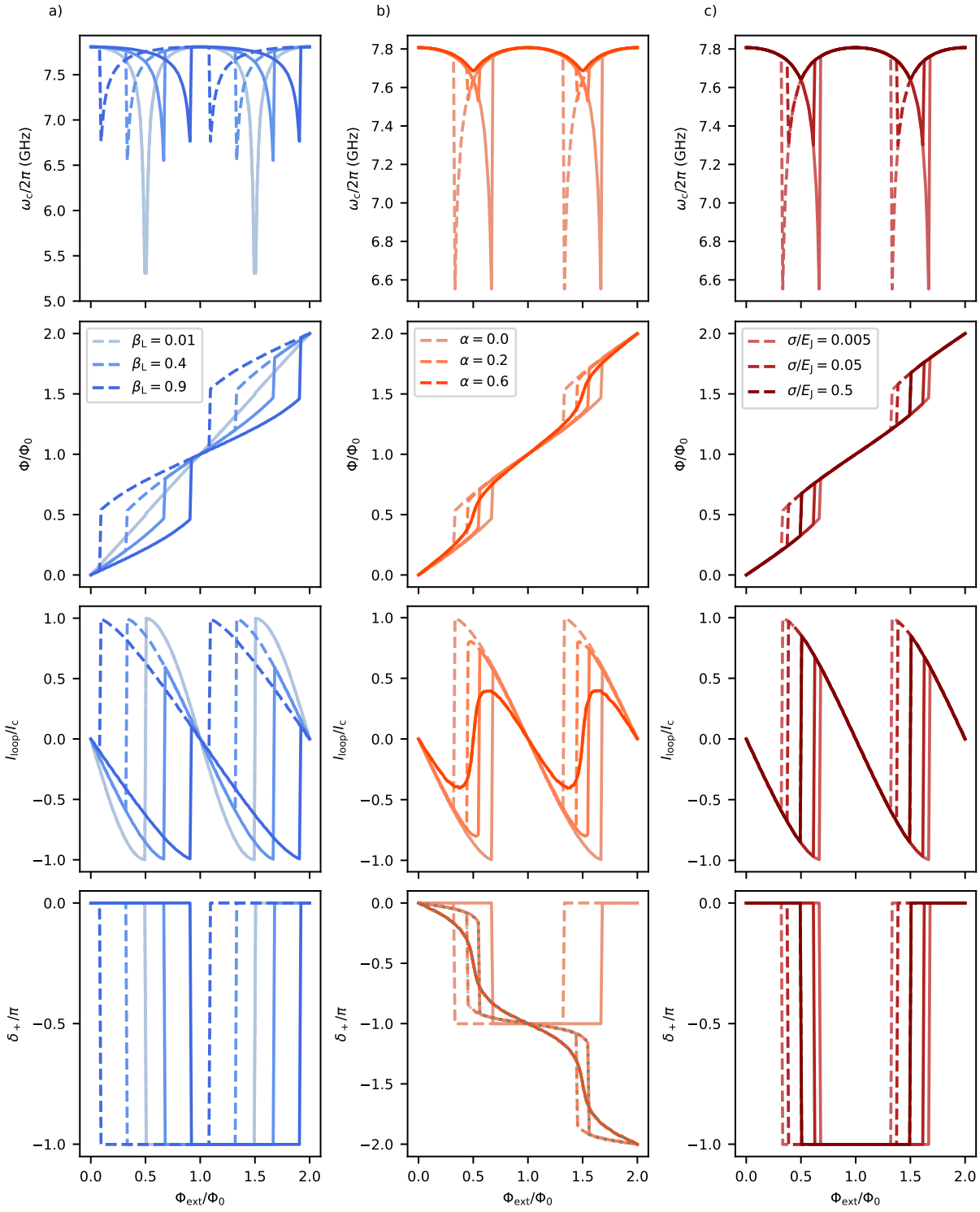

Fig. 3.9 Flux tuning behavior for different sets of parameters for both sweep directions (solid and dashed). Changes in resonance frequency ω_c, loop flux Φ/Φ_0,loop current I_{loop} and δ_+ for various values of β_L in **a)**, α in **b)**, and σ/E_J in **c)**. Unless otherwise noted, parameters used are: $\beta_L = 0.4, \alpha = 0, \eta = 0, \sigma/E_J = 0.005, \beta_R = 0.1, j_{tr} = 0$

δ_+ increases, resulting in larger regions in which hysteresis is visible, as is evident when comparing the solid and dashed lines in Fig. 3.9a). As the flux induced by the loop current scales with the linear loop inductance, the observed flux Φ starts to deviate from the applied flux Φ_{ext} for larger β_{L}, resulting in a flatter slope of the loop flux. For the curve with the highest β_{L}, the loop current always remains in the same orientation, such that Φ is consistently smaller/larger than Φ_{ext}. An important consequence of the flat slope in Φ for a larger loop inductance is a reduced tunability of ω_{c}. The coordinate δ_+ exhibits a binary behavior, taking values of either 0 or π. This is a direct consequence of the constraint that no current flows through the SQUID (equivalent to a weak excitation of the SQUID-cavity), requiring the transport current given by Eq. (3.25) to vanish, which is fulfilled for $\sin(\delta_+) = n\pi$.

By changing the asymmetry α, we decrease the critical current of one JJ, which results in a lower maximal loop current, as can be seen in Fig. 3.9b). Upon flux tuning, $\alpha \neq 0$ results in an additional shift of the particle trajectory along δ_+. For the highest values of α, a continuous connection between neighboring minima develops, such that we observe a gradual change (e.g. loop flux Φ and δ_+) instead of a discrete jump in the flux tuning. The path taken in δ_+ follows the requirement of no overall transport current across the SQUID given by Eq. (3.25). For visualization purposes, the resulting δ_+ by evaluating $j_{\text{tr}} = 0$ for the obtained δ_- is depicted as the gray dotted line. Lastly, the continuity in the particle position also lifts the hysteresis observed by flux tuning and leads to additional lower sweet spots. However, the appearance of the lower sweet spot also depends on β_{L} relative to α. Therefore, for large β_{L}, the absence of a lower sweet spot does not necessarily indicate the absence of junction asymmetry α.

Increasing the noise present in the system σ does not influence the qualitative tuning behavior, as the curves for the different σ shown in Fig. 3.9c) overlap. However, for large enough noise, the hysteresis is completely washed out, as the particle immediately adjusts to any newly formed global minimum in the potential.

3.3.2.2 Simulation for a DC-transport-current

To understand the tuning behavior of a driven SQUID-cavity (especially the frequency shift due to its $\mathcal{K}$ nonlinearity), we first discuss its response to an applied DC transport current. From these simulations, the behavior upon driving can be deduced by assuming that the corresponding AC-current is a weighted average over the DC response. This is justified as long as the plasma frequency, which is the frequency at which the particle can respond to any change in the potential, is much larger than the frequency of the AC drive. This allows the particle to instantaneously react to any changes in the potential landscape[1]. Similar to the previous section, we will infer from the particle trajectory in the SQUID potential the changes in ω_{c} using Eq. (3.37), Φ/Φ_0 using Eq. (3.31), and circulating current $I_{\text{loop}}/I_{\text{c}}$ using Eq. (3.28). As the interplay between flux quantization and nonlinearity is important, simulations are performed for various flux bias points.

Figs. 3.10a-c) show the response of a symmetric SQUID-cavity as the applied DC-transport-current is increased. The applied current results in a tilt of the potential along the δ_+ axis.

[1]For SQUID-cavities in this thesis, the observed resonance frequency is around $\omega_{\text{c}}/2\pi \approx 8\,\text{GHz}$. For the simulations, we can safely set an upper bound to the junction capacitance of $C_{\text{J}} = 1\,\text{pF}$, which, with a critical current of $I_{\text{c}} = 8.6\,\mu\text{A}$, leads to a plasma frequency of $\omega_{\text{p}}/\pi \approx 25\,\text{GHz}$.

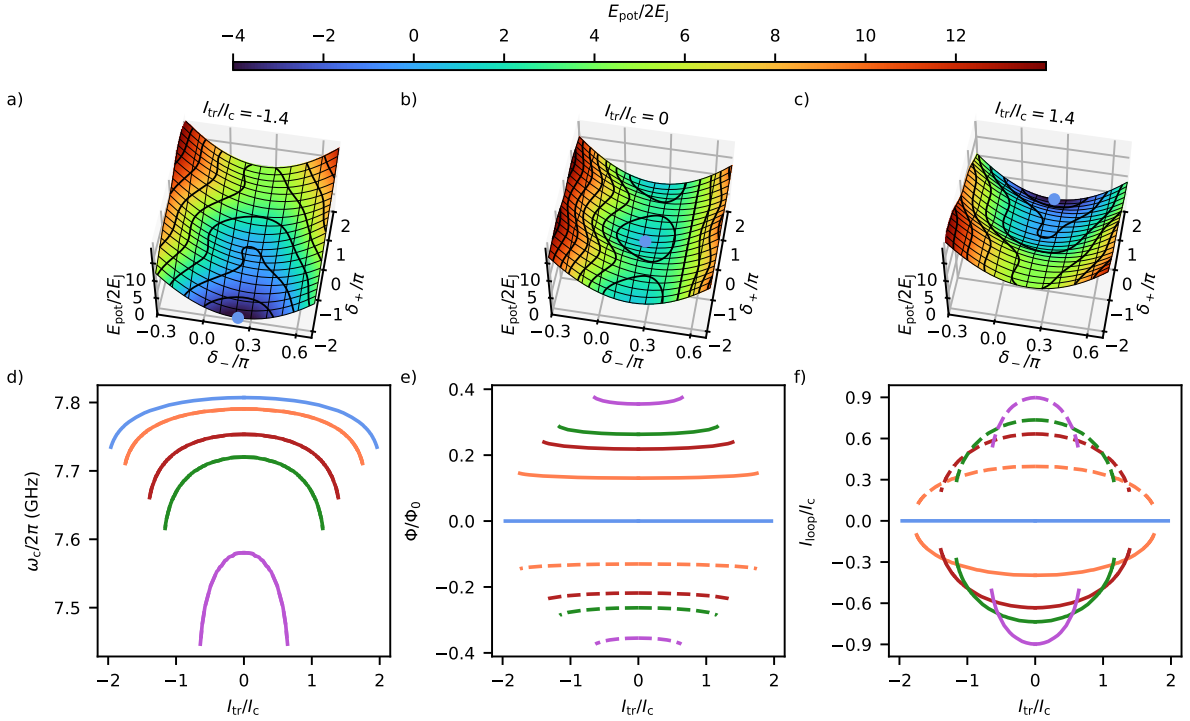

Fig. 3.10 **a-c)** Potential landscape of a SQUID for different transport currents plotted against δ_-, δ_+ at $\Phi_{ext}/\Phi_0 = 0.25$. **d-f)** Tuning behavior of the resonance frequency $\omega_c/2\pi$, loop flux Φ/Φ_0 and loop current I_{loop}/I_c against applied current for positive (solid) and negative (dashed) external flux Φ_{ext}/Φ_0. Parameters used: $\beta_L = 0.4, \alpha = 0, \eta = 0, \beta_R = 0.1, \sigma/E_J = 0.005, |\Phi_{ext}|/\Phi_0 = [0.0, 0.15, 0.25, 0.3, 0.4]$.

This leads to a gradual shift of the minimum the particle resides in until the sum of transport current and loop current exceeds the critical current of one junction at $(I_{tr}/2 + I_{loop})/I_c = 1$ assuming for simplicity $\alpha = 0$. Exceeding this limit, the system becomes unstable as the phase particle rolls down the potential landscape which corresponds to the breakdown of superconductivity of the junction. Tuning the frequency away from the sweet spot by applying a larger $|\Phi_{ext}|$, we see in Fig. 3.10d) that the frequency shift with current increases due to the larger SQUID-participation. For external fluxes $|\Phi_{ext}| > 0$ and no applied current, the SQUID potential has two sets of minima - at even and odd δ_+/π with a small difference in δ_-. As the applied transport current tilts the potential in δ_+, the particle gradually moves from one set of minima to the other along a trajectory in δ_- and δ_+ as can be seen also in Fig. 3.5. The change in δ_- is needed to maintain the applied transport current given by Eq. (3.25). This leads to a change in the amplitude of the loop current, which decreases for larger transport currents across the SQUID. Moreover, the loop flux $|\Phi|$ simultaneously increases as the shielding due to the loop currents becomes less effective.

The influence of the screening parameter β_L, asymmetry in critical current α and geometric inductance asymmetry η on the SQUID response under a transport current are shown in Fig. 3.11 at two different values of the applied external flux $\Phi_{ext}/\Phi_0 = \pm 0.25, \pm 0.4$.

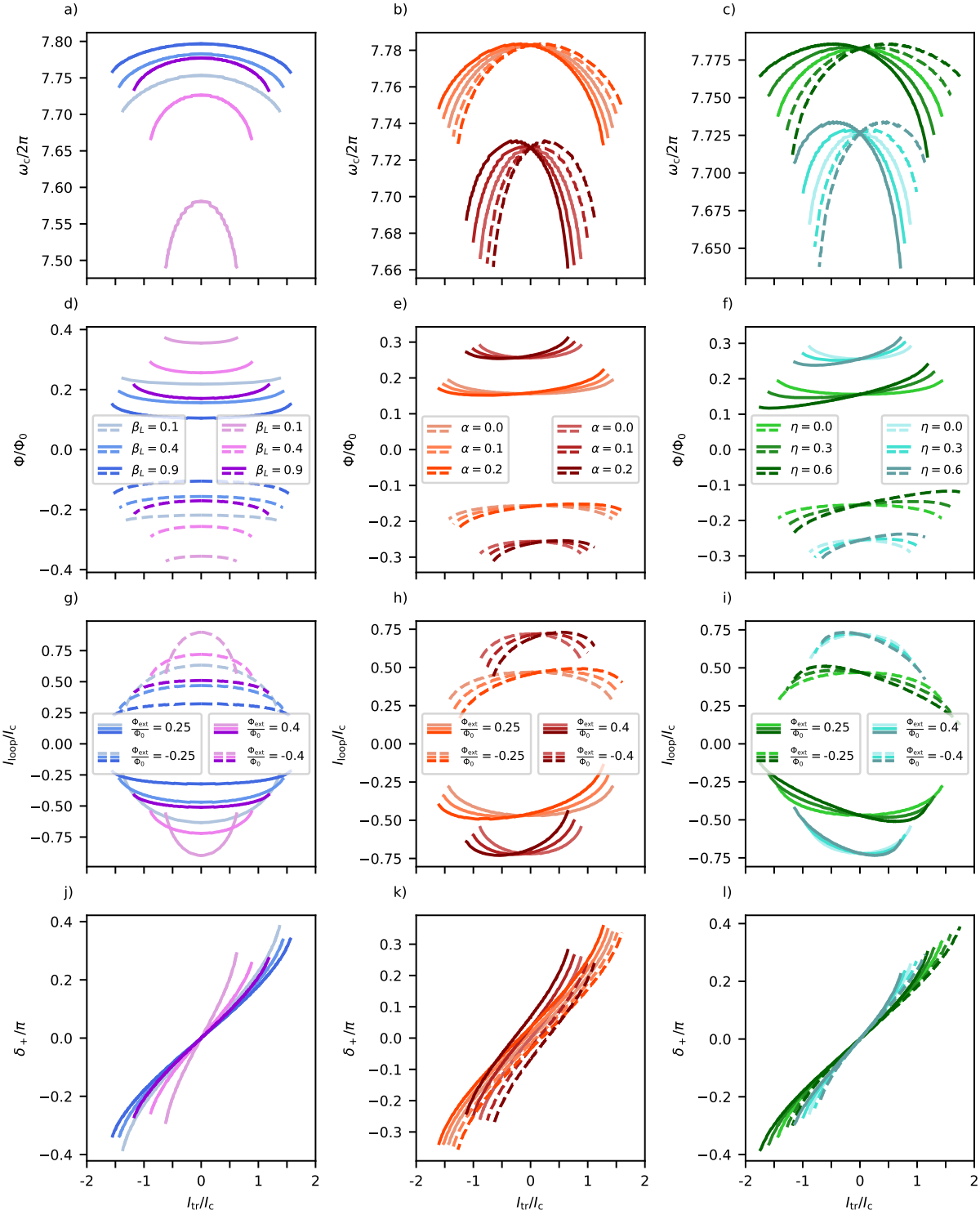

Fig. 3.11 Effects on the SQUID quantities against applied transport current for different sets of parameters for two different external fluxes (positive and negative flux values as solid and dashed curves). Changes for different values of **a**) β_L, **b)** α and **c)** η. Unless otherwise noted, parameters used are: $\beta_L = 0.4, \alpha = 0, \eta = 0, \beta_R = 0.1, \sigma/E_J = 0.005$

As the screening parameter is increased, we observe an increase in the offset in ω_c and a decrease in the curvature with current for both flux points. Corresponding to the frequency behavior, we see the expected changes in loop flux and loop current for an increased loop inductance as depicted in Fig. 3.9. The observed SQUID response for larger values of β_L is explained by the increased self-induced loop flux which reduces the overall tunability, as discussed during the analysis of the flux tuning behaviour in the section 3.3.2.1. As the SQUID behavior under driving depends primarily on the loop flux Φ/Φ_0, changes with respect to β_L are due to the observed offset in this quantity.
For an asymmetric SQUID, we see that for increasing α the SQUID response is no longer symmetric around $I_{tr} = 0$, but instead shifts depending on the sign of the applied flux. For higher fields, this effect becomes more pronounced. We can explain this by taking the total current $I_i = I_{tr}/2 \pm I_{loop}$ across each junction into account. Applying a transport current decreases the total current through one junction while increasing it for the other. In the case that the total current through the weaker junction (lower I_c) is decreased, a transport current effectively reduces the asymmetry in junction inductance. For a specific amplitude of I_{tr}, the asymmetry can balance out, which maximizes the SQUID inductance and allows the highest I_{loop} amplitude at a given Φ_{ext}. These larger loop currents lead to a reduction in the loop flux $|\Phi/\Phi_0|$ due to the effectively larger screening and an increase in ω_c. Thus, α leads to a partially positive frequency shift in ω_c upon applying a current across the SQUID.
In case of an inductance asymmetry η, the observed behavior in ω_c and Φ is similar to the case of α. However, I_{tr} causes in this case a direct change in flux, rather than just causing different loop currents to flow. Thus, this created flux adds to the total loop flux Φ/Φ_0, which leads to a change in loop current I_{loop} to ensure flux quantization.

3.3.2.3 Simulation for an AC transport current

Having discussed the SQUID's behavior under a DC transport current, we now turn to the SQUID response driven by an AC transport current. Based on the results from Fig. 3.11 for different values of β_L, α, and η, we focus here for brevity only on the influence of α and β_L, as the parameter η exhibits a qualitatively similar effect to that of α. Furthermore, we assume that the phase particle reacts instantaneously to potential changes due to the applied current, resembling the currents that flow on resonance in the cavity. As mentioned in the section above, this assumption holds as long as the plasma frequency ω_{pl} is larger than ω_c. Thus, the cavity response can be obtained by averaging the DC response over a *sinusoidally* varying transport current.

To illustrate the effect of an AC drive at different flux points, the first three rows of Fig. 3.12 show the SQUID-cavity frequency ω_c upon tuning the external flux for DC transport currents of $I_{tr}/I_c = 0, \pm 0.7$ and various combinations of $\alpha = 0.0, 0.2, 0.6$ and $\beta_L = 0.1, 0.4, 0.6$. For no asymmetry, the applied currents lead to a symmetric decrease in the resonance frequency of the cavity on both sides of the lobe. For larger β_L, the applied current close to $\Phi_{ext}/\Phi_0 = 0.5$ together with the built-up loop current exceeds the critical current and therefore is not shown. For increasing asymmetry, one can observe that the positive and negative current result in a different frequency shift, which depends on the sides of the lobe. This can be explained by the fact that the applied current either adds to or partially cancels the loop current over the weaker junction as discussed for the DC transport current above. If the current cancels at the weaker junction, we expect a smaller frequency shift of the cavity, whereas we expect a larger one in the

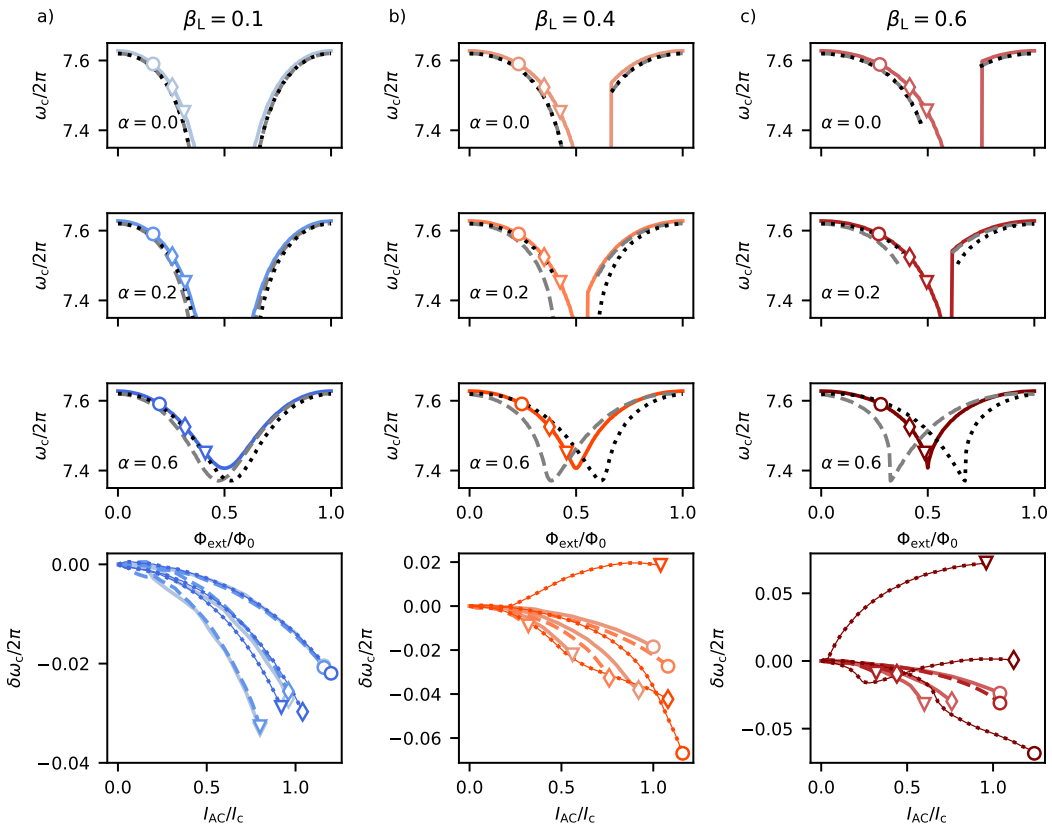

Fig. 3.12 SQUID-cavity frequency upon driving with a constant applied DC transport current - $I_{tr}/I_c = 0, \pm 0.7$ as colored solid and dashed black(+)/grey(−) lines - upon flux tuning for various combinations of $\alpha = 0.0, 0.2, 0.6$, and $\beta_L = 0.1, 0.4, 0.6$ in **a),b),c)**, respectively. For three distinct points, the cavity response to an AC transport current is obtained by averaging the DC response over a *sinusoidally* varying transport current. Parameters used: $\eta = 0.0$, $\beta_R = 0.1$, $\sigma/E_J = 0.005$

opposite case. As the loop current changes orientation for the different lobes, the influence of the positive and negative currents on ω_c reverses. Increasing with the asymmetry between the junctions, this effect leads to an asymmetry of the resonance frequency upon driving on either side of $\Phi_{ext}/\Phi_0 = 0.5$ – an increased frequency shift on one side, a smaller one on the other – most clearly visible for $\alpha = 0.6$.

We further see that for larger screening parameters β_L this effect is enhanced. This is because the curvature of the quadratic term – corresponding to flux quantization – in the SQUID potential Eq. (3.36) scales inversely with β_L. With a wider potential and the asymmetry α, the potential barrier between the two solutions with opposite circulating current is effectively decreased. Depending on the direction of the current, the corresponding tilt either pushes the particle to the next solution at an earlier flux bias point or pushes it towards its initial solution delaying the switching to a later flux bias. Thus, this push on the phase particle explains the skewed flux tuning with a present transport current.

For each set of β_L and α, the cavity response upon applying an AC transport current is shown for three distinct resonance frequencies in the bottom row of Fig. 3.12. As mentioned earlier, the screening parameter only has a minor influence on the observed frequency shift $\delta\omega_c$, as is evident from comparing the cases for $\alpha = 0$ - corresponding to the faint colors. For the lowest values of β_L, we observe exclusively negative frequency shifts, which become slightly smaller with increasing α. However, the tuning behavior drastically changes for larger β_L and $\alpha \neq 0$ as the frequency shift either levels out or even becomes positive for higher driving powers at resonance frequency close to the lower sweet spot. This can be understood by comparing the flux tuning for the undriven case to the driven ones at $\alpha = 0.6$. Due to the increased tilt of the flux tuning for larger β_L values in the presence of a transport current, an AC drive only leads to a positive shift in frequency for applied fluxes close to $\Phi_{ext}/\Phi_0 = 0.5$. However, this is not observed for the lowest β_L, emphasizing that this positive frequency shift is an interplay between both – α and β_L – parameters.

The simulation results imply that we expect to find a transition from a net negative $\mathcal{K}$ (negative frequency shift) to a net postive $\mathcal{K}$ (positive frequency shift) for an asymmetric SQUID-cavity. A similiar change in $\mathcal{K}$ is observed in so called *superconducting nonlinear asymmetric inductive elements* (SNAILs). Here, an uneven distribution of junctions within the SQUID-loop create an effective tunable SQUID asymmetry. This tunable asymmetry allows to insitu tune SNAILs to a dressed $\mathcal{K}$-free operating point by applying a flux and drive [82].

3.4 Magnetomechanical Coupling Scheme

Building on the toolbox of superconducting circuits introduced in the previous sections, we now introduce the inductive coupling scheme studied in this work. We explain how we use a magnetized cantilever to couple the motion of the cantilever to the SQUID-cavity. We then theoretically study how the cavity's response to an external magnetic field changes because of the additional moving magnet in close proximity.

3.4.1 Working principle

A schematic illustration of the optomechanical system studied in this work is shown in Fig. 3.13a). The mechanical element – an atomic force microscopy (AFM) cantilever – is placed centrally above the loop of a SQUID-cavity. To couple the center of mass motion of the AFM cantilever to the photon field in the cavity, we attach a strong permanent magnet to its tip. The phononic excitation leads to an oscillation of the distance between the magnet and the SQUID, and thus causes a periodic flux modulation in the SQUID loop. According to Eq. (3.37), this causes a displacement-dependent shift of the cavity resonance frequency, realizing the optomechanical coupling between the phononic mode of the cantilever and the photon field of the cavity as discussed in section 2.1. With its high sensitivity to magnetic fields, even flux changes caused by displacements on scales of 0.01 fm – significantly smaller than an atom with 100 fm – result in detectable frequency shifts, making the SQUID a remarkable tool to reach the single photon strong coupling regime of optomechanical systems [75].

The coupling strength in optomechanical systems is defined as the frequency change induced by the zero-point motion of the mechanical element Eq. (2.4). However, this term can be

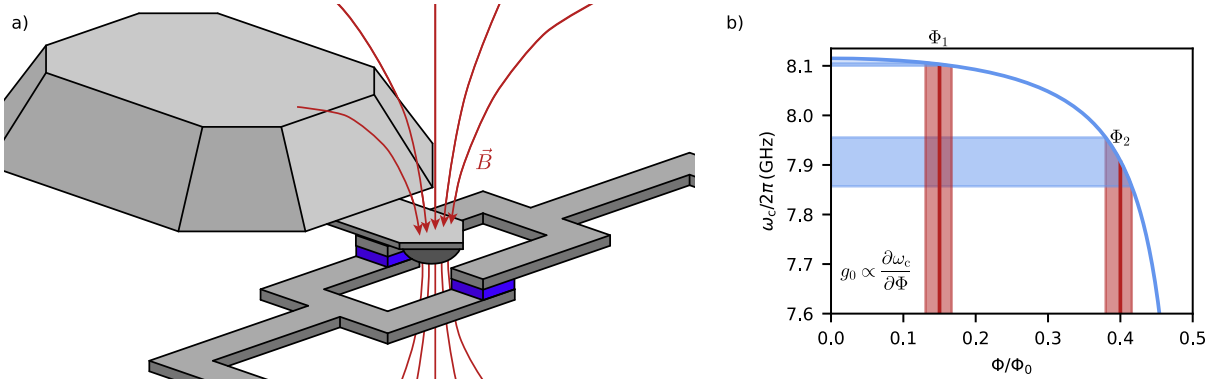

Fig. 3.13 **a)** Illustration of the inductive coupling scheme between a SQUID-cavity and a cantilever. The cantilever is equipped with a magnetic particle magnetized in a direction perpendicular to the SQUID-loop and directly placed above the SQUID-loop. **b)** Representation of the flux tunability of the coupling constant g_0. Working at different bias fields Φ_1, Φ_2, the same flux change due to a given amplitude for the cantilever motion (red area) results in different variations of the cavity frequency (blue areas). This difference in g_0 corresponds the flux slope $\partial\omega_c/\partial\Phi$ such that $g_0(\Phi_2) > g_0(\Phi_1)$.

rewritten in the inductive scheme as

$$g_0 = z_{\mathrm{zpm}} \frac{\partial \omega_c}{\partial z} = z_{\mathrm{zpm}} \frac{\partial \Phi}{\partial z} \frac{\partial \omega_c}{\partial \Phi}. \tag{3.41}$$

Here, the first term corresponds to the change in loop flux at the SQUID induced by the zero-point motion of the mechanical oscillator. We refer to this as the *geometric* factor, as it depends on the magnetization as well as the precise equilibrium distance, orientation, and placement of the magnet relative to the SQUID loop. The second term characterizes the system's frequency response to changes in flux threading the SQUID loop, as indicated by the slope in Fig. 3.13b) and is referred to as the *flux-tunable* factor. We can significantly enhance the sensitivity of the system by independently tuning the cavity to a bias point with a steep flux dependence of the resonance frequency via an externally applied field discussed in section 3.3.2.1. This allows us, to realize exceptionally high coupling strengths with this inductive coupling scheme. Compared to a capacitive coupling such inductively coupled systems have risen in popularity in the last decade due to their in-situ tunability and therefore high achievable single-photon coupling strengths g_0 [3, 48–50].

3.4.2 Influence of the In-Plane Field of a Permanent Magnet

As discussed in section 3.2.2, any in-plane field experienced by a JJ leads to a modulation of its critical current. A permanent magnet placed in the SQUID's vicinity will inevitably generate an in-plane field. By assuming a magnetic dipole m_z magnetized perpendicular to the loop to maximize coupling and a constant field across the junctions, the in-plane flux threading the junctions is given by

$$\Phi_{||}^{\pm} = A_{\mathrm{eff}} B_{||} = A_{\mathrm{eff}} m_z \frac{3\mu_0}{4\pi} \frac{x_p(1 \pm \delta x) z}{\left(\left(x_p(1 \pm \delta x) \right)^2 + z^2 \right)^{\frac{5}{2}}}. \tag{3.42}$$

The effective crossection of the junction A_{eff} is given by the junction separation and half of the thickness of the electrodes (see section 3.2.2). We place the cantilever at an in-plane distance x_{p} from the junction and further allow for a misalignment δx of the magnet, placing it closer to one of the JJ. The dipole is positioned above the SQUID at a distance z. According to Eq. (3.23), the critical current and the other parameters affected by the in-plane magnetic field can be written as:

$$I'_{\text{c},i} = I_{\text{c}}(1 \mp \alpha)\left|\frac{\sin\left(\pi\Phi^{\pm}_{||}/\Phi_0\right)}{\pi\Phi^{\pm}_{||}/\Phi_0}\right|, \tag{3.43a}$$

$$I'_{\text{c}} = \frac{I'_{\text{c},1} + I'_{\text{c},2}}{2}, \tag{3.43b}$$

$$\alpha' = \frac{I'_{\text{c},2} - I'_{\text{c},1}}{I'_{\text{c},2} + I'_{\text{c},1}}, \tag{3.43c}$$

$$\beta'_{\text{R}} = \beta_{\text{R}}\frac{I_{\text{c}}}{I'_{\text{c}}}, \tag{3.43d}$$

$$\square' = \square\frac{I'_{\text{c}}}{I_{\text{c}}} \text{ for } \square\epsilon\{E_{\text{J}}, \beta_{\text{L}}\} \tag{3.43e}$$

Figs. 3.14a) and d) show the changes observed for the critical current for different positions of the cantilever above the squid loop. This change directly gives the scaling for E'_{J} and β'_{L} according to Eq. (3.43e). Corresponding to Eq. (3.43d) and Eq. (3.43c) the scaling for the participation ratio β'_{R} (Fig. 3.14b/e), and asymmetry α' (Fig. 3.14c/f) is given upon placing a dipole magnet above the SQUID, respectively. Similar to a single junction, the in-plane field leads to a reduced effective critical current I'_{c} scaling with m_{z}. This leads to a decrease in β_{L} and an increase in β_{R}, resulting in a SQUID-cavity with a reduced hysteresis, enhanced tunability, and lower sweet spot frequency upon mounting the magnetic cantilever. In addition, even a small misalignment (δx) can result in significant asymmetry upon tuning the external flux bias. If the in-plane field exceeds one Φ_0 in the junctions at a given distance z, we observe a dip in I'_{c} to 0 as visible in Fig. 3.14d) for a perfectly aligned cantilever $\delta x = 0$, resulting in a spike in β'_{R}. On the contrary, we observe a kink in I'_{c} and an asymmetry of $\alpha' = \pm 1$ for a misalignment leading to a flux of Φ_0 in only one junction.

3.4.3 Influence of the Out-of-Plane field of a Permanent Magnet

The inductive coupling scheme discussed here depends on the flux change induced within the SQUID loop by the component of the dipole magnetic field perpendicular to the loop. The overall magnetic flux threading the SQUID loop can be written as

$$\begin{aligned}\Phi_{\text{ext}}(z) &= \Phi_{\text{ext}} + \Phi_{\text{mag}}(z)\\ &= \Phi_{\text{ext}} + \int_S B_z(z)dS\\ &= \Phi_{\text{ext}} + \frac{\mu_0 m_{\text{z}} R^2}{2(R^2+z^2)^{3/2}},\end{aligned} \tag{3.44}$$

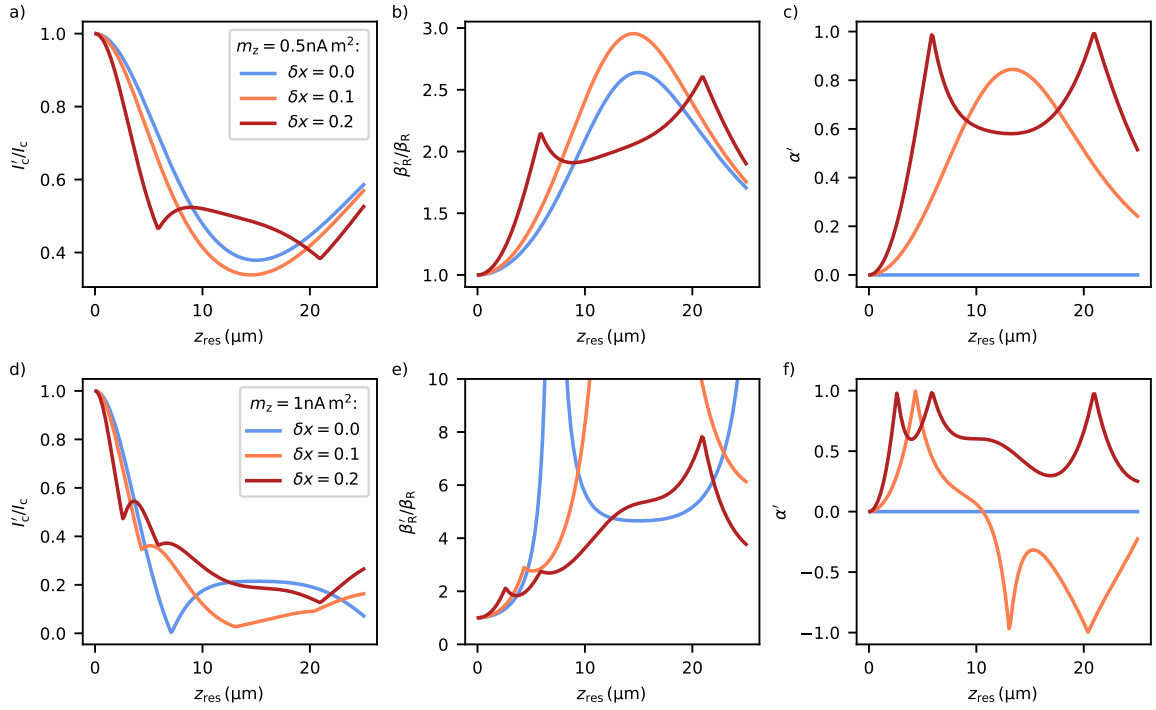

Fig. 3.14 **a)** and **d)** effect on the SQUID's critical current (direct proportional to the scaling of the screening parameter β_L' and Josephson Energy E_J'), **b)** and **e)** the participation ratio β_R', and **c)** and **f)** asymmetry α' due to the in-plane component of a magnetic dipole field as a function of the magnet height above loop. We consider two different dipole moments magnetized perpendicular to the SQUID loop $m_z = 0.5, 1\,\mathrm{nA\,m^2}$ with a misalignment of $\delta x = [0, 0.1, 0.2]$. Other parameters: $x_p = 30\,\mu\mathrm{m}$, $A_{\mathrm{eff}} = 3\,\mu\mathrm{m} \times 300\,\mathrm{nm}$.

assuming a circular loop with area $A_{\mathrm{loop}} = \pi R^2$ and that the dipole axis lines up with the center of the SQUID loop.

As discussed in chapter 3.2.3, any flux threading the SQUID induces loop currents to maintain flux quantization. These currents generate a magnetic field that exerts a force on the magnet, which results in a static deflection of the cantilever. The force on the cantilever can be written as

$$F_{\mathrm{sq}} = m_z \frac{\partial}{\partial z} B_{\mathrm{sq}}(z) = m_z \frac{\partial}{\partial z} \left(\frac{\mu_0 R^2 I_c' j_{\mathrm{loop}}}{2(R^2 + z^2)^{3/2}} \right) = \frac{\partial}{\partial z} \left(E_J' j_{\mathrm{loop}} \frac{2\pi \Phi_{\mathrm{mag}}(z)}{\Phi_0} \right), \tag{3.45}$$

depending on the magnetic moment m_z, the distance to the SQUID loop z and the loop current j_{loop} combined with the changes to the SQUID critical current I_c' by the *in-plane* component of the field due to the magnetic particle. Furthermore, this force also represents the *backaction* force seen by the cantilever in this optomechanical setup. As the force scales with the loop currents, we expect stronger feedback upon flux tuning to a steeper flux bias point, which consistently corresponds to an increased sensitivity (as illustrated in Fig. 3.13), making the mechanism reciprocal. From Eq. (3.44) and Eq. (3.45), we can extract the geometric sensitivity to one *zero point motion* of the cantilever z_{zpm} (corresponding to the *geometric* factor in section

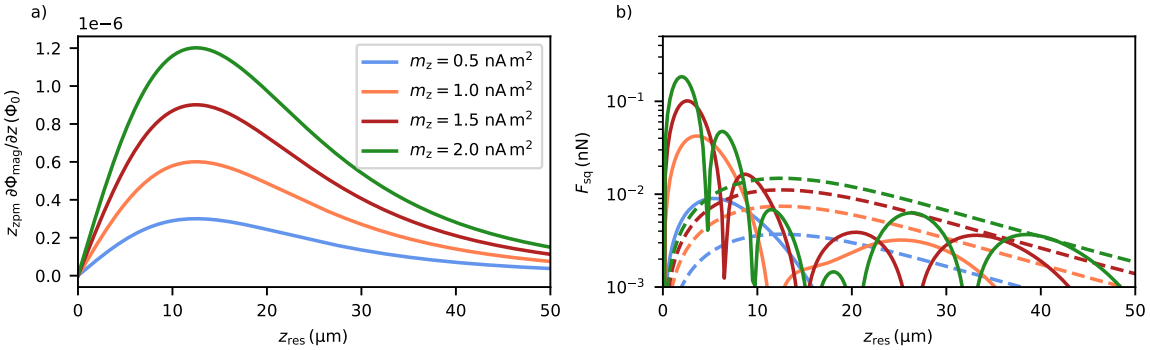

Fig. 3.15 **a)** Geometric flux sensitivity with z_{zpm} and **b)** gradient force on the cantilever for $j_{\mathrm{loop}} = 1$ as a function of the resting position of the cantilever. The solid lines account for the variation of the critical current due to the in-plane field, whereas the dashed lines do not. Other parameters: $R = 25\,\mu\mathrm{m}$, $x_{\mathrm{p}} = 30\,\mu\mathrm{m}$, $\delta x = 0$, $A_{\mathrm{eff}} = 3\,\mu\mathrm{m} \times 300\,\mathrm{nm}$.

3.4.1) and the force enacted by SQUID, as shown for different cantilever resting positions z in Fig. 3.15. The highest sensitivity is found at $z = R/2$, where we also find the largest force on the cantilever in the simple model without the changes due to the *in-plane* field (dashed lines). However, due to the *in-plane* component, the position of the magnet significantly modifies the critical current, such that force and geometric sensitivity deviate from the ideal case and attain their maximum values for different positions above the SQUID loop. Ideally, the cantilever should be positioned where both the sensitivity and the force are maximized, enabling effective sensing and feedback. However, uncertainties in the magnetic moment of the particle make it difficult to precisely predict this optimal position (see measurement results on the magnetic moment of the particles in section 4.3.5).

Coupled to a mechanical object, the SQUID potential is significantly altered as the resting position of the cantilever is displaced by loop currents. This leads to a changed loop flux due to the *out-of-plane* field and a change in critical current due to the *in-plane* field of the particle. Following a similar approach as for the bare DC-SQUID we start with the set of equations defined within the *RCSJ*-model for the junctions and the force on the cantilever given by the spring force plus the magnetic force from circulating currents:

$$\begin{aligned} -(1-\alpha')\sin(\delta_1) + j_{\mathrm{loop}} &= -\frac{1}{E_{\mathrm{J}}'}\frac{\partial E_{\mathrm{pot}}}{\partial \delta_1} \\ -(1+\alpha')\sin(\delta_2) - j_{\mathrm{loop}} &= -\frac{1}{E_{\mathrm{J}}'}\frac{\partial E_{\mathrm{pot}}}{\partial \delta_2} \\ -k\Delta z + \frac{\partial}{\partial z}\left(E_{\mathrm{J}}'\frac{2\pi\Phi_{\mathrm{mag}}(z)}{\Phi_0} j_{\mathrm{loop}}\right) &= -\frac{\partial E_{\mathrm{pot}}}{\partial z}. \end{aligned} \tag{3.46}$$

Here, the loop current is given by $j_{\mathrm{loop}} = \frac{1}{\pi\beta_{\mathrm{L}}'}\left(\delta_2 - \delta_1 - 2\pi\Phi_{\mathrm{ext}}(z)/\Phi_0 + 1/2\,\eta\pi\beta_{\mathrm{L}}' j_{\mathrm{tr}}\right)$. After integration and comparison to solve for the constants, the total potential of the SQUID–mechanical

oscillator system is found as

$$\begin{aligned}\frac{E_{\mathrm{pot}}(\delta_+,\delta_-,z)}{2E_\mathrm{J}'} &= 1-\cos(\delta_+)\cos(\delta_-)+\alpha'\sin(\delta_+)\sin(\delta_-)\\ &\quad+\frac{1}{4E_\mathrm{J}'}k(z-z_{\mathrm{res}})^2+\frac{1}{\pi\beta_\mathrm{L}'}\left(\delta_- -\pi\frac{\Phi_{\mathrm{ext}}(z)}{\Phi_0}\right)^2\\ &\quad-\frac{I_{\mathrm{tr}}}{2I_\mathrm{c}'}\delta_+ +\frac{I_{\mathrm{tr}}}{2I_\mathrm{c}'}\eta\left(\delta_- -\pi\frac{\Phi_{\mathrm{ext}}(z)}{\Phi_0}\right).\end{aligned}$$

The total potential resembles that of a bare SQUID-cavity given in Eq. (3.36) for the most part. However, due to the flux introduced by the cantilever, the term assigned to the flux quantization now additionally depends on the cantilever position. With an oscillation of the cantilever, this term will lead to a change in δ_- and thus represents the coupling mechanism between SQUID and cantilever. The spring term in the potential ensures that the force exerted by the loop currents on the cantilever is balanced out. This interplay results in a changed resting position of the cantilever with the phase particle trajectory through the potential. Furthermore, for an applied transport current j_{tr} a loop inductance asymmetry η alters the loop flux/loop current and now additionally depends on the flux created by the magnet.

3.4.4 Simulation of the flux tuning

Similar to the SQUID-cavity, we can characterize the tuning behavior of the SQUID-cantilever system by tracking the position of a particle in the potential given by Eq. (3.47). To reduce the computational time, we simplify the potential to two dimensions by utilizing the relation between δ_+ and δ_- given by the equation for the transport current (Eq. (3.25)). As shown in Fig. 3.9, within the SQUID potential, the minimum followed by the particle agrees with the calculated solutions for δ_+. As the cantilever position does not directly influence δ_+, we can now solve Eq. (3.25) for a given j_{tr} at each point in δ_-. As this equation is periodic, we evaluate the potential for each set of (δ_-, z) and $\delta_+(\delta_-, j_{\mathrm{tr}}) + n\pi$ and choose the solution corresponding to the overall lowest total potential energy. Thus, the obtained potential in (δ_-, z) has a double parabolic shape – orignating from the flux quantization and the spring potential. Lastly, thermal excitations of the cantilever induce an additional source of flux noise, which is taken into account by assuming a larger noise term σ.

The system response is visualized in Fig. 3.16 by plotting the cavity resonance frequency ω_c, loop current $I_{\mathrm{loop}}/I_\mathrm{c}$, static deflection of the cantilever $(z-z_{\mathrm{res}})/z_{\mathrm{zpm}}$ and change of the mechanical frequency $\delta\omega_\mathrm{m}$ upon tuning the external flux. The first three parameters are directly obtained by using the potential to calculate the change in the particle position depending on the externally varied applied flux. The mechanical frequency shift is calculated by deflecting the cantilever around its newly found resting position at each applied flux. As the SQUID responds fast enough, the phase particle instantaneously adjusts to the flux change related to the deflection, occupying a new minimum with respect to δ_-. By fitting the obtained minimum for each deflection with a polynomial of second order, we extract the effective spring constant and thus the frequency of the cantilever $\omega_\mathrm{m} = \sqrt{k/m_{\mathrm{eff}}}$.

For the different β_L in Fig. 3.16, we see that the *in-plane* field of the magnet leads to a significant reduction of the critical current I_c with a maximal $I_{\mathrm{loop}}^{\mathrm{max}}/I_\mathrm{c} = 0.04$. Therefore, β_L (see Eq. (3.42)) is effectively decreased to $\beta_\mathrm{L} \approx 0$ for the parameter range considered here such

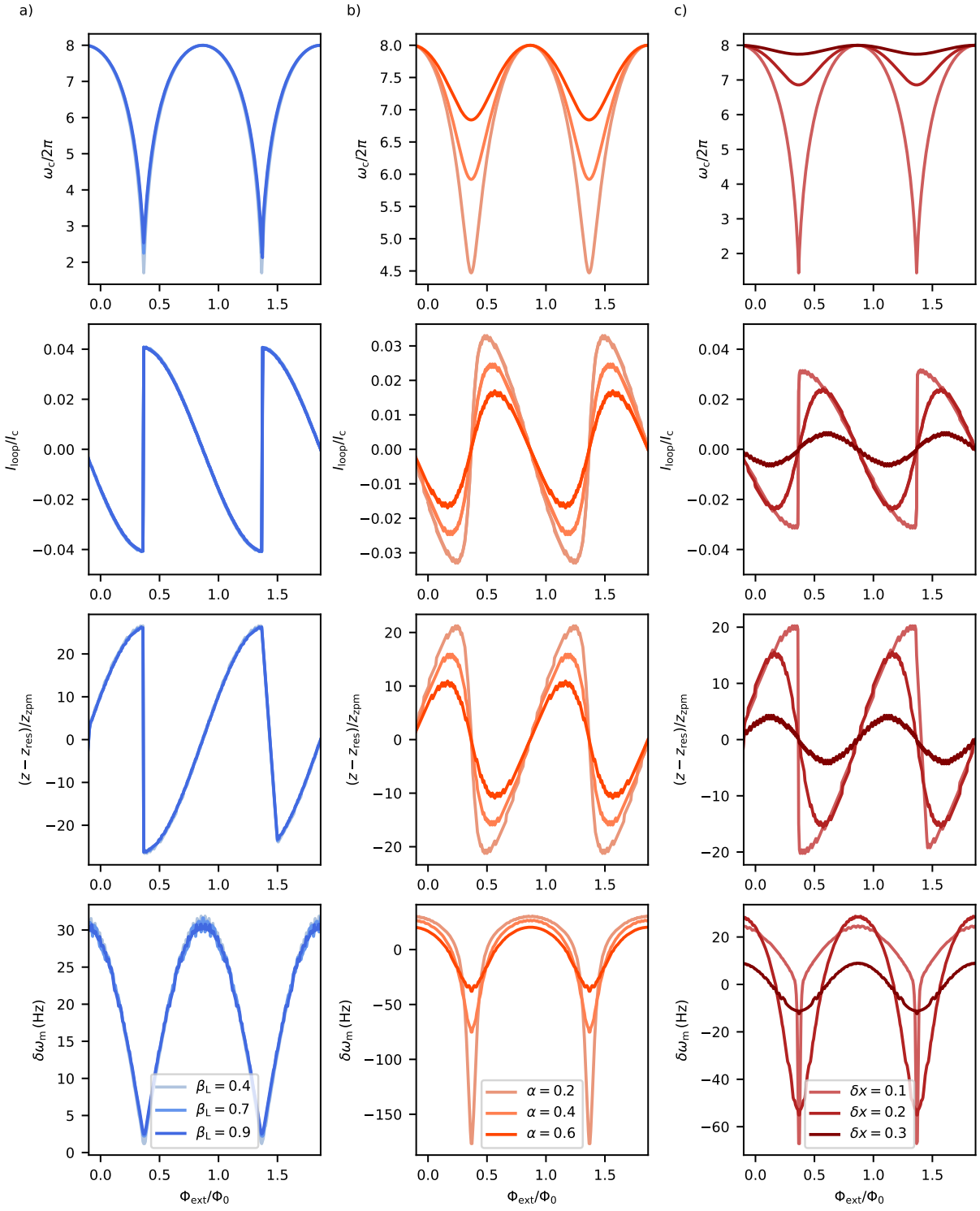

Fig. 3.16 Applying an external magnetic field to the SQUID-cantilever system. By tracking the trajectory of a phase particle, the cavity resonance frequency ω_c, loop current I_{loop}/I_c, static deflection of the cantilever $(z - z_{res})/z_{zpm}$ and change of the mechanical frequency $\delta\omega_m$ are calculated for **a)** $\beta_L = 0.4, 0.7, 0.9$, **b)**$\alpha = 0.2, 0.4, 0.6$ and an off-center displacement **c)** $\delta x = 0.1, 0.2, 0.3$. Fixed parameters for the SQUID are $\beta_L = 0.4$, $\alpha = 0$, $\eta = 0$, $\beta_R = 0.1$, $\sigma/E_J = 0.01$, $j_{tr} = 0$ and for the cantilever $k = 40\,\mathrm{N m}$, $m = 5\,\mathrm{nAm}^2$, $m_{eff} = 15\,\mathrm{ng}$, $z_{res} = 12\,\mu\mathrm{m}$, $\delta x = 0$, $x_p = 30\,\mu\mathrm{m}$, $R = 25\,\mu\mathrm{m}$, $A_{eff} = 3\,\mu\mathrm{m} \times 300\,\mathrm{nm}$

that we obtain identical flux tuning, resemvling the behavior of a non-hysteretic SQUID-cavity (see Fig. 3.9). The obtained static deflection of the cantilever is directly related to the loop current, with the maximal deflection aligning with the highest amplitude found in I_{loop}. For the mechanical frequency, we observe a shift to higher frequencies as a function of the gradient of I_{loop} with respect to flux. For the considered SQUID asymmetry α, wee see the same changes for ω_{c}, I_{loop} and the deflection z. However, the asymmetry leads to a strong gradient in the obtained loop current close to its lower sweet spot, which results in a significant mechanical frequency shift. With increasing asymmetry α, the gradient in I_{loop} decreases, accompanied by a smaller mechanical frequency shift. The tuning behavior for different displacements of the magnetic particle δx resembles the response of the one obtained for an asymmetric SQUID. For a magnet displaced further from the SQUID's center, the influence of the *in-plane* field component on the critical current of one junction increases, leading to a higher asymmetry. As the static deflection of the cantilever is not high enough to alter the ratio between the two junctions during the flux tuning, the system response remains consistent with that of an asymmetric SQUID.

CHAPTER 4

Experimental setup

In this chapter, we present the experimental platform employed throughout this thesis. We begin with an overview of the operating principle of the dilution cryostat and present modifications that were implemented to suppress mechanical vibrations at the experimental setup. Next, we describe the experimental setup, starting with the microwave cavity design and fabrication process. Following this, we explain the modifications to the *Atomic Force Microscope* (AFM) cantilevers and the procedure to mount these on SQUID cavities. The measurement setup is introduced, featuring a rectangular waveguide coupled to the cavities in a notch/hanger configuration. We proceed with an explanation of the circle fit routine developed by Probst et al. [83], which is used to characterize the microwave cavities. To account for the Kerr-nonlinearity of our cavities, we extended this routine by introducing an additional fitting step. To determine the mechanical mode occupation of the cantilever we discuss the calibration method by Gorodetksy et al. [84] and its implementation in the microwave regime. Lastly, the wiring setup used for the results presented in this thesis is covered.

4.1 Cryostat

To operate our SQUID cavities, it is necessary to cool the experiment below the superconducting transition temperature of Niobium at 9.25 K [76]. For cavities with a microwave resonance frequency of around 8 GHz to remain in their thermal ground state requires even lower temperatures of below 350 mK. To meet these requirements, our setup is mounted to the baseplate of a *Oxford Triton 400* dilution refrigerator typically at $30 - 100$ mK.

4.1.1 Cooling principle

Fig. 4.1 shows a schematic representation of such a refrigerator consisting of 5 thermally isolated stages with temperature decreasing from top to bottom. To reach temperatures down to 30 mK, the cryostat relies on two separate cooling systems. The first is the pulse tube (PT) cooler, which provides cooling by adiabatic expansion of high-pressure helium gas ($20 - 25$ bar),

reaching temperatures of $\sim 50\,\mathrm{K}$ at the first stage and 4 K at the second stage of the cryostat. The lower stages are then cooled by a mixture of ^{4}He and ^{3}He within the dilution unit. Thermally anchored to the PT and each subsequent stage, the mixture is circulated through the cryostat. After reaching a temperature of about 4 K, the mixture condenses within the mixing chamber at the base plate. Evaporative cooling, achieved by continuously pumping the condensate, further cools the mixture to 800 mK, where a phase transition occurs, separating the dilute (predominantly ^{4}He) and concentrated (predominantly ^{3}He) phases. A pump is used to continuously extract ^{3}He from the dilute phase, and to reinject the extracted ^{3}He back into the mixing chamber to the concentrate phase. As ^{3}He atoms cross from the concentrated phase into the dilute phase, they absorb heat and thus provide a continuous cooling process. By circulating the ^{3}He, the base plate can be cooled to approximately 30 mK [85, 86].

4.1.2 Suspension setup

To ensure proper thermalization of the experimental setup, components are typically rigidly screwed to the base plate, providing high contact pressure and thereby maximizing thermal contact [87]. However, the cryostat operates in a vibration-rich environment due to the presence of several active pumping systems - predominantly the pulse tube compressor and rotary valve, but also the fore pump, turbo pump, and the compressor associated with the dilution unit. The mechanical vibrations are most prominent in the 5-10 kHz range with additional low frequency components at 1.4 Hz and 140 Hz due to the stepper motor of the rotary valve [88, 89]. Hosting a mechanically compliant element within our experiment makes us susceptible to mechanical vibrations of any kind and thus renders a rigid connection to the cryostat environment unfavorable.
To decouple our system from vibrations of the cryostat, we implemented a passive one-stage suspension setup consisting of a nylon wire and a steel spring forming an elastic pendulum based primarily on the setup in [89]. Thus, for the *xy* direction (parallel to the floor of the lab), the natural frequency of the setup is given by the pendulum component

$$\omega_{\mathrm{xy}} = \sqrt{\frac{g}{l}} \tag{4.1}$$

with the total pendulum length l and the g the earth gravitational constant. The natural frequency in vertical z direction is governed by the spring as

$$\omega_{\mathrm{z}} = \sqrt{\frac{k_{\mathrm{spring}}}{m_{\mathrm{exp}}}} \tag{4.2}$$

with the spring constant k_{spring} and the total mass of the experiment m_{exp}. To quantify the effectiveness of a vibration isolation system, one commonly uses the concept of *transmissibility* as a function of frequency, defined as the ratio of the response amplitude of the isolated object $A(\omega)$ to the amplitude of the base excitation $B(\omega)$. For a simple damped spring-mass system, the displacement transmissibility $\mathcal{T}(\omega)$ is given for the respective direction $i = x, y, z$ by [90]

$$\mathcal{T}_i(\omega) = \frac{A_i(\omega)}{B_i(\omega)} = \sqrt{\frac{1 + \left(2\zeta \frac{\omega}{\omega_i}\right)^2}{\left(1 - \frac{\omega}{\omega_i}^2\right)^2 + \left(2\zeta \frac{\omega}{\omega_i}\right)^2}}, \tag{4.3}$$

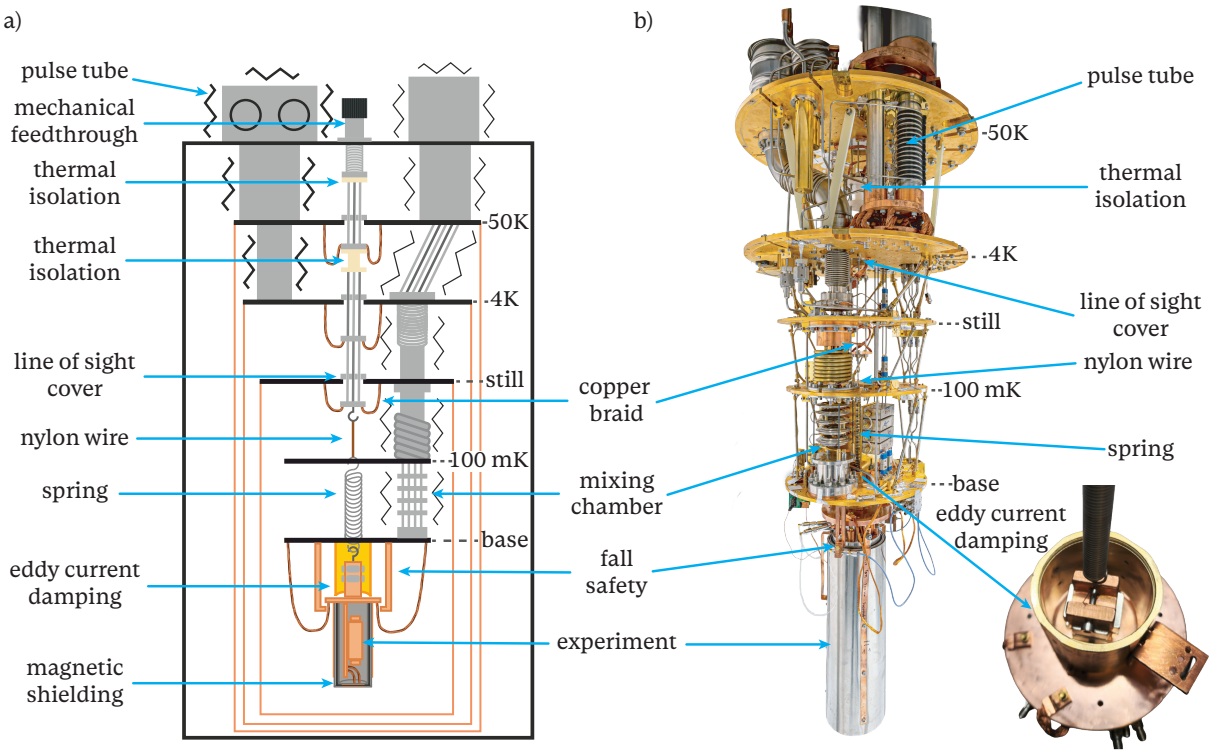

Fig. 4.1 **a)** Schematics of a dilution cryostat with a built-in suspension setup. To decouple from vibrations created mainly by the pulse tube and the mixing chamber, the experiment, including the magnetic shields, is suspended with a spring and a nylon wire. For safety reasons, copper L-pieces secure the experiment from a fall. To ensure sufficient thermalization, copper braids connect the copper T-beam (on which the waveguide is mounted) to the base plate. Additionally, the magnetic shields are also thermalized to the T-Beam using copper braids and through three thin copper sheets on the outside. To prevent a resonant ring up of the suspension setup, 8 magnets are placed within a brass tube as an eddy current damper. To improve the thermalization, a mechanical feedthrough was added, which allowed us to rest the experiment on the safety L-pieces during coolown, and lift it later to ensure mechanical decoupling. The section connecting the feed through to the nylon wire is made of stainless steel rods to minimize heat flow between neighboring thermal stages. Between each cryostat plate, three rods connect through a line-of-sight cover to a small plate thermalized by copper braids to the plate above. To reduce the heat load on the first two plates PTFE thermal isolation pieces are added between the rods. **b)** Photograph of the setup including the feedthrough, with a zoom-in on the eddy current damper (by D. Jordan).

with the damping ratio defined as $\zeta = c/\left(2m_{\text{exp}}\omega_i\right) = 1/\omega_i\tau$ given by the damping coefficient c or time constant τ. For $\zeta < 1$ the system is considered underdamped, $\zeta = 1$ critically damped, and $\zeta > 1$ overdamped. Fig. 4.2a) shows the transmissibility of the vertical component for different damping ratios. Increasing the damping leads to a reduction of the transmissability around the resonance frequency of the setup, where the observed height is given by $\mathcal{T}(\omega_i) = 1/2\zeta$. For an

Iteration	CD	C-braids	EC-damper	MW-cable	Feedthrough	Comment
1	*CD32*	4	×	*Delft*	×	-
2	*CD38*	3	✓	*Delft*	×	-
3	*CD42*	3	✓	*Delft*	×	C-braids to the shields
4	*CD50*	3	✓	*Elspec*	✓	annealed C-braids

Tab. 4.1 Overview of the four main iterations of the setup with the corresponding cooldown number (CD), accounting for the number of attached copper braids (C-braids), installed eddy current damper (EC-damper), which microwave cables were used, installed feedthrough and any additional comments.

underdamped system, we see that any noise around ω_i would be significantly enhanced. However, above ω_i increasing the damping reduces the isolation to $\mathcal{T}(\omega \gg \omega_i) = 2\zeta\omega_i/\omega$, whereas for an undamped system one observes an isolation following $\mathcal{T}(\omega \gg \omega_i) = (\omega_i/\omega)^2$. Therefore, a compromise has to be found between sufficient reduction of the on-resonance response of the system and good isolation in the high frequency limit.

In a first iteration, the setup was suspended from the still plate to achieve reasonable damping in xy direction, resulting in a total length of $l = 30\,\mathrm{cm}$. To support the total mass of the experiment, a stainless steel spring with spring constant of $k_{\mathrm{spring}} = 700\,\mathrm{Nm}$ was used. Including the magnetic shielding - a mu-metal/Niobium/mu-metal tri-layer shield - the total weight of the setup is $m_{\mathrm{exp}} = 5.5\,\mathrm{kg}$. Thus, the resulting frequencies are $\omega_{\mathrm{xy}}/2\pi = 0.9\,\mathrm{Hz}$ and $\omega_{\mathrm{z}}/2\pi = 1.8\,\mathrm{Hz}$. In order to minimize the vibrations that couple in through the microwave in-/output lines low, we initially used cryoflex cables from *Delft circuits*. Due to electrical performance issues these cable were later replaced with *MK-5005* flexible coaxial cables from *Elspec*. We ensure thermalization of the setup by using 3 flexible OFHC (oxygen-free high conductivity)-copper braids attached to a copper lid holding the T-beam with the waveguide. To thermalize the shield, three copper sheets are rigidly connected to the outside mu-metal layer and the copper lid. We further implemented L-pieces connected to the base plate to act as a fall safety in case of material failure of the elastic pendulum, as shown in Fig. 4.1a). The details for the four main iterations of the setup are summerized in Tab. 4.1: To characterise the isolation, we briefly turned on the pulse tube cooler at room temperature and measured the mechanical vibrations with an accelerometer attached to the setup, either rigidly connected to the to the base plate or suspended from the still plate as shown in Fig. 4.2b). With the suspension, we achieve a damping of the vibrational noise in the low frequency range up to 1 kHz by $\sim 20\,\mathrm{dB}$. Above 1 kHz, the detection is limited by the rigidity of the cable connected to the accelerometer.

As demonstrated by measurements on the optomechanical setup in section 5.2.1 (see, e.g., Fig. 5.16), the low-frequency component of the PT, which lies close to the frequency of the z-mode of the spring, led to a resonant ring-up of the first iteration of the supended setup, before installing the eddy current damping system in Fig. 4.1b). Under these conditions, measurements on the mechanical occupation became impractical. Thus, the resonant response of the suspension had to be damped while keeping vibrations coupled into the system low. Therefore, in a second iteration of the setup, we implemented a damping mechanism based on eddy currents, which allows for a contact-free damping of the suspension setup. Assuming a dipole moving in front of

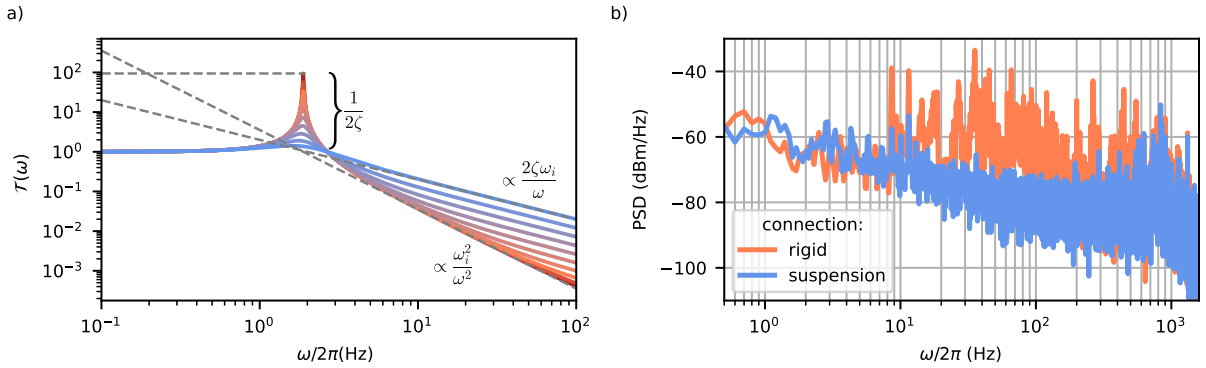

Fig. 4.2 **a)** Transmissibility $\mathcal{T}(\omega)$ of a spring setup against frequency ω. Parameters used $m = 5.5\,\mathrm{kg}, k = 700\,\mathrm{Nm}$ and ζ =0.5−50%. **b)** Power spectral density of the vibrations at the experiment at room temperature, connected rigidly to the base and using the suspension setup. The pulse tube was turned on for each measurement to reproduce the conditions during during cryostat operation.

a conducting sheet at a distance d, the energy dissipated by the setup scales approximately as

$$P_{\mathrm{diss}} \propto \frac{v^2 m_\perp^2 w}{\rho d^4} \tag{4.4}$$

with the velocity v, magnetisation $m_\perp$ perpendicular to the sheet of thickness w and the resistivity ρ [91]. Hence, to achieve reasonable damping, strong permanent magnets close to a thick metal of low resistivity are desirable.

We tested the damping induced by 8 NdFeB-magnets ($22 \times 10\,\mathrm{mm}$) attached to the suspension setup moving within a brass tube of thickness $w = 5\,\mathrm{mm}$ and distance $d \approx 8\,\mathrm{mm}$ as depicted in Fig. 4.1a). With an attached accelerometer (type *KS76C.100 - MMF*) we measured the ringdown of the setup after manually exciting it at room temperature. The resulting damped oscillation for different setup modifications are shown in Fig. 4.3. For the free-hanging setup, we observe a ringdown with a time constant of $\tau = 140\,\mathrm{s}$ which results in a damping ratio of $\zeta = 0.06\%$. By adding the eddy current damping setup, we achieve an increase in damping by about a factor of 2, hence a damping ratio of $\zeta = 0.12\%$. Furthermore, we attached three copper braids to the setup necessary in the experiment to ensure thermalization. As the measurements indicate, it is crucial that the braids have appropriate length and flexibility, and that they are connected to the setup without mechanical tension. Even though increasing the resonant damping significantly if mounted under tension, the copper braids will couple in higher frequency vibration to the system. The reduction of the time constant with braids under tension reduces $\tau = 49\,\mathrm{s}$, which will introduces mechanical noise into the system at higher frequencies. An appropriate assembly – freely hanging braids connected to the setup without strain – ensures that mechanical vibrations coupled in through the braids are kept to a minimum, as demonstrated by only a minor change in $\tau = 66\,\mathrm{s}$.

Measurements in section 5.2.1 demonstrate that the damping achieved with this configuration is sufficient to prevent sustained oscillations of the suspension system, while simultaneously providing effective decoupling of the experiment from the higher frequency mechanical vibrations of the PT. This eddy current damping setup has been in place since the second iteration of the isolation setup.

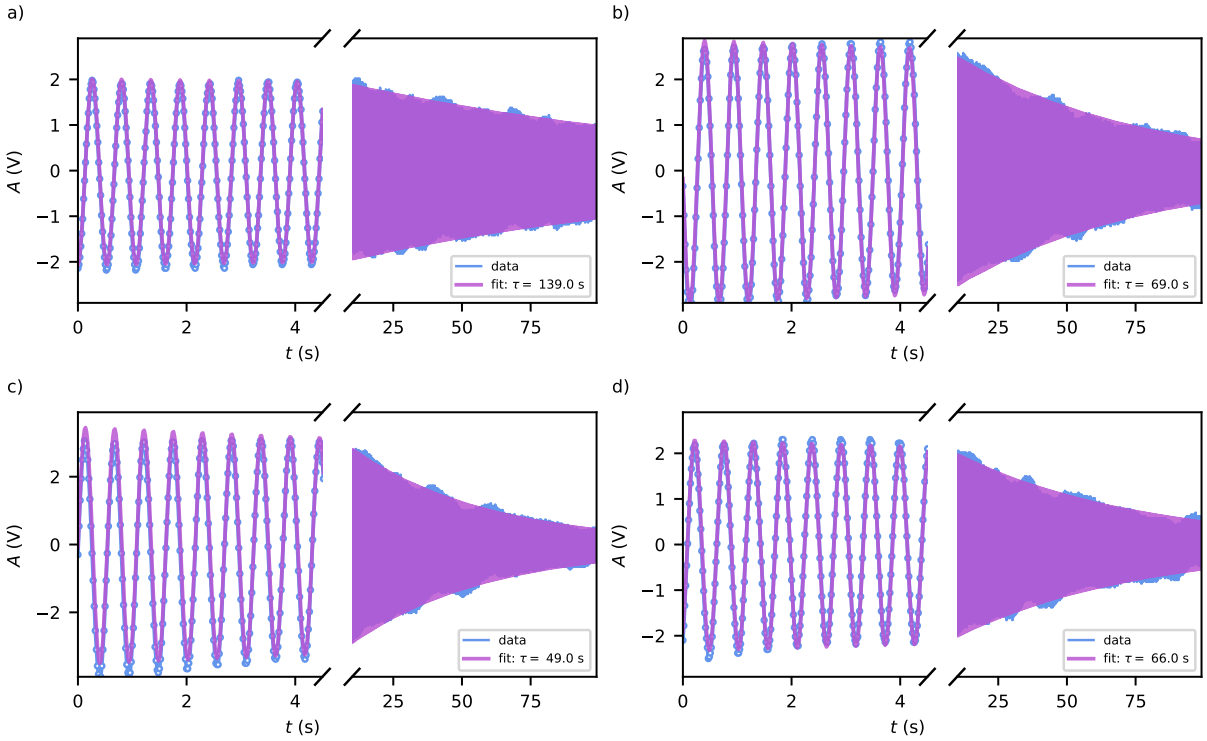

Fig. 4.3 Ringdowns of the setup measured with an accelerometer for different configurations at room temperature. **a)** Free hanging suspended setup and **b)** with eddy current damping. **c)** and **d)** suspended setup with eddy current damping with copper braids for thermalization under tension and hanging free, respectively. *Measurements by Alexandra Egger under my supervision.*

4.1.3 Thermalisation

A significant drawback of the design is that the mechanical isolation setup also leads to thermal decoupling of the experiment from the base plate. In Fig. 4.4a) we compare the time needed for the experiment to thermalize for the second and the third iteration of the setup. Here, we attach a temperature sensor to the copper lid of the experimental setup and track its temperature during the cooldown. With a rigid connection to the base plate using two M3 screws, the setup needs 1.5 days to reach a base temperature of 35 mK (grey line in Fig. 4.4a). The temperature of the experiment follows the temperature of the base plate measured independently by a second sensor on the base plate, signifying the efficient thermal coupling between this rigidly connected setup and the base plate. By implementing the suspension setup with three copper braids attached to it (second iteration Tab. 4.1), we observe that it takes 7 days for the experiment to cool below 100 mK and an additional 10 days to reach base temperature (orange). At a temperature of around 1 K, the temperature of the experiment starts to deviate from that of the base plate. Futhermore, the influence of the hotter mass next to the base plate is visible on the cooldown rate of the base plate itself, with the base plate now requiring 6 days to reach 35 mK (brown).

Trying to extract the thermalization rate from the experiment temperature below 300 mK by fitting the data with a simple one stage model (base coupled to experiment) failed. This led to the assumption that thermal contact to the magnetic shield – contributing almost the entire mass

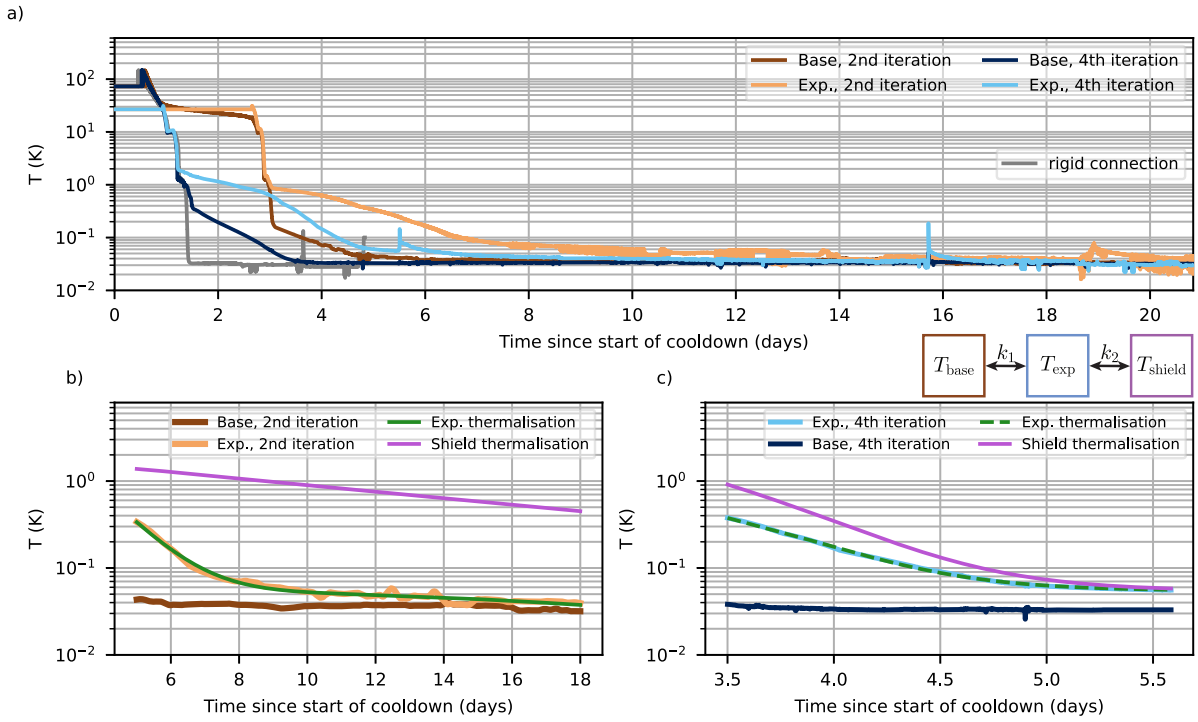

Fig. 4.4 **a)** Thermalization of the experiment for the second iteration of the suspension setup versus the fourth one (see Tab. 4.1 for details) with temperature sensor attached to the experiment (Exp.) and another one rigidly to the base plate (Base). For comparison, the temperature of the experiment rigidly connected to the base plate is shown. **b)** Zoom-in on the thermalization for the initial and improved setup after reaching 300 mK. The data is is fitted to extract the rates of heat transfer between the base plate and the experiment (k_1), as well as the thermal contact of the experiment to the magnetic shields (k_2) through the copper sheets for the first and the additional copper braids for the third iteration. This allows us to additionally infer the shield temperature.

to the experiment with around 5 kg – is an additional critical limitation for the thermalisation. Fitting a two-stage model as schematically shown in Fig. 4.4 allows for an adequate description of the data. We find that the shields remain at a significantly higher temperature of $\sim 500\,\mathrm{mK}$ even after the experiment reaches the base temperature of 35 mK. This corresponds to a slow thermalization rate between the suspended shield and the base plate which is only $k_2/k_1 = 0.1$ of that between the suspended experiment and the base plate.

To reduce the cooldown time, we undertook several modifications to the setup, which resulted in the fourth and latest iteration of the suspension setup as shown in Fig. 4.1. First, we used polished copper discs in between the different layers at the bottom of the magnetic shield. By a tight connection through three *M2.5* screws, the copper disks in between the separate layers increase the thermal contact. Furthermore, we added two copper braids from the T-beam to the inner shield layer, such that the shield is thermalised via the copper sheets on the outside as well as these copper braids on the inside.

Secondly, we replaced the copper braids connecting the copper lid of the experiment to the base plate with thermally annealed copper braids, which offer reportedly higher thermal conductivity and increased flexibility [92]. The heat treatment was done at 300°C under a nitrogen atmosphere by the group of Prof. Wieczoreck at the University of Chalmers.
Lastly, we implemented a mechanical vacuum feedthrough as shown in Fig. 4.1. The feedthrough extends from the top of the cryostat through the central line-of-sight port, passing below the still plate via three stainless steel rods. These rods are stepwise thermalized at each stage by copper braids to the plate above. To minimize radiation heating of the lower plates, the line-of-sight ports are covered by stainless steel disks with small holes for the rods. To further reduce the thermal contact between the upper plates, the rods are interrupted by Teflon spacers. Below the still plate, the rods are connected to the elastic pendulum suspending our experiment. The travel length of the feedthrough of roughly 8 cm enables us to rest the suspension setup with its 5.5 kg onto the three (fall safety) copper L-pieces, which are directly screwed to the base plate. The combined influence of these changes on the thermalisation of the setup is shown in Fig. 4.4a). The fourth/final iteration of the setup reaches 100 mK within 4.5 days, which is an improvement by 2.5 days compared to the previous iterations. Furthermore, the base plate cools down to 35 mK two days faster. The sudden spike in temperature at 5.5 days corresponds to lifting the setup using the feedthrough. Fitting the temperature time dependence in Fig. 4.4c) reveals increased rates, with $k_1'/k_1 = 7$ and $k_2'/k_2 = 30$, further confirming the improvement achieved in thermalization. However, with this setup in the third iteration, we observe that the base and the can temperature start to deviate at $\sim 1\,\mathrm{K}$.

The current limitations of the thermalization are estimated in the master's thesis of C. Dejaco, who worked with me on this project [80]. His analysis summarizing findings from [87, 92–98] and the main results are briefly presented here for completeness.

The thermal conductivity of a sample can be divided into electron and phonon transport within the bulk and at contact surfaces. For the bulk, one first observes an increase in thermal conductivity towards low temperatures, as collisions between the transport channels become less frequent. In this regime, the conductivity is limited by material impurities. For even lower temperatures, phonons start to freeze out, resulting in an electron-dominated heat transport [99]. Due to its high electric transport properties, OFHC-copper has one of the highest thermal conductivities of $2000\,\mathrm{W/(K \cdot m)}$ at 20 K, below which it starts to decrease linearly [94]. By annealing the copper under an inert atmosphere, even higher thermal conductivities can be obtained [92], making annealed OFCH-copper a desirable candidate for thermalization at cryogenic temperatures.
However, in addition to the bulk properties, the heat transfer across contact surfaces plays a major role. Scaling with the applied pressure and surface roughness, a temperature scaling of $\propto 1/T$ for oxygen-free contact areas is found, whereas even a small oxide layer can lead to a $1/T^2$ dependence [96]. Thus, rigidly screwed connections – providing preload forces on the order of 1 kN for a single M3 screw – of polished copper pieces are desirable for good thermal contact. Regarding the final iteration of the suspension setup, taking these factors into account, the thorough analysis in [80] led to the following conclusions. The initial increase in thermalization can be attributed to the setup resting on the three copper holders combined with the increased thermal conductivity of the annealed copper braids. Down to 10 K, the additional heat transport over the bulk of the holders speeds up the thermalization. However, due to the rather low contact force of 55 N solely given by the weight of the experiment, for lower temperatures,

the thermal transport is limited by the surface contact. This possibly explains the observed deviation between base plate an experiment tempeartures at around 1 K.

Besides polishing and surface treatments, further enhancements regarding the thermalization of the setup - while maintaining our mechanical decoupling - may be achieved by a new copper braid design. The copper braids used so far are clamped to a solid copper piece for screw mounting. However, as found in [87], this pressed contact constitutes the dominant limitation on thermal conductivity at low temperatures below 1.5 K. A significant improvement could be achieved by establishing a welded joint between the braid and the screw mount. Thus, we plan to implement such welded copper braids in the next iteration of the suspension setup, with tests regarding their thermal conductivity currently ongoing. Furthermore, we intend to anneal the critical elements of the setup at temperatures up to 800 °C under vacuum. It is expected that this should further enhance the bulk thermal transport properties, with the additional benefit of increasing the flexibility of the used copper braids.

4.2 Microwave Platform

In this section, we discuss the design and fabrication process of the SQUID cavities used in this thesis. Next, we introduce the rectangular 3D waveguide as the environment used to measure the samples and discuss the circle fit routine to characterise them. Lastly, the complete microwave wiring in the cryostat is presented.

4.2.1 SQUID cavities - design and fabrication

Both generations of SQUID cavities used in this thesis were fabricated by the company *STAR Cryoelectronics*, using a Nb/Al-AlOx/Nb-trilayer fabrication process, which enables the realization of reproducible Josephson-junctions. The first generation pictured in Fig. 4.5b) is the one used by D. Zöpfl in [2–4] with *U*-shaped Nb microstrip cavities on a silicon substrate. The lengths of resonator legs were designed to be either 3.3/3.5 mm and the SQUID at the voltage antinode consisted of either a washer or conventional type with a loop area of $20\,\mu\text{m} \times 60\,\mu\text{m}$. The second generation pictured in Fig. 4.5a) and c) follows a similar design with leg lengths of 3.1/3.3 mm and washer-type SQUIDs with a loop area of $35\,\mu\text{m} \times 35\,\mu\text{m}$ on a higher resistivity silicon substrate ($> 10\,\text{k}\Omega\,\text{cm}$). For both generations, samples are labeled following the designation *oWSQL#*, representing *Old generation Washer SQuid Long* and the batch number.
Following the description in [2], the base electrode consisting of the Nb/Al-AlOx/Nb-trilayer is deposited in the first step of the fabrication. The total thickness of the base electrode is 270 nm, where the Al contributes 9 nm at the top. In the next step, the junctions are defined by using a resist mask, after which the top Al-AlOx/Nb-layer is removed by reactive ion etching (RIE) in all areas except the junctions. Subsequently, one of the cavity legs is defined in the leftover Nb, and the bottom layer of the SQUID-cavity is complete. To isolate the bottom layer, 300 nm SiO_2 is deposited, through which vias are etched at the position of the junctions. In the last step, a top Nb-layer of 300 nm is deposited and defined by RIE, forming the other leg of the cavity. The position of the junction can be seen in Fig. 4.5d) as the small circle. The Nb of the top electrode is visible in white and the bottom electrode below the SiO_2 in blue. The dielectric SiO_2-layer represents a source of dielectric losses, especially in regions of high electric fields encountered towards the end of the cavity legs. Therefore, it was removed (on a special request) in a last step everywhere except the SQUID area, where it remains as a purple square.

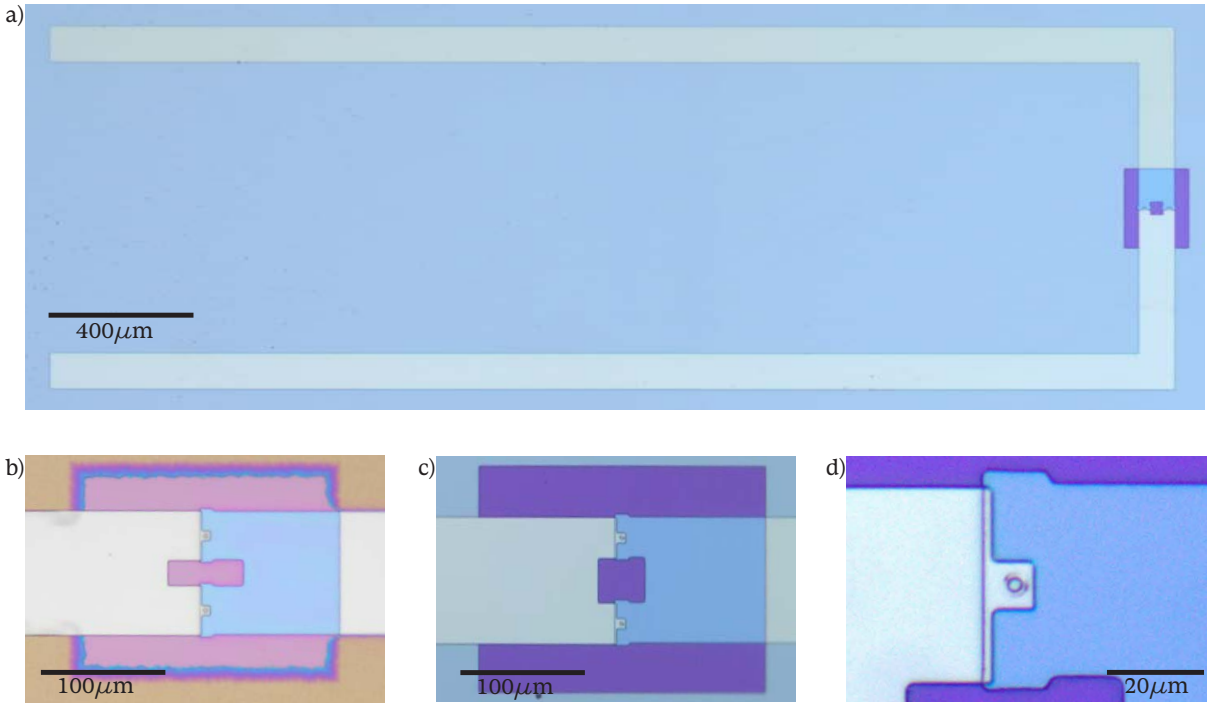

Fig. 4.5 **a)** Microscope image of the full cavity. **b)** and **c)** zoom-in on the SQUID loop for the first and second generation samples. **d)** Zoom-in on one of the JJs of a second generation device.

The considerations behind design choices can be split into the cavity and the SQUID considerations. From HFSS simulations and based on previous measurements in [2], the leg lengths of the cavity were chosen to obtain resonance frequency around 7.8–8.2 GHz and 8.5–9.0 GHz for the first and second generation, respectively. To obtain a reasonable tuneability of the SQUID-cavity, a low critical current and a small loop inductance are desirable (high β_R and low β_L see section 3.3). In the trilayer fabrication process by *StarCryo*, the critical current is determined by the junction area and the critical current density. For our design, we selected the smallest available one of 8.4μA. Even though a small loop area is beneficial for a good tunability of the SQUID-cavity, the magnetic field sensitivity increases with the loop area. As the goal of the setup is to detect the mechanical motion of a cantilever through a magnetic field change, tuneability and sensitivity had to be balanced. We settled on a loop area of $20 \times 60\,\mu$m roughly matching the cantilever dimensions and allowing for a certain degree of displacement during the mounting process. Accounting for improvement in the precision with which we could mount cantilevers, for the second generation we decided on a square loop with a size of $35 \times 35\,\mu$m to match the magnetic particle's size. With that we maintain the same detection efficiency, as most of the magnetic field is funneled into the SQUID by simultaneously decreasing β_L (as the linear inductance reduces).

4.2.2 Microstrip Cavity – waveguide coupling

A 3D rectangular waveguide serves as a controllable environment to interact with the microstrip cavity, as schematically shown in Fig. 4.6a). The waveguide walls confine the electromagnetic

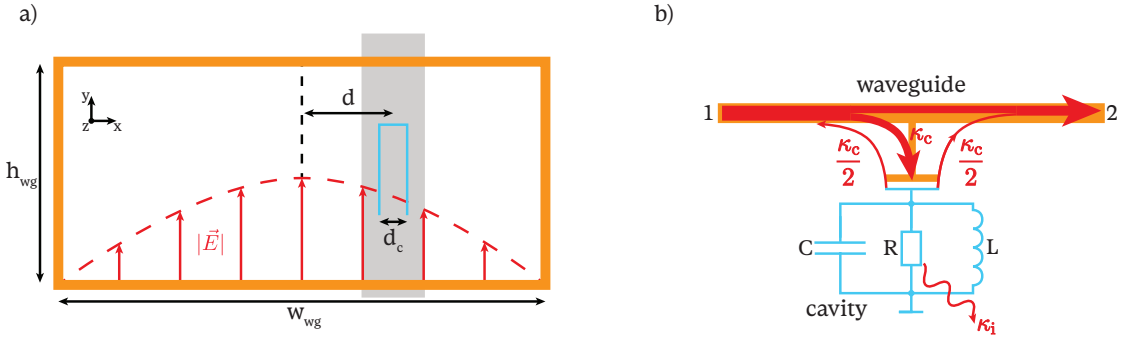

Fig. 4.6 **a)** Schematic cross-section of the rectangular waveguide, perpendicular to its propagation direction. The red dashed line represents the electric field of the fundamental TE_{10} mode. A difference in electric field between the cavity legs leads to capacitive coupling with the waveguide mode. This coupling can be tuned by adjusting the chip position d. **b)** Circuit representation of the cavity in the notch/hanger-configuration, showing capacitive coupling to the waveguide mode with an external loss rate κ_c. The internal loss rate κ_i of the cavity is depicted as a resistor. Red arrows indicate the path of an incoming probe tone. Half of the cavity-emitted signal is reflected back toward the waveguide input, while the other half - being phase-shifted - interferes with the uncoupled portion of the probe tone at the output.

field, enabling propagation along its longitudinal axis. By solving Maxwell's equations, the electric field of the fundamental waveguide mode TE_{10} is given by [100]

$$\vec{E} = E_0 \cos(\pi d / w_{wg}) \vec{e}_y, \tag{4.5}$$

with the electric field amplitude E_0, the off center displacement d and the waveguide width w_{wg}. Propagation through the waveguide is only possible above the cutoff frequency $\omega_{10}^{cut} = \pi/(w_{wg}\sqrt{\mu_0 \epsilon_0})$ with the vacuum permittivity and permeability of the electric and magnetic field, respectively. Our U-shaped cavities are placed inside the waveguide, whose walls function as the ground plane for the cavity. The separation between the two cavity legs d_c leads to an electric field difference ΔE at the legs for an off-center displacement d. This field difference leads to a capacitive coupling to the waveguide mode with a coupling rate

$$\kappa_c \propto \Delta E \propto \sin(\pi d / w_{wg}), \tag{4.6}$$

allowing us to manipulate and detect the cavity mode. This configuration is also referred to as a hanger/notch type coupling, whose circuit equivalent is shown in Fig. 4.6b). One benefit of this 3D design for common planar structures is that the coupling can be tuned by changing the placement d of the cavities, which is studied in [30] and [80]

Within our experiment we rely on a standardized *WR-90* waveguide with a height $h_{wg} = 11\,\text{mm}$ and width $w_{wg} = 23\,\text{mm}$ shown in Fig. 4.7. For such a waveguide, the cutoff frequency is 6.5 GHz. Coils from a superconducting wire (*Supercon Inc. 54S43* ∅0.1 mm) are wound around the ends of the waveguide with up to 100 turns to allow for frequency tuning of the cavities by applying an external magnetic field. To connect the waveguide to our microwave wiring, we use commercially available couplers by *Huber and Suhner*.

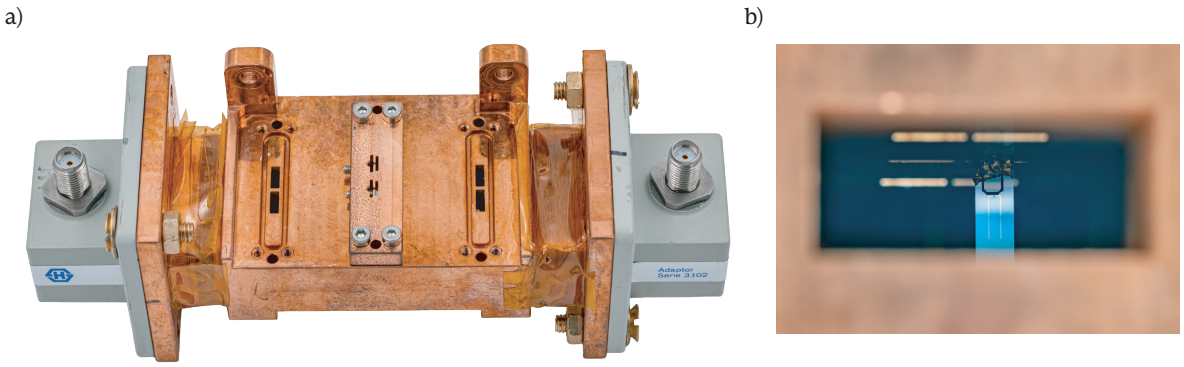

Fig. 4.7 **a)** Photograph of a typical waveguide used in this thesis. To connect the waveguide to the microwave wiring, it is connected to couplers with SMA connectors. To apply magnetic fields, the waveguide features two superconducting coils at the ends. The microstrip cavities are fixed in a sample holder and placed into the waveguide through slits in the waveguide wall. **b)** Photograph of a cavity with a cantilever placed inside the waveguide (Photos by D. Jordan).

4.2.3 Characterisation via Circle fit

The cavities within the waveguide are characterised by using the *circle-fit-routine* [83]. Therefore, we measure the scattering parameter S_{21} – the transmission from port 1 to port 2 through the waveguide – to capture the response of the cavity. Realizing a notch-type configuration, this complex response of the cavity is given by [83, 101]

$$S_{21}(\omega) = ae^{i\alpha}e^{-i\tau\omega}\left(1 - \frac{Q_l/|Q_c|e^{i\varphi}}{1+2iQ_l\frac{\omega-\omega_c}{\omega}}\right). \tag{4.7}$$

The first factor in front of the term in brackets represents the influence on the signal from the environment (i.e., the microwave wiring consisting of attenuators, cables, amplifiers, and the waveguide), with a total attenuation a, a phase offset α, and an additional frequency-dependent phase factor, taking into account the electrical delay τ of the system. The second factor in the brackets corresponds to the response of a cavity with resonance frequency ω_c, total/loaded quality factor $Q_l = \omega_c/\kappa_l$ and complex coupling quality factor $Q_c = \omega_c/\kappa_c e^{-i\varphi}$. By using a complex coupling quality factor, we consider a possible impedance mismatch between the waveguide and the cavity.
Based on [83, 101], the individual steps performed by the circle-fit-routine in order to fit the model in Eq. (4.7) to scattering data are shown in Fig. 4.8 on the complex plane as well as the change in amplitude $|S_{21}|^2$ (phase $\angle(S_{21})$) of the signal as a function of detuning. Here, we use simulated data to illustrate the steps involved in extracting cavity parameters from experimentally measured data in this thesis. The fit procedure itself is based on [83, 101]. The environmental influence results in an intertwined loop in the complex plane associated with an offset in magnitude and a linear slope in phase against detuning. For a frequency-tunable sample, the background in the absence of the cavity can be measured by flux detuning the sample. Otherwise, we use the off-resonant point on either side of the resonance frequency to extrapolate a linear background. This background can then be accordingly subtracted as shown in Fig. 4.8a) and b). After background subtraction, the normalized signal on the complex plane corresponds to a circle of diameter $Q_l/|Q_c|$, with the off-resonant point at $(1,0)$. An impedance mismatch

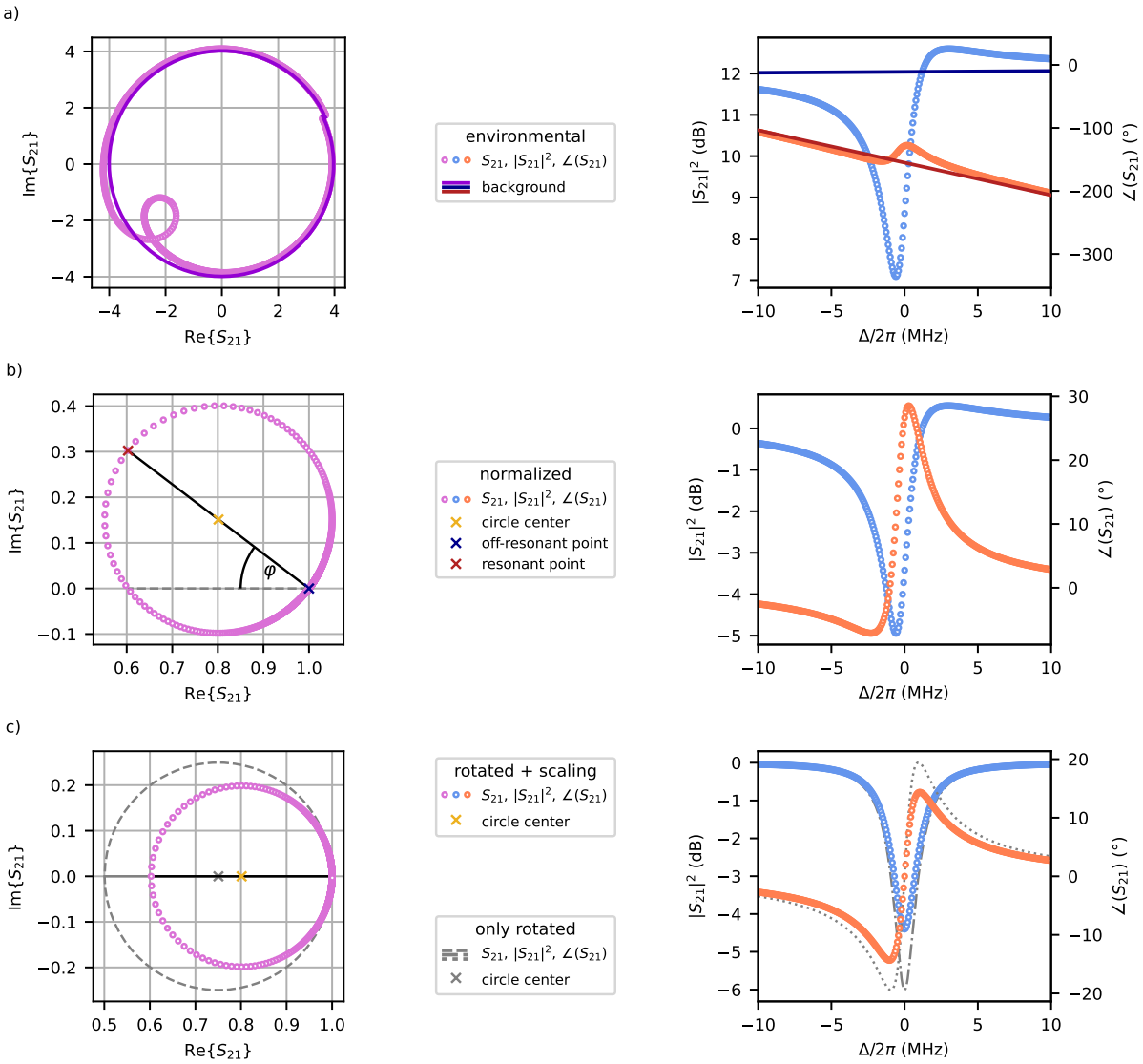

Fig. 4.8 Circlefit procedure on the S_{21}-parameter simulated for a cavity probed in a notch configuration. Plotted on the left in the complex plane and on the right amplitude and phase as a function of detuning: **a)** the environmental background can be subtracted by either applying a linerar fit to the offresonant part of the magnitude and phase data, or by directly measuring the background with the cavity detuned. **b)** In the complex plane the circle is fitted to extract the center-, off-resonant- and resonant-point. Any impedance mismatch between the cavity and the measurement circuit causes a rotation of the circle about the offresonant point by an angle φ. **c)** The fit routine corrects for this impedance mismatch by not only rotation by this angle, but also by scaling the radius as shown in [101].

results in a rotation of the circle around the off-resonant point parametrized by an angle φ, and manifests in an asymmetric shape of the cavity response about the resonance frequency in $|S_{21}|^2$ and $\angle(S_{21})$. Rotating and rescaling the diameter by $\cos(\varphi)$ [101] corresponds to the response of an identical cavity but with perfect impedance matching. Fitting the matched circle with Eq. (4.7) with $\varphi = 0$, the internal quality factor can be calculated as

$$1/Q_\mathrm{i} = 1/Q_\mathrm{l} - 1/Q_\mathrm{c}^\mathrm{eff}. \tag{4.8}$$

If we do not correct for for the rotation, φ has to be fitted as a parameter and Q_i can be calculated with the effective rescaled coupling quality factor $Q_\mathrm{c}^\mathrm{eff} = |Q_\mathrm{c}|/\cos(\varphi)$.
Regarding the coupling quality factor, one can distinguish between three regimes. In case of $Q_\mathrm{i} \approx Q_\mathrm{c}^\mathrm{eff}$, the system resides in the critically coupled regime where the internal and the coupling losses contribute equally to Q_l. For $Q_\mathrm{i} \ll Q_\mathrm{c}^\mathrm{eff}$ the setup is undercoupled, where the internal losses dominate the overall cavity loss, whereas for an overcoupled system $Q_\mathrm{i} \gg Q_\mathrm{c}^\mathrm{eff}$ the losses come mainly from the coupling.

4.2.4 Nonlinear circle fit

The circle fit model presented above can, however, only describe the response of the SQUID cavities studied in this thesis when probed with low power. As discussed in chapter 3.2.3, the SQUID is an intrinsically nonlinear element, which results in a nonlinear response of the SQUID cavities for large probe powers (chapter 3.3). The effective shift in the resonance frequency to first order can be given by

$$\omega_c \to \omega_c - \mathcal{K}\bar{n}_\mathrm{c}, \tag{4.9}$$

with the mean intracavity photon number $\bar{n}_\mathrm{c}$ and the Kerr-constant $\mathcal{K}$. We can model the scattering parameter S_{21} for a nonlinear cavity by solving the cubic equation

$$\bar{n}_\mathrm{c}\left[(\Delta + \mathcal{K}\bar{n}_\mathrm{c})^2 + \frac{\kappa_\mathrm{l}^2}{4}\right] = \frac{\kappa_\mathrm{c}}{2} 2\pi \frac{P_\mathrm{d}}{\hbar\omega_\mathrm{d}}, \tag{4.10}$$

for $\bar{n}_\mathrm{c}$, with an input photon number rate $\bar{n}_\mathrm{in} = 2\pi P_\mathrm{d}/\hbar\omega_\mathrm{d}$ given by the microwave power P_d at the cavity. Here, the coupling rate κ_c in Eq. (2.19) has to be modified by a factor of 1/2 to be compatible with conventions used to derive the S_{21}-response in Eq. (4.7) for a cavity coupled in a notch configuration. Also, the critical input power at which the cavity becomes bistable has to be changed by the same factor, leading to

$$\bar{n}_\mathrm{in,bi} = 2\frac{\kappa_\mathrm{l}}{\kappa_\mathrm{c}} \frac{\kappa_\mathrm{l}^2}{3\sqrt{3}\mathcal{K}}. \tag{4.11}$$

The effects of a Kerr nonlinearity on the S_{21}-parameter are shown in Fig. 4.9 upon increasing the input power. Following the shark-fin-shape of the intracavity photon number (as discussed in chapter 2.2), an asymmetry arises in the amplitude and phase response of $S_{21}(\Delta)$. For a frequency upsweep, the resonance shifts towards the drive until the maximum $\bar{n}_\mathrm{c}^\mathrm{max}$ on resonance is reached. For $\mathcal{K} > 0$, we see a steeper slope for detunings below and shallower slope above $\omega_c - \mathcal{K}\bar{n}_\mathrm{c}^\mathrm{max}$. Due to the steep slope, the point density on the complex circle decreases towards $\omega_c - \mathcal{K}\bar{n}_\mathrm{c}^\mathrm{max}$. Exceeding $\bar{n}_\mathrm{in,bi}$, the complex circle features a discontinuity: this corresponds to switching between the two branches. In this regime, depending on whether the pump frequency is swept up or down, the cavity response either follows the low or high photon number branch, as long as the sweep time is slower than the cavity dynamics defined by κ_l and and the system is

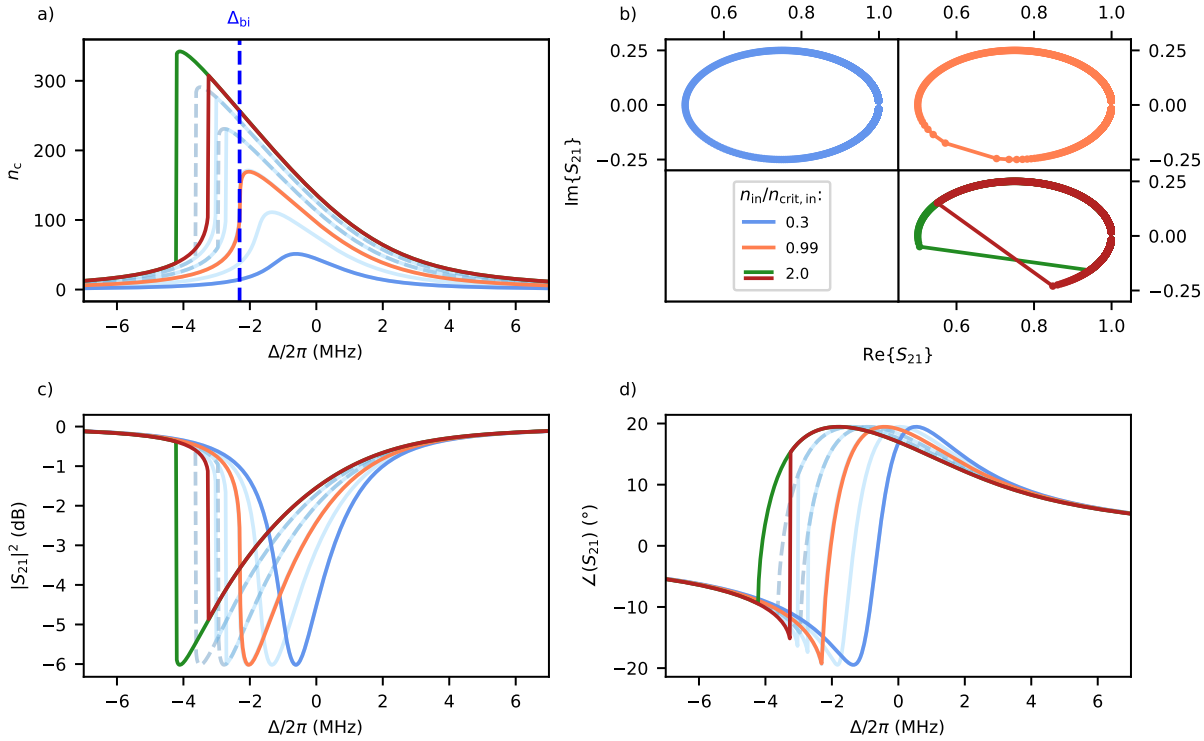

Fig. 4.9 Simulated S_{21}-data measured for a nonlinear Kerr cavity measured in a notch configuration at different input powers as a function of drive detuning. Depending on the output power, the different regimes are indicated by color as: linear (blue), nonlinear (orange), and bistable with the low/high photon number branch (red/green). **a)** Intracavity photon number, **b)** S_{21}-data in the complex plane, magnitude and phase in **c)** and **d)** versus detuning. For powers above the bistable input power, the cavity response bifurcates into the high and low photon number branches. Parameters used: $Q_l = 3000, Q_c = 6000, \omega_c/2\pi = 8\,\mathrm{GHz}, \mathcal{K}/2\pi = 12\,\mathrm{kHz}$

noise-free. For a notch configuration, the intracavity photon number on resonance $\Delta = -\mathcal{K}\bar{n}_c^{\max}$ can be derived as [102]

$$\bar{n}_c = \frac{4}{\kappa_l^2}\frac{\kappa_c}{2}2\pi\frac{P_d}{\hbar\omega_d}. \tag{4.12}$$

4.2.5 Microwave wiring

The microwave setup used throughout this thesis is based on the setup developed in [2–4], with minor changes in each iteration. Fig. 4.10 shows the wiring used in [5].

The wiring can be divided into two separate signal pathways combined at the cryostat input and output. The input signal is attenuated at the 4 K stage and the baseplate to shield the cavities from room temperature thermal noise. At the baseplate, the signal is further filtered with a 12 GHz *low pass filter* (*K & L 6L250*) and a homebuilt *Eccosorb* filter before the waveguide. After repeated cooldown cycles, the flexible microwave cables from Delft Circuits exhibited detrimental aging. To mitigate crosstalk caused by reflections, we added a thermalized

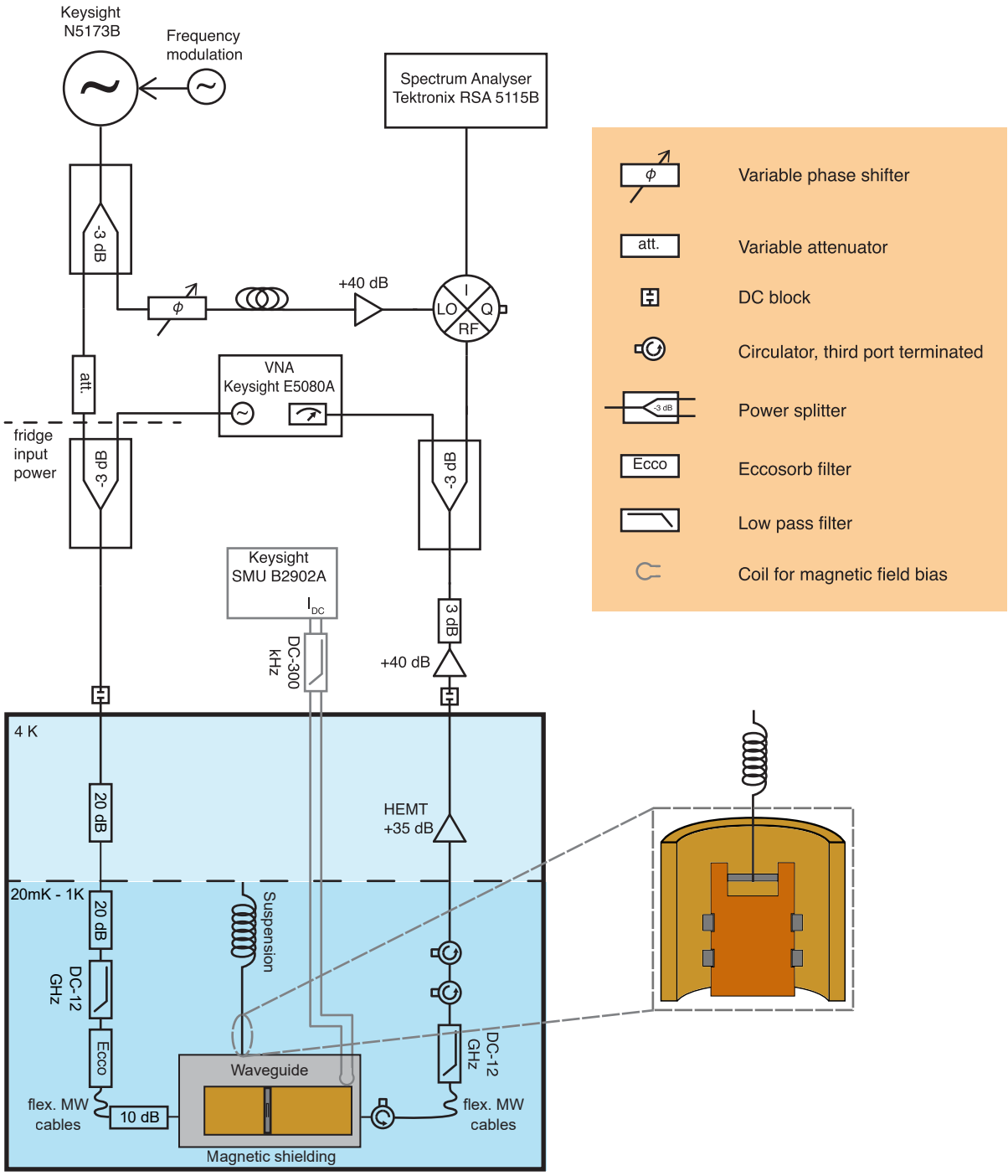

Fig. 4.10 Microwave measurement setup. During the course of the experiment, the setup outside the fridge was alternated slightly. Here (as in [5]), the final version of the setup is show.

attenuator in front of the waveguide and an additional cryogenic circulator at the waveguide output. Following another flexible microwave cable, a 12GHz low-pass filter *K & L 6L250* and two cryogenic isolators from *Quinstar* were added to shield the samples from thermal noise and reflected signals on the output side. To minimize losses, superconducting output lines are

used to transport the signal from the baseplate to the *high electron mobility transistor* (HEMT) amplifier (from *Low Noise Factory*) with a noise temperature of $2-4\,\mathrm{K}$. The signal is further amplified by an additional room temperature amplifier before being channeled into room measurement electronics.

For characterization of the cavity response, we use a *vector network analyzer* (*Keysight E5080A*, VNA). The VNA sweeps a probe tone across a set frequency range; to extract the complex scattering parameter S_{ij}, the VNA compares the transmitted signal through the system, which undergoes an amplitude and phase change, with the original probe tone. To probe and induce backaction on the mechanical mode, we use a *Keysight N5173B* signal generator (EXG) with a frequency modulation module. The coherent tone is split, with one part of it going towards the cryostat input passing through a digital attenuator (*Mini circuit RCDAT-30G-30*) to adjust the input power to the waveguide. The other part is transmitted to the *local oscillator* (LO) port of an IQ-mixer *Marki MMIQ-0416LS* to mix down the signal from the cryostat at the *radio frequency* (RF) port to baseband. To match the electric delay through the setup, the LO signal is passed through a carefully calibrated *delay line* with a variable phase shifter (*Vaunix LPS-123*) to adapt for small phase changes. A room temperature amplifier ensures that the mixer has the required power at the LO-port. The down-mixed signal at the I-port of the mixer is connected to a spectrum analyzer (*Tektronix RSA 5115N*) to capture the mechanical signature, as further explained in section 4.3.2.

4.3 Mechanics Platform

Within this section, we introduce the cantilever as a mechanical oscillator and present the samples used in this thesis. We cover the modification process of gluing a magnetic particle to the cantilever tip as well as the mounting of the cantilever chip onto the SQUID-cavity in a flip-chip process. Lastly, magnetometer measurements on the magnetic material used are discussed.

4.3.1 Theoretical description

A cantilever is a rigid beam that is clamped on one side and free at the other. The bending modes of such a resonator depend on the material properties such as the Young's modulus E, the density ρ, and the cantilever dimensions, thickness t, width w, and length l. Following Euler-Bernoulli beam theory, the effective mode frequency is given by [103]

$$\omega_{\mathrm{m}}^{(n)} = \frac{\lambda_{\mathrm{n}}^2 t}{\sqrt{12} l^2}\sqrt{\frac{E}{\rho}}. \tag{4.13}$$

Here, $\lambda_{\mathrm{n}} \approx 1.87, 4.69, 7.86$ for $n = 1, 2, 3$ is the mode parameter of the n-th bending mode. From Eq. (4.13) the resonance frequency of the second mode for a cantilever beam is $\omega_{\mathrm{m}}^{(2)} \approx 6.3\omega_{\mathrm{m}}^{(1)}$. This large frequency, along with the fact that its mode shape often means that the magnetic particle sits at a node, allows us to assume that we only see the fundamental mode couple to the SQUID-cavity. For the small displacements relevant in this thesis, the cantilever can be approximated by a harmonic oscillator. Within this limit, we can calculate the spring constant of the bending mode to be [103]

$$k = \frac{E w t^3}{4 l^3}. \tag{4.14}$$

Comparing the resonant frequency of the effective spring $\omega_\mathrm{m} = \sqrt{k/m_\mathrm{eff}}$ to Eq. (4.13), we can assign an effective mass

$$m_\mathrm{eff} \approx \frac{m_\mathrm{beam}}{4} = \frac{\rho t w l}{4} \tag{4.15}$$

to the motion. By loading the cantilever with an additional mass m_a right at the tip (see Fig. 4.13b)), we can approximate the change in frequency to be

$$\omega'_\mathrm{m} = \sqrt{\frac{k}{m_\mathrm{eff}+m_\mathrm{a}}} = \omega_\mathrm{m}\sqrt{\frac{m_\mathrm{eff}}{m_\mathrm{eff}+m_\mathrm{a}}}, \tag{4.16}$$

which remains accurate for $m_\mathrm{a}/m_\mathrm{eff} \leq 3$ [1, 104].
In this thesis, we use commercially available tipless Si-cantilevers *AlO-TL* from *Budget Sensors* with four cantilevers per chip. The one with the highest frequency shown in Fig. 4.13a) has dimensions of $t \times w \times l = 2.7(0.5)\,\mu\mathrm{m} \times 50(2.5)\,\mu\mathrm{m} \times 100(5)\,\mu\mathrm{m}$. With the density $\rho_\mathrm{Si} = 2330\,\mathrm{kg/m^3}$ [105] we can estimate the mass of the cantilever to be $m_\mathrm{beam} = 31(6)\,\mathrm{ng}$, which corresponds to an effective mass of $m_\mathrm{eff} = 8(2)\,\mathrm{ng}$. The nominal spring constant is given to be $40\,\mathrm{N/m}$, leading to a nominal frequency of $350\,\mathrm{kHz}$. However, the manufacturer also specifies that variation in fabrication could lead to a broad range in spring constant 7–$160\,\mathrm{N/m}$ and resonance frequency 200–$500\,\mathrm{kHz}$.

4.3.2 Mechanical mode detection

4.3.2.1 Theoretical derivation

In optomechanical experiments, one often does not detect the mechanical signal $z(t)$ in real-time, but measures its *power spectral density* (PSD) in the frequency domain [23]. According to the Wiener-Kinchin theorem [106], the PSD of such a mechanical motion is defined as the Fourier transformation of the autocorrelation function

$$S_{zz}(\omega) = \int_{-\infty}^{\infty} \langle z(t)z(0)\rangle e^{i\omega t} dt, \tag{4.17}$$

and is usually measured with a spectrum analyzer. For mechanics with a finite linewidth Γ_m and a large temperature T ($k_\mathrm{B}T/\hbar > \omega_\mathrm{m}$), the *fluctuation-dissipation theorem* links the PSD to the imaginary part of the mechanical susceptibility $\chi_\mathrm{m}^{-1}(\omega) = -i(\omega-\omega_\mathrm{m})+\Gamma_\mathrm{m}/2$ [107, 108]. The PSD can be written in terms of χ_m as

$$S_{zz}(\omega,T) = \frac{2k_\mathrm{B}T}{\omega}\,\mathrm{Im}\{\chi_\mathrm{m}\} = \frac{2k_\mathrm{B}T}{m_\mathrm{eff}}\frac{\Gamma_\mathrm{m}}{(\omega_\mathrm{m}^2-\omega^2)^2+\Gamma_\mathrm{m}^2\omega^2}. \tag{4.18}$$

Following [106], with *Parseval's theorem* we find that the variance of the displacement $\langle z^2\rangle$ of the mode can be expressed in terms of the integral of the PSD

$$\frac{\langle z^2\rangle}{z_\mathrm{zpm}^2} = \frac{1}{z_\mathrm{zpm}^2}\int_{-\infty}^{\infty} S_{zz}(\omega,T)\frac{d\omega}{2\pi} = S_{zz}(\omega_\mathrm{m},T)\frac{\Gamma_\mathrm{m}}{4z_\mathrm{zpm}^2} = 2\left(\bar{n}_\mathrm{m}+\frac{1}{2}\right), \tag{4.19}$$

which is directly propotional to the average occupation of the mode $\bar{n}_\mathrm{m}$ [1].[1] The third relation is valid for a Lorentzian shaped peak (Eq. (4.18)), relating its integral to its maximum and

[1] The factor of 2 in last equality of Eq. (4.19) arises because the PSD in Eq. (4.18) is an even function of frequency, yielding two identical contributions at $\omega = \pm\omega_\mathrm{m}$ when integrate over the full range $\{-\infty,\infty\}$.

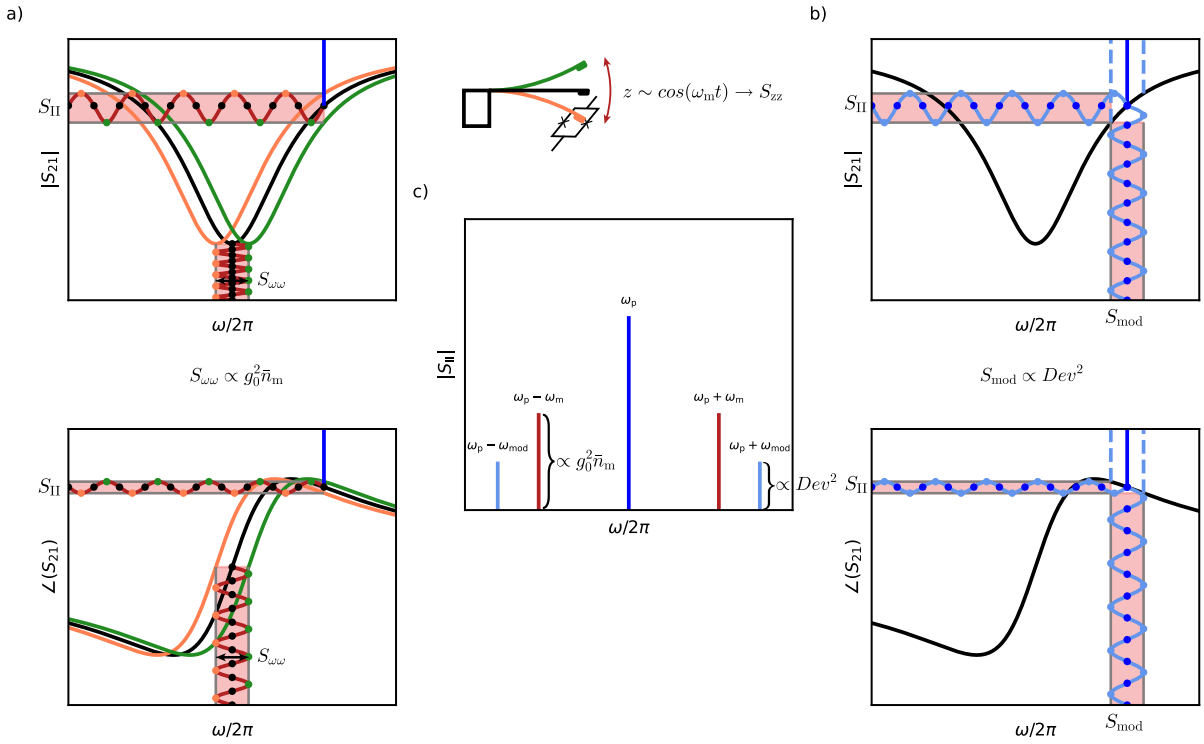

Fig. 4.11 Detection and calibration principle of the mechanical mode with a probe tone. a) The mechanical motion with the PSD $S_{zz}(\omega)$ modulates the resonance frequency of the cavity by a corresponding PSD $S_{\omega\omega}(\omega)$. We probe the cavity at a fixed frequency ω_p (vertical blue line) and measure the PSD $S_{II}(\omega)$ (shown in c). Due to the cavity frequency oscillations, the probe tone undergoes an amplitude and phase modulation transmitted through the system with a transfer function K. This causes two sidebands to appear in the spectrum spaced by $\pm\omega_m$ from the probe tone. **b)** A weakly frequency modulated probe tone with the PSD $S_{mod}(\omega)$ and modualtion frequency ω_{mod} undergoes the same transduction, leading to an additional sideband pair at $\pm\omega_{mod}$ within the probe's spectrum. **c)** Spectrum of frequency modulated probe tone combined with a mechanically induced modulation. For $\omega_m \approx \omega_{mod}$, both sideband pairs undergo the same transduction in the cavity response, and so the relative size of the pairs can be used to calibrate the spectrum/PSD at ω_m.

linewidth. Thus, from Eq. (4.18) we see that for a thermalized mechanical mode, the area under the measured signal increases linearly with temperature.

The signal transmitted through the waveguide with the intensity fluctuation defined by the PSD $S_{II}(\omega)$ depends on the induced frequency fluctuations of the SQUID-cavity with the PSD $S_{\omega\omega}(\omega)$. The transfer function $K(\omega)$ of the setup gives the absolute scaling of the intensity fluctioan and thus can be written as [84]

$$S_{II}(\omega) = \frac{K(\omega)}{\omega^2} S_{\omega\omega}(\omega). \tag{4.20}$$

The optomechancial coupling strength g_0 directly relates $S_{\omega\omega}(\omega)$ to the power spectral density

of the mechanical mode

$$S_{\omega\omega}(\omega) = \left(\frac{g_0}{z_{\mathrm{zpm}}}\right)^2 S_{\mathrm{zz}}(\omega). \tag{4.21}$$

Thus, we need a calibration method that first allows us to measure the transfer function $K(\omega)$. With this, we can convert $S_{\mathrm{II}}(\omega)$ measured by a spectrum analyzer into $S_{\omega\omega}(\omega)$. We can calculate with this the power spectral density of the position fluctuation $S_{\mathrm{zz}}(\omega)$ as illustrated in Fig. 4.11. The calibration method by Gorodetsky et al. [84] relies on a homodyne detection scheme using a frequency modulation with known modulation index on the probe tone as a reference signal to calibrate for the transfer function. The following calculations are largely based on the supplementary of our work [4].
We start with the general response $u_{\mathrm{p}}(t)$ of a probe tone at frequency ω_{p} which interacts with a cavity whose resonance frequency is modulated at ω_{i}. The interaction results in both amplitude and phase modulation of the probe tone in the time domain

$$u_{\mathrm{p}}(t) = A_{\mathrm{p}}(1+\eta\sin(\omega_{\mathrm{i}}t))\cos(\omega_{\mathrm{p}}t+\nu\sin(\omega_{\mathrm{i}}t)), \tag{4.22}$$

where A_{p} is the probe tone amplitude and η and ν the modulation indices. To determine η and ν, we have to consider the slope of both amplitude and phase of the cavity response S_{21} under the modulation amplitude $\Delta\omega_{\mathrm{amp}}$

$$\eta = \left.\frac{\partial|S_{21}|}{\partial\omega}\right|_{\omega=\omega_{\mathrm{p}}} \cdot \Delta\omega_{\mathrm{amp}} =: \alpha\cdot\Delta\omega_{\mathrm{amp}}, \tag{4.23}$$

$$\nu = \left.\frac{\partial\angle(S_{21})}{\partial\omega}\right|_{\omega=\omega_{\mathrm{p}}} \cdot \Delta\omega_{\mathrm{amp}} =: \beta\cdot\Delta\omega_{\mathrm{amp}}. \tag{4.24}$$

Here, we assume that for small $\Delta\omega_{\mathrm{amp}}$ the cavity shape can be considered to be linear, with α and β the slope in amplitude and phase, respectively. Furthermore, we consider here the normalized/background corrected cavity response, such that far off resonance we can assume $\alpha,\beta\to 0$. For an optomechanical system, the modulation amplitude is related to the coupling strength g_0 and the mechanical occupation $\bar{n}_{\mathrm{m}}$ (see chapter 2.1)

$$\Delta\omega_{\mathrm{amp}}^{\mathrm{m}} = 2\sqrt{\bar{n}_{\mathrm{m}}}g_0, \tag{4.25}$$

which relates $S_{\omega\omega}(\omega)$ to $\bar{n}_{\mathrm{m}}$, from which we can extract S_{zz}. The same arguments hold for a frequency-modulated probe tone scanning a static cavity as shown in Fig. 4.11b). Thus, for the calibration tone with a peak frequency deviation Dev resulting in a modulation index of $Dev/\omega_{\mathrm{mod}}$, we find

$$\Delta\omega_{\mathrm{amp}}^{\mathrm{mod}} = Dev. \tag{4.26}$$

To calculate the effects on our measured signal, we introduce the Bessel functions to rewrite the phase modulation in Eq. (4.22)

$$u_{\mathrm{p}} = A_{\mathrm{p}}(1+\eta\sin(\omega_{\mathrm{i}}t))\sum_n J_n(\nu)\cos(\omega_{\mathrm{p}}t+n\omega_{\mathrm{i}}t), \tag{4.27}$$

with J_n the Bessel function of n-th order. Assuming small modulation amplitudes and using trigonometric identities, we derive

$$\begin{aligned} u_\mathrm{p} =& A_\mathrm{p}\left[\cos(\omega_\mathrm{p}t) + \frac{\nu}{2}\cos((\omega_\mathrm{p}+\omega_i)t) - \frac{\nu}{2}\cos((\omega_\mathrm{p}-\omega_i)t)\right] \\ &+ \frac{\eta}{2}A_\mathrm{p}\left[\sin((\omega_\mathrm{p}+\omega_i)t) - \sin((\omega_\mathrm{p}-\omega_i)t)\right], \end{aligned} \tag{4.28}$$

which separates the contributions of the amplitude and phase modulation to the signal. To relate this to the PSD measured at the spectrum analyzer, we apply a Fourier transformation to Eq. (4.28). Here, we take into account the fact that the displayed spectrum is typically folded by the spectrum analyzer, as it only measures positive frequencies, which introduces a factor of two. With this, we obtain the intensity fluctuation measured with the spectrum analyzer at the probe and modulation frequency as

$$\begin{aligned} S_{II}^\mathrm{p} =& |2u_\mathrm{p}(\omega=\omega_\mathrm{p})|^2 = A_\mathrm{p}^2 \\ S_{II}^\mathrm{i} =& |2u_\mathrm{p}(\omega=\omega_\mathrm{p}+\omega_\mathrm{i})|^2 = \frac{\eta^2+\nu^2}{4}A_\mathrm{p}^2. \end{aligned} \tag{4.29}$$

By simultanously frequency modulating the probe tone with a modulation frequency ω_mod and a frequency modulation of the cavity due to the mechanical displacement with ω_m, we obtain two sidebands in the spectrum of the probe tone, the mechanical signature at $S_{II}^\mathrm{m} = S_{II}(\omega=\omega_\mathrm{p}+\omega_\mathrm{m})$ and the calibration tone at $S_{II}^\mathrm{mod} = S_{II}(\omega=\omega_\mathrm{p}+\omega_\mathrm{mod})$ as depicted in Fig. 4.11c).

At this point, we have to account for the finite linewidth of the PSD of the mechanical mode for a consistent comparison of the power residing in the mechanical and the calibration signal. Therefore, we have to integrate over the mechanical signature, leading to [84]

$$S_{II}^\mathrm{m} \to \int_{-\infty}^{\infty} \frac{S_{II}}{ENBW}\frac{d\omega}{2\pi} = \frac{S_{II}(\omega_\mathrm{m})}{ENBW}\frac{\Gamma_\mathrm{m}}{4} \tag{4.30}$$

with the measurement bandwidth $ENBW$ of the spectrum analyzer given in units of Hz. This step is necessary, as the spectrum analyzer returns the power spectrum of the signal and not the PSD. To integrate the signal, we need the power density, and thus have to divide by $ENBW$, where we need an extra 2π to match the units to angular frequency – as for the mechanical linewidth Γ_m.
Regarding the probe and the calibration tone, we can consider them as δ-peaks such that the measured height in the spectrum represents the total power residing in the signal. By replacing the modulation indices in Eq. (4.29) with Eq. (4.24), we obtain the relation between the modulation amplitude of the calibration tone and the mechanical mode

$$\begin{aligned} Dev^2 =& \frac{4}{(\alpha^2+\beta^2)A_\mathrm{p}^2}S_{II}(\omega_\mathrm{mod}) \\ g_0^2\bar{n}_\mathrm{m} =& \frac{1}{(\alpha^2+\beta^2)A_\mathrm{p}^2}\frac{S_{II}(\omega_\mathrm{m})\Gamma_\mathrm{m}/4}{ENBW}. \end{aligned} \tag{4.31}$$

We can assume that the transfer function through the system given by the first factor in Eq. (4.31) is flat in frequency, if the frequency difference between calibration and the mechanical modulation is small ($|\omega_\mathrm{m}-\omega_\mathrm{mod}| \ll \kappa_\mathrm{l}$). The ratio of these equations finally leads to the expression given in [84]

$$g_0^2\bar{n}_\mathrm{m} = \frac{\mathrm{Dev}^2}{4}\frac{S_{II}(\omega_\mathrm{m})\Gamma_\mathrm{m}/4}{S_{II}(\omega_\mathrm{mod})ENBW}. \tag{4.32}$$

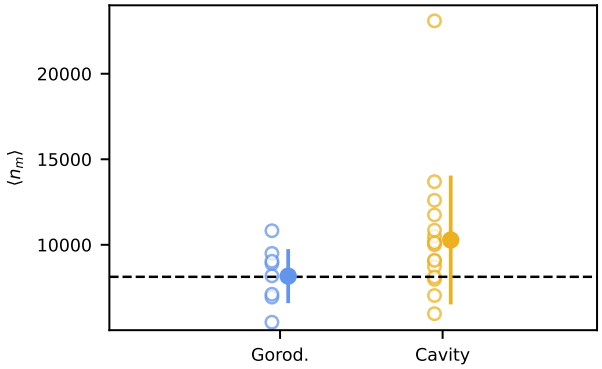

Fig. 4.12 Comparison between extracted phonon occupation for the Gorodetsky calibration method [84] and using the *cavity-slope* response over several measurements (unfilled circles) and averaged (filled) (data also shown in [4]). The dashed line represents the expected thermal occupation.

Eq. (4.32) tells us that we can account for the system's transfer function by comparing the mechanical signal to the sideband generated because of the frequency modulation of the probe tone.
Another look at Eq. (4.29) reveals that we can also use the signal at the probe tone together with the S_{21}-slopes in amplitude α and phase β to account for the system transduction leading to

$$g_0^2 \bar{n}_\mathrm{m} = \frac{1}{\alpha^2 + \beta^2} \frac{S_{II}(\omega_\mathrm{p} + \omega_\mathrm{m})\Gamma_\mathrm{m}/4}{S_{II}(\omega_\mathrm{p}) ENBW}. \tag{4.33}$$

To extract the slopes of the cavity, we use the circle fit routine presented above. Furthermore, we have to take into account that we measure in the Notch configuration, which implies that the mechanical signal scatters forward and backward. Thus, we only measure half of the mechanical signal, whereas for the probe tone the transduction is given by $S_{21}(\omega = \omega_\mathrm{p})$ of the cavity response. Including these factors, the *cavity-slope* calibration allows us to verify the Gorodetsky method [4]. For this, we take several measurements of the thermalized mechanical mode, once with the Gorodetsky method by downmixing the signal, including the frequency modulation of the probe, and once by extracting the *cavity-slope*, including the amplitude of the probe tone to calibrate for the transfer function. Fig. 4.12 displays the comparison between both calibration methods, where we find good agreement in the obtained mechanical occupation. As both calibrations rely on independent methods, the agreement verifies the Gorodetsky calibration method. However, from the results in Fig. 4.12, one advantage of the Gorodetsky method is evident. As we take the mechanical measurement and calibration simultaneously in a single spectrum, the cavity shape is automatically taken into account, making it very robust against any frequency drifts or other external noise affecting the cavity. On the contrary, the *cavity-slope* method relies on two separate measurements – the spectrum for the mechanics/probe peak height and a VNA scan for the cavity response – which degrades its reliability when the cavity resonance between the two measurements changes. This decreased robustness against noise is reflected in the larger spread obtained for the *cavity-slope* method compared to the Gorodetsky method.

4.3.2.2 Experimental implementation

The final setup to implement the calibration method is shown in Fig. 4.10. For the experimental realization of the calibration method described in [84], one has to consider the following aspects.

Modulating the probe tone generates a calibration sideband (see Fig. 4.11) used to determine the transfer function by comparison with the mechanical signal. The calibration tone appears at the modulation frequency ω_{mod} in the down-mixed signal, and its amplitude depends on the peak deviation of the frequency modulation Dev. To ensure Eq. (4.32) holds, we set the modulation close to the mechanical frequency $\omega_{\mathrm{mod}}/2\pi = \omega_{\mathrm{m}}/2\pi + 300\,\mathrm{Hz}$, allowing us to assume that the transduction on this frequency scale is effectively flat.

Increasing Dev enhances the peak height of the calibration tone, which is generally beneficial for the calibration method. However, large deviations are avoided for two reasons: (1) frequency modulation mimics flux noise, averaging the signal across the deviation range and washing out sharp backaction features, particularly problematic in strong backaction measurements; (2) to allow for a fair comparison of the power residing in the calibration and mechanical sidebands, higher-order sidebands must be suppressed. We therefore limit the modulation index to $Dev/\omega_{\mathrm{mod}} < 1$, and steadily increase the deviation until the calibration sideband rises 3 dB above the noise floor, enabling robust detection (usually around $Dev/\omega_{\mathrm{mod}} \simeq 0.4$).

To isolate the transfer function of the cavity, we mix down the signal from the cryostat with the frequency modulated probe tone as the LO of the IQ-mixer. Therefore, we have to match not only the phase but also the overall electrical length between the LO and RF ports. The electrical length of the LO is matched to the one through the system by using a *delay line*. We adjust the length of the *delay line* until the difference to the delay in the fridge is typically $< 10\,\mathrm{ps}$ and therefore significantly smaller than one oscillation period of an $\sim 8\,\mathrm{GHz}$ signal. For each probe frequency, we adjust for any remaining phase difference – caused by ripples in the transmission through the system and delay line – with a variable phase shifter to ensure that the signal from the experiment is mixed down with the exact same signal initially sent into the cryostat. To verify that the signals in both pathways are matched, we measure the leakage of the system - a spectrum with the cavity detuned. If the calibration tone remains within the noise floor for the leakage measurement, the LO and RF signals cancel each other, indicating that the experiment is well matched.

4.3.3 Sample preparation

The in-house procedure to equip the cantilever with a magnetic particle described in this section is up to small modifications identical to the one described in [2, 80]. The modified cantilever is schematically shown in Fig. 4.13b).
In the initial step, *Neodymium Iron Boron* (NdFeB) powder obtained from *Nanoshel* is ground to a particle size of approximately $20\,\mu m$. The resulting fine powder is then dispersed onto a glass slide patterned with niobium structures that replicate the dimensions of the cantilever, serving as a size reference [80]. An appropriate particle is selected under the optical microscope and is picked up with a probe station tip. Separately, a drop of epoxy *Stycast 1266* is applied to the cantilever tip by hand using a thin copper wire with a diameter of $50\,\mu\mathrm{m}$. With the probe station, the particle is brought close to the epoxy droplet, where it is drawn onto the cantilever by adhesive force. To cure the epoxy, the cantilever is placed onto a hot plate at $50^{\circ}\,\mathrm{C}$ for 2 hours. In a last step, the particle is magnetized in a 2 T permanent magnet [109].

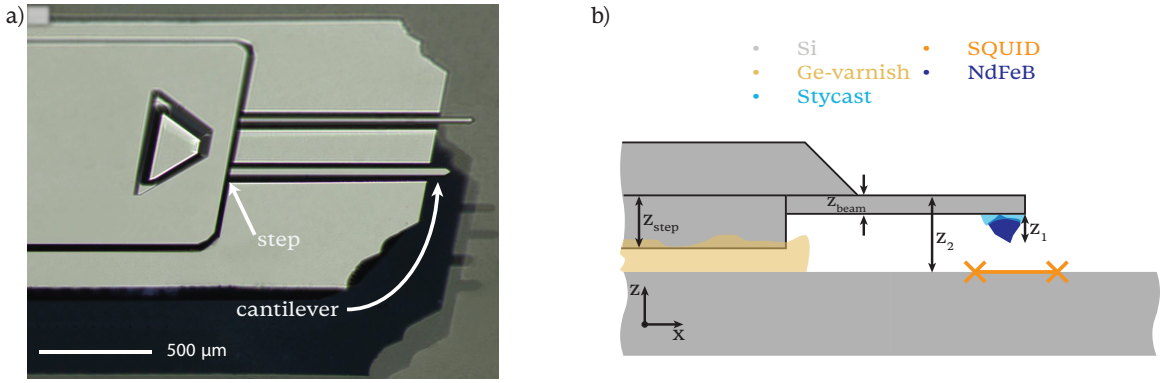

Fig. 4.13 **a)** Microscope image of the AFM-chip backside. At the end, two cantilevers are visible, where only the shorter one with $l \approx 100\,\mu$m is used. The step towards the center of the chip is used as a spacer between the magnet and the SQUID loop. **b)** Illustration of the mounted cantilever with a NdFeB particle glued to its tip. The cantilever is flipped and pressed onto a GE-varnish drop, where the step of $z_{\text{step}} \approx 20\,\mu$m functions as a reproducible spacer.

To attach the cantilever chip to the silicon chip, a drop of GE-varnish is positioned roughly 1 mm above the SQUID-loop. Using a 'flip-chip' process, the cantilever is aligned to the SQUID-loop, as illustrated in Fig. 4.13b). Originally, this alignment was performed 'by hand' under a microscope using two tweezers: one to adjust the relative positioning of the cantilever and SQUID loop, and the other to firmly press the cantilever chip onto the GE-varnish. In order to ensure proper adhesion, pressure had to be maintained for about one minute while preserving the alignment. Although the handling process improved with experience and over multiple iterations, the overall reproducibility remained low. In particular, the vertical distance z_2 – primarily determined by the amount of GE-varnish and the applied pressure – varied significantly. Removing the pressure prematurely, before the glue had dried sufficiently, would often result in a misplacement of the cantilever. Furthermore, the survival rate of the cantilevers during this process was approximately 50%, indicating limited reliability of the manual method.

As mentioned in section 3.4.1, the coupling g_0 between the cantilever and the cavity crucially depends on the precise positioning and vertical distance on the μm-scale. For an increased coupling, a small separation between the magnet particle and the SQUID chip ($z_2 - z_1$ in Fig. 4.13b) is desirable. Therefore, we improved the mounting process by designing a new mounting stage shown in Fig. 4.14. Using the mounting stage, we achieved a 100% survival rate so far. The mounting stage consists of two pieces. The translation stage holds the cavity within a groove and allows for alignment in the xy-plane with two micrometer screws. The cantilever chip is placed in a precisely machined groove at the counterpart. Both chips are held in place by a vacuum. The stage holding the cantilever is flipped and screwed upside down to the z-translation stage. With visual feedback under an optical microscope, the cantilever is carefully lowered onto the cavity chip. By keeping the chip surfaces parallel, the machined parts ensure proper alignment during contact. To ensure a reliable z_2 distance, a $20\,\mu$m-step of the cantilever chip as shown in Fig. 4.13a) functions as a reproducible spacer. Thus, the xy-alignment is controlled by the translation stage, while the reproducibility of the vertical distance is ensured by the step on the cantilever chip. To avoid misalignment upon release, the setup is held in place for at least 1 hour to allow the GE-varnish to cure.

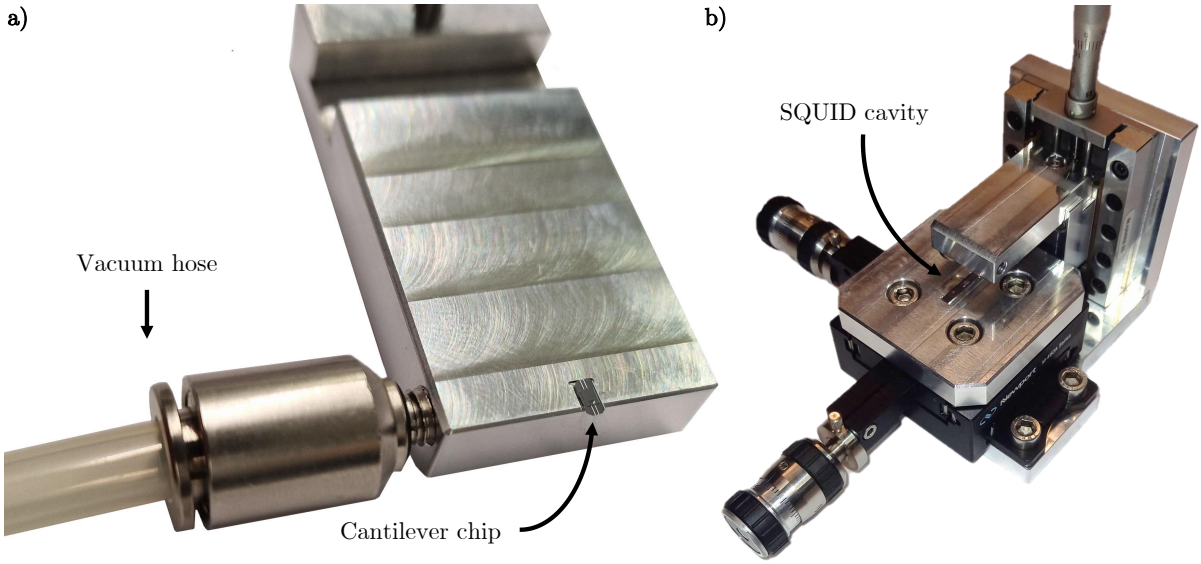

Fig. 4.14 Mounting stage for μm-precise placement of the cantilever. **a)** The cantilever is placed within a groove in the upper part of the stage and held in place by vacuum (picture taken by C. Dejaco). **b)** The cavity chip is placed within a groove in the lower part of the stage. An xy-translation stage allows for precise alignment between SQUID-loop and cantilever under a microscope. The cantilever is lowered by an z-translation stage until contact is made with the SQUID-cavity chip. This allows us to apply an even and continuous pressure.

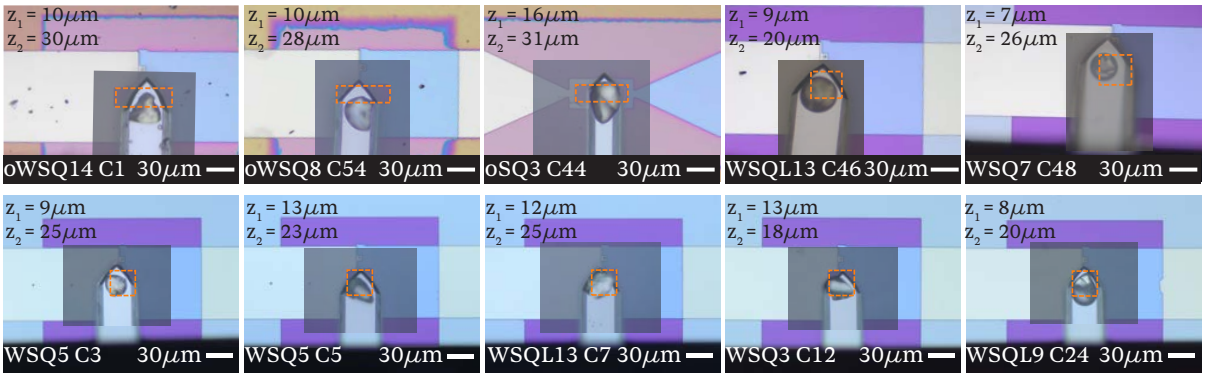

Fig. 4.15 Microscope images of mounted samples overlaid with microscope pictures of the magnetic particle. Orange lines denote the SQUID loop. Top row: Samples mounted manually. Bottom row: Samples mounted using the mounting stage. Images in the bottom row taken by C. Dejaco.

4.3.4 Magnetomechanical samples

In Fig. 4.15, a few examples of 10 prepared magnetomechanical samples are shown. To highlight the particle shape and position, the microscope pictures from the mounted cantilever are overlaid with an image of the particle, which is usually not visible as the partilce is attached to the backside of the cantilever. The relevant distances – the particle height z_1 and the vertical distance z_2 – are approximated by using the focus of the optical microscope. To emphasize the

alignment in the xy-plane, the SQUID-loop is traced with an orange square.
Comparing the particles of the prepared samples, one can see the non-uniform composition of the powder we use. From pyramidal shapes as in *oWSQ14/WSQ3* to flakes in *WSQ7/oWSQ8* the lateral dimensions of the particles vary from $20\,\mu$m to $50\,\mu$m (as inferred by comparing to the known cantilever width of $50\,\mu$m). Furthermore, we observe a spread in the approximated height of $z_1 = 7\text{-}16\,\mu$m. From this, it is evident that further improvements towards more uniform particles can be made. Instead of an inhomogeneous NdFeB powder, one could use microspheres as provided by [80]. Another approach would be to grow a magnetic film onto the cantilever itself. However, as this process is rather time consuming, one can only grow thin sheets up to $\approx 10\,$nm. Combined with the fact that the magnetic moment would align in plane with the film without an additional introduced anisotropy, the achieved coupling to SQUID would be assumably too low.

Comparing the mounted samples regarding xy-alignment in Fig. 4.15, one has to distinguish the manually aligned samples shown in the first row from the ones aligned using the mounting stage in the bottom row of Fig. 4.15. The manually mounted samples show a rather wide spread of the vertical distance with a mean of $\bar{z}_2 = 27.0(4.4)$. Furthermore, most of the samples exhibit a tilt of the cantilever in xy, which typically is the result of releasing the cantilever with the GE-varnish not completely cured. Regarding the particle position, most of them only align partially with the SQUID-loop. The difference in alignment, as well as the wide spread in the vertical distance, further reduces the reproducibility of the experiment.In these aspects, an increased reproducibility is evident in the samples mounted. The average height $\bar{z}_2 = 22.2(2.9)$ is smaller and has a smaller spread compared to the manually mounted ones. The variation in height when mounted with the stage is attributed to different amounts of GE-varnish used. With the almost perfect alignment of the magnetic particle with the SQUID-loop, the samples shown demonstrate the improvements achieved with the mounting stage.

As a final remark regarding the sample preparation, it has to be noted that the particles and samples presented for the manual alignment suffer from *survival bias*. The observed spread in particles is usually even larger than the one presented here, with z_1 down to $3\,\mu$m or up to $35\,\mu$m. Compared to the crystalline structure observed in the pictures, some particles exhibit a granular texture. If size or structure does not match the criteria (crystalline structure, dimensions of $\sim 20\,\mu$m and distance of $z_2 \approx 20\,\mu$m), the cantilevers are discarded, which results in an overall low yield of one good cantilever out of five prepared ones. Also, for the manually mounted samples, we used to remount cantilevers if the alignment/distance did not suffice. For obvious reasons, samples that were destroyed during the mounting are also not represented.

A recently acquired AFM allows us to study the influence of attaching a particle to the cantilever tip. We measure the oscillation amplitude of the cantilever upon excitation by a piezoelectric actuator prior to and after mounting the particle by focusing the AFM laser onto its tip.
The results show that the resonance frequency upon mounting decreases by 140 kHz. Additionally, after attaching the particle, the linewidth decreases by a factor of ≈ 3. This is to be expected, as the losses for the fundamental mode of a cantilever are given by clamping losses and damping of the surrounding air (scaling with the area of the cantilever) [110, 111]. Thus, increasing the effective mass of the oscillation, while keeping the losses constant to first order, results in a decrease in linewidth. With Eq. (4.16), we can estimate the additional mass to

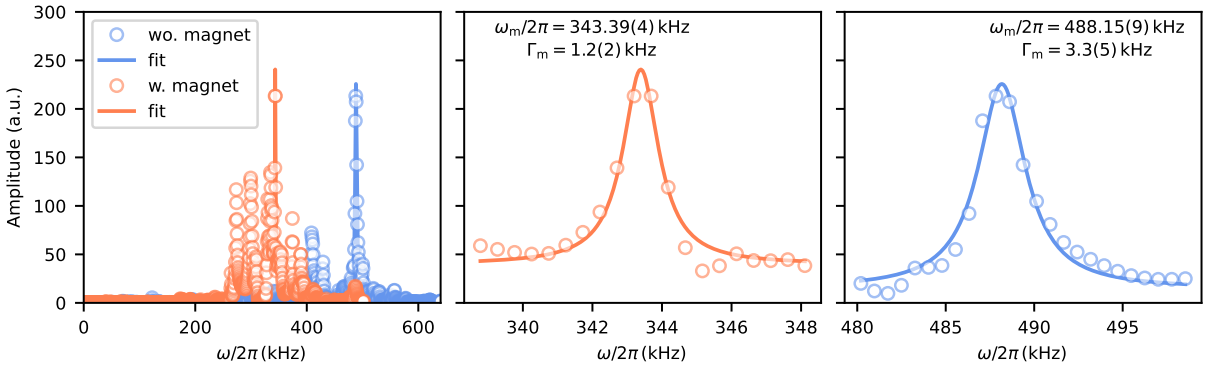

Fig. 4.16 Measurements on *C3* prior to and after mounting the particle using the AFM at room temperature. On the right, zoom-in on the highest amplitude peaks with Lorentzian-like fits (Eq. 4.18) to extract resonance frequency and linewidth. The appearance of multiple peaks might be related to additional vibrational noise or stray reflections of the laser.

be $m_a = 8.0(1.6)\,\mathrm{ng}$. We can separately estimate the mass by assuming the particle to be an ellipsoid, with a dimension of $25(2)\,\mu\mathrm{m} \times 25(2)\,\mu\mathrm{m} \times 9(1)\,\mu\mathrm{m}$, which together with the density of NdFeB $\rho_{\mathrm{NdFeB}} = 7.6(2)\,\mathrm{kg/m^3}$ [112] results in $m_a' = 22(4)\,\mathrm{ng}$ [80]. The discrepancy between the two values might arise from the fact that m_a is only the effective mass of the particle, which changes when the particle is not placed at the end of the cantilever. Morever, it is possible that the stycast affects the bending and mode shape of the cantilever adding to the discrepancy. Taking the actual position of the particle into account and considering the mode shape of the cantilever, in [80] the absolute mass is calculated from the frequency change, resulting in $m_a'' = 19(4)\,\mathrm{ng}$, which is in good agreement with the estimated value based on the optical size. Thus, the investigation of the changes in the frequency from the AFM measurements turns out to be a useful tool to estimate the particle mass.

For the samples presented in Fig. 4.15, the mechanical signatures measured within the actual optomechanical setup at cryogenic temperatures is depicted in Fig. 4.17. To avoid backaction effects (see chapter 2.3.1), these measurements were done at low drive powers. To extract the resonance frequency and linewidth, we fit the obtained data with the Lorentzian-like function in Eq. 4.18.
For two of the samples (*oSQ3 C44* and *WSQ3 C13*), we could not find a mechanical signature, although indications for the present mechancis in proximity to the cavity were present, as discussed in section 5.1.4 for *oSQ3 C44* and in [80] for *WSQ3 C12*. All other samples show a mechanical peak corresponding to the mechanical mode. Accounting for the manufacturer-specified spread in resonance frequencies for the cantilevers used, in conjunction with changes due to mounting the particle, the range of frequencies obtained is reasonable.
The fact that the frequency of the mechanical peak of $\omega_m^{\mathrm{cav}}/2\pi = 345.4(1)\,\mathrm{kHz}$ for C3 measured using our optomechanical setup agree to a reasonable degree with that measured with the AFM for the same device ($\omega_m^{\mathrm{AFM}}/2\pi = 343.39(4)\,\mathrm{kHz}$) instills confidence in the OM detection scheme. The small increase in resonance frequency can be attributed to a rise of the Young's modulus towards lower temperatures [113]. According to Eq. (4.13), the mechanical frequency scales directly with the Young's modulus, explaining the increase in frequency [80]. The significant reduction in linewidth can be attributed to the effective elimination of air damping due to the

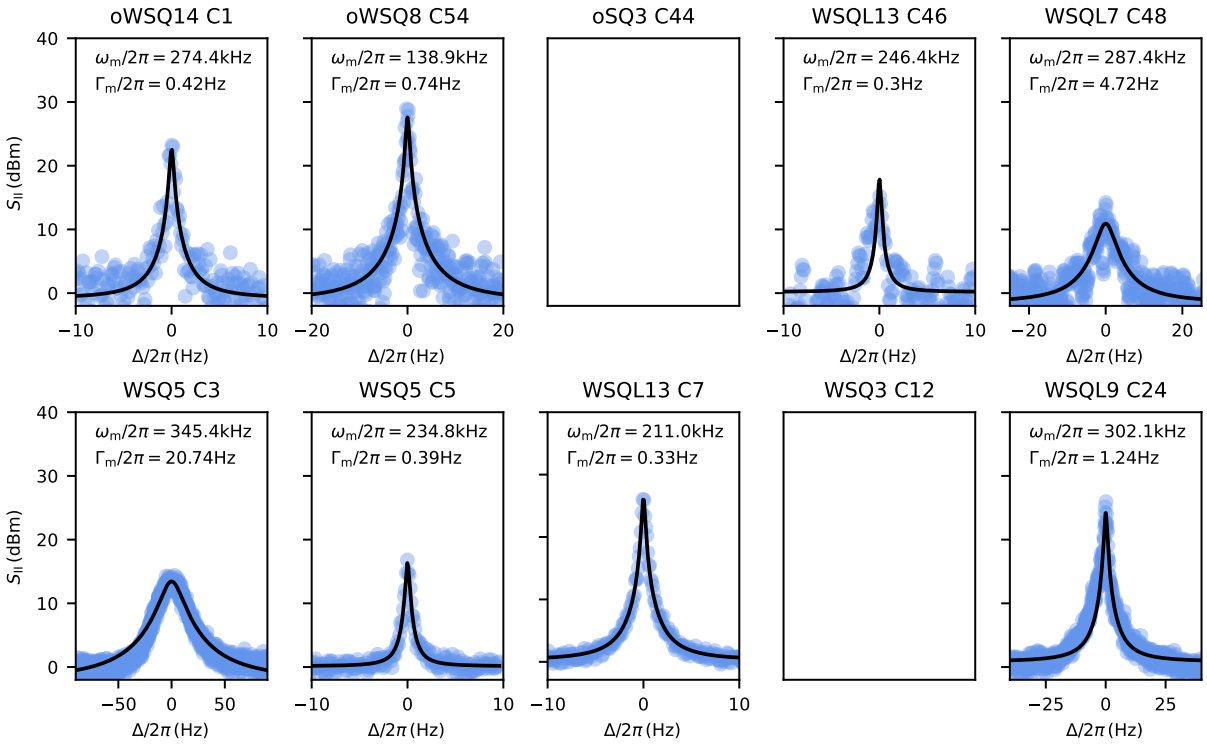

Fig. 4.17 Mechanical signal of the samples shown in Fig. 4.15 (nomenclatur *cavity name + cantilever number*). For *oSQ3 C44* and *WSQ3 C12*, no mechanical signature could be found, whereas for all the other samples, a clear peak could be assigned to the cantilever mode. Data from the bottom row taken by C. Dejaco.

cryogenic vacuum environment. Furthermore, it has been found that the remaining loss mechanism – clamping losses – decreases significantly with decreasing temperature [111], which results in an overall reduced mechanical linewidth.

4.3.5 Particle characterization

The magnetic properties of the NdFeB particles were characterized by measuring the magnetic moment of five samples (see Fig. 4.18) using a SQUID magnetometer (*Quantum Design MPMS-XL5*) at the University of Linz, in collaboration with Univ.-Prof. A. Ney. The selected particles are representative of the typical size, crystal structure, and shape used in the actual experiment. To allow for characterization, each particle is glued with epoxy *Stycast 1266* to a $4\,\mathrm{mm} \times 4\,\mathrm{mm}$ silicon chip.

To closely replicate the experimental conditions, the measurements performed by A. Ney start with several zero-field-cooled (*ZFC*) cycles. In order to do so, the magnetization of the particle is tracked while ramping down the temperature with no applied magnetic field. Before cooling down, the *samples I-III* are magnetized at room temperature in the direction of the pick-up loop. They are first magnetized in a 2 T field and monitored in a *ZFC* cycle. Subsequently, they are magnetized at room temperature again, but this time in a 5 T field, before another *ZFC* cycle. *Sample IV* was magnetized *in-house* in our usual 2 T field. Therefore, an additional *ZFC* cycle was measured without applying a magnetic field before following the sequence for

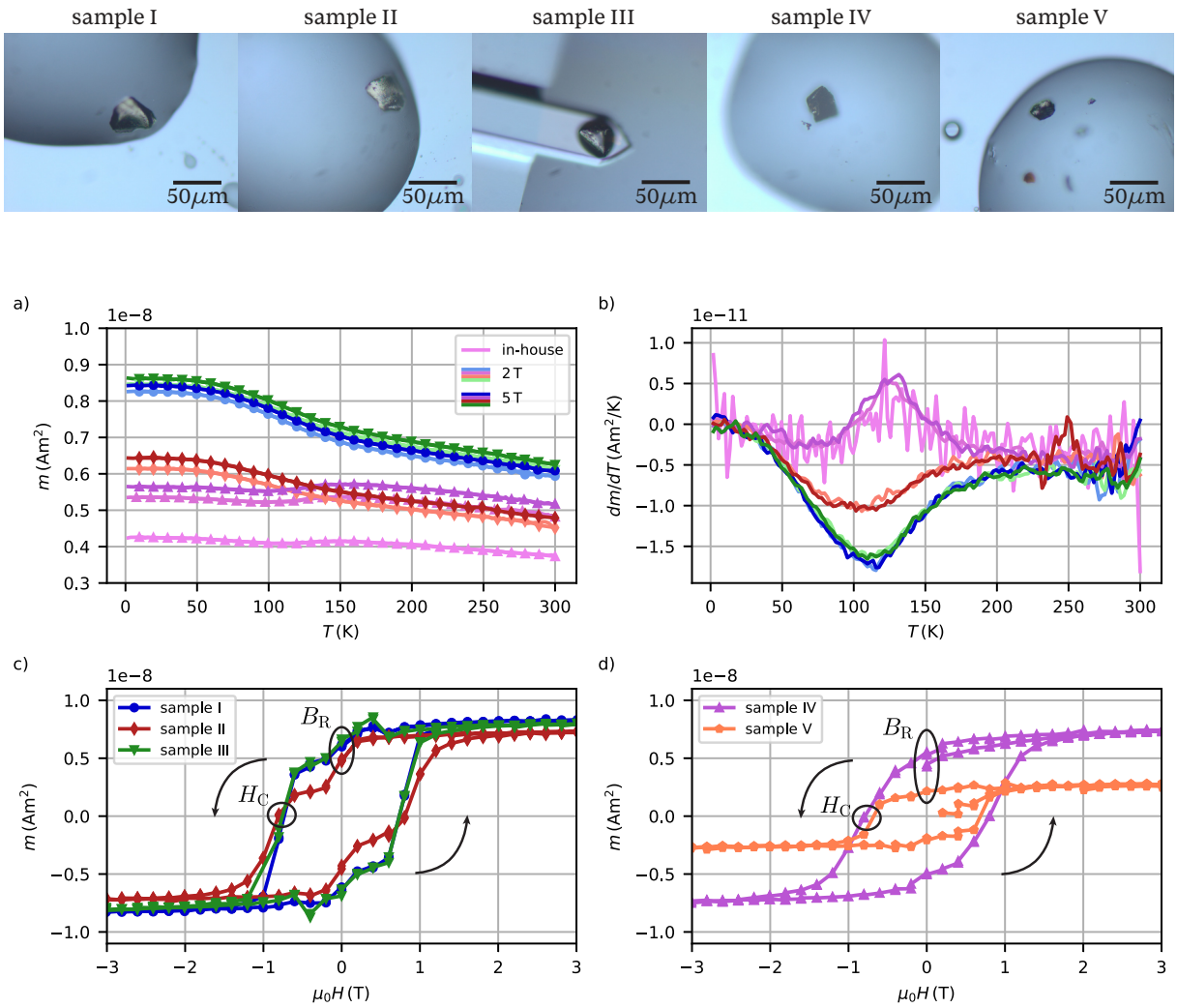

Fig. 4.18 NdFeB-samples prepared for characterization in a SQUID magnetometer (*Quantum Design MPMS-XL5*) at the University of Linz. The particles are glued with epoxy *Stycast 1266* to a 4 mm×4 mm silicon chip. *Sample I,II* (blue ○, red ◇) and *V* (orange ⬠) unmagnatized bare particles, *sample III* (green ▽) unmagnetized and mounted to a cantilever and *sample IV* (purple △) sample magnetized with the in-house 2T field.**a) -b)** Zero field cooled (*ZFC*) magnetic moment m and dm/dT of the particles after magnetization with the *in-house* magnet and magnetization within the SQUID magnetometer with a field of 2 T and 5 T, respectively. **c)-d)** Magnetization curves for the different samples (for clarity plotted seperately) sweeping the external magnetic field from $\mu_0 H = 0\,\mathrm{T} \rightarrow 5\,\mathrm{T} \rightarrow$-5 T $\rightarrow 5\,\mathrm{T}$ at room temperature. The remanent field B_R and the coercivity $\mu_0 H_\mathrm{C}$ of the samples are marked. For all samples except *sample V*, measurements were done after applying the 5 T for the *ZFC* measurement. All measurements performed by Univ.-Prof. Dr. A. Ney at the University of Linz.

the other samples.
The ZFC magnetization data in Fig. 4.18a)-b) reveal features characteristic of multi-stage magnetization processes in NdFeB materials. For sample *I-III*, as we lower the temperature, the magnetic moment gradually increases and saturates around 50 K. Additionally, an inflection point is found around $T_{\mathrm{sr}} \approx 115\,\mathrm{K}$ (visible in Fig. 4.18b)) consistent with findings in [114]. This behaviour is associated with a spin reorientation transition of NdFeB at $T_{\mathrm{sr}} = 100 - 135\,\mathrm{K}$ depending on the particle size. Below T_{sr}, the magnetization gradually shifts away from the crystallographic c-axis onto a cone with the opening angle increasing with decreasing temperature due to competing anisotropies, resulting in a steady increase in the magnetic moment [114]. Below approximately 50 K, this reorientation saturates, reaching an opening angle of the cone of 31°, which results in a plateau in the signal [115]. For *sample IV*, the observed trend is slightly different, exhibiting an overall less pronounced change in magnetization. Compared to the first three samples, the particle appears darker and displays a more amorphous, granular structure under optical microscopy. In the case of amorphous NdFeB, the spin-reorientation transition has been reported to vanish entirely [114], which may explain the temperature dependence observed in this sample.
After magnetizing the samples by applying 5 T, the magnetic signal in the subsequent *ZFC* measurement shows no significant increase compared to the signal obtained after 2 T. However, for the *in-house* magnetized *sample IV*, magnetizing the sample in the 2 T field increased the magenetic moment by 25 % compared to that after just in-house magnetization. This may suggest that our in-house magnetization is insufficient to fully align the magnetic domains, or that the particles partially demagnetize over time during the transport to Linz. The latter might be supported by the general observation that more armophous materials exhibit weak magnetic anisotropy and relatively low coercivity, which facilitates demagnetization [116].

After the *ZFC* measurements, magnetization curves were recorded at room temperature by sweeping the external magnetic field in the sequence $\mu_0 H = 0\,\mathrm{T} \rightarrow 5\,\mathrm{T} \rightarrow -5\,\mathrm{T} \rightarrow 5\,\mathrm{T}$. With this order of measurements, the samples were already exposed to the 5 T field due to the *ZFC* measurements. To obtain the virgin magnetization curve of the NdFeB material, *sample V* was measured without the *ZFC* cycle.
The magnetization curves measured for *sample I-III* in Fig. 4.18c) show qualitatively the same behaviour. An applied field of 2 T is sufficient to fully magnetize the particles. This statement is further supported by the virgin magnetization curve taken for *sample V* in Fig. 4.18d). The obtained remanent field is $B_{\mathrm{R}} \approx 0.5/0.6 \cdot 10^{-8}\,\mathrm{Am}^2$ with small variations attributed to particle size. These values are compatible with the magnetic signal obtained at the start of the *ZFC* at 300 K. This indicates that the particles maintain their magnetization over the time of the *ZFC* measurements. For the recoil curve, the coercive field is $\mu_0 H_{\mathrm{C}} \approx 0.8\,\mathrm{T}$. However, all samples show a gradual decrease to an intermediate magnetization plateau at $\mu_0 H \approx 0.2\,\mathrm{T}$. These properties can be assigned to two different grain contributions in the magnet: a rather soft magnetic one that leads to the gradual decrease and a hard magnetic one characterized by a high coercivity of $\mu_0 H_{\mathrm{C}} \approx 0.8\,\mathrm{T}$, which is in good agreement with [117]. The lower intermediate magnetization for *sample II* can be interpreted as a larger contribution of the soft magnetic grain. *Sample IV* lacks the intermediate step upon reducing the magnetic field in Fig. 4.18d), but rather exhibits a continuous decrease with a comparable coercivity $\mu_0 H_{\mathrm{C}} \approx 0.8\,\mathrm{T}$. Contrary to the other samples, the initial magnetization at the start of the measurement sequence is lower than both the magnetization observed upon reducing the magnetic field towards $\mu_0 H = -5\,\mathrm{T}$ and the value recorded at the beginning of the *ZFC* measurement. Both these properties can be

explained by a more amorphous topology of *sample IV*. Due to the amorphous structure, this particle can be considered as an assembly of various magnetic grains and domains, which leads to a reduced capability to maintain a certain magnetization. This manifests in the gradual change in the magnetization curve, demagnetization over time, and a less pronounced spin-reorientation transition [114, 116, 117].

Summarizing the findings from the magnetometer measurement, we can assume a magnetic moment of roughly $m = 7\,\mathrm{nA\,m^2}$ for particles typically mounted in our experiment - scaling with the particle size. By assuming a NdFeB sphere of radius $R = 10\,\mu\mathrm{m}$ and with the remanent magnetic field of NdFeB $B_{\mathrm{rem}} = 1.2\,\mathrm{T}$ [118], we can calculate the theoretically expected magnetic moment as

$$m_{\mathrm{theo}} = \frac{B_{\mathrm{rem}}}{\mu_0}\frac{4}{3}\pi R^3 = 4\,\mathrm{nA\,m^2}, \tag{4.34}$$

being in good agreement with the measurement results. Furthermore, the magnetization curves indicate that the magnetization with the *in-house* 2 T magnet should suffice to fully magnetize our samples. However, the particles - depending on their crystal structure - might demagnetize over time due to oxidation and mechanical perturbations. Thus, repeated remagnetization of the samples should be considered in the future. Lastly, there might be an influence of the overall topology based on correlating optical microscopy observations with measured magnetic properties. However, this remains only a preliminary indication, and additional samples need to be characterized to draw a definitive conclusion.

CHAPTER 5

Results

In this chapter, we discuss the main measurement results based on the theory, methods, and experimental setup from the previous chapters. The three main sections of this chapter can be divided into: tuning behavior of the cavity in the presence of the mechanical cantilever in section 5.1, backaction-free measurement of the mechanical mode focusing on the influence of the suspension setup in section 5.2, backaction measurements on the mechanical mode with our intrinsically nonlinear cavity in section 5.3. If not otherwise stated, the measurements presented were carried out on sample *oWSQ14 C1*.

5.1 SQUID-Cavity Characterisation

This section starts by analysing how the cavity response changes with a mounted cantilever. Here, we demonstrate how flux tuning is affected by the presence of a cantilever, followed by changes observed upon re-positioning the cantilever across multiple cooldowns. We then investigate the cavity response as a function of drive power, starting with results from the nonlinear circle fit routine for *oWSQ14*. Subsequently, we discuss an anomaly in Kerr – power-dependent resonance frequency shift which moves to higher frequencies – which appears for several samples but only after mounting a cantilever. The section concludes with a second frequency shift observed for samples with a cantilever, distinct from the first in that it occurs on a time scale of seconds. Cooldowns reappearing throughout this chapter are numbered by *CD#*. A thorough characterisation of the bare cavities can be found in previous works by two of my colleagues: [2, 30] by David Zöpfl or the master's thesis from Christian Dejaco [80], performed under my supervision.

5.1.1 Cavity flux tuning behavior upon cantilever mounting

The cavity tuning behavior before and after mounting the cantilever is shown in Fig. 5.1, for *oWSQ14*. For this, we gradually increase the current through one of the waveguide coils and

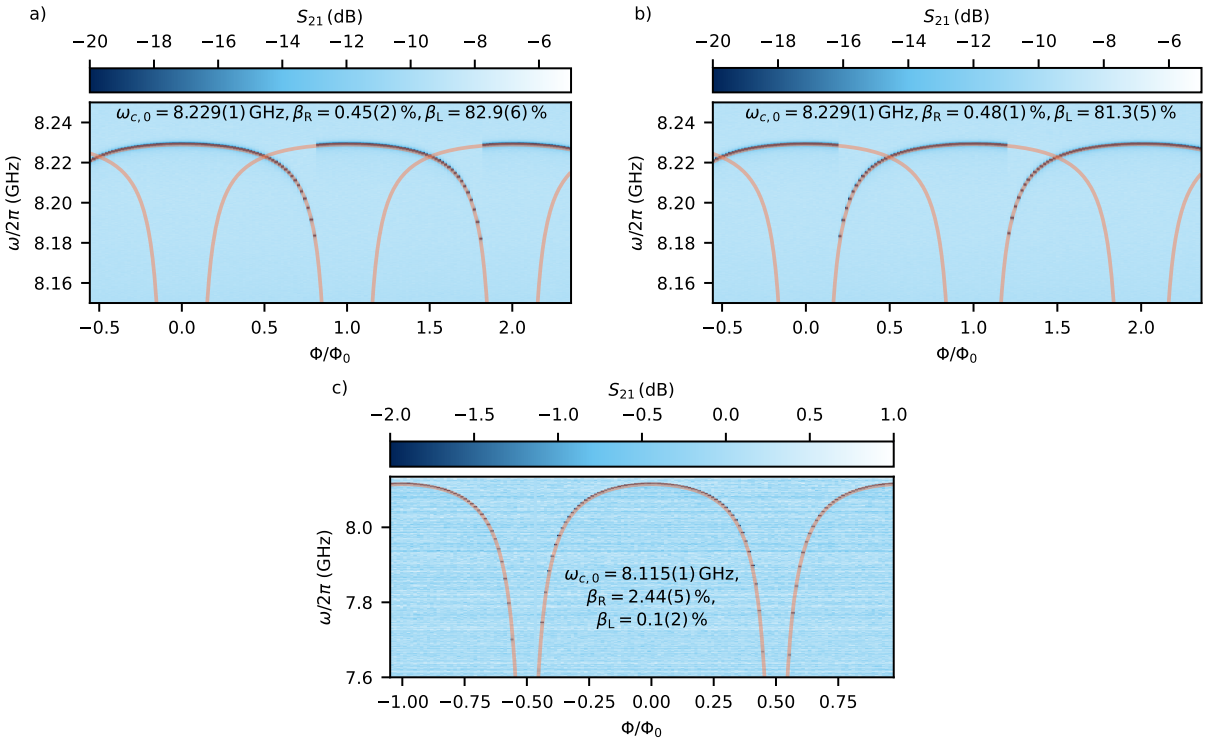

Fig. 5.1 Fluxmap of sample *oWSQ14*: **a)** Flux up sweep and **b)** flux down sweep before mounting the cantilever (*CD10*). **c)** Flux up sweep after mounting the cantilever (*CD42*). The tuning behavior is fitted with Eq. (3.31) and Eq. (3.37) to extract the parameters shown.

scan the cavity response using the vector network analyzer (VNA). Before mounting the cantilever, we observe a hysteretic flux tuning behavior of the samples as evident by comparing the tuning in Fig. 5.1a-b). With the mounting of the cantilever, the cavity shows an increased frequency tunability up to 500 MHz and a non hysteretic tuning behavior. This is accompanied by a drop in the sweet spot resonance frequency $\omega_{c,0}$ of 114 MHz and the shielding parameter β_L, combined with an increase in the SQUID participation ratio β_R. These values are extracted through a fitting routine to the tuning behavior based on Eq. (3.31) and Eq. (3.37) [80].

By mounting the cantilever, we place a dielectric medium – the doped silicon cantilever body – in the vicinity of the cavity, which increases its overall capacitance, causing its resonance frequency to drop. However, this would cause only a minor change in tuning behavior, which is not sufficient to explain the changes observed. Additionally, the doped silicon leads to a decrease in the quality factor, as studied in [80].
As theoretically shown in section 3.4, the magnetic field of the particle mounted to the cantilever has a major influence on the tuning and can be separated into the *in-plane* and *out-of-plane* components. As shown in Fig. 3.14, depending on the magnetic moment and exact placement of the particle, the *in-plane* field threading the junction cross-section can lead to a reduction of the critical current. According to Eq. (3.42), we expect an increase in β_R, which leads according to Eq. (3.37) to a decrease in $\omega_{c,0}$. Furthermore, a lower critical current corresponds to a smaller β_L. The *in-plane* component can be viewed as a rather static influence on the SQUID-parameter

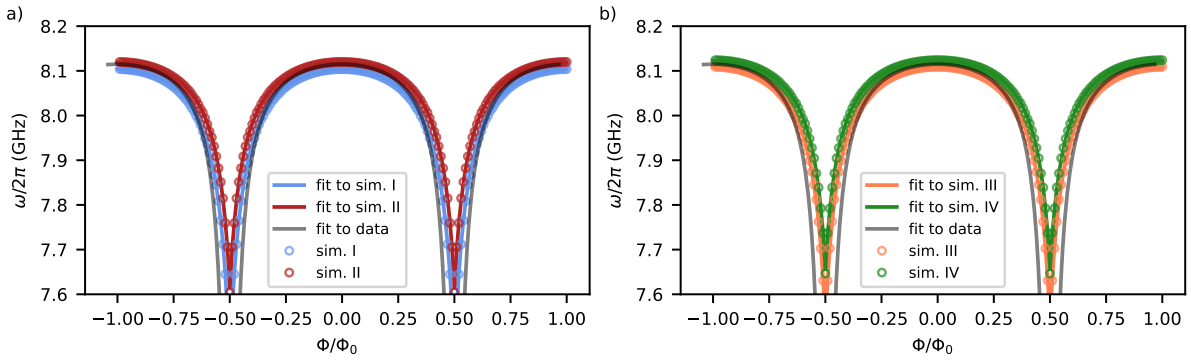

Fig. 5.2 Comparison of the tuning behavior measured after mounting the cantilever from Fig. 5.1 (grey line) with results from the theoretical model in section 3.4. From a range of values for the distance z_2, the magnetization m and the displacement δx, we picked four examples resembling the observed tuning behavior. As for the data, the simulation results are fitted with Eq. (3.31) and Eq. (3.37) to extract the tuning parameters. All relevant values are displayed in Tab. 5.1.

unlike the *out-of-plane* component. As shown in Fig. 3.16, the build-up of the screening currents leads to a displacement of the cantilevers' resting position, which in turn modifies the overall flux threading the loop. This dynamic interplay of displacement and flux results in an effective reduction of the screening parameter β_L. Combining these effects, the observed changes in Fig. 5.1 – lowering of the sweet spot frequency with a reduction of β_R and a less hysteretic tuning due to lower β_L – match with the expected tuning behavior of the cavity in the presence of a magnetic cantilever as derived in section 3.4.

To qualitatively verify this, we use the simulations presented in section 3.4. Therefore, we have to estimate the system parameters discussed in chapter 4. The fabrication process of the SQUID cavities states an Al layer height of 9 nm. However, the 300 nm Nb layers above and below the junction expel any magnetic field from their interior and funnel half of it towards the junction from both sides. This leaves us with an effective height of $\approx 300\,\mathrm{nm}$. We estimate the width of the junction to be $3\,\mu\mathrm{m}$ from the optical pictures, which results in an effective area of $A_{\mathrm{eff}} = 300\,\mathrm{nm} \times 3\,\mu\mathrm{m}$. The critical current of the junction is $8.6\,\mu\mathrm{A}$ (a value given by the manufacturer). For simplicity, we assume a circular SQUID-loop of radius $30\,\mu\mathrm{m}$. For the particle, using the optical microscope, we assume a height of $10\,\mu\mathrm{m}$ and a vertical distance cantilever-SQUID of 30 nm (as measured for the sample in Fig. 4.15). Thus, we place the effective dipole around $z_2 = 22$–$27\,\mu\mathrm{m}$ above the SQUID for the simulations. The lateral distance to the junction is given by the SQUID-loop plus the width of the washer arms as $30\,\mu\mathrm{m}$ and we assume a range of off-center displacements 0–10%. Lastly, we assume the particle has a magnetic dipole moment of around $2\text{–}7\,\mathrm{nA\,m^2}$ (chosen from the magnetometer measurements in section 4.3.5 and the size of the actual particle). For the SQUID-parameters we use the extracted values from fitting to the tuning behavior in Fig. 5.1 without a mounted cantilever: $\omega_{c,0}/\pi = 8.229(1)\,\mathrm{GHz}$, $\beta_R = 0.45(2)\,\%$, and $\beta_L = 82.9(6)\,\%$.

From the parameter range assumed for the particle, we pick four configurations, which display a qualitative resemblance to the experimentally measured flux tuning observed in Fig. 5.1c). To extract the effective tuning parameters, we fit the simulations with the same procedure as for the data. Fig. 5.2 shows the simulation results with according fits (and the fit curve for Fig.

	oWSQ14	*oWSQ14 C1*	sim. I	sim. II	sim. III	sim. IV
$\omega_{c,0}^{fit}/2\pi$ (GHz)	8.229(1)	8.115(1)	8.104(1)	8.119(1)	8.108(1)	8.123(1)
β_R^{fit} (%)	0.45(2)	2.44(5)	3.49(1)	2.99(2)	3.26(2)	2.82(2)
β_L^{fit} (%)	82.9(6)	0.1(2)	10.1(1)	11.9(1)	10.9(1)	11.7(1)
$\beta_R'^{sim}$ (%)	–	–	3.57	3.17	3.44	3.07
$\beta_L'^{sim}$ (%)	–	–	10.4	11.8	10.8	12.2
$z_2 - z_1$ (μm)	–	–	24.5	26.3	23.3	23.3
m (nA m^2)	–	–	4.9	2.2	3.4	4.0
δx (%)	–	–	0	1	8	10

Tab. 5.1 Overview of the fit results of the measured and simulated flux tuning behavior. For the simulations we use the fit results from *oWSQ14* as the SQUID parameters. Additionally, we display the particle paramaters and the changes due to the *in-plane* field to $\beta_R'^{sim}$ and $\beta_L'^{sim}$ for the set of simulations.

5.1c), with the simulation parameters and extracted values summarized in Tab. 5.1.
The comparison reveals qualitatively good agreement between simulations and measurement. In particular, the reduction of the sweet spot frequency and the fitted value of β_R are well captured. However, the β_L obtained from the simulations deviate significantly from the experimental ones. This results in a systematically shifted tuning behavior relative to the experimental one around $\Phi/\Phi_0 = \pm 0.5$. Since we find good agreement in β_R, the lower β_L obtained for the experiment might indicate that the displacement of the cantilever due to the loop currents has a larger influence on the SQUID tuning as in the simulations. This suggests that the particle does not act as a simple dipole but rather as an extended object interacting with the loop in a more complex manner, potentially involving higher order terms or the creation/displacment of flux vortices in the cavity. Nevertheless, despite the simplifications in the model, the simulations already reproduce the main features of the experimental flux tuning with reasonably good agreement.

5.1.2 Cavity flux tuning behavior across cooldowns

Across multiple cooldowns, the flux tuning behavior of cavities with a cantilever can change significantly even without changes in the alignment between cavity and cantilever, as shown in Fig. 5.3 for *oWSQ14 C1* or discussed for other samples in [80]. *oWSQ14 C1* initially exhibited a hysteretic tuning behaviour prior to mounting the cantilever; after mounting the cantilever, we see non-hysteretic tuning and are able to tune the resonance frequency by 500 MHz as shown in Fig. 5.1. This behaviour persisted over several cooldowns with only minor fluctuations in its sweet spot frequency (at integer Φ_0). However, in *CD32*, where we also installed the first iteration of the suspension setup, the fluxmap developed an additional lower sweet spot (at half Φ_0). This prevented us from reaching the large $\partial\omega_c/\partial\Phi$ previously accessible and hence sets a limit to the achievable g_0 (see section 3.4.1). This was accompanied by a decrease in $\omega_{c,0}$ and β_L and persisted over several cooldowns. Interestingly, we observed that the tuning behavior changed when we cycled the setup above the critical temperature of Nb to 10 K, as evident by comparing Fig. 5.3b) and c). Without any visible indication of a shift in its alignment when optically imaged prior to cooldown *CD35*, we remagnetized and remounted the cantilever, placing it closer to the SQUID with $z_2 = 20\,\mu$m due to the findings of the magnetization experiments from Linz in section 4.3.5. However, the lower sweet spot remained across the following cooldowns, always limiting the tunability. Consequently, we repositioned the cantilever again to

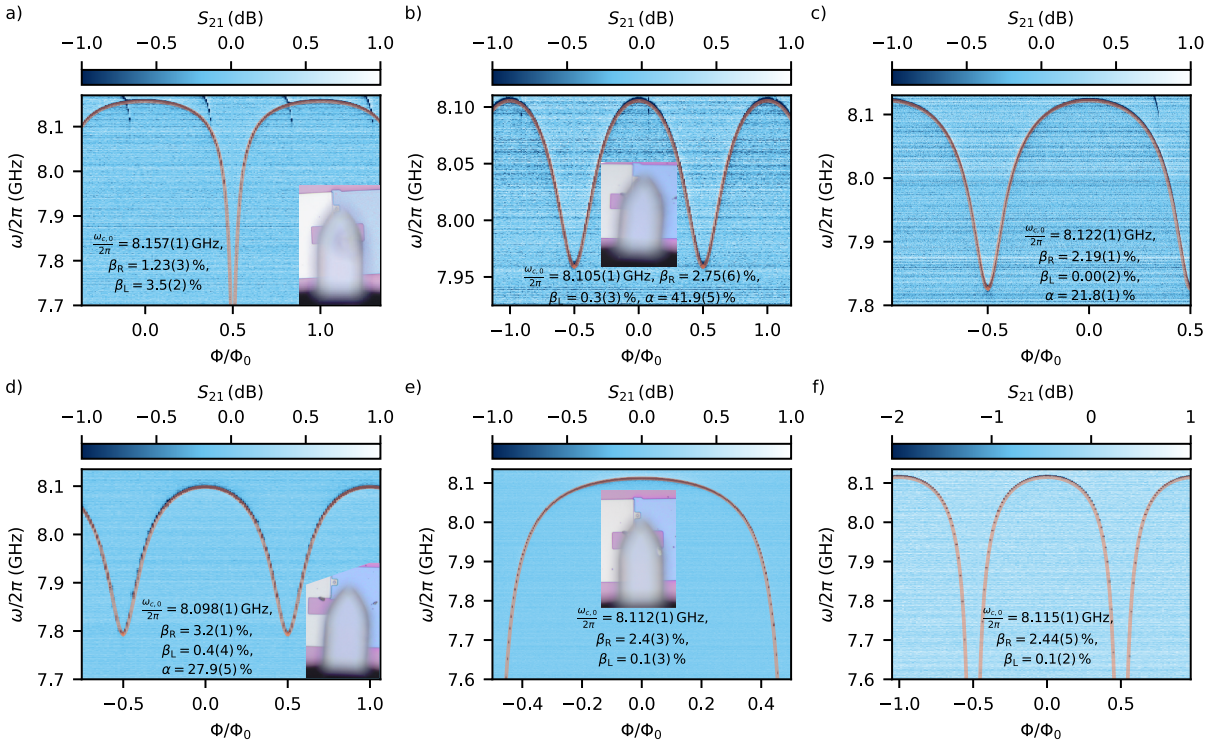

Fig. 5.3 Fluxmaps of sample *oWSQ14 C1* over several thermal cycles: **a)** *CD 31*, with the cantilever vertical distance $z_2 = 30\,\mu$m. **b)** *CD 32*, installation of the first iteration of the suspension setup. **c)** *CD 32*, after thermal cycling to 10 K. **d)** *CD 35*, after remagnetizing the sample and remounting it, resulting in a SQUID-cantilever vertical distance of $z_2 = 20\,\mu$m. **e)** *CD 41*, repositioning the cantilever leading to a vertical distance $z_2 = 29\,\mu$m and **f)** *CD 42*.

improve the alignment before cooldown *CD41*. With $z_2 = 29\,\mu$m, the sample regained its tuning behaviour prior to *CD32* with an overall reduced $\omega_{c,0}/\beta_L$ and increased β_R.

Small variations of the flux tuning behavior observed upon thermal cycling of our samples can most likely be attributed to changes in the magnetization of NdFeB. NdFeB undergoes a spin reorientation transition at 130 K (as discussed in section 4.3.5), where the magnetization falls onto a cone from the easy axis with an opening angle of up to 31°. With slight changes of the magnetization alignment on the cone, the *in-plane* field seen by the junctions might vary between cooldowns. At temperatures far below its transition temperature, we expect the magnetization of NdFeB to adopt a stable state. However, changes observed by thermal cycling to 10 K (*CD32* 5.3b and 5.3c) indicate that the tuning behavior is also influenced by the superconducting transition of Nb in a large bias field. Cooling Nb, a type II superconductor, below its critical temperature of ≈ 8 K in a large magnetic bias field results in the creation of flux vortices penetrating the material. Any vortex trapping close to the junction could alter its critical current and thus the tuning behavior of the SQUID [119]. Therefore, we believe the interplay between changes in magnetization and vortex trapping in a large bias field accounts for the slight tuning variations between cooldowns. However, the fact that the sample usually maintains a similar tunability over several cooldowns indicates the existence of a stable configuration, which

is determined by the alignment, room temperature magnetization, and crystal structure of the particle.

A drastic change in the tuning behavior between cooldowns – *CD31* (Fig. 5.3a)) and *CD32* (Fig. 5.3b)) or *CD35* (Fig. 5.3d)) and *CD41* (Fig. 5.3e)) – hints at a significant change to the system configuration. Simultanous to the installation of the suspension setup between *CD 31* to *CD 32*, the alignment of the cantilever changed, leading to an off-center placement of the particle. As seen from the simulations in section 3.4, even a small displacement leads to a significant asymmetry of the SQUID and thus explains the appearence of a lower sweet spot. After two attempts to realign the setup, we could restore the initial flux tunability of the sample, prior to cooldown *CD41*. However, we observed those drastic changes without any visible indication of a displacement of the cantilever for other samples [80]. As seen for one of the samples in 4.3.5, consisting of several competing grain boundaries, the magnetization of the NdFeB-particles can be mechanically disturbed or change over time. A flip occurring in these domains could lead to an abrupt, substantial change in magnetization, which could drive the system toward a new configuration – defined by trapped vortices and a reoriented magnetization direction following the spin reorientation transition – and thereby alter the SQUID's properties.

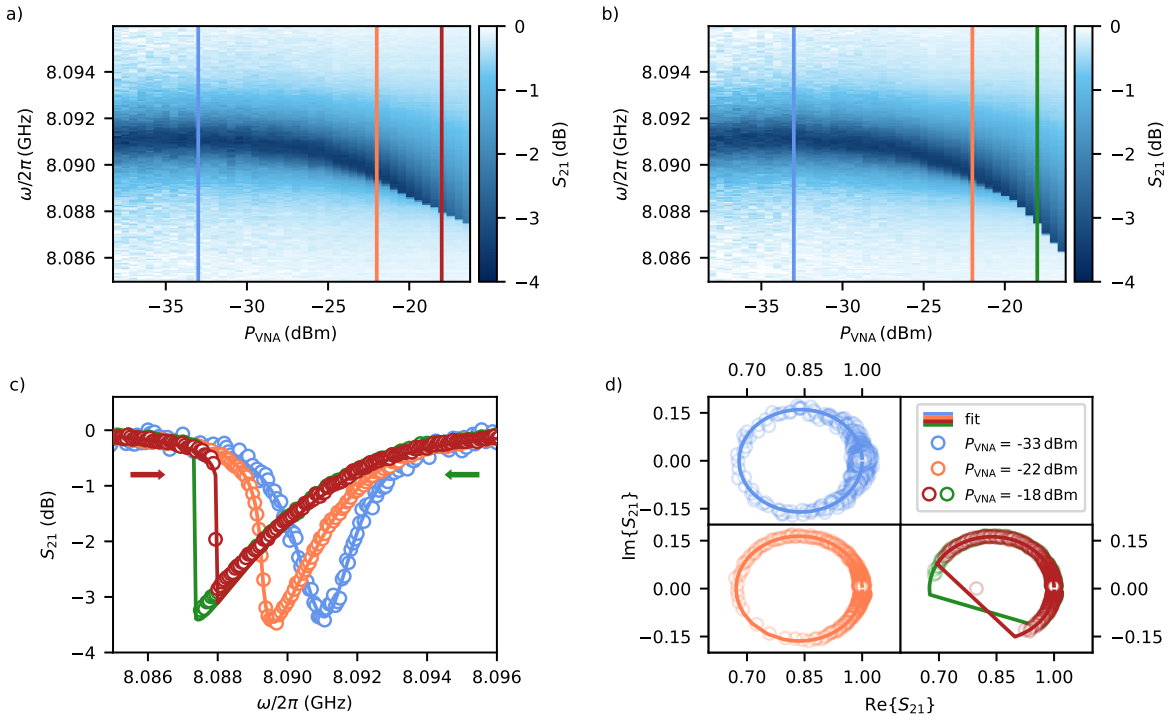

Fig. 5.4 **a)** and **b)** cavity response with increasing drive strength scanning the low and high photon number branch, respectively. **c)** Amplitude data at 3 different powers, where for the highest power the signal bifurcates. Low and high branch are accessed by scanning the drive from different directions indicated by the arrows. **d)** Data in the complex plane (*CD 42*). Data shown in the supplementary material of [5].

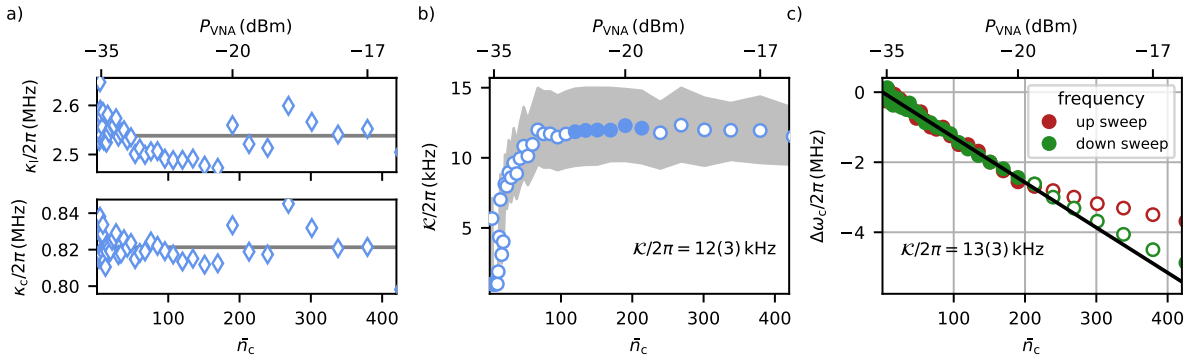

Fig. 5.5 **a)** Loaded κ_l and external κ_c linewidth, **b)** Kerr $\mathcal{K}$ extracted from the nonlinear circle fit routine versus the intracavity photon number on resonance $\bar{n}_c$ (Eq. (4.12)). Vertical lines in **a)** represent the mean values $\kappa_l/2\pi = 2.54(3)\,\mathrm{MHz}$ and $\kappa_c/2\pi = 0.821(7)\,\mathrm{MHz}$. Filled markers in **b)** are used to calculate the average $\mathcal{K}/2\pi = 12(3)\,\mathrm{kHz}$ with the error given by the uncertainty of the input attenuation, assumed to be $\pm 1\,\mathrm{dB}$ (grey area). **c)** Resonance frequency shift with increasing intracavity photon number on resonance $\bar{n}_c$ for a frequency up and down sweep. Solid markers before bifurcation of the cavity indicate points used for a linear fit to extract $\mathcal{K}/2\pi = 13(3)\,\mathrm{kHz}$ with the error due to input attenuation uncertainty $\pm 1\,\mathrm{dB}$ [102].

5.1.3 Characterization of the Kerr nonlinearity

The nonlinear behavior of the cavity for *oWSQ14 C1* is characterized by measuring its response with a VNA at various probe powers, as shown in Fig. 5.4a) and b). As the probe power increases, the cavity resonance initially undergoes a frequency shift accompanied by an asymmetric line shape. When the drive power exceeds the critical input power $\bar{n}_{in,bi}$ (Eq. (4.11)), the resonance splits into two distinct branches. In both branches, the detuning at which the cavity switches to the opposite branch is evident from the discontinuous jump in the response. Depending on the direction of the frequency sweep – represented by the arrows in Fig. 5.4c) – either the low or high photon number branch can be accessed [5].

Taking the input attenuation into account, we extract the system parameters by fitting successive cavity responses recorded at increasing probe powers with the model introduced in section 4.2.4 and displayed in Fig. 5.5. We obtain that the cavity is under-coupled with an overall mean loaded linewidth of $\kappa_l/2\pi = 2.54(3)\,\mathrm{MHz}$ and coupling rate $\kappa_c/2\pi = 0.821(7)\,\mathrm{MHz}$. Starting from low probe powers, we see a gradual trend in both linewidths until the results start to scatter as the system hits the critical input power at $P_{\mathrm{VNA}} = 20\,\mathrm{dBm}$, corresponding to an intracavity photon number on resonance of $\bar{n}_c = 200$. The extracted values for $\mathcal{K}$ converge with increasing input power to $\mathcal{K} = 12(3)\,\mathrm{kHz/photon}$. The grey area in Fig. 5.5b) represents the estimated error of $\mathcal{K}$, derived by fitting the data assuming an uncertainty of the input attenuation $\pm 1\,\mathrm{dB}$. Another method to determine $\mathcal{K}$ is to track the shift of the resonance frequency $\Delta\omega_c$, corresponding to the amplitude minimum of the normalized and matched S_{21}-data [102]. A linear fit versus intracavity photon number on resonance $\bar{n}_c$ yields $\mathcal{K}/2\pi = 13(3)\,\mathrm{kHz}$. We again assume an input attenuation uncertainty of $\pm 1\,\mathrm{dB}$, which is used to estimate the given error. The results of both methods are in good agreement, confirming the validity of the nonlinear circle-fit approach.

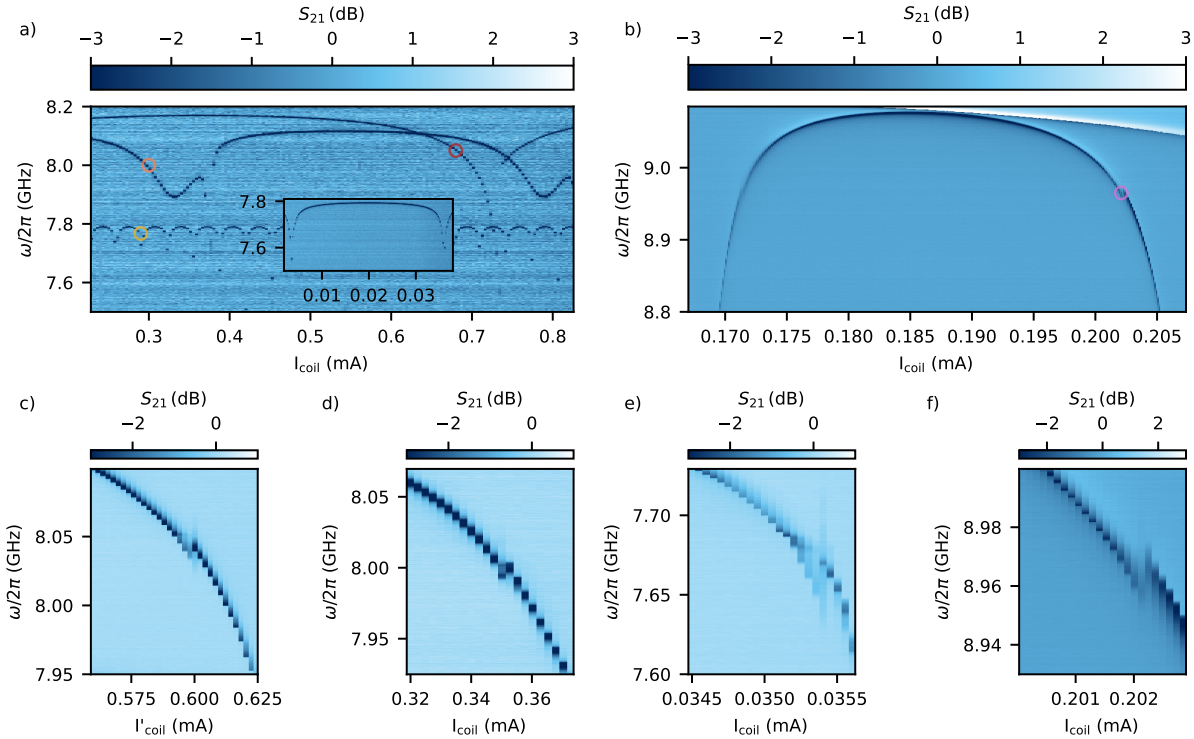

Fig. 5.6 Fluxmaps for 4 samples with cantilever during two different cooldowns. **a)** shows *oWSQ14 C1*, *oSQ3 C44* and *oWSQ8 C54* (zoom-in displayed in the inset) in descending sweet spot frequency (*CD 29*) and **b)** *WSQ5 C5* (*CD 50*). Zoom-in to highlight the Kerr anomaly at higher drive powers for each sample with *oWSQ14 C1*, *oSQ3 C44*,*oWSQ8 C54* and *WSQ5 C5* in **c)**, **d)**, **e)** and **f)**, respectively.

5.1.4 Kerr anomaly

For SQUID-cavities, we expect $\mathcal{K}$ to increase when flux biasing the device away from the sweet spot, as discussed in section 3.3 and experimentally shown in [120] and for our stripline cavities [80]. However, after mounting the cantilever, we observe regions of flux bias where this expected monotonic increase is absent, as already observed for *oWSQ14 C1* in the work of a former colleague, David Zöpfl [2, 4]. We visualize this region by taking a flux map at high probe power with the VNA, as shown for 4 samples in Fig. 5.6. The four samples all exhibit different tuning behavior, such as a hysteretic one for *oWSQ14 C1*, full tunability for *oWSQ8 C54* and *WSQ5 C5*, and a lower sweet spot for *oSQ3 C44*.[1] As seen in the zoom-in in Fig. 5.6c-d), tuning the

[1]The reason behind the periodically reappearing additional dip in the fluxmap of *oSQ3 C44*, as well as the slight asymmetry in slope for *WSQ5 C5*, remains unclear for now. We suspect that these features might be caused by an interplay between the deflection of the cantilever's resting position and the changes in SQUID properties due to the corresponding magnetic *in-plane* field. However, attempts to reproduce this behavior within our current model have so far been unsuccessful, suggesting the presence of second-order effects not yet accounted for. Potential candidates would be surface spin demagnetization or movable flux vortices, both of which would depend on the cantilever's resting position and the associated shielding currents.

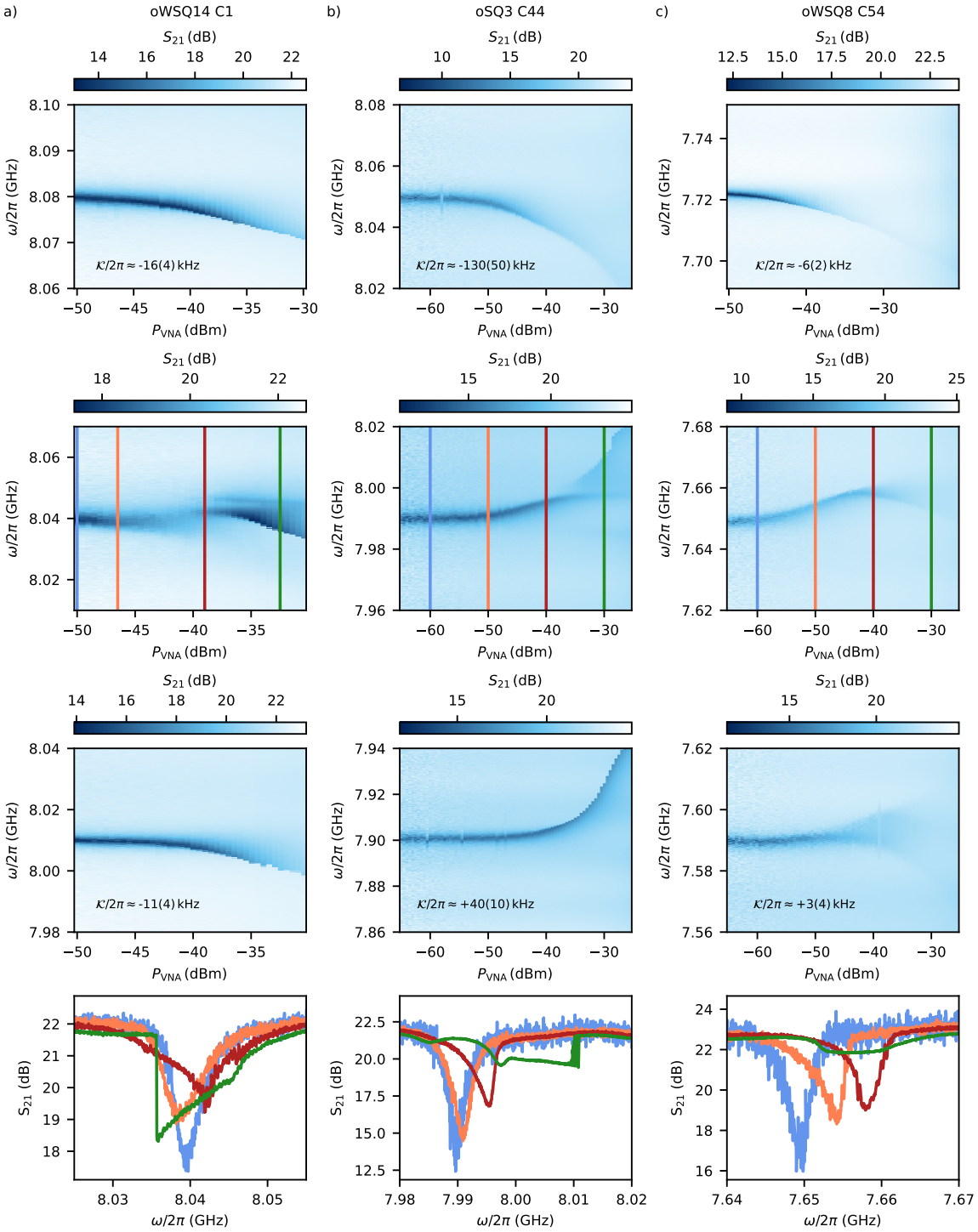

Fig. 5.7 Power scans for the samples **(a)** *oWSQ14*, **(b)** *oSQ3* and **(c)** *oWSQ8* sorted by column. First row corresponds to scans above, second row around, and third row below the Kerr anomaly. Last row represents linecuts of the scans in the second row corresponding to the vertical lines (*CD 29*).

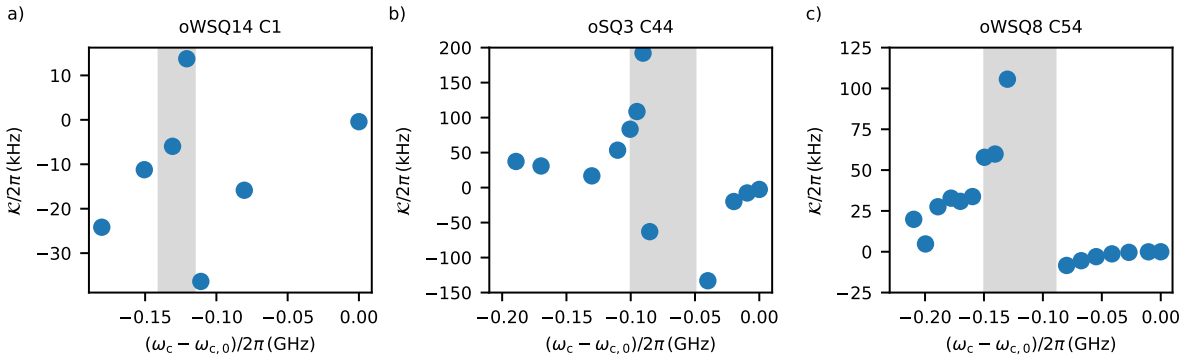

Fig. 5.8 Kerr values extracted by a linear fit to the shifted resonance frequency by estimating the probe power for sample **a)** *oWSQ14*, **b)** *oSQ3*, and **c)** *oWSQ8*. The grey area marks the frequency range of the Kerr anomaly.

cavity towards the anomaly, the system response shortly vanishes. After the feature, the cavity reappears with a slightly increased frequency.

To further investigate the anomalous Kerr feature, we take power sweeps shown in Fig. 5.7a-c) at frequencies above, around, and below the feature for samples *oWSQ14 C1*, *oSQ3 C44*, and *oWSQ8 C54*, respectively. For all samples in the first row of Fig. 5.7 above the anomaly, we observe a typical Kerr shift with increasing probe power. Within the region of the anomaly (second row), we observe that all samples initially exhibit a positive frequency shift to some extent. Linecuts in the bottom row show a steeper slope at the higher frequency side, indicating the presence of an effective positive Kerr (opposite to the expected one). At intermediate powers, the response of *oWSQ14 C1* first vades out with a small frequency downshift, followed by a gradual frequency upshift with increasing response. At higherst powers we observe a discontinuity characteristic for a negative Kerr and the appearance of an additional dip at higher frequencies. Also *oSQ3 C44* develops a second dip at higher powers, which resembles a positive Kerr resonator in the bistable regime, shifting up in frequency. Similar to *oWSQ14 C1*, *oWSQ8 C54* first shows a frequency upshift, which reverts to a frequency downshift at highest powers. Below the anomaly, all three samples exhibit different behaviors. *oWSQ14 C1* shows a frequency downshift similar to above the anomaly, as expected for a Kerr nonlinear cavity. Tuning towards its lower sweet spot, *oSQ3 C44* displays a monotonic frequency upshift resembling a positive Kerr. *oWSQ8 C54* first shows a positive frequency shift and becomes very shallow as it fans out in frequency for even higher powers.

Similar to the results shown in Fig. 5.5, we can extract $\mathcal{K}$ above and below the anomaly by estimating the probe power at the cavity.[1] Fig. 5.8 displays the extracted values for $\mathcal{K}$ for each of the samples with the frequency range of the Kerr anomaly highlighted by the grey area. Extrapolating the trend for *oWSQ14 C1* above the anomaly, we see that below it $\mathcal{K}$ is effectively reduced, while remaining negative, as already found in previous works [2, 4]. For the other two samples, we see that the initial negative Kerr above the anomaly is followed by a positive Kerr below. Whereas $\mathcal{K}$ for *oSQ3 C44* steadily increases below the anomaly, for *oWSQ8 C54* the positive Kerr slowly decreases.

[1] Due to the lack of a separate characterization of the input attenuation, the exact values of $\mathcal{K}$ should be interpreted with caution. Nevertheless, since the same attenuation is used for all samples, a comparison of their relative values for $\mathcal{K}$ remains meaningful.

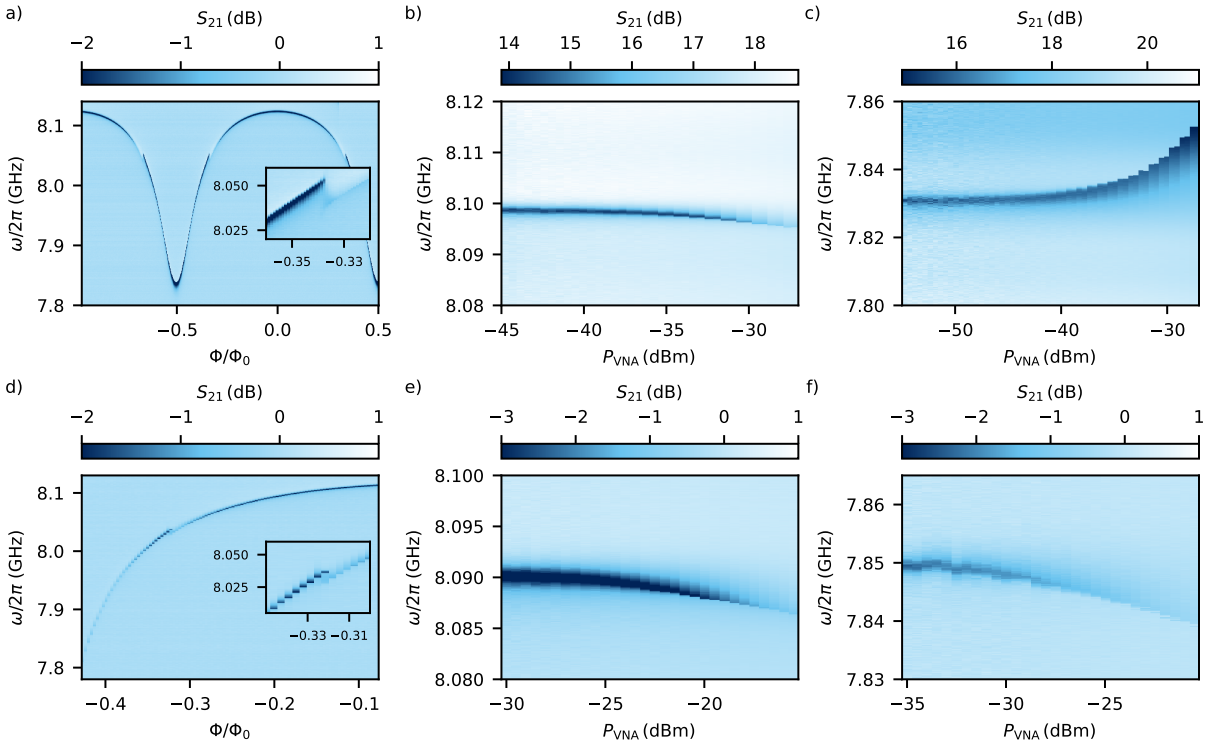

Fig. 5.9 Kerr anomaly for sample *oWSQ14 C1* for two different cooldowns: **a-c)** *CD32* with a lower sweet spot and **d-f)** *CD42* with full flux tunability. Sweet spot frequency $\omega_{c,0}/2\pi = 8.122(1)\,\mathrm{GHz}$ and $\omega_{c,0}/2\pi = 8.098(1)\,\mathrm{GHz}$ for the cooldowns, respectively (see Fig. 5.3).

An attempt to explain this phenomenon was developed in the course of the work presented in [2, 4] using a lumped-element model. By describing the junctions within the RCSJ model, the voltage response of the circuit is simulated to an applied AC driving current at different frequencies. With this, a similar behavior to the one observed for *oWSQ14 C1* could be simulated, with an overall negative $\mathcal{K}$ except for a certain frequency range with a positive $\mathcal{K}$ at intermediate powers. In the model, the shift is associated with the third harmonic of the cavity getting close to the plasma frequency of the junction, resulting in an energy transfer between the modes. However, this model fails to explain the positive $\mathcal{K}$ for *oSQ3 C44* at bias frequencies below the anomaly.

The positive $\mathcal{K}$ for *oSQ3 C44* at bias frequencies below the anomaly might arise from its asymmetry in the junction critical current caused by the *in-plane* field component of the magnetic particle. As simulated for different asymmetries in section 3.3.2.3 and shown in Fig. 3.12, an asymmetric SQUID can produce a positive frequency shift under driving when matched with an appropriate screening parameter. In this case the anomaly would correspond to the range in bias frequencies where the effective $\mathcal{K}$ changes sign. This behavior is further supported by the measurements presented in Fig. 5.9. Here, we compare the power tuning behavior of *oWSQ14 C1* with a lower sweet spot present (*CD32*) to the fully flux tunable case (*CD42*). At bias frequencies above the Kerr anomaly, we observe the expected negative Kerr behavior in both

cases, whereas below it the cavity exhibits a strictly positive Kerr in case of *CD32* with a lower sweet spot. With the fully tunable setup (*CD42*), below the anomaly region the Kerr returns to a negative value, but its magnitude is reduced as already seen in Fig. 5.8a). Interestingly, the emergence of a positive Kerr coincides in bias frequency with the anomaly region in the case of an asymmetric SQUID – for both *oWSQ14 C1* (*CD32*) and *oSQ3 C44* (*CD29*). This might suggest that the anomaly is caused by a junction asymmetry. However, this model fails to explain why for some cooldowns (*CD29*,*CD42*) the Kerr remains negative below the anomaly. This behavior may arise from not accounted higher-order nonlinear terms, which might be indicated by the appearence of an additional dip for *oWSQ14 C1* and *oSQ3 C44* in Fig. 5.6. Or the model might break at these points due its simplifications, which neglects for now any dynamics arsing from the cantilever motion and assumes that the system parameters remain constant upon driving.

The reason for the positive Kerr regarding *oWSQ8 C54* with no indication of a current asymmetry could be explained by the presence of an asymmetry in the loop inductance. Whereas both of the asymmetries lead to a tilt in the frequency shift upon driving the cavity and thus can result in a positive frequency shift, an inductance asymmetry remains undetectable upon flux tuning as discussed in section 3.3. Another plausible explanation could be that the range of the anomaly, obscured by the noise induced from the cantilever, extends further than anticipated. Thus, for larger detunings from the anomaly, the cavity might recover its negative $\mathcal{K}$ characteristics, as the trend of $\mathcal{K}$ might indicate in Fig. 5.8c).

A consequence of this nontrivial $\mathcal{K}$ behavior at different working points is the inability to compare cooling traces beyond the $\mathcal{K}$ anomaly to theory predictions [2, 4]. In the theory, we assume a power-independent $\mathcal{K}$, which remains negative even at higher coupling strengths g_0 further down the fluxmap. As the discussion above shows, these assumptions are not met in the reality of the experiment. Nevertheless, the effective reset of $\mathcal{K}$ in case of *oWSQ14 C1* turns out to be beneficial for our cooling capability of the mechanical mode at higher g_0, as it allows us to reach higher intracavity photon numbers before reaching bistability [4].

5.1.5 Slow frequency shift

Additionally to the Kerr-induced frequency shift shown in Fig. 5.4 and the Kerr-anomaly in Fig. 5.6, we observed another frequency shift δf of the cavity.[1] First indications of the presence of the shift emerged while taking VNA traces with increasing power and two different VNA bandwidths (BW). The BW refers to the width of the VNA detection filter, setting measurement time per frequency point, and hence controls the measurement noise. The effect of the frequency shift δf on the cavity response is visualized in Fig. 5.10 by VNA scans on the left and right side of the fluxmap with the BW set to 1 kHz and 1 Hz. For the fast scan at low powers, the cavity response is identical on either side of the fluxmap. However, scanning at a high power reveals a difference in its behavior depending on the fluxmap side its measured at. On the left, the response associated with the cavity switching between the low and high photon number branch is frequency wise pulled apart. In contrast, the different branches appear to be pushed towards each other on the right side. Furthermore, the response of the cavity residing in the high branch for the up and down sweep does not coincide (specifically within the frequency range

[1] The presented data and discussion in this section are part of the main text and supplementary material of my publication in [5].

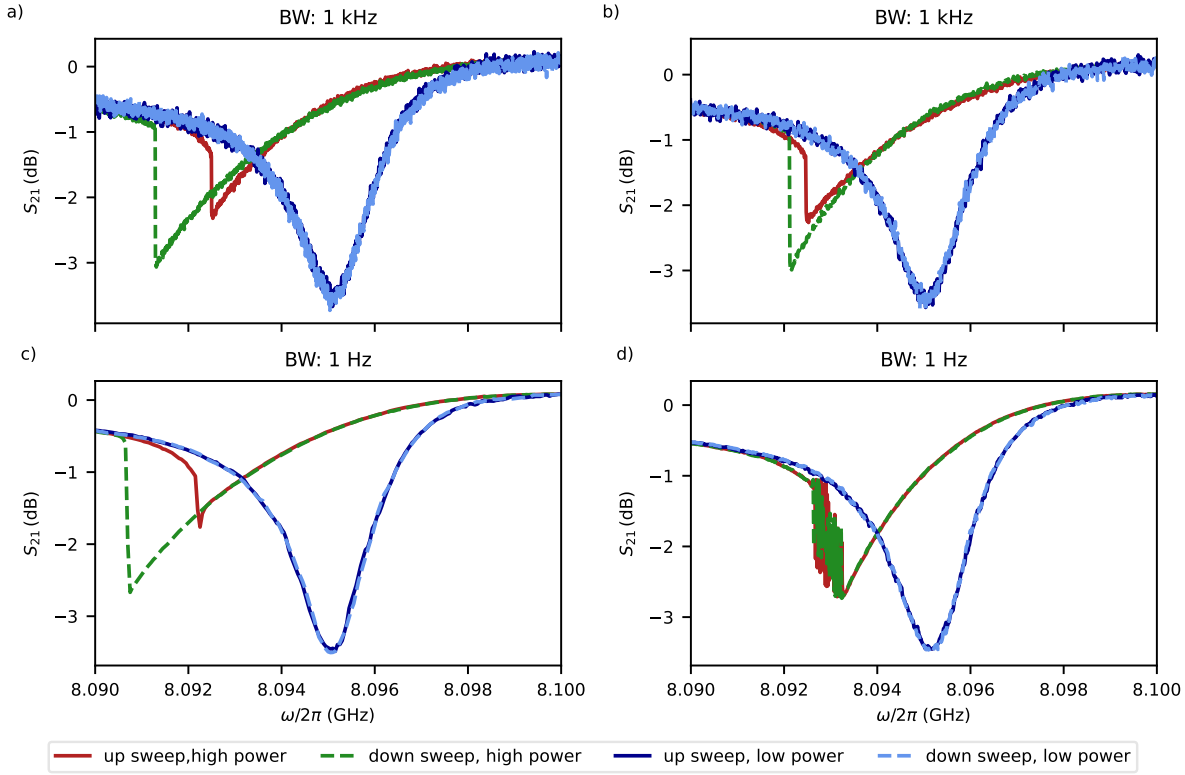

Fig. 5.10 VNA scans for low and high powers with different bandwidths. **a)-b)** fast and **c)-d)** slow VNA scans on the left and right side of the flux map, respectively. To access the low and high photon number branch each trace is taken as a frequency up and down sweep. For high powers the fluxmap side dependence for the high and low photon number branch is visible, especially for the slow scan (*CD42*).

8.092 − 8.094 GHz), which might indicate that the acquisition rate exceeded the intrinsic system dynamics. Reducing the BW by 3 orders of magnitude, the cavity response for the frequency up and down sweep on both sides of the fluxmap align, from which we conclude that the cavity is probed in a newly found steady state. The corresponding timescale for the system to reach the steady state has to be on the timescale of seconds – the BW of the VNA being 1 Hz. Additionally, on the left side of the fluxmap, the switching of the high to low photon number branch is shifted further down in frequency, compared to the fast measurement. In contrast, on the right side, the slow measurement reveals a continuous switching between the two distinct branches. As a consequence of this behavior, on the right side of the fluxmap, selecting either of the branches is not possible.

To further investigate this shift, we weakly probe the cavity response in the presence of a strong drive tone. By populating the cavity with the drive, we expect from discussion above that the resonance frequency shifts from its initial frequency f_i until it reaches a new steady state f_ss on the timescale of seconds. To quantify the timescale of this shift $\delta f = f_\mathrm{ss} - f_\mathrm{i}$, we measure the evolution of the cavity response by probing it at different times after turning off the drive tone. Therefore, we initialize the cavity in the high photon number branch – which restricts us to working on the left side of the fluxmap – and keep the drive at a constant cavity detuning. As shown in Fig. 5.11a) $\delta f(t)$ follows an exponential decay back to its initial value. A fit to the

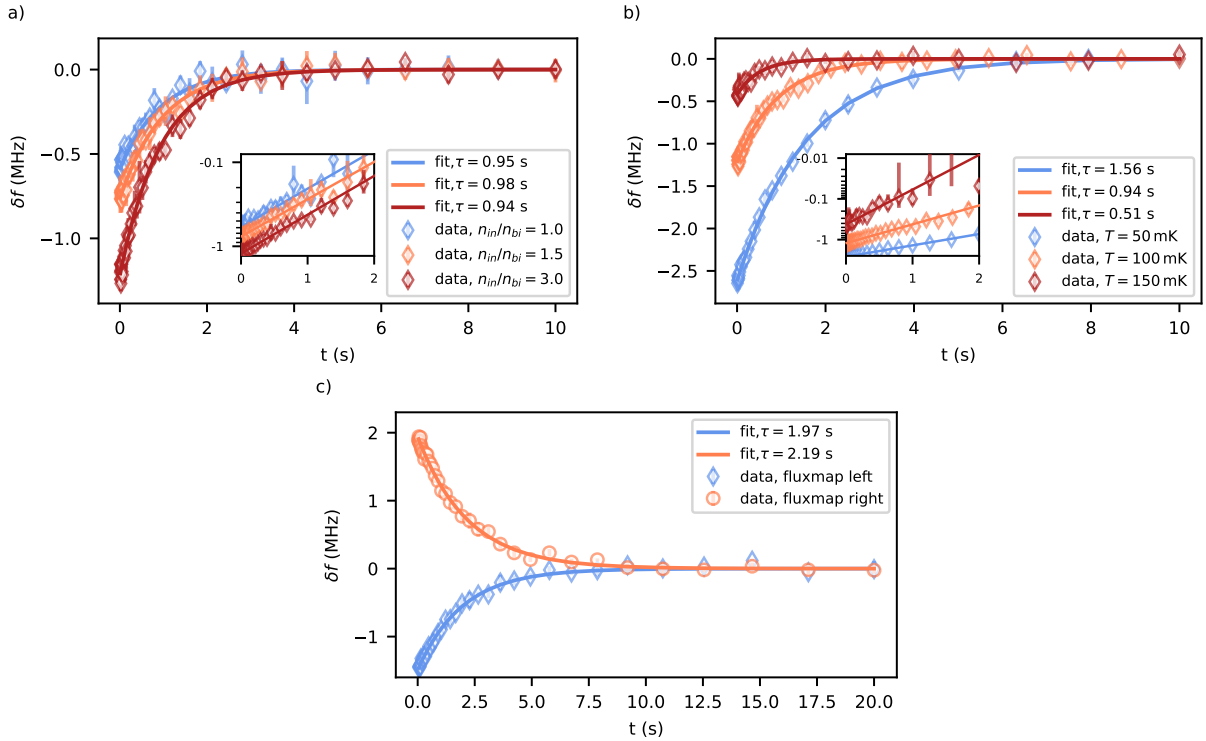

Fig. 5.11 **a)** Relaxation of the frequency shift δf after driving the cavity at different powers, for the cavity being initialized in the high photon number branch at the same detuning to the drive. Solid lines represent an exponential fit to extract the timescale $\overline{\tau} = (0.96 \pm 0.02)\,\mathrm{s}$. The inset shows a zoom-in on the data plotted on a log-scale at $T_{\mathrm{base}} = 100\,\mathrm{mK}$, **b)** δf at different base temperatures for the same drive power $n_{\mathrm{in}}/n_{\mathrm{bi}} = 3.0$. **c)** Comparison of the relaxation process measured on the left side and right side of the fluxmap at $T_{\mathrm{base}} = 50\,\mathrm{mK}$ and $n_{\mathrm{in}}/n_{\mathrm{bi}} \approx 1.0$ [5](*CD42*).

data yields a slow relaxation time of $\overline{\tau} = (0.96 \pm 0.02)\,\mathrm{s}$ independent of the intracavity photon number set by the drive power. In contrast, the amplitude of δf significantly depends on the drive tone power.
In Fig. 5.11b), we repeat the measurement at different base temperatures, while keeping the input power constant at $n_{\mathrm{in}}/n_{\mathrm{bi}} = 3.0$. We observe that with increasing temperature, the time scale as well as the amplitude of the shift reduces. Furthermore, when the cavity is tuned to the right side of the fluxmap instead of the left side, a positive frequency shift is observed (Fig. 5.11c). Taken at the same bias frequency and with the same input power, fitting the relaxation rate yields comparable parameters regardless of which side it is measured.

As indicated by the increase of the δf amplitude with drive power in Fig. 5.11, we can use the photon number dependence of δf to determine in which state the cavity ended up after applying the drive. In the low photon number branch, we expect significantly fewer intracavity photons compared to the high branch, thus δf will be small for the low and large for the high photon number branch. The ability to use the observed shift to distinguish the photon branches is displayed in Fig. 5.12a). Here, we extract δf as above for different cavity-drive detunings

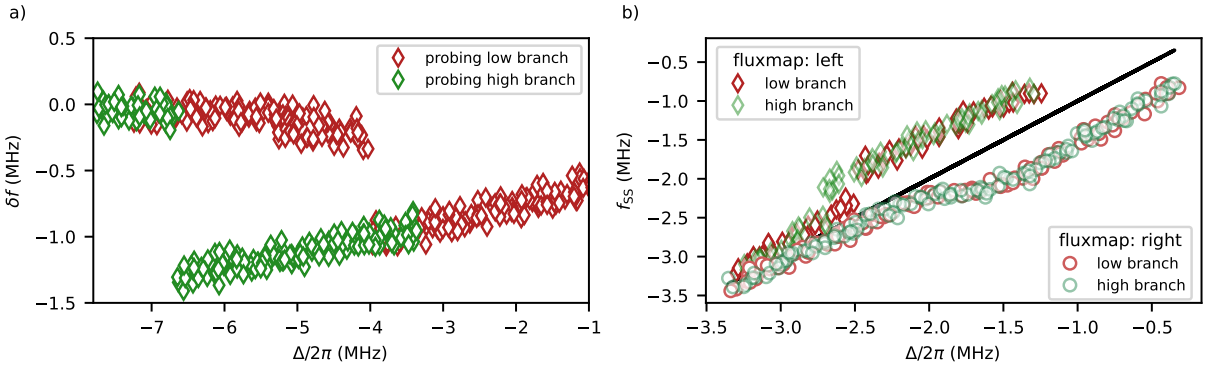

Fig. 5.12 **a)** Frequency shift δf against drive-cavity detuning Δ for a drive strength $n_{in}/n_{bi} = 3.0$. Probing the different branches by tuning the drive towards the cavity from low/high frequencies to scan the low (red) and high (green) photon number branch. **b)** Probing the low and high photon number branch for the left and right side of the fluxmap [5] as a function of the drive-cavity detuning Δ.

Δ at a constant drive exceeding the critical input power. Residing in the low photon number branch, the cavity shift increases slowly as we start to populate the cavity tuning towards the high photon number branch. Thus, we observe a small frequency shift due to the overall low intracavity photon numbers. Subsequently, a distinct frequency jump to a larger δf is obtained upon switching into the other branch due to the sudden increase in intracavity photon numbers. Initializing the cavity in the high photon number branch, the intracavity photon number significantly exceeds the one in the low photon number branch towards the detuning indicating the end of the bistable range. Beyond the bistable range, the intracavity photon number drops abruptly. Accordingly, a gradual increase of δf is visible, followed by a step to $\delta f \approx 0$ aligning with the cavity switching branches. Within the bistable frequency range, the cavity shows two distinct values for δf associated with the two cavity states. As a consequence, we can unambiguously distinguish which of the two branches the cavity resides in for a set drive detuning by tracking the cavity shift. Furthermore, the observed frequency shift suppresses continuous switching between the states during a measurement for detunings within the bistable range. Because on the left side of the fluxmap the cavity resonance shifts to lower frequencies with increasing intracavity photon number, a transition from the low to the high photon number branch results in a cavity shift, effectively increasing the detuning between the drive and frequency associated with the switching event. When switching in the opposite direction, the strongly shifted cavity returns to its initial frequency, leaving the drive far detuned from resonance. In both cases, switching the state results in a frequency shift that prevents to restore the initialized state.

In contrast to the behaviour on the left fluxmap side, the positive frequency shift on the right side does not allow to distinguish the different branches, as shown by the steady state frequency f_{ss} in Fig. 5.12b). Regardless of the branch being probed, the cavity settles to the same f_{ss} over a broad range of initial frequencies. Exceeding $n_{\mathrm{in}}/n_{\mathrm{bi}} > 1$, a continuous switching between the branches can be observed as such a shift causes the drive to tune in and out of the resonance, as illustrated in Fig. 5.10d). With this behavior, beyond bifurcation the system cannot be initialized with certainty in either of its states on the right side of the fluxmap. However, for input powers $n_{\mathrm{in}}/n_{\mathrm{bi}} < 1$ the positive shift acts as an effective negative feedback loop, stabilizing the resonance against slow frequency fluctuations and thereby proving beneficial for

backaction measurements prior to the onset of bistability, similar to observations reported in [49].

To sum up the characteristics of the observed frequency shift δf, its amplitude scales with the intracavity photon number, whereas the timescale does not. With increasing temperature, we observe a decrease in its amplitude and timescale. Lastly, the direction of the shift depends on the sign of the fluxmap slope. Radiation pressure on the mechanical resonator seems at first glance a plausible explanation for the shift. As discussed and shown in section 3.3, flux tuning the cavity to lower frequencies leads to a circulating current within the SQUID due to flux quantisation. The created magnetic field of the SQUID due to the screening currents displaces the cantilever from its resting position as shown in Fig. 3.16. For each flux point, the system balances the flux threading the loop from the *out-of-plane* component of the magnetic particle and its distance given by the circulating current. However, populating the cavity with a drive – a current across the SQUID as in Fig. 3.10 – decreases the amplitude of the screening current in the SQUID loop. The reduced magnetic field causes the mechanical resonator to move towards its initial resting position. This displacement changes the magnetic flux from the magnetic tip threading the SQUID, shifting the resonance of the cavity. An increased cavity population would further decrease the circulating current, resulting in the cantilever moving closer to its initial position and thus leads to a larger shift of the cavity frequency. This agrees with the observation that the amplitude of the frequency shift increases with input power. The observation that the time dynamics remains unchanged with the drive power contrary to the amplitude, indicates that the relaxation process is not governed by cavity dynamics or backaction effects, but rather by mechanical properties. Following this assumption, we would not expect a dependence of the relaxation time on the drive power, as the cantilever properties remain unchanged as soon as the drive is turned off. However, as we will see in section 5.2.2, the linewidth of the mechanical resonator grows significantly with its bath temperature. Interestingly, the relative changes in Γ_m with temperature (Fig. 5.18d) match the changes observed for τ, although the absolute values are off by a factor of ~ 2. Therefore, it seems plausible to assume, that the timescale on which the shift δf is observed in Fig. 5.11b) is indeed related to the intrinsic linewidth Γ_m. Nevertheless, for a classical radiation pressure model and from simulations using our model, the frequency shift should scale with $\delta f \propto -g_0^2$, which contradicts the difference in directions of δf depending on the side of the fluxmap.

Another explanation could be that the Kerr-constant $\mathcal{K}_\mathrm{eff}$ of the cavity is altered by the optomechanical coupling given by Eq. (2.18) and depicted in Fig. 2.2 [53]. However, the change to $\mathcal{K}_\mathrm{eff}$ in the regime we operate the system at would be too small to explain the observed shift and also fails to describe the fluxmap side dependence due to its g_0^2 scaling.

Magnetic surface spins are also potential contributors to the observed frequency shift. At low temperatures, these spins are expected to align due to the close proximity of the magnet at the cantilever tip, producing a constant magnetic flux offset in the SQUID loop. A larger AC-current corresponding to driving the cavity can scramble a fraction of these spins, thereby reducing the offset magnetic flux at the SQUID. As a consequence, the fluxmap would horizontally shift towards absolute zero flux (e.g., a shift of the fluxmap to the left in Fig. 5.1). Matching the observation, this would cause the frequency on the left and right fluxmap side to shift in $\delta f < 0$ and $\delta f > 0$, respectively. Furthermore, larger input powers and therefore higher AC currents would correspond to a larger magnetic field change, since more spins would be scrambled. This would result in a larger effective shift, matching the obtained power dependence of δf. Lastly,

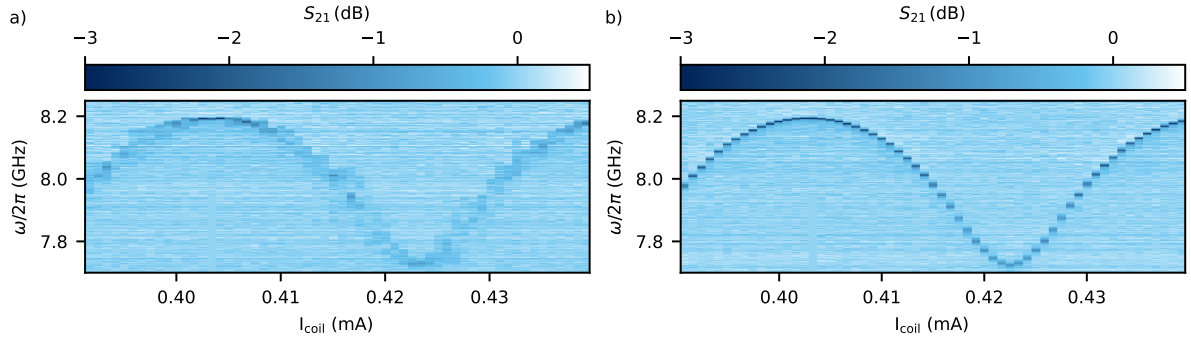

Fig. 5.13 Fluxmaps of *WSQL9 C24* (*CD50*) with the mechanical feedthrough **a)** with the experiment resting on the thermalisation pieces, **b)** after lifting the setup.

the relaxation time of the spins should feature the same timescale dependence on temperature as observed for the frequency shift and, since higher temperatures allow for a higher degree of initial disorder, it would also explain the change in amplitude. Nevertheless, experimentally quantifying the influence of surface spins remains challenging, and further advances are required to verify this hypothesis.

5.2 Mechanical Mode in the Absence of Backaction

Within this section, we present measurements of the mechanical resonator in the absence of backaction. We start by assessing how well the suspension setup isolates the mechanical mode from environmental vibrations. Further, we show measurments responsible for the implementation of the eddy current damper. Subsequently, we characterize the thermalisation of the mechanical mode. Here, we also compare the mode occupation for the pulse tube (PT) – the primary resource of vibrations – turned off versus turned on. The section concludes by characterizing a shift of the mechanical frequency depending on the bias frequency of the cavity.

5.2.1 Performance of the suspension setup

One can get a qualitative estimate of the mechanical noise exciting the cantilever by monitoring the cavity while flux tuning. As the coupling strength increases towards lower bias points, the mechanical motion progressively washes out the cavity response. This effect becomes more pronounced for higher mechanical excitation, since the frequency shift induced by the optomechanical coupling scales as $g_0\sqrt{\bar{n}_\mathrm{m}}$. By implementing the mechanical feedthrough, we can perform an in-situ comparison of the mechanically induced cavity noise before and after suspending the setup, as shown in Fig. 5.13. Before lifting the setup, the cavity response is barely visible except close to the upper sweet spot, indicating a highly excited mechanical mode driven by vibrations from the PT. Upon lifting the setup with the feedthrough, we can detect a clear cavity response throughout the whole fluxmap, which is a good indication of sufficient mechanical isolation from its environment.

The influence of the PT on the mechanical mode can be seen in the stability measurements displayed in Fig. 5.14. Here, we repeatedly monitor the cavity over a certain time span. Prior to the installation of the suspension setup (Fig. 5.14a)), a clear change in cavity shape is visible as

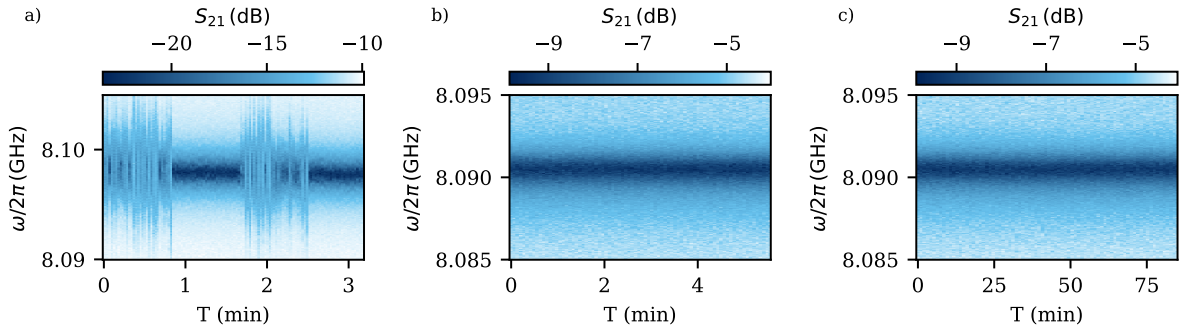

Fig. 5.14 **a)** Difference in cavity response PT on to PT off for a rigidly connected setup (data taken from [2]). **b)** and **c)** short and long time measurement of the cavity response PT on with the setup suspended.

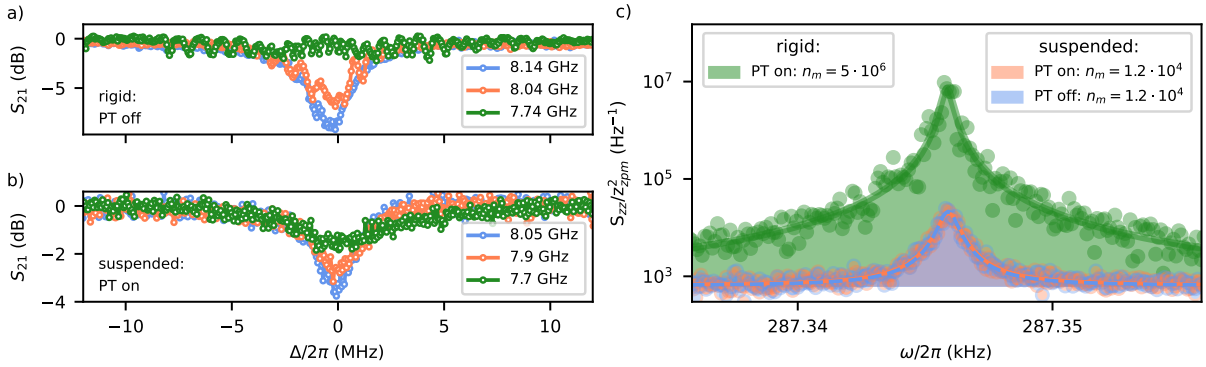

Fig. 5.15 **a)** Mechanical induced noise on the cavity response for three different bias points for the rigidly connected setup, PT off (Data taken from [2]). **b)** For similar bias points, cavity response for the suspended setup PT on. **c)** Mechanical spectra for a rigidly connected setup PT on and for the suspended setup PT on and PT off at 150 mK at an intermediate coupling strengths [5].

soon as the PT is turned on. However, with the suspended setup, we obtain a clear cavity signal with the PT running, comparable to the one obtained for the rigidly connected setup PT off. Even over the time span of an hour, the system remains stable without any indication of vibrational noise or flux drift. Additionally, to validate the performance of the suspension setup, we compare the cavity response at higher coupling strengths with measurements obtained using the rigidly connected setup. The results are shown in Fig. 5.15a) and b). Even for the PT off, the cavity response for the rigidly connected setup is dominated by a noise pattern with increasing flux sensitivity, with the main components of the noise below 100 Hz [2]. The presence of this noise renders any mechanical measurements impossible, thereby preventing us from operating the system at these high coupling strengths. Repeating the measurement at similar coupling strengths for the suspended setup PT on, we obtain a qualitatively clean cavity response. The cavity broadening observed at the highest coupling strength can be attributed to the optomechanical interaction. As we scan the cavity slower than the mechanical frequency, we effectively average over the oscillating cavity response caused by the high coupling to the mechanics, resulting in a broader appearance of the cavity scaling as $\kappa_l \propto \sqrt{\bar{n}_{\mathrm{m,th}}} g_0$. These results suggest

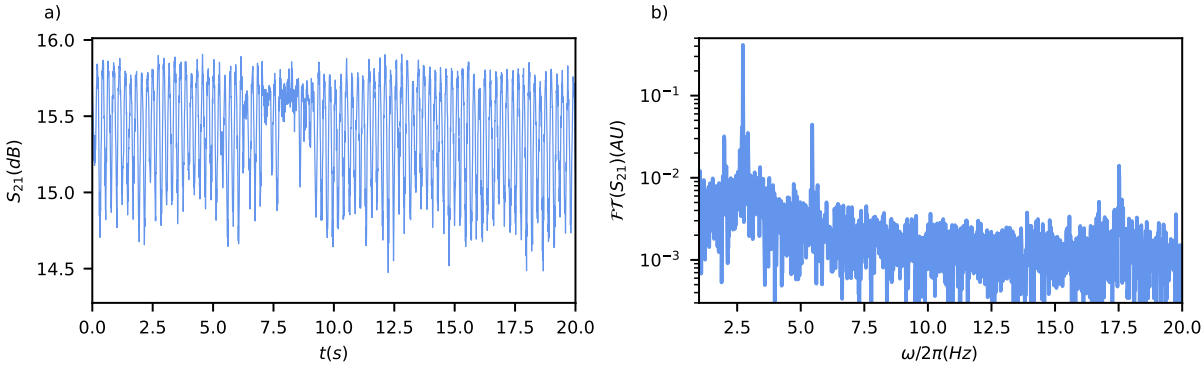

Fig. 5.16 **a)** 0 Hz-span VNA measurement on resonance with the cavity (with cantilever mounted) showing a clear oscillation. **b)** Fourier-transform of the data with a clear peak at 2.7 Hz.

that even PT on the suspension setup achieves a significant decoupling of the mechanical mode from the vibration environment of the cryostat. Measurements on the mechanical occupation displayed in Fig. 5.15c) further validate the good performance of the suspension setup. Here, we measure the thermal occupation of the mechanical mode by probing the system on resonance with a weak tone to avoid backaction. PT on with a rigidly connected setup, the mechanical occupation is 400 times higher than the thermally expected one. However, upon turning off the PT we typically measure the mechanical mode to be thermal [2]. This further underscores the detrimental influence of the PT vibrations on the system. By suspending the experiment, we observe a thermal mechanical occupation regardless of the PT state.

In summary, these measurements demonstrate the effective performance of the vibration isolation. Data from both the cavity and the mechanical mode indicate a nearly complete decoupling from the primary source of vibrational noise – the pulse tube – as well as an overall reduction of the vibrational environment seen by the cantilever. This improvement should, in principle, enable operation at higher coupling strengths than prior to implementing the suspension setup. Another important benefit of the setup is that it drastically increases our data acquisition rate. With the rigidly connected setup, mechanical measurements required us to turn off the PT. However, turning off the PT steadily increases the cryostat input pressure of the mixture and warms up the cryostat, starting from the upper plates. To allow for stable and continuous operation of the cryostat, we were forced to limit our measurement times per day to a few, distributed slots. With the stability gained by decoupling from the PT vibrations due to the suspended setup, measurements on the mechanics are not bound to any external conditions and can run as long as necessary.

To conclude this section, it is important to mention what happens if the suspension setup itself remains undamped. By continuously improving the setup, for example through the use of flexible microwave cables and copper braids, the quality factor of the suspension's eigenmode became sufficiently high to observe a ring-up. This caused a noise pattern similar to the one shown in Fig. 5.15a) while scanning cavity. By placing the VNA on resonance of the cavity and recording its transmission over time, a coherent oscillation was visible (Fig. 5.16). A Fourier transformation reveals that the main component is found at 2.7 Hz, which agrees with the expected resonance frequency of the vertical motion. As the noise caused by the eigenmode of

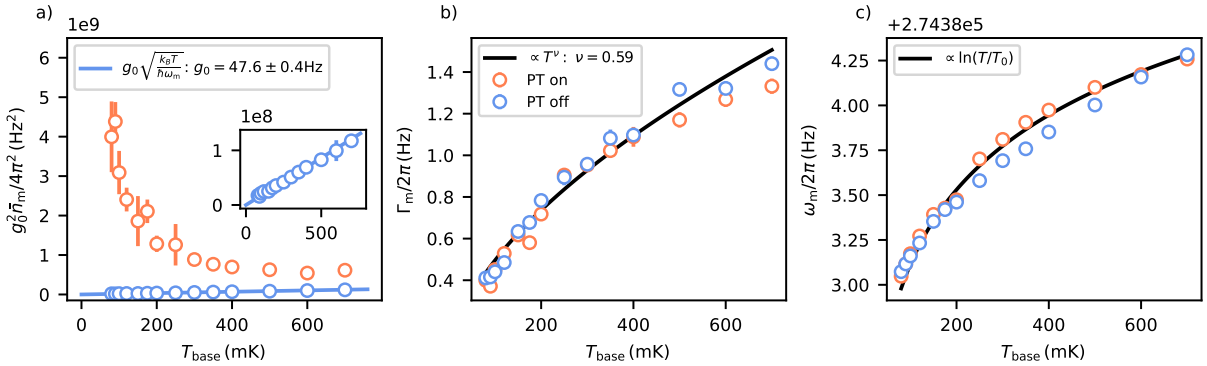

Fig. 5.17 Temperature ramp at $\omega_c/2\pi = 8.152\,\mathrm{GHz}$ with the setup rigidly connected to the base plate PT on versus PT off (*CD18*): **a)** mechanical occupation with a linear fit to extract the coupling strength, **b)** mechanical linewidth with a $\propto T^\nu$-fit and **c)** frequency with a $\propto \ln(T/T_0)$-fit [121–123]. Data taken from [2].

the spring renders the vibration isolation ineffective, we had to implement a damping mechanism which simultaneously preserves the vibrational decoupling from the cryostat. As described in chapter 4, we installed an eddy current damper, which enabled us to acquire the results presented in the following sections.

5.2.2 Determination of the optomechanical coupling via temperature scans

Using the Gorodetsky calibration method to correct for the system's transfer function (sec. 4.3.2), Eq. (4.32) shows that the mechanical signal is proportional to $g_0\sqrt{\bar{n}_\mathrm{m}}$. To independently extract the coupling rate, we have to know the mechanical occupation. To do this, we measure the mechanical signal at different base temperatures at the same bias frequency of the cavity. To ensure a thermal mode occupation, we avoid backaction by using a weak probe tone on resonance with the cavity. Assuming a thermalized mode, the mechanical occupation $\bar{n}_\mathrm{m}$ depends linearly on the mode temperature according to the Bose-Einstein distribution in Eq. (2.23). Consequently, for a thermalised mechanics, fitting the slope of the extracted $g_0^2\bar{n}_\mathrm{m}$ against temperature allows a determination of the coupling strength g_0.[1] In the following, we present temperature scans from one cooldown without and three representative cooldowns with the suspension setup installed. Since this measurement scheme requires the mechanical mode to be thermal, this provides an additional means to verify the performance of the vibration isolation in each cooldown.

Fig. 5.17 displays the result of the temperature scan measuring with PT on and PT off for the rigidly connected setup. As we expect from Eq. (2.23), we see a clear linear trend in mechanical occupation PT off with increasing temperature, where a linear fit yields a coupling strength of $g_0/2\pi = 48.7(4)\,\mathrm{Hz}$. In contrast, turning the PT on results in a highly excited mechanical occupation, which increases significantly towards lower temperatures. This behavior is most likely linked to the reduction in mechanical linewidth Γ_m. The narrow linewidth and therefore long-lived excitations at low temperatures leads to a ring up of the mechanical mode. As Γ_m broadens with temperature, the response of the mechanics to the PT is reduced (see Eq.

[1] The data acquisition procedure itself at each base temperature is identical to the one discussed in section 5.3.1.

(4.3)), resulting in a gradual decrease of $\bar{n}_\mathrm{m}$ [2].
The discrepancy in $\bar{n}_\mathrm{m}$ between PT off and PT on is not present in the obtained mechanical linewidth and frequency. Following [122], a T^ν temperature dependence is fitted to the mechanical linewidth Γ_m yielding $\nu = 0.59$ and a logarithmic scaling with temperature is fitted to the mechanical frequency ω_m. The obtained restults agree with findings for micromechanical resonators at low temperatures in Refs. [121–124]. Here, the authors attribute the temperature scaling obtained for Γ_m and ω_m to the coupling to tunneling TLS. The oscillation of the mechanical resonator leads to a time-varying elastic strain field, which brings the TLS out of thermal equilibrium. Coupling to the mechanical mode, the flow of energy corresponding to the relaxation of the TLS with $T_{1,\mathrm{TLS}}$ acts as an additional damping mechanism to the natural linewidth of the mechanics. Naturally, $T_{1,\mathrm{TLS}}$ decreases towards higher temperatures, leading to an induced broadening with temperature as $\Gamma_\mathrm{m} \propto T^\nu$. The exact scaling depends on the coupling mechanism, where one finds $\nu = 0.5$ for phonon coupling in the 1D case, and $\nu = 1$ for electron coupling in general and phonon coupling in 2D [122]. At higher temperatures, Γ_m will saturate as the TLS reach population equilibrium. As the dominant phonon wavelength of Si at 1 K is $\sim 0.1\,\mu$m [125], we would expect a 3D temperature dependence given by the cantilever dimensions. However, studies on silicon resonators coated with aluminium in the normal and superconducting state allowed to investigate the importance of normal-state electrons on the TLS induced damping mechanism [123]. In the superconducting state without normal-state electrons a $\Gamma_\mathrm{m} \propto T^{1.5}$ scaling was found, whereas in the normalconducting state a $\Gamma_\mathrm{m} \propto T^{0.65}$ scaling could be observed, similar to the one in Fig. 5.17. As the AFM cantilevers used in out system are doped to avoid charge build up, the temperature dependence might indicate a dominant electron contribution to the relaxation processes at hand. Furthermore, the coupling to the TLS also results in a change in the speed of sound, which causes a frequency shift of the mechanics given by $(\omega_\mathrm{m} - \omega_{\mathrm{m},0})/\omega_{\mathrm{m},0} = C \ln(T/T_0)$ (C represents the TLS coupling strength and $\omega_{\mathrm{m},0}$ is the mechanical reference frequency at temperature T_0). The good agreement of Γ_m and ω_m indicates that – for both PT on and PT off – the physical temperature of the mechanical mode (and the TLSs) thermalizes to the actual base temperature. This further supports the assumption that the increased occupation for PT on is caused by external excitations rather than an elevated intrinsic temperature of the mode.

Fig. 5.18 shows the result of the mechanical characterization during the temperature scans for the installed suspension setup throughout 3 cooldowns. *CD41* is represented twice Fig. 5.18b) and c), as we attached an additional temperature sensor on the experiment to track thermalization of the suspended can. Each cooldown exhibits a temperature dependence similar to that of the rigidly connected setup, with $\Gamma_\mathrm{m} \propto T^\nu$ and an average exponent of $\bar{\nu} = 0.59(3)$. However, instead of clear logarithmic temperature dependence of ω_m associated with the coupling to TLS, we observe a rather linear dependence[1]. If these changes correlate to the installation of the isolation setup or the repositioning of the cantilever discussed in Fig. 5.3 can not be distinguished. Nevertheless, the clear temperature dependence indicates a thermalization of the mechanical mode, which is further supported by the mostly linear temperature dependence of the extracted mode occupation. Within one of the first cooldowns using the suspension setup *CD35* shown in Fig. 5.18a), the mechanics exhibits systematically higher $\bar{n}_\mathrm{m}$ for PT on compared to PT off, increasing with temperature. Interestingly, the behavior PT on differs clearly to the one observed for the rigidly connected setup in Fig. 5.17. It has to be mentioned that for this cooldown

[1] For the two frequency outliers in *CD41*, which represent chronological the first measurments in Fig. 5.18b) and c), the spectrum analyzer was not locked to the probe, which explains the frequency offset.

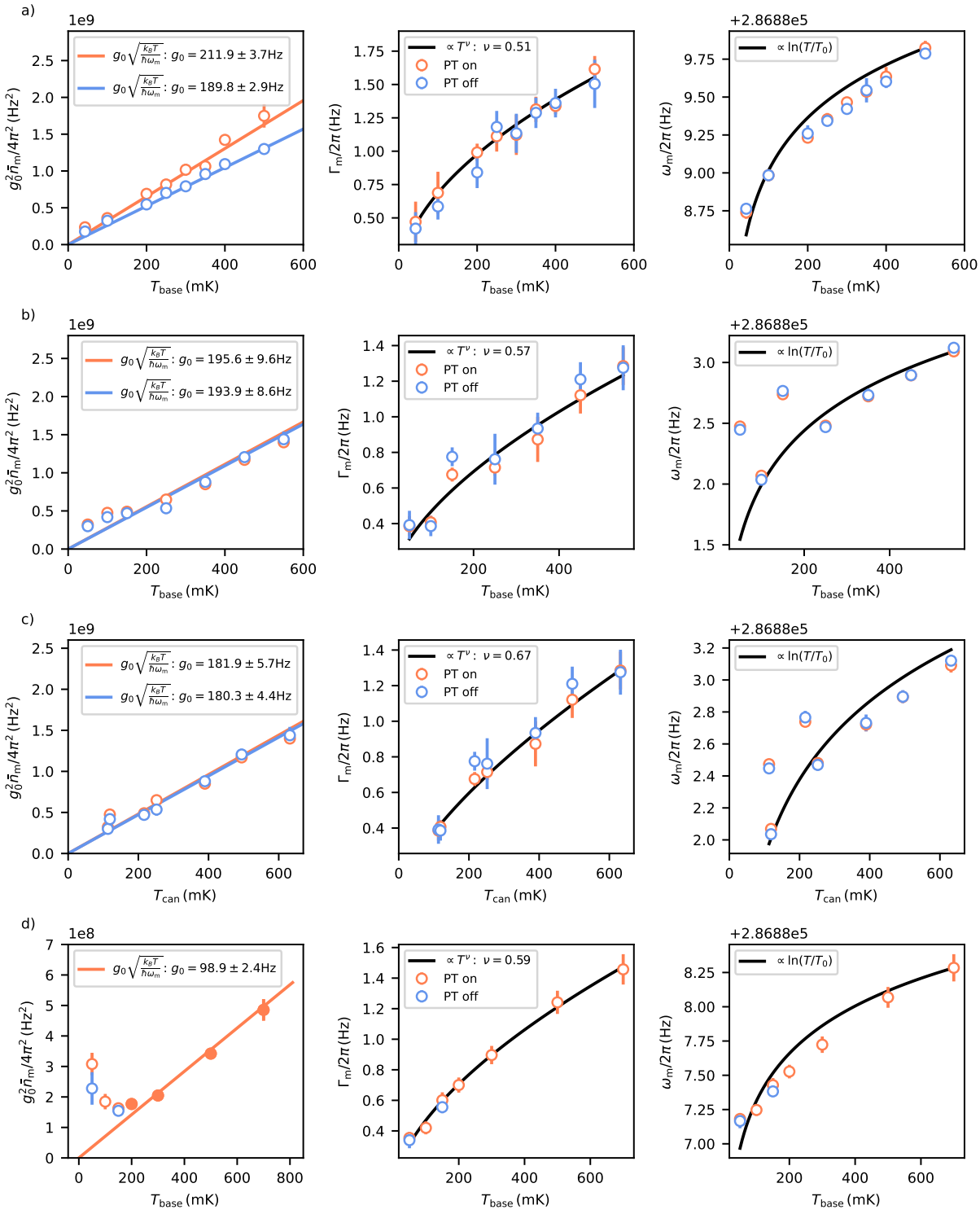

Fig. 5.18 Temperature ramp PT on versus PT off for different cooldowns with the installed suspension setup. For each cooldown we display the mechanical occupation with a linear fit to extract the coupling strength, the mechanical linewidth with a $\propto T^\nu$-fit, and frequency with a $\propto \ln(T/T_0)$-fit [121–123]. **a)** *CD35* at $\omega_c/2\pi = 8.072\,\mathrm{GHz}$ with 4 Copper braids connected and no eddy current damper. **b/c)** *CD41* at $\omega_c/2\pi = 8.0665\,\mathrm{GHz}$ with an additional temperature sensor on top of the experimental setup with 3 Copper braids connected, plotted against temperature according to the base/experiment sensor, respectively. **d)** *CD42* at $\omega_c/2\pi = 8.0955\,\mathrm{GHz}$ with the suspension setup with 2 Copper braids from base connected to the experiment and 2 additional copperbraids from the T-beam to the inner shields.

	CD18	*CD35*	*CD41*	*CD42*
$z_2\,(\mu\mathrm{m})$	30(1)	20(1)	29(1)	29(1)
$g_0\,(\mathrm{Hz})$	47.6(4)	189.8(2.9)	180.3(4.4)	98.9(2.4)
$g_{\mathrm{geo}}\,(\mu\Phi_0)$	0.299(3)	0.63(1)	0.38(1)	0.41(1)

Tab. 5.2 Vertical distance z_2, measured coupling strength g_0, and calculated geometric factor g_{geo} for different cooldowns.

the eddy current damper was not installed. Whereas a clear indication of the eigenmode as seen in Fig. 5.16 was missing, the PT could drive the eigenmode of the suspension. With an increase in the cantilever linewidth, the coupling to the system oscillation would increase, which could lead to the observed discrepancy. The additional temperature sensor for *CD41* in Fig. 5.18b) and c) reveals that, especially for low base temperatures, the experiment lags behind, highlighting the importance of sufficient wait times to ensure proper thermalization. Otherwise, we see that the progressive improvements in the overall setup result in an identical mechanical occupation for PT on and off. As we identified in section 4.1.3, the magnetic shielding of our experiment in particular caused the slow thermalization of the can, we attached two additional copperbraids from the T-beam to the shields for cooldown *CD42*. However, for this cooldown we observed an increase of $\bar{n}_{\mathrm{m}}$ towards lower temperatures in Fig. 5.18d), which limits the lowest achievable mode occupation to an effective bath temperature at 150 mK. This behavior might indicate that the magnetic shield reaches – due to an insufficient thermal contact to base – an equilibrium temperature higher than the base temperature. This could be caused by heat radiation off the copper shield connected to the still plate, which remains at $\approx 1\,\mathrm{K}$. By thermally anchoring the T-Beam to the shield, it seems plausible that the whole system including our mechical resonator remains at an elevated temperature. For comparable systems in literature, this thermal bottoming out of mechanical resonators is reported [28, 126]. Nevertheless, the linear temperature dependence above 150 mK still allows for an extraction of the coupling strength.

The extracted coupling strength over the different cooldowns allows us to compare the geometric factor $g_{\mathrm{geo}} = \partial\Phi/\partial z\, z_{\mathrm{zpm}} = g_0/(\partial\omega_{\mathrm{c}}/\partial\Phi)$ (Eq. (2.4)). Therefore, we divide the extracted g_0 by the frequency slope at the bias frequency of the temperature scan obtained from the fluxmaps in Fig. 5.3 (fluxmap for *CD18* not shown here). The results together with the corresponding vertical distance z_2 of the sample configuration are summarized in Tab. 5.2. We find throughout the cooldowns a quite consistent geometrical coupling factor, except for the g_{geo} extracted from cooldown *CD35*. Here, the sample position changed, resulting in a vertical distance of $z_2 = 20(1)\,\mu\mathrm{m}$. With the magnet closer to the SQUID, we would expect a higher geometrical coupling factor, agreeing with the increased g_{geo} for *CD35*. Furthermore, the geometrical factor with $g_{\mathrm{geo}} \approx 0.4\,\mu\Phi_0$ is of the same order of magnitude as calculated for a magnetization of $m_z = 1-5\,\mathrm{nA\,m^2}$ in our simplified model shown in Fig. 3.15a). This value of m_z also aligns with findings of comparable samples in the magnetometer measurements shown in section 4.3.5.

5.2.3 Mechanical frequency shift with flux bias

In addition to the thermally induced changes in the mechanical properties, we observe a change of the cantilever properties depending on the flux bias applied to the SQUID. To investigate this flux dependence, we detect the mechanical mode in Fig. 5.19a) at the same cavity bias frequency over the range of $30\,\Phi_0$ and for different bias frequencies within the lobe around $0\,\Phi_0$ applied flux.

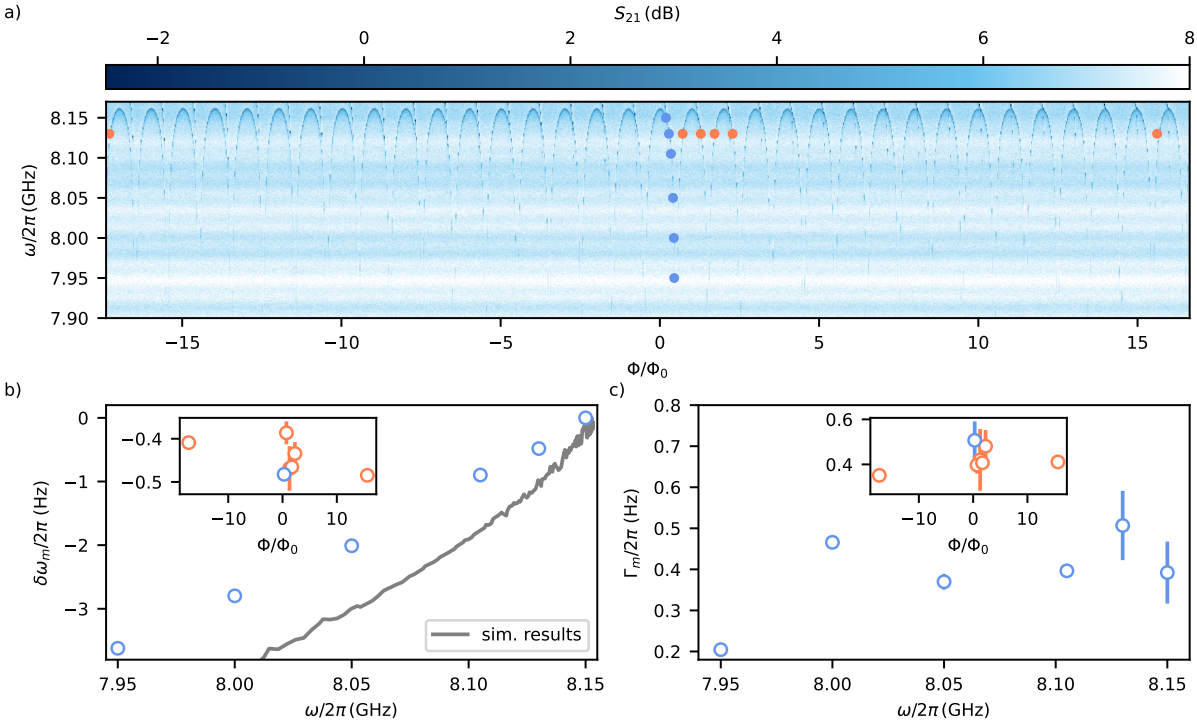

Fig. 5.19 **a)** Fluxmap over several Φ_0 with markers to indicate measurement points to extract the mechanical **b)** frequency and **c)** linewidth. The grey line in **b)** corresponds to the shift obtained using our model. (*CD31*)

As visible in Fig. 5.19b), the mechanical frequency shifts linearly with the cavity frequency, whereas it remains effectively constant over several flux lobes as shown in the inset. For the mechanical linewidth in Fig. 5.19c), no dependency on the applied flux nor cavity frequency can be found. As shown for the simulations in Fig. 3.16, we expect a frequency shift of the mechanics due to the formed screening currents in the SQUID. Since the amplitude of the screening current is directly related to the cavity frequency, the dependence of the mechanical shift on the cavity frequency matches the trend and magnitude predicted by our model. Starting from the bare SQUID parameters extracted from the flux-tuning behavior, we reproduce the tuning characteristics of *CD31* shown in Fig. 5.3. With a distance of $z_2 - z_1 = 26.4\,\mu$m and a magnetic moment of $m_z = 2.4\,\mathrm{nA\,m^2}$, the simulated mechanical frequency shift qualitatively agrees with the experimental data, exhibiting a similar dependence on ω_c and a comparable magnitude. However, as seen for the simulated fluxmaps in Fig. 5.2, the simplification within the model prevent a fully quantitative agreement. As the screening current remains the same at a constant cavity frequency at higher flux lobes, the invariance of the frequency shift over $30\,\Phi_0$ further supports this hypothesis that the frequency shift is caused by the change in the screening currents. However, as the cantilever moves within the magnetic field created by the screening currents, the creation of eddy currents within the cantilever/magnetic particle should lead to an increased damping towards higher loop currents at lower cavity frequencies. Indeed, this behavior was found for another of our samples in [80]. For the sample shown here, the absence of frequency dependence of the linewidth might indicate that the added damping is negligible

compared to other damping mechanisms present.

5.3 Backaction Measurements with a Nonlinear Cavity

In this section, we present the results of the mechanical mode under backaction of our nonlinear SQUID-cavity. Therefore, we start with a short discussion of the data acquisition and treatment. Then, we use the theoretical model introduced in chapter 2.3 to explain the cooling of the mechanical mode at low coupling strength. Subsequently, we increase the coupling to investigate how much additional optical damping we can induce in the mechanics. Lastly, to our knowledge, we demonstrate for the first time backaction cooling beyond bistability of the cavity with good agreement with the theoretical predictions.

5.3.1 Data acquisition and treatment

The original data acquisition and treatment was developed by M. L. Juan and D. Zöpfl for Ref. [3, 4] and was adapted for my publication [5] discussed in section 5.3.4. As the Appendix of [2] provides a thorough explanation, we restrict ourselves here to the key points.

For the data acquisition, we start to match our delay line by setting our digital phase shifter (see Fig. 4.10) to allow for the Gorodetsky calibration discussed in section 4.3.2. A sufficient matching is achieved if the calibration sideband for a maximized modulation amplitude corresponding to $Dev = \omega_{\mathrm{mod}}$ (typically factors $3-10$ higher than the one used in the measurement) resides below the noise floor of the spectrum analyzer with the cavity detuned (leakage check). To avoid the necessity of redoing the matching for each detuning Δ, we keep the drive at a fixed frequency and flux tune the cavity. To achieve the desired detuning, we utilize an autotune routine based on the flux slope extracted from a narrow fluxmap around the drive frequency. As the set detuning is reached, we start one data set consisting of five repeated pairs of measurements: a VNA trace followed by turning on the drive and taking the mechanical spectrum. This is important to correlate the detected mechanical signal to a precise detuning, as the sensitivity to flux noise or frequency drifts increases for the narrow cooling features in the nonlinear backaction regime. After one data set, we reevaluate the detuning and retune if necessary. Repeating this four times results in 20 spectras for one set of detuning. The measurement is then concluded by a leakage check of the calibration with the cavity far detuned.
We begin the data treatment by evaluating the leakage for the set detuning. If the leakage exceeds a threshold, the whole data set for this detuning is discarded. Then, we check for present flux noise during each data set. Therefore, we extract the cavity frequency from the VNA traces. If within one data set, the obtained detunings vary amongst each other more than a set treshhold or are shifted to far from the set detuning, we discard the whole data set. The remaining data is rearranged by applying a k-means binning [127], grouping points with similar detunings. Each of those bins again consists of 20 spectrum traces and is divided into five groups. After removing excess noise peaks, the mechanical signal is fitted with Eq. (2.16) and each data point in the presented cooling traces corresponds to the average of the groups for each bin with the standard error. As we frequency tune the cavity instead of the pump, in a last step we have to renormalize the extracted occupation $\bar{n}_{\mathrm{m}}$ and frequency shift $\delta\omega_{\mathrm{m}}$ for the small difference in g_0 and ω_{m} (sec. 5.2.3). Extracting g_0 from our temperature scans and scaling it correctly with the frequency slope, we fit the mechanical linewidth and frequency shift with our theory model from

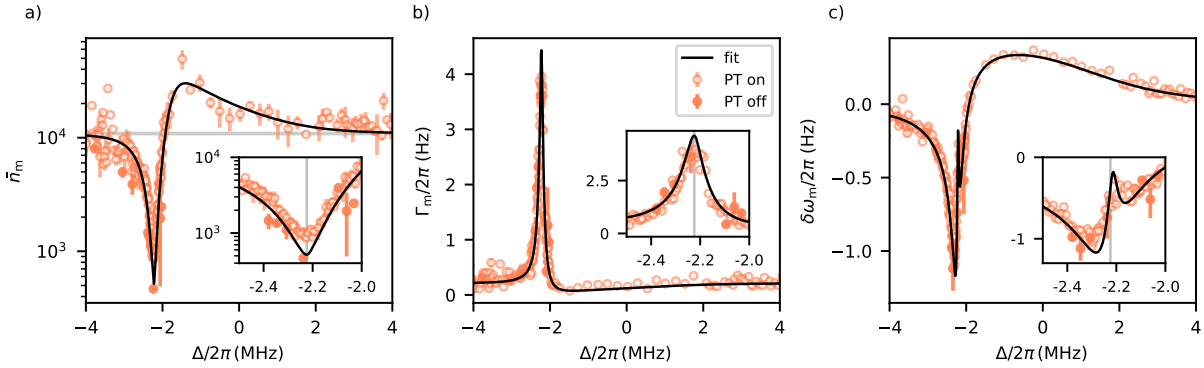

Fig. 5.20 Cooling trace at a bias frequency of $\omega_c/2\pi = 8.0905\,\mathrm{GHz}$ corresponding to $g_0/2\pi = 102.5\,\mathrm{Hz}$ with the suspension setup PT on vs PT off. **a)** mechanical occupation, **b)** mechanical linewidth, **c)** mechanical frequency. Insets highlight the frequency range of best cooling (grey line). The fit yields $\mathcal{K}/2\pi = 15.0(2)\,\mathrm{kHz}$ and $\bar{n}_{\mathrm{in}}/\bar{n}_{\mathrm{in,bi}} = 0.936(4)$ (*CD41*).

chapter 2.3 to extract the input photon number rate $\bar{n}_{\mathrm{in}}/\bar{n}_{\mathrm{in,bi}}$ and the $\mathcal{K}$ nonlinearity, which turned out to be the most robust fitting option.

5.3.2 Nonlinear Backaction at low and intermediate g_0

Fig. 5.20 shows a cooling trace taken at a low $g_0/2\pi = 102.5\,\mathrm{Hz}$ and an input power close to the onset of bistability. For the data presented, we took advantage of the enhanced data acquisition rate due to the implementation of the suspension setup, enabling us to measure with the PT running. For comparison, a few data points were taken with the PT off. As we see, the vibrations of the PT lead to a slightly elevated mode occupation $\bar{n}_{\mathrm{m}}$ around the detuning corresponding to best cooling. As we cool the mechanical mode from its thermal occupation of $\bar{n}_{\mathrm{m}} \approx 10^4$ down to $\bar{n}_{\mathrm{m}} \approx 500$ PT off, any excess population of the mechanical mode due to residual PT noise becomes visible. By comparing to the PT off results at best cooling, we can estimate this excess population to around $\bar{n}_{\mathrm{m,noise}} \approx 500$. With $\bar{n}_{\mathrm{m,noise}}$ being an order of magnitude lower than the thermal occupation, the difference between PT on and off within the temperature scan in Fig. 5.18b/c) could not be resolved, where we found reasonable agreement within the given uncertainties for both cases.
However, even at such high input power associated with a significant narrowing down of the cooling feature and thus increased sensitivity to flux noise, we see that neither linewidth Γ_{m} nor frequency shift $\delta\omega_{\mathrm{m}}$ is influenced by the PT state. From the absence of a PT related bottoming out in Γ_{m} and $\delta\omega_{\mathrm{m}}$ as reported for backaction measurment with the rigidly connected setup [2], we can conclude that cooling efficiency is not significantly affected by the PT noise at these coupling strengths for the suspended setup. However, we still observe some influence of the PT reflected in the increased phonon occupation.

Fitting our nonlinear cooling model to the extracted Γ_{m} and $\delta\omega_{\mathrm{m}}$ PT on data yields a $\mathcal{K}/2\pi = 15.0(2)\,\mathrm{kHz}$ and $\bar{n}_{\mathrm{in}}/\bar{n}_{\mathrm{in,bi}} = 0.936(4)$. The obtained $\mathcal{K}$ is in good agreement with the results obtained by fitting the cavity response of $\mathcal{K}/2\pi = 12(3)\,\mathrm{kHz}$ at a similar flux bias point in *CD42* shown in Fig. 5.5. We see that the fit curve captures well the best cooling for the PT off measurement, which further supports our statement of the PT induced excess occupation. Furthermore, this close to the onset of bistability, we see in the data that maximal $\delta\omega_{\mathrm{m}}$ deviates

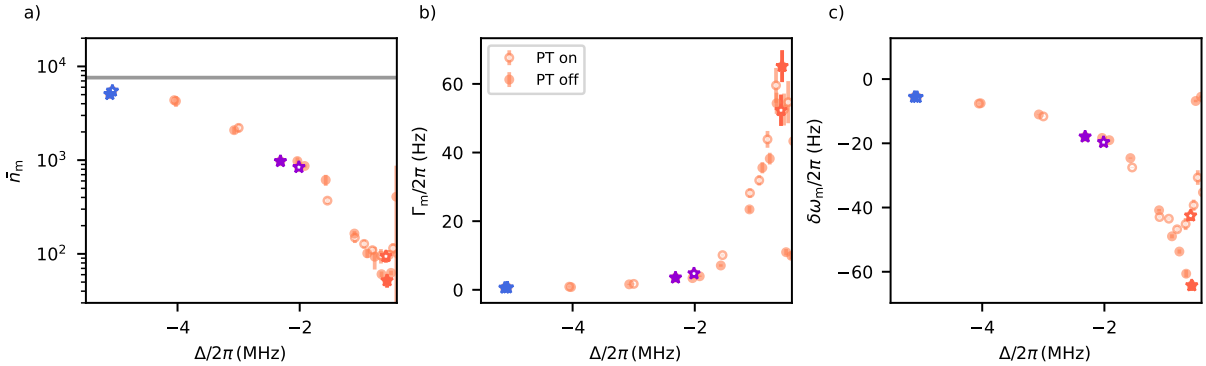

Fig. 5.21 Cooling trace at a bias frequency of $\omega_c/2\pi = 7.915\,\mathrm{GHz}$ corresponding to $g_0/2\pi = 850\,\mathrm{Hz}$ with the suspension setup PT on vs PT off. **a)** mechanical occupation, **b)** mechanical linewidth, **c)** mechanical frequency. As we operate the system below the Kerr-anomaly, a fit with the theoretical model is not possible. For the higlighted detunings (stars) the corresponding spectra are shown in Fig. 5.22. (*CD32*)

from the best cooling in Γ_m and $\bar{n}_m$ as highlighted by the grey line in the inset of Fig. 5.20. As discussed in the theory section 2.3, this effective resemblance to the resolved case is expected to arise due to the nonlinearity of our cavity. However, due to vibrational noise in the system, such a clear experimental verification was not possible before the implementation of the vibration isolation.

To investigate the overall achievable cooling on the mechanical mode with the suspension setup, we take a cooling trace at an intermediate coupling strength of $g_0/2\pi = 850\,\mathrm{Hz}$. The input power is set to the equivalent of the VNA power needed to reach bistability in the cavity response. In Fig. 5.21, the resulting cooling trace is presented. Due to the additional complexity of the Kerr anomaly below a cavity frequency of $\omega_c/2\pi = 8.04\,\mathrm{GHz}$, a fit to the data with the theory model is not possible at these coupling strengths. A clear indication of the presence of the Kerr anomaly is that we find best cooling close to $\Delta/2\pi \approx 0\,\mathrm{MHz}$, whereas for the lower g_0 measurement in Fig. 5.20 best cooling is found at $\Delta/2\pi = -2\,\mathrm{MHz}$. Overall, we achieve a minimal phonon occupation of ~ 50 for PT off and a slightly elevated occupation of ~ 90 PT on, which corresponds to a reduction of 160 and 90 in the occupation starting from $\bar{n}_{m,th}(100\,\mathrm{mK}) \approx 8000$, respectively. The same factor as found for the occupation PT off is obtained for the optomechanical induced damping for both PT states, increasing the linewidth from $\Gamma_m/2\pi = 0.4\,\mathrm{Hz}$ to $\Gamma_m/2\pi = 65\,\mathrm{Hz}$. However, in comparison to the PT off data, the observed frequency shift $\delta\omega_m$ PT on bottoms out towards $\Delta/2\pi = 0\,\mathrm{MHz}$. This observed trend for the PT on data suggests that residual noise washes out the cavity response, causing a decrease in the cooling capability at the chosen coupling strength and this initial iteration of the suspension setup (*CD32*).
This is further supported by looking at the spectra displayed in Fig. 5.22 for the highlighted detunings. To properly visualize the reduced mode occupation via the measured spectra, we have to rescale the measured intensity spectrum S_{II} to its position spectral density S_{zz} using the Gorodetsky calibration (sec. 4.3.2). As we tune the drive towards the cavity, we observe for a constant deviation of the frequency modulation an increase of the calibration tone height $S_{II}(\omega = \omega_{mod})$. As we use $S_{II}(\omega = \omega_{mod})$ to calibrate our system, an increase in its height directly corresponds to a higher detection efficiency in S_{zz} of our system. Since this arises directly from

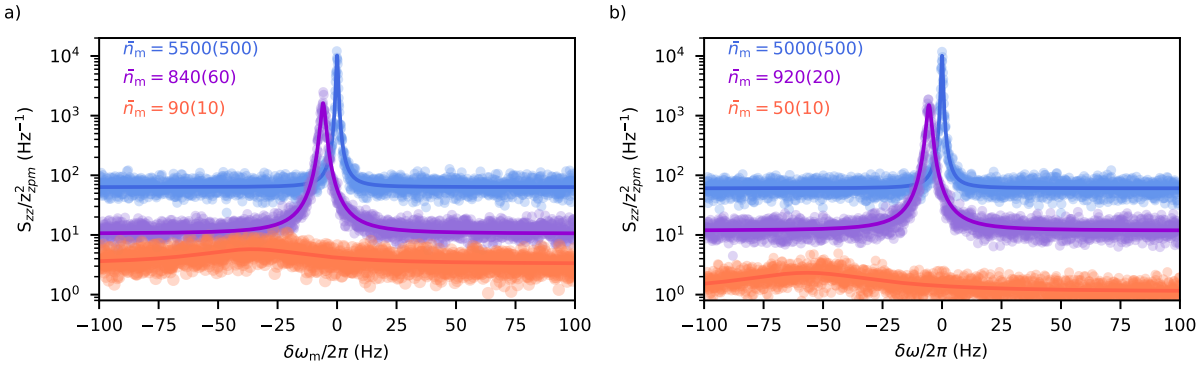

Fig. 5.22 Mechanical spectra for the highlighted detuning in Fig. 5.21 **a)** PT on and **b)** PT off. With the use of the Gorodetsky calibration (sec. 4.3.2), we rescale the measured spectrum $S_{II} \rightarrow S_{zz}$. It is worth noting that the offset at different detunings is not artificial, but rather arises directly from our detection efficiency, which is enhanced by the nonlinearity. Solid lines are fits according to Eq. (2.16). (*CD32*)

the enhanced transduction of the cavity response (i.e. a steep slope in amplitude and phase), the skewed cavity response due to its nonlinearity provides an additional boost to the detection efficiency. Thus, with the nonlinear mode shape, the effective detection noise-floor decreases as it is visible for the spectra shown in Fig. 5.22. Whereas we observe qualitatively comparable spectra for none and intermediate cooling regardless of the PT state, at strong cooling, the higher observed background level PT on is evidence for a reduced detection efficiency. This is typically an indication of noise causing frequency fluctuations that wash out the steep response of the nonlinear cavity. This corresponds to a decrease in the cooling capability PT on as observed in Fig. 5.21.

5.3.3 Nonlinear Backaction at high g_0

To investigate the cooling behavior at high coupling strength, we tune the bias frequency of our cavity to $\omega_c/2\pi = 7.76\,\mathrm{GHz}$, which corresponds to a $g_0/2\pi = 3.52\,\mathrm{kHz}$. Similar to before, the drive power is set to the VNA power required to reach bistability in the cavity response. The resulting cooling trace is depicted in Fig. 5.23. Furthermore, for the detuning associated with best cooling, we additionally take measurements with the PT off. However, for these points, an extraction of the mode occupation via a fit to the spectra is not possible as shown for two spectra in Fig. 5.24. Rather than a single peak, the mechanical signature splits into three distinct yet weak signals at those detunings. Interestingly, two peaks appear at $\delta\omega_m < 0$ associated with strong and intermediate cooling, whereas the third one is found at $\delta\omega_m > 0$ assigned to heating of the mechanics. To extract the corresponding phonon numbers displayed in Fig. 5.23, we rescale the spectra with the Gorodetsky method and rely on a manual integration over the whole range yielding a mechanical occupation of $\bar{n}_m = 37$ and $\bar{n}_m = 24$ for the spectra displayed in Fig. 5.24.

It is not yet clear why three peaks are observed instead of a single one, unlike the measurements at intermediate g_0 in Fig. 5.22. Nevertheless, a possible explanation could be the slow frequency shift δf discussed in section 5.1.5. As we observed, this frequency shift not only scales in amplitude with drive power but also flux sensitivity and thus g_0. Measuring on the right

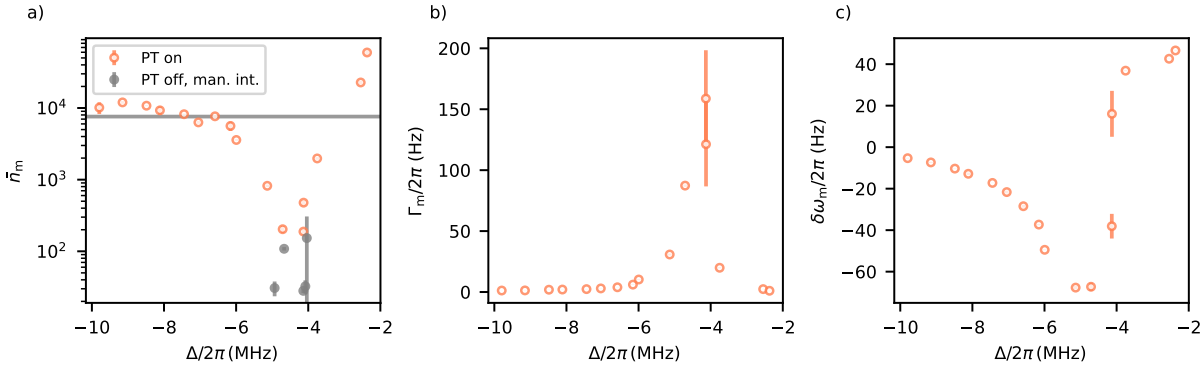

Fig. 5.23 Cooling trace at a bias frequency of $\omega_c/2\pi = 7.75\,\mathrm{GHz}$ corresponding to $g_0/2\pi = 3.52\,\mathrm{kHz}$ with the suspension setup. **a)** mechanical occupation PT on by fitting and PT off by manual integration of the spectra, **b)** mechanical linewidth, **c)** mechanical frequency. As we operate the system below the Kerr-anomaly, a fit with the theoretical model is not possible. (*CD50*)

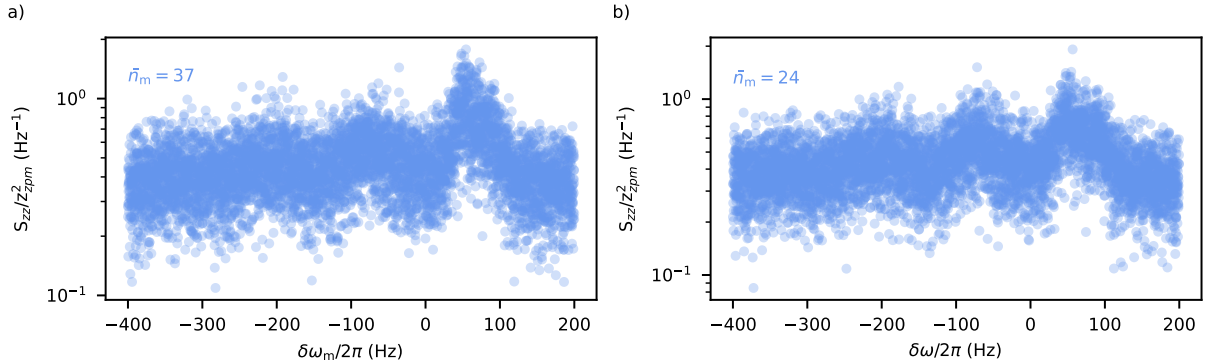

Fig. 5.24 Spectra PT off at a bias frequency of $\omega_c/2\pi = 7.75\,\mathrm{GHz}$ corresponding to $g_0/2\pi = 3.52\,\mathrm{kHz}$ for the cooling trace shown in Fig. 5.23. The mechanical occupation of $\bar{n}_m = 37$ and $\bar{n}_m = 24$ is extraced using manual integration. (*CD50*)

fluxmap side in combination with the large g_0 and a strong input power close to bistability, δf might lead to sustained oscillations of the cavity. This is especially relevant close to the detuning associated with optimal cooling, where we expect the steepest change in photon number with detuning. Thus, during the acquisition time of the mechanical signal, the effective detuning might oscillate between strong cooling and heating. However, before bifurcation of the cavity, the back-action would change gradually during the data acquisition resulting in a single yet asymmetric mechanical peak as discussed in [2, 4]. Although, if the input power actually exceeds the bistable cavity input power, the cavity would abruptly switch between the two photon number branches as shown in Fig. 5.10, leading to cooling or heating. This state switching – instead of a gradual changing detuning during the data acquisition – would lead to the appearance of distinguishable peaks in the spectrum as seen in Fig. 5.24. Any presence of flux noise and the frequency modulation of the drive tone needed for the calibration routine would further amplify this effect.

To decrease the influence of δf, we slightly reduce the drive power to avoid a state switching of the cavity and turn the frequency modulation off. On one hand, this allows us to frequency

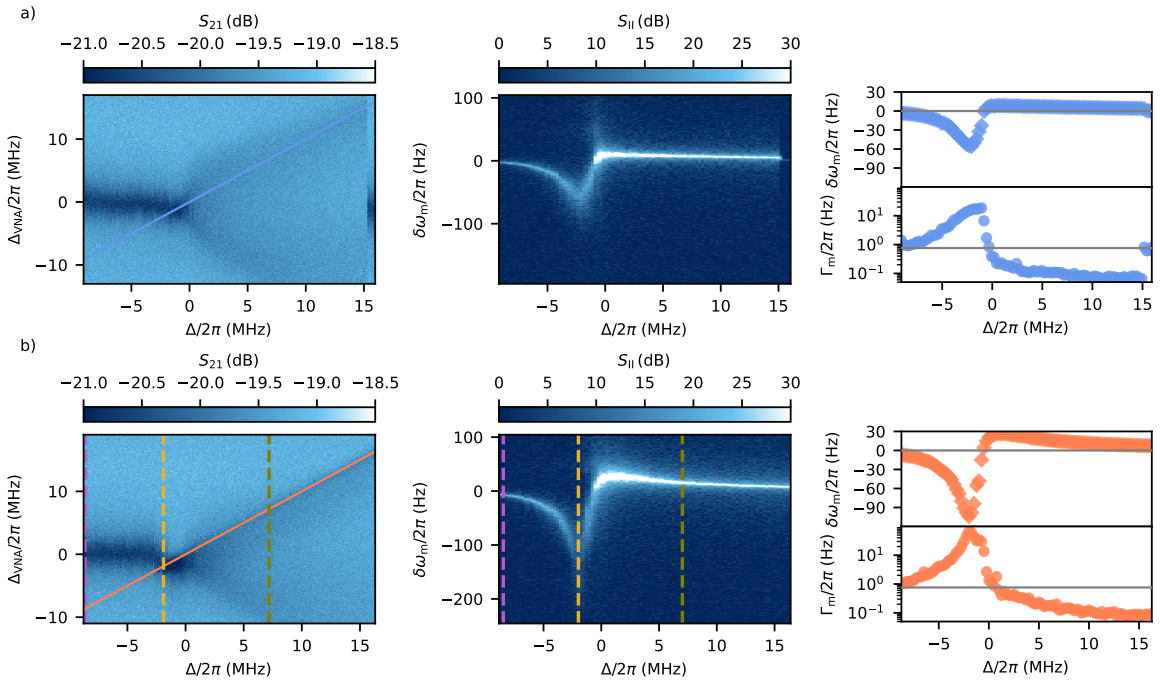

Fig. 5.25 Cooling trace at a bias frequency of $\omega_c/2\pi = 7.75\,\mathrm{GHz}$ corresponding to $g_0/2\pi = 3.52\,\mathrm{kHz}$. Instead of the cavity, we frequency tune the drive, while keeping it turned on for the whole measurement. For each drive frequency, we take a weak VNA scan of the cavity, and every third VNA measurement five spectra. VNA measurement with the drive frequency (solid line), mechanical spectra, and extracted mechanical frequency shift and linewidth for a drive power **a)** 5 dB and **b)** 2 dB less than the VNA power needed to reach bistability. Slices marked with the dashed lines are displayed seperately in Fig. 5.26. (*CD50*)

tune our drive instead of the cavity, as we do not require matching the delay line for a proper calibration as mentioned in section 5.3.1. On the other hand, without calibration, a precise determination of the mode occupation is no longer possible. However, we can use the broadening of the mechanical linewidth Γ_m to estimate an upper and lower limit for $\bar{n}_m$ at negative detunings. Therefore, we use Eq. (2.41) and overestimate the Stokes process Γ_S for cooling by calculating its value on resonance of the Kerr-shifted cavity at a detuning $\Delta = -\bar{n}_c\mathcal{K}$. For this detuning, Γ_S and the intracavity photon number $\bar{n}_c$ are given by

$$\Gamma_S(\Delta = -\bar{n}_c\mathcal{K}) = g_0^2\bar{n}_c\kappa_l\frac{\omega_m^2 + \kappa_l^2/4}{(\omega_m^2 + \kappa_l^2/4)^2 + \kappa_l^2\omega_m^2} \tag{5.1}$$

$$\bar{n}_c(\Delta = -\bar{n}_c\mathcal{K}) = \frac{4}{2}\frac{\kappa_c}{\kappa_l^2}2\pi\frac{P_g}{\hbar\omega_c} \tag{5.2}$$

neither of which is dependent on $\mathcal{K}$. For a lower limit, we neglect the unwanted backaction heating of the cavity completely, which results in the bounds for $\bar{n}_m$ as

$$\bar{n}_{th}\frac{\Gamma_{m,0}}{\Gamma_m} \leq \bar{n}_m \leq \bar{n}_{th}\frac{\Gamma_{m,0}}{\Gamma_m} + \frac{\Gamma_S(\Delta = -\bar{n}_c\mathcal{K})}{\Gamma_m}, \tag{5.3}$$

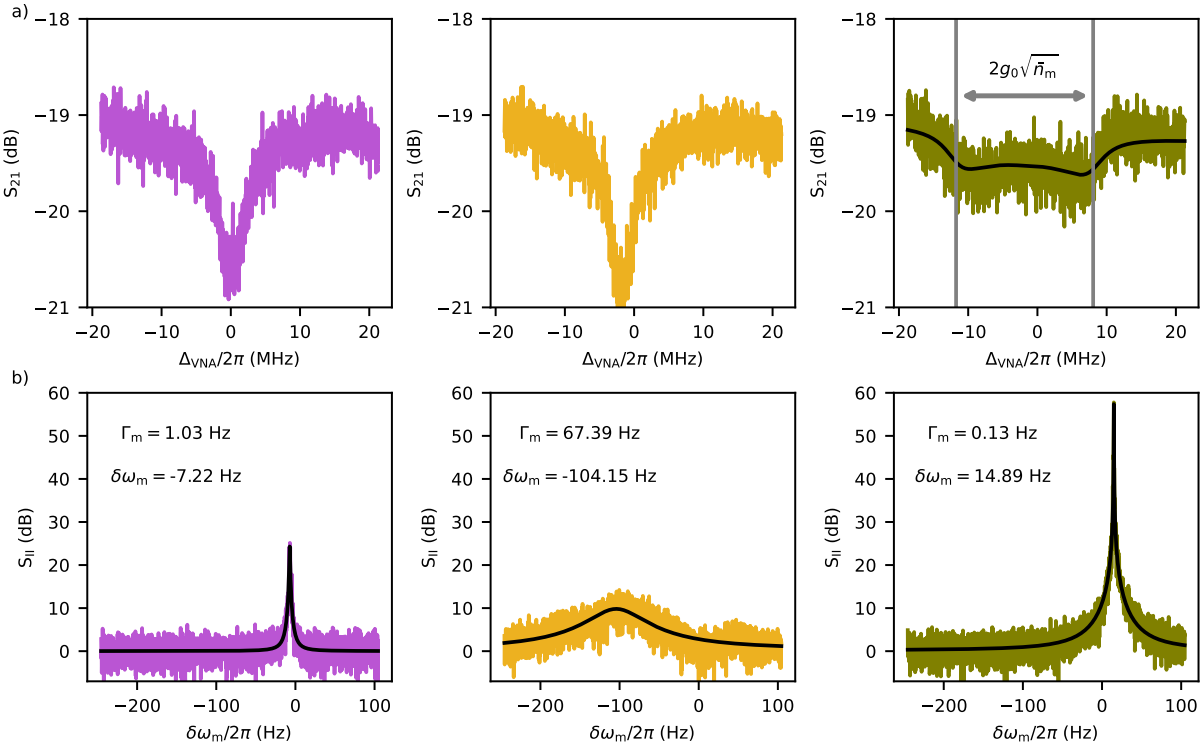

Fig. 5.26 Linecuts of **a)** the VNA and **b)** spectra measured in Fig. 5.25b). The solid line for the olive-colored VNA trace represents a model including the optomechanically induced frequency shift. For the spectra, solid lines are fits according Eq. (2.16). (*CD50*)

with $\Gamma_{m,0}$ the natural mechanical linewidth and $\bar{n}_{th}$ the thermal mode occupation. These limits will be used to estimate the final phonon occupation $\bar{n}_m$ in the following.

The resulting cooling traces for a drive power 5 dB and 2 dB less than the equivalent VNA power needed to reach bistability are displayed in Fig. 5.25a) and b), respectively. To ensure that the cavity remains at in a steady state due to the frequecy shift δf, we keep the drive on during the whole measurement and gradually tune it through the cavity. At each detuning, a weak VNA scan of the cavity is performed. Every third scan is accompanied by the acquisition of five spectra, whose average is fitted to extract the mechanical frequency shift and linewidth. For both input powers, the cavity response initially remains unaffected for the drive far detuned, with a steadily increasing effect on the mechanical properties due to the induced backaction. As the drive approaches the cavity resonance, we observe a sudden frequency change of the cavity response, which is caused by its Kerr-nonlinearity in combination with δf. This aligns with the largest induced optomechanical damping on the mechanics. As we start to heat the mechanical mode – indicated by the increase in signal intensity in the spectra – the cavity response significantly broadens and becomes shallow. Following the drive, the cavity continues to broaden until it snaps back to its undriven state for large drive detunings, accompanied by the mechanics returning to its backaction-free signature (see Fig. 5.25a) at $\Delta/2\pi \approx 15$ MHz).

Fig. 5.26 shows linecuts of the measurements in Fig. 5.25b) for the three highlighted de-

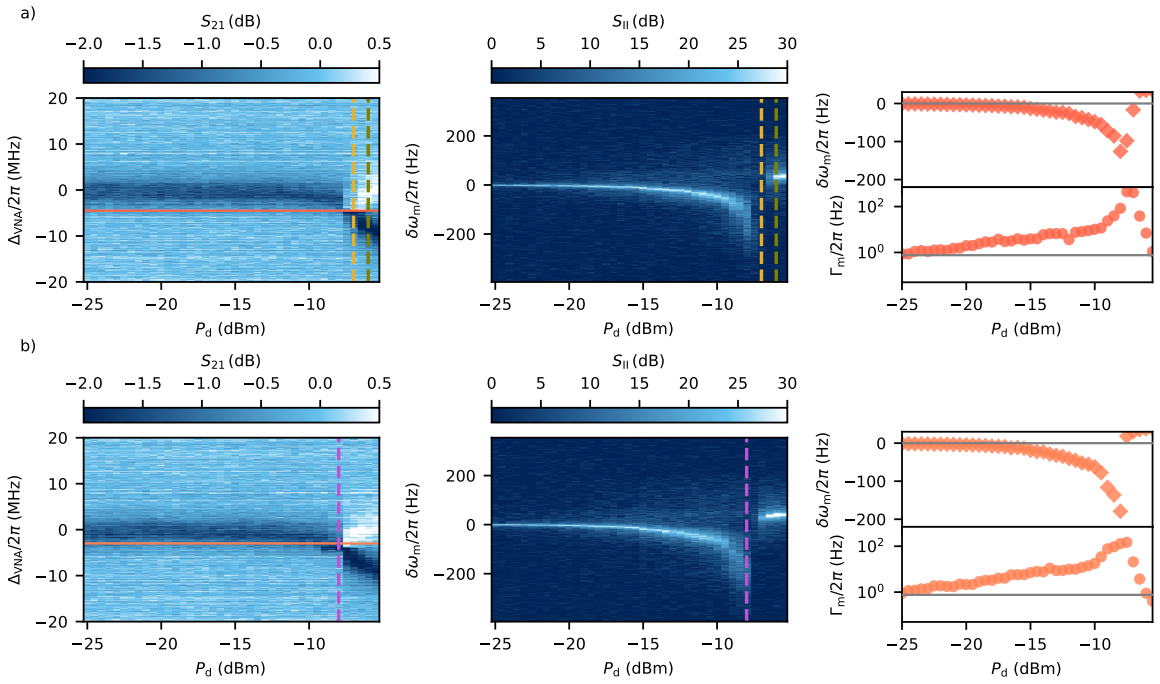

Fig. 5.27 Cooling trace at a bias frequency of $\omega_c/2\pi = 7.75\,\mathrm{GHz}$ corresponding to $g_0/2\pi = 3.52\,\mathrm{kHz}$. During the measurement, the drive remains on while the drive power is continuously increased. At each power, we take a weak VNA scan of the cavity and five spectra. VNA measurement with the drive frequency (solid line), mechanical spectra, and extracted mechanical frequency shift and linewidth for a detuning of the drive of **a)** $\Delta/2\pi = 4.5\,\mathrm{MHz}$ and **b)** $\Delta/2\pi = 4.0\,\mathrm{MHz}$. Slices marked with the dashed lines are displayed seperately in Fig. 5.28. (*CD50*)

tunings. Already at a detuning of $\Delta = 10\,\mathrm{MHz}$, we acquire a strong mechanical signal already indicating a small effect of backaction as seen by $\delta\omega_\mathrm{m} < 0$. Even with the reduced power and without the frequency modulation of the drive, for the detuning corresponding to best cooling we can see the appearance of weak second peak next to a highly damped mechanical mode. However, relative to the signal in Fig. 5.24, the feature appears less pronounced, as indicated by its smaller amplitude compared to the main peak. The observed broadening of the cavity response, as soon as we start to heat the mechanical mode, can be understood as a resonant driving of the mechanics. With the drive kept on while varying the detuning, the increased mechanical occupation induces an oscillation of the cavity resonance at the mechanical frequency, with amplitude proportional to $2g_0\sqrt{\bar{n}_\mathrm{m}}$. As the mechanical mode does not ring down during one oscillation, this frequency shift of the cavity is sufficient to pull the cavity back into the drive, which resonantly heats the mechanical mode. This broadening in the cavity response continues towards larger drive detunings as long as the mechanical occupation increases and breaks down when the occupation saturates, which depends on the applied power. Therefore, the broadening for the higher drive power is obtained over a larger range of detunings. As a consequence, we can use the cavity broadening to roughly extract the mode occupation. To model this, we sinusoidally modulate the cavity resonance frequency with an amplitude $2g_0\sqrt{\bar{n}_\mathrm{m}}$ and average over one period. The resulting cavity response assuming this model can be seen for

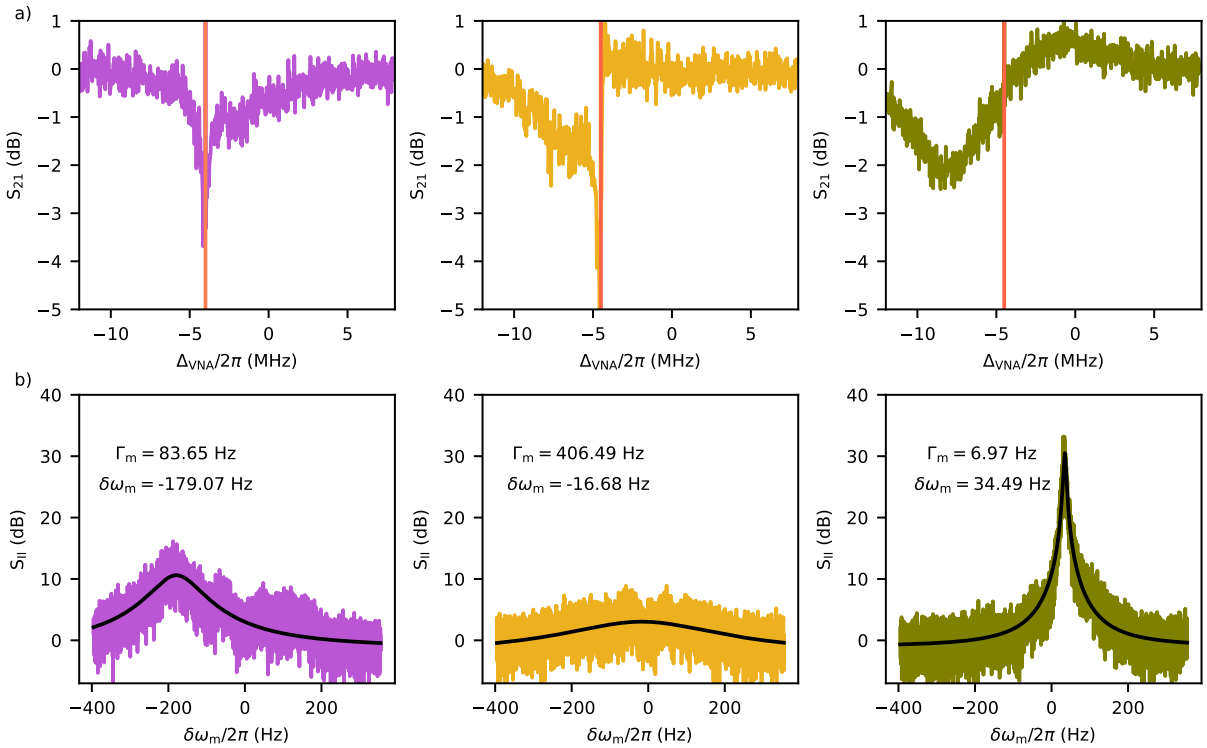

Fig. 5.28 Linecuts of **a)** the VNA and **b)** spectra measured in Fig. 5.27. The colored vertical lines in the VNA measurements represent the drive detuning for the corresponding cooling trace. For the spectra, solid lines are fits according to Eq. (2.16). (*CD50*)

the heating trace in Fig. 5.26c) corresponding to a mode occupation of $\bar{n}_m \approx 8 \cdot 10^6$.

Instead of sweeping the detuning of the drive, we choose a range of fixed detuning associated with good cooling, judging from Fig. 5.23, and continuously increase the drive power. Two of the obtained cooling traces at a drive detuning of $\Delta/2\pi = -4.5\,\mathrm{MHz}$ and $\Delta/2\pi = -4.0\,\mathrm{MHz}$ are shown in Fig. 5.27. With increasing drive power, the backaction on the mechanics steadily grows, as visible from the measured spectra. Initially, the drive induces a gradual shift of the cavity resonance frequency as it starts to populate the cavity. This is followed by a sudden jump of the cavity accompanied by an increased depth of the cavity response, which aligns with the largest broadening of the mechanical linewidth. For even higher power, the cavity signal starts to develop a double feature – a dip followed by a peak – called a signal and idler typically observed for strongly driving Kerr-cavities [49, 128]. The appearance of this additional mode by weakly scanning the cavity response in the presence of a strong drive is attributed to parametric amplification and degenerate four-wave mixing [49]. To provide a more detailed view, linecuts for the highlighted powers in Fig. 5.27 are shown in Fig. 5.28. For both detunings at the drive power associated with best cooling, the VNA traces clearly show a very narrow and deep dip around the drive tone. The appearance of such an effective resonance with a reduced linewidth was observed for a similar setup in [49]. Here, the reduction in linewidth was attributed to an internal feedback-loop canceling flux noise due to a Kerr shift in combination with a power saturation of TLS due to the presence of the strong pump. As mentioned in sec.

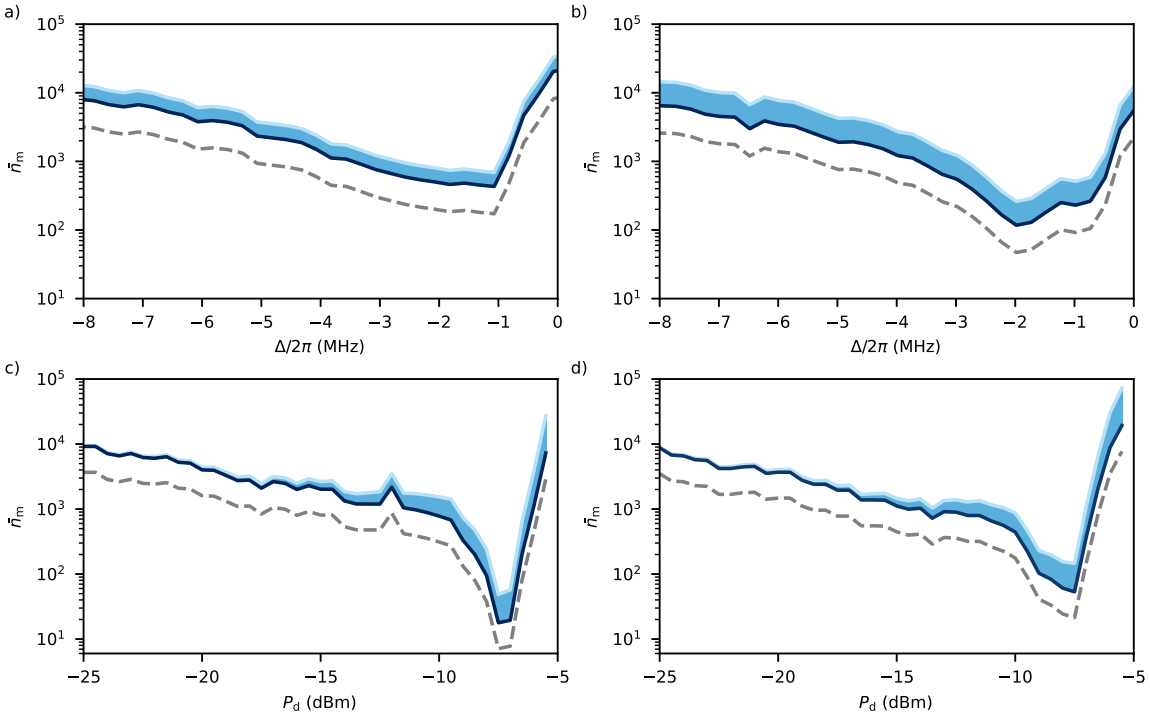

Fig. 5.29 Lower and upper cooling limits calculated from the extracted mechanical linewidth Γ_m using Eq. (5.3) for the mechanical mode thermalized to a base temperature of 100 mK. The dashed line represents the lower limit for a base temperature of 40 mK. Corresponding cooling traces: Tuning the drive frequency at constant power **a)** 5 dB ($P_d = -12$ dBm) and **b)** 2 dB ($P_d = -9$ dBm)) less than the VNA power needed to reach bistability in Fig. 5.25. For increasing the drive power at constant detuning **c)** $\Delta/2\pi = -4.5$ MHz and **d)** $\Delta/2\pi = -4.0$ MHz in Fig. 5.27.

5.1.5, the additional frequency shift δf in our system on the right side of the fluxmap could also lead to a similar stabilization of the cavity frequency. However, as observed at higher powers with the appearance of a broad signal and idler resonance, heating of the mechanical mode and state swapping beyond bistability due to δf degrade this stabilization effect for too high input powers. As for the frequency tuning of the drive, without the modulation of the drive tone the obtained mechanical spectra appear cleaner with a maximum linewidth of the mechanics of $\Gamma_m/2\pi \approx 406$ Hz corresponding to a 500 fold increase of its natural linewidth of $\Gamma_{m,0}/2\pi = 0.8$ Hz.

To summarize the measurements at high $g_0/2\pi = 3.52$ kHz, we use the obtained linewidths from the cooling traces shown in Fig. 5.25 and Fig. 5.27 to estimate the resulting mechanical mode occupation using Eq. (5.3). We see that, due to the conservative choice of input power for tuning the drive frequency, the overall achievable cooling is reduced compared to measurements where the drive power is increased at constant detuning. Nevertheless, upon comparison, the different measurements yield matching results at the corresponding points of same frequency and same power. Together with the fact that the cooling obtained for the method with proper calibration in Fig. 5.23 falls slightly above the lower bound displayed in Fig. 5.29c), this is a

good verification of this method to estimate $\bar{n}_{\mathrm{m}}$.

The lowest mode occupation reached within this system before the suspension setup was $\bar{n}_{\mathrm{m}} = 14$ in [4], which is close to the values obtained in this chapter. However, one has to emphasize that this low occupation was obtained at a base temperature of 40 mK. The expected limit corresponding to this lower base temperature is depicted as the grey dashed line in Fig. 5.29. This new lower bound would indicate that the suspension setup might enable us to cool below a mode occupation of $\bar{n}_{\mathrm{m}} \leq 10$. Nevertheless, the direct comparison of the results presented here and in [4] - even though measured on the same sample - should be regarded with some caution, as repositioning of the cantilver with repeated cooldowns resulted in slightly changed system parameters as discussed in chapter 5.1 and 5.2.

5.3.4 Nonlinear Backaction in the bistable regime

For the results discussed so far, we restricted the drive power to be below the critical input power of the cavity $\bar{n}_{\mathrm{in,bi}}$ (Eq. (4.11). Within this section, we will discuss the backaction on the mechanics obtained for input powers exceeding $\bar{n}_{\mathrm{in,bi}}$, based on my publication in [5].

To measure backaction on the mechanics beyond the bistability of the cavity, it is crucial that we can distinguish the different cavity states - the low and high photon number branches. It is therefore necessary to adapt the acquisition and data treatment introduced in Section 5.3.1. Instead of directly turning on the drive at a set detuning Δ, we slowly sweep the drive towards the desired Δ to ensure a steady state of the cavity. By using a frequency up/down sweep, we can select the low/high photon number branch beyond the bifurcation of the cavity, respectively. Furthermore, we implement a fast VNA measurement triggered by turning off the drive to track the influence of δf on the cavity frequency during the acquisition time of the spectrum. Due to the discussed properties of δf in section 5.1.5, we utilize δf on the left side of the flux map to determine the cavity state during the measurement to avoid data points containing a switching event.

Fig. 5.30a-c) shows a cooling trace at moderate drive powers and a coupling strength of $g_0/2\pi = (99 \pm 1)\,\mathrm{Hz}$ to minimize the influence of flux noise. Fitting the data with the derived theory in chapter 2.1.1, we observe good agreement with the experimental results. The fit yields an input photon number of $\bar{n}_{\mathrm{in}}/\bar{n}_{\mathrm{in,bi}} = (0.54 \pm 0.02)$ and a Kerr constant of $\mathcal{K}/2\pi = (14 \pm 1)\,\mathrm{kHz}$, which is in good agreement with the results from fitting the cavity response shown in Fig. 5.5. The displayed thermal phonon number (grey line) corresponds to an extracted effective bath temperature of $T_{\mathrm{eff}} = 267\,\mathrm{mK}$ even though we set the base temperature of the fridge to 100 mK. This is a consequence of the bottoming out of the mode occupation below a base temperature of 250 mK shown in Fig. 5.18d).

Cooling traces for increased input powers corresponding to $\bar{n}_{\mathrm{in}}/\bar{n}_{\mathrm{in,bi}} = 1.9$ and $\bar{n}_{\mathrm{in}}/\bar{n}_{\mathrm{in,bi}} = 3.0$ are shown in Fig. 5.30d-f) and i-g), respectively. For the different input powers, over a detuning range of $\sim 0.4\,\mathrm{MHz}$ and $\sim 2\,\mathrm{MHz}$, we observe two distinct backaction curves of the mechanics depending on the selected branch. The solid lines in the plots depict the theoretical prediction extrapolated from the parameters obtained from the fit in Fig. 5.30a-c). Even though we increased the input power by a factor of ~ 4 and ~ 6, resulting in a cavity well beyond the bifurcation point, the prediction accurately describes the data for the two different branches.

In both cases, the backaction in the low photon number branch exhibits a narrow cooling feature up to the point at which the cavity switches to the high photon number branch, having reached the end of the bifurcation region. Upon switching, the cavity resides in the high photon

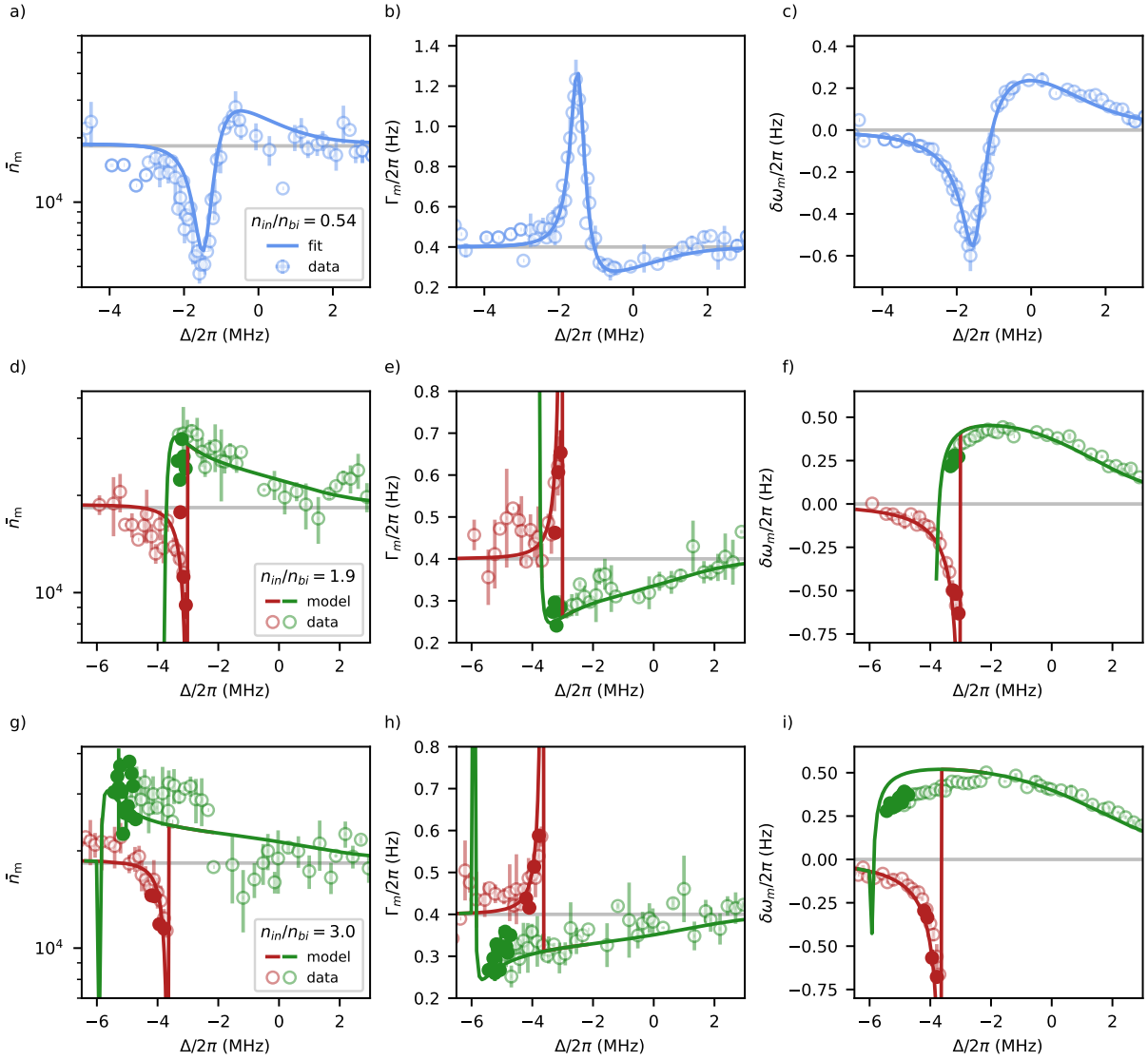

Fig. 5.30 Cooling traces at $g_0/2\pi = 99\,\mathrm{Hz}$. **a)** Phonon number $\bar{n}_\mathrm{m}$, **b)** linewidth $\Gamma_\mathrm{m}/2\pi$ and **c)** frequency shift $\delta\omega_\mathrm{m}/2\pi$ for intermediate powers $\bar{n}_\mathrm{in}/\bar{n}_\mathrm{in,bi} = 0.5$. Grey lines display a steady state at an effective bath temperature $T_\mathrm{eff} = 267\,\mathrm{mK}$. Phonon number $\bar{n}_\mathrm{m}$, linewidth $\Gamma_\mathrm{m}/2\pi$ and frequency shift $\delta\omega_\mathrm{m}/2\pi$ for higher powers of $\bar{n}_\mathrm{in}/\bar{n}_\mathrm{in,bi} = 1.9$ in **d-f)** and $\bar{n}_\mathrm{in}/\bar{n}_\mathrm{in,bi} = 3.0$ in **g-i)**, respectively. Data and theoretical extrapolation from $\bar{n}_\mathrm{in}/\bar{n}_\mathrm{in,bi} = 0.5$ in red for the low and green for the high photon number branch. Filled circles correspond to data taken with the pulsetube of the cryostat turned off to further reduce vibrations in the system. *(CD42)*

number branch, where the photon number spectrum of the cavity results in backaction heating. The obtained experimental data agrees well with the predictions, and the detuning at which branch switching is observed matches the theory.

In the high photon number branch, we observe heating over a wide range of detunings before the cavity state switches. The very narrow cooling feature in this branch remains experimentally inaccessible. This is due to constant heating of the mechanical mode, leading to a highly excited state as we tune the probe tone slowly in from the blue side to ensure staying in the high photon number branch. The corresponding large motional amplitude of the mechanical mode leads to fluctuations of ω_c, which results in the cavity switching branches before reaching the cooling feature in the high photon number branch.

In summary, the obtained experimental results demonstrate that our system can be reliably operated even beyond the cavity bifurcation, thereby extending previous observations of backaction cooling in nonlinear systems [4]. Due to the control over the selected branches – taking advantage of the frequency shift δf – in this regime we achieved good agreement with the underlying theory. Extrapolating the fit results over a factor 6 in input power we can precisely predict the obtained cooling behavior demonstrating a good understanding of processes at hand. However, remaining system noise limits the achievable cooling as it prevents us from accessing the narrow frequency range in which best cooling is expected. Nevertheless, the presented results show that state manipulation in optomechanical systems should not be restricted only to the linear regime. Harnessing system nonlinearities may offer novel mechanisms and operating modes to be explored, particularly for optomechanical systems in the unresolved sideband regime.

CHAPTER 6

System Outlook

The results presented in the previous chapter demonstrate that the implementation of vibration isolation significantly improved the system's stability, enabling continuous cooling of the mechanical mode during steady cryostat operation. Despite the increased cooling capability due to the intrinsic nonlinearity of the cavity, as experimentally shown in section 5.3.3, the theoretical cooling limit discussed in section 2.3.3 prevents the system from reaching the mechanical ground state. This limitation remains as long as our system resides in the unresolved sideband regime.

In order to push beyond this boundary, alternative approaches must be considered. In this chapter, we present one such strategy, based on hybridizing our optomechanical system with an auxiliary high quality cavity as proposed in Ref. [6]. We begin with a brief theoretical introduction, building on the framework developed in Chapter 2, and present a proof of principle measurement. This is followed by a discussion of a refined setup concept based on a post 3D-cavity [129, 130], together with corresponding simulations, design choices, and characterization measurements. The chapter concludes with an outlook on the next steps using this method to reach the motional ground state of our mechanical resonator.

6.1 Optomechanical System with an Auxiliary Cavity

In optomechanical systems operating in the unresolved sideband regime, radiation-pressure backaction on the mechanical resonator prevents cooling to the ground state. To overcome this limitation with the current setup, consisting of a SQUID-cavity inductively coupled to a mechanical cantilever, we propose to harness the coupling of the optomechanical cavity to an auxiliary cavity with a high intrinsic quality factor. With the hybridzation of the photonic modes, ground state cooling might be realized along two distinct ways. First, the hybridization leads to an indirect coupling of the high-Q mode to the mechanics. Even though the effective coupling strength will be reduced compared to the bare coupling of the mechanics to the om. cavity, the high-Q mode would reside in the resolved sideband regime, consequently allowing for ground state cooling. Second, quantum interference between the photonic modes, similar to a Fano res-

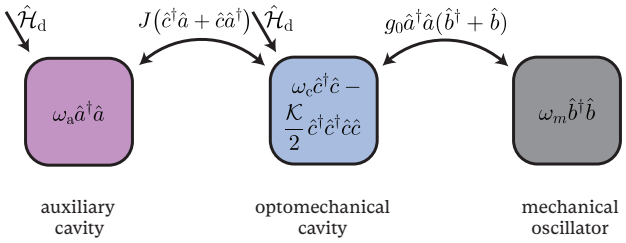

Fig. 6.1 Schematic representation of the proposed coupling scheme of an optomechanical system to a high-Q auxiliary cavity.

onance [131, 132], can suppress unwanted backaction heating, thereby enabling cooling beyond the conventional limit as proposed by [6].

6.1.1 Theoretical description

This section draws in part on the approach of [6], while a full theoretical description of the setup shown in Fig. 6.1 is currently in preparation by our theoretical collaborators G. Kufatty-Anton et al. in the group Prof. A. Metelmann (Karlsruher Institute of Technology). The Hamiltonian describing the coupling between the high-Q auxiliary cavity $\hat{a}$ and om. cavity $\hat{c}$ ($Q_{\mathrm{l,a}} \gg Q_{\mathrm{l,c}}$) is governed by the Jaynes-Cumming (JC) Hamiltonian [133]. This modifies the bare Hamiltonian $\hat{\mathcal{H}}_0$ from Eq. (2.1) leading to the system Hamiltonian

$$\begin{aligned}\hat{\mathcal{H}}/\hbar &= \hat{\mathcal{H}}_0'/\hbar + \hat{\mathcal{H}}_\mathrm{int}/\hbar + \hat{\mathcal{H}}_\mathrm{d}/\hbar \\ &= -\Delta_\mathrm{a}\hat{a}^\dagger\hat{a} - \Delta_\mathrm{c}\hat{c}^\dagger\hat{c} - \frac{\mathcal{K}}{2}\hat{c}^\dagger\hat{c}^\dagger\hat{c}\hat{c} + J\left(\hat{c}^\dagger\hat{a}+\hat{c}\hat{a}^\dagger\right) + \omega_\mathrm{m}\hat{b}^\dagger\hat{b} + \hat{\mathcal{H}}_\mathrm{int} + \hat{\mathcal{H}}_\mathrm{d},\end{aligned} \tag{6.1}$$

which is valid for $J \ll \omega_\mathrm{c}, \omega_\mathrm{a}$. Here, $\Delta_i = \omega_\mathrm{d} - \omega_i$ is the drive-cavity detuning, J the cavity-cavity coupling strength, $\hat{\mathcal{H}}_\mathrm{int}/\hbar$ represent the interaction Hamiltonian introduced in Eqs. (2.4), and $\hat{\mathcal{H}}_\mathrm{d} = (\alpha_{\mathrm{d,a}}\hat{a}^\dagger + \alpha_{\mathrm{d,c}}\hat{c}^\dagger) + \mathrm{h.c.}$ the time independent external drive. A direct consequence of the modified $\hat{\mathcal{H}}_0'/\hbar$ – the J-term – is the appearance of an avoided crossing of the cavities as soon as the cavities start to hybridize at small detunings $\delta = \omega_\mathrm{a} - \omega_\mathrm{c}$. The eigenfrequencies of the coupled cavities are given by

$$\omega_\pm = \frac{\omega_\mathrm{c}+\omega_\mathrm{a}}{2} \pm \sqrt{(\delta/2)^2 + J^2}, \tag{6.2}$$

which close to resonance $\delta \approx 0$ results in an avoided crossing of $2J$ as shown in Fig. 6.3b) or Fig. 6.2d), which is a useful feature to determine the coupling strength in simulations and experiments. Due to hybridization, a clear distinction between the separate modes is no longer possible; thus, we refer to the observed modes as *high-Q-like* and *om.-like*.

To get more insight into the system dynamics, we simplify the system by assuming $\mathcal{K} = 0$, use the linearization identical to section 2.1.1[1] and move to the hybrid basis by using a symplectic transformation as

$$\delta\hat{a} = \cos(\theta)\hat{d}_+ + \sin(\theta)\hat{d}_-, \tag{6.3}$$

$$\delta\hat{c} = \sin(\theta)\hat{d}_+ + \cos(\theta)\hat{d}_-, \tag{6.4}$$

[1] Namely $\hat{a} \to \bar{a} + \delta\hat{a}/\hat{c} \to \bar{c} + \delta\hat{c}$ by introducing the steady state amplitudes $\bar{a}/\bar{c}$ of the cavities.

with the rotation angle θ determined by the set of equations

$$\begin{aligned}\tan(2\theta) &= -\frac{2J}{\delta},\\ \cos(2\theta) &= -\frac{\delta/2}{\sqrt{(\delta/2)^2+J^2}},\\ \sin(2\theta) &= \frac{J}{\sqrt{(\delta/2)^2+J^2}}.\end{aligned} \tag{6.5}$$

In the last equation, we see that for $\delta/J \gg 0$ or $\delta/J \ll 0$, we obtain the unhybridized modes $\delta\hat{c} = \hat{d}_+ \vee \hat{d}_-$ and $\delta\hat{a} = \hat{d}_- \vee \hat{d}_+$, respectively. With the rotation θ defined by Eq. (6.5), the bare Hamiltonian in the hybridized basis reads

$$\hat{\mathcal{H}}'_{0,h}/\hbar = -\Delta_+\hat{d}_+^\dagger\hat{d}_+ - \Delta_-\hat{d}_-^\dagger\hat{d}_- + \omega_\mathrm{m}\hat{b}^\dagger\hat{b}, \tag{6.6}$$

with the hybrid detuning $\Delta_\pm = \omega_\mathrm{d} - \omega_\pm$. To obtain the linewidth of the hybrid modes, we use the rotation defined by Eq. (6.4) on the input-output theory introduced in sec. 2.2 together with $\hat{\mathcal{H}}'_{0,h}$ resulting in

$$\kappa_+ = \kappa_{\mathrm{l,a}}\cos^2(\theta) + \kappa_{\mathrm{l,c}}\sin^2(\theta), \tag{6.7}$$

$$\kappa_- = \kappa_{\mathrm{l,a}}\sin^2(\theta) + \kappa_{\mathrm{l,c}}\cos^2(\theta), \tag{6.8}$$

where we used the total linewidth of the respective cavity. The linearized interaction Hamiltonian can be rearranged to illustrate how the hybrid modes interact with the mechanical mode

$$\begin{aligned}\hat{\mathcal{H}}'_{\mathrm{int,h}}/\hbar =& g_0\left[\sin^2(\theta)\sqrt{\bar{n}_+} + \sin(\theta)\cos(\theta)\sqrt{\bar{n}_-}\right]\left(\hat{d}_+ + \hat{d}_+^\dagger\right)\left(\hat{b}^\dagger + \hat{b}\right) +\\ & g_0\left[\cos^2(\theta)\sqrt{\bar{n}_-} + \sin(\theta)\cos(\theta)\sqrt{\bar{n}_+}\right]\left(\hat{d}_- + \hat{d}_-^\dagger\right)\left(\hat{b}^\dagger + \hat{b}\right),\end{aligned} \tag{6.9}$$

with $\bar{n}_\pm = |d_\pm|^2$ the occupation of the hybridized modes. We can use the relations for θ (Eq. (6.5)) to further rewrite the equation in terms of J and δ

$$\begin{aligned}\hat{\mathcal{H}}'_{int,h}/\hbar =& \frac{g_0}{2}\left[\left(1 + \frac{\delta/2}{\sqrt{(\delta/2)^2+J^2}}\right)\sqrt{n_+} + \frac{J}{\sqrt{(\delta/2)^2+J^2}}\sqrt{n_-}\right]\left(\hat{d}_+ + \hat{d}_+^\dagger\right)\left(\hat{b}^\dagger + \hat{b}\right) +\\ & \frac{g_0}{2}\left[\left(1 - \frac{\delta/2}{\sqrt{(\delta/2)^2+J^2}}\right)\sqrt{n_-} + \frac{J}{\sqrt{(\delta/2)^2+J^2}}\sqrt{n_+}\right]\left(\hat{d}_- + \hat{d}_-^\dagger\right)\left(\hat{b}^\dagger + \hat{b}\right).\end{aligned} \tag{6.10}$$

This shows that both modes of the hybridized system couple effectively to the mechanical mode with a modified coupling strength given by J and δ. In the unhybridized case $|\delta| \gg J$, we recover the standard coupling scheme between the mechanical mode and the om. cavity as derived in Eq. 2.9.

Depending on the coupling strength J, we can either use the resolved sideband approach or the Fano-like interference to potentially achieve cooling beyond the conventional backaction limit[6, 132]. For $J \gg \kappa_{\mathrm{l,a}}, \kappa_{\mathrm{l,c}}$ and $J < |\delta|$, one of the hybrid modes maintains primarily the high-Q character of the two cavities such that $\kappa_+ \vee \kappa_- \approx \kappa_{\mathrm{l,a}}$. Even though the coupling of this "high-Q-like" mode to the mechanics is reduced compared to the bare coupling g_0, the system

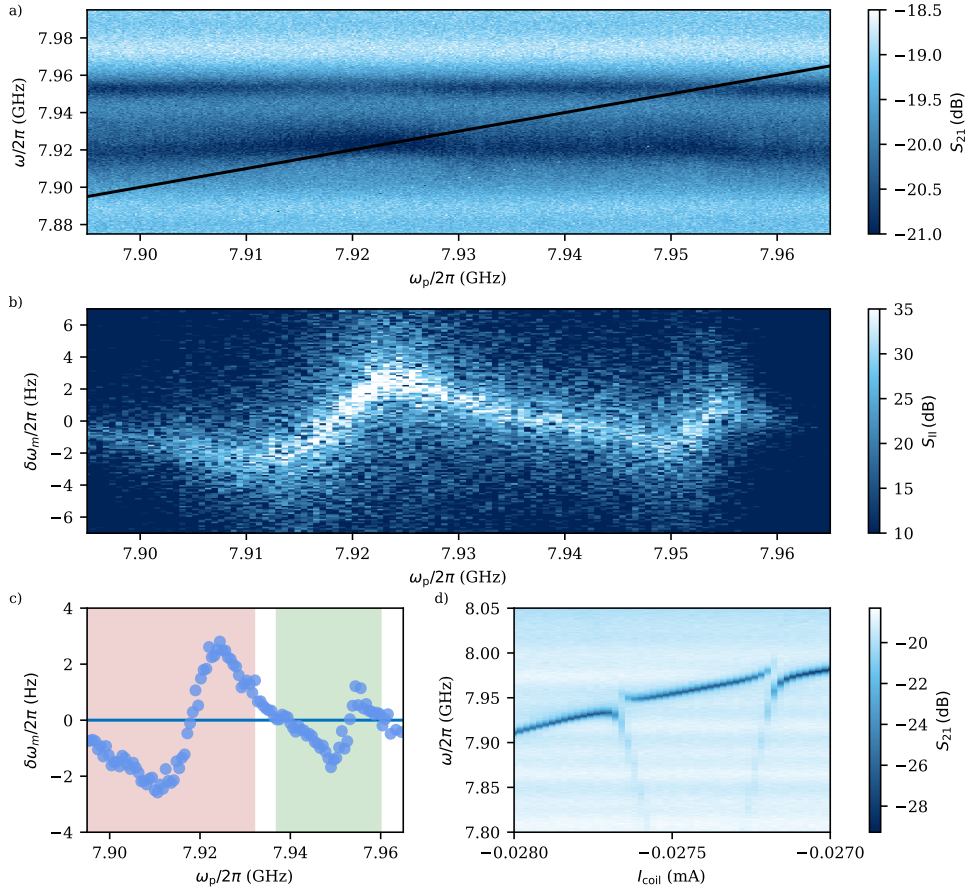

Fig. 6.2 **a)** Weak VNA measurements of two hybridized microstrip cavities – dark blue bands – while frequency tuning a drive (solid black line). **b)** Measured mechanical signature for varying detuning of the drive and **c)** extracted mechanical frequency shift. **d)** Avoided crossing of the two microstrip cavities upon flux tuning with $J/2\pi \approx 1.7\,\mathrm{MHz}$.

resides in the resolved sideband regime, which significantly lowers the backaction limit. For the Fano-like approach, as mentioned in [132], the intra cavity coupling has to fulfill the condition $J < \kappa_{\mathrm{l,a}}$. Then for small detuning δ, the interference of the cavities allows for a suppression of the Stokes process Γ_{S} leading to a decreased backaction limit as explained in [6].

6.1.2 Proof of principle

As a proof of principle experiment, we placed two of our u-shaped SQUID cavities – each mounted with a cantilever – side by side in one of the clamps of the waveguide shown in Fig. 4.7. The proximity of the cavity legs gives rise to a capacitive coupling, thereby realizing the Hamiltonian in Eq. (6.1). However, as both cavities are mounted with a cantilever and are placed symmetrically around the center of the waveguide, their linewidths are comparable, such that we do not expect an enhancement in the backaction due to hybridization. Nevertheless, we can determine if both modes effectively couple to the same cantilever.
Therefore, we tune the external flux to extract the coupling strength of the cavities as depicted in Fig. 6.2d). With a coupling strength of $J/2\pi \approx 1.7\,\mathrm{MHz}$, we fully hybridize the cavities

as shown in Fig. 6.2a) and frequency tune a drive tone through the hybridized modes. From the frequency shift of the measured mechanical signal, we can clearly distinguish two ranges of drive frequencies with independent signatures of backaction (red and green marked areas in Fig. 6.2c)). The drive frequencies for each section of backaction align with the respective resonances of the hybridized modes. This verifies that we can enact backaction on the mechanics through a capacitively coupled auxiliary cavity as the theory calculations predict.

6.2 Microstrip Cavity - Post-Cavity Setup

According to [6], minimizing the linewidth of the auxiliary cavity is advantageous. With quality factors exceeding $Q_\mathrm{l} > 10^8$ [129], superconducting post cavities – a well-established system in our group [130, 134, 135] – offer an optimal platform as the auxiliary cavity in our system with two additional benefits. First, the superconducting body of the post-cavity naturally shields the SQUID-cavity from any external flux noise. Second, the coupling between the cavities can be tuned by moving the SQUID-cavity residing in a tunnel out/into the post-cavity field. The cavity design employed in our group is a coaxial $\lambda/4$ post-cavity [136], which combines the concepts of a circular waveguide section on top of a coaxial transmission line as shown in Fig. 6.3a). The coaxial section builds a post, which is terminated by an open circuit at the top and shorted at the bottom. The post length l defines the cavity resonance with $l \approx \lambda/4$ with a field maximum at the post top. The waveguide section is designed with a cutoff frequency higher than the resonance frequency of the cavity, resulting in an exponential suppression of the field above the post, which allows for an appropriate choice of the waveguide length for high-quality factors. A thorough explanation of the general design of the post cavities in our lab can be found in the thesis of P. Heidler and I. Yang [136, 137].

In the following, we discuss the design choices made for the auxiliary post-cavity based on simulations done with the High Frequency Structure Simulator (HFSS) tool in the ANSYS software simulations.

6.2.1 HFSS-Simulation and Design

To examine the coupling between our u-shaped SQUID-cavity and the post-cavity, we simulate the eigenmodes of the system within HFSS shown in Fig. 6.3. We include the SQUID by adding a lumped element with a defined capacitance C_J and inductance L_J, and mimic the frequency tuning behavior of the SQUID-cavity by sweeping L_J. For a set placement of the SQUID-cavity with respect to the post-cavity, we frequency tune the SQUID and extract the intra cavity coupling J from the avoided crossing with the post-cavity.

To understand the scaling of J we repeat this procedure by displacing the SQUID-cavity further from the post in horizontal δx and vertical δh direction. $\delta x = 0$ corresponds to the legs of the microstrip cavity being positioned at the post, whereas $\delta h = 0$ denotes the case where the upper leg is flush with the top of the post. By moving the cavity further into the tunnel and thus away from the maximal field of the post cavity, we see that first the coupling strength drops from $200\,\mathrm{MHz} \rightarrow 10\,\mathrm{MHz}$ at $\delta x = 3\,\mathrm{mm}$. With the cavity completely residing in the tunnel, where we expect an exponential decay of the overall post-cavity mode, we first obtain a slight increase of the J, followed by a gradual decline. Changing the height of the SQUID, we observe the highest couplings for the lower leg align with the top of the post. With the u-shaped design, the microstrip cavity couples to gradients in the electric field. Therefore, due to the exponential decay in the waveguide section of the post-cavity (see Fig. 6.4a), we expect the highest couplings

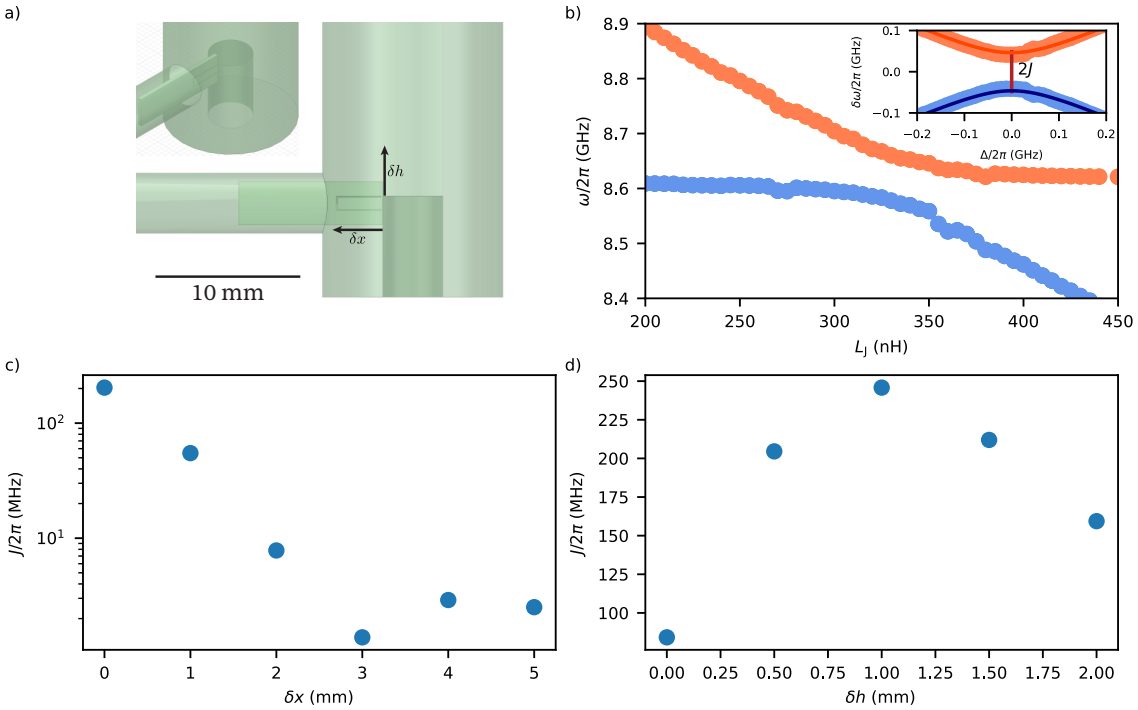

Fig. 6.3 **a)** HFSS-model used to extract the coupling strength J between a post-cavity and a U-shaped microstrip cavity. **b)** Simulation of a frequency sweep by modulating the effecting junction inductance L_J crossing the fixed frequency resonance of the post-cavity - inset shows the extracted coupling ($J/2\pi = 50\,\mathrm{MHz}$). **c)** Dependence of the coupling strength on the distance between legs of the cavity to the post at a height $\delta h = 0.5\,\mathrm{mm}$. **d)** Dependence of the coupling strength on the height of the cavity to the post at a distance $\delta x = 0.0\,\mathrm{mm}$

to the post-cavity mode at $\delta h = 1\,\mathrm{mm}$.

Based on the simulation results, we developed the experimental design of the aluminium post-cavity shown in Fig. 6.4a). We decided for a post length of $l = 6.7\,\mathrm{mm}$ corresponding to a resonance frequency $\omega_\mathrm{a}/2\pi = 8.6\,\mathrm{GHz}$. With a length of the waveguide section $L = 25\,\mathrm{mm}$, the post-cavity mode is sufficiently attenuated to allow for a high quality factor. The coupling port is placed within the waveguide section to weakly couple to the post-cavity, allowing for readout of the cavity in reflection S_{11}. The length of the coupling pin gives in the end the external coupling Q_c to the post-cavity. The resonator tunnel hosting the SQUID-cavity is placed at a height corresponding to the SQUID-cavity aligning with the post at $\delta h = 1\,\mathrm{mm}$ for maximal coupling strength. A seperate side port is added to the resonator tunnel, to allow for a direct readout of the SQUID-cavity. To allow for flux tuning, another slot is added at roughly the position of the SQUID loop to host a flux hose. We rely on these flux hoses developed within our group [57, 138] to allow for a flux tuning of our SQUID-cavities inside the superconducting material of the post-cavity. Fig. 6.4b) shows the second generation of the flux hose, first mentioned in [137]. A coil is wound along the groove to generate a magnetic field. Due to the Meissner effect, the tube shape of the superconducting hose funnels the field towards its end due

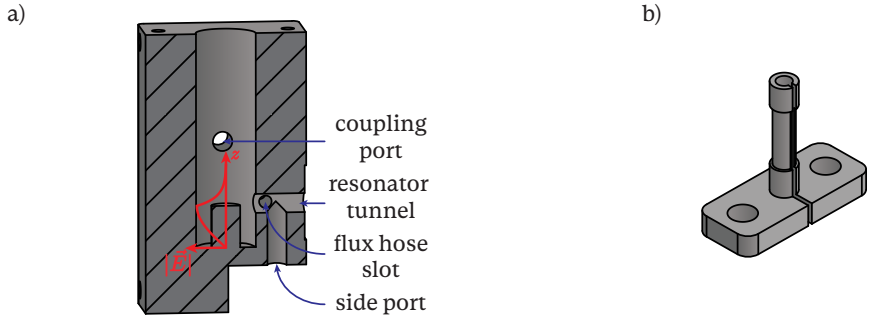

Fig. 6.4 **a)** Illustration of a high-Q post-cavity with a schematic representation of the elect. field amplitude $|\vec{E}|$. The sample can be inserted via the resonator tunnel, where an additional side port is added to allow for direct readout of the OM. sample. For flux tuning, a slot to fit a flux hose perpendicular to the OM. sample is added. The high Q cavity can be read out via a coupling pin at the coupling port. **b)** Illustration of the flux hose design used in this setup.

to shielding currents, thus seperating the cavity from the coil, shielding it from potential losses. The slit along the flux hose prevents flux quantization, allowing for arbitrary fluxes to reach the SQUID-cavity. The end of the flux hose has to be placed in proximity to the SQUID-loop to achieve reasonable tuning, which together with the SQUID-cavity design restricts us to a set δx. To realise the resolved approach introduced in sec. 6.1, we decided on a placement of the flux hose corresponding to a SQUID-cavity displacement $\delta x = 1.5\,\mathrm{mm}$, which sets the coupling strength around $J/2\pi = 40\,\mathrm{MHz}$. To achieve these couplings, we further have to dice the silicon of the microstrip cavities (shown in Fig. 4.5) at the bottom to resemble the actual simulation setting.

6.2.2 Measurement results

After the assembly of the whole setup, we measure the response of the cavities in reflection S_{11} through the respective port with a VNA while sweeping the current through the flux hose. The resulting fluxmaps are depicted in Fig. 6.5a-b) measuring the optomechanical SQUID-cavity and in Fig. 6.5c-d) the post-cavity. From the SQUID-cavity response, we see that the fluxhose allows us to tune several flux lobes. The current up and down sweep clearly shows a hysteretic tuning behavior with an irregular shape at $I_{\mathrm{coil}} = 0.25\,/\,{-1.75}\,\mathrm{mA}$. We associate this feature with the mounted cantilever, as we observed similar tuning behaviors only for other optomechanical samples. At a bias point close to $\omega/2\pi = 8.5\,\mathrm{GHz}$ we observe a bending of the cavity frequency tuning, which by scanning the post-cavity turns out to be an avoided crossing. From the avoided crossing, we can deduce a coupling strength of roughly $J/2\pi = 15\,\mathrm{MHz}$. The slight deviation from the expected $J/2\pi = 40\,\mathrm{MHz}$ can be attributed to a certain degree of misalignment and left over silicon of the cavity chip after dicing. Nevertheless, the achieved coupling strength should still be sufficient to enable operation within the resolved regime approach. More unexpectedly, however, the linewidth of the post-cavity mode was with $\kappa_{\mathrm{l,a}}/2\pi = 1\,\mathrm{MHz}$ broader than anticipated, indicating unaccounted loss mechanisms.

To clarify this discrepancy, we investigated the individual components of the auxiliary setup separately in order to identify the origin of the reduced quality factor. The results of these

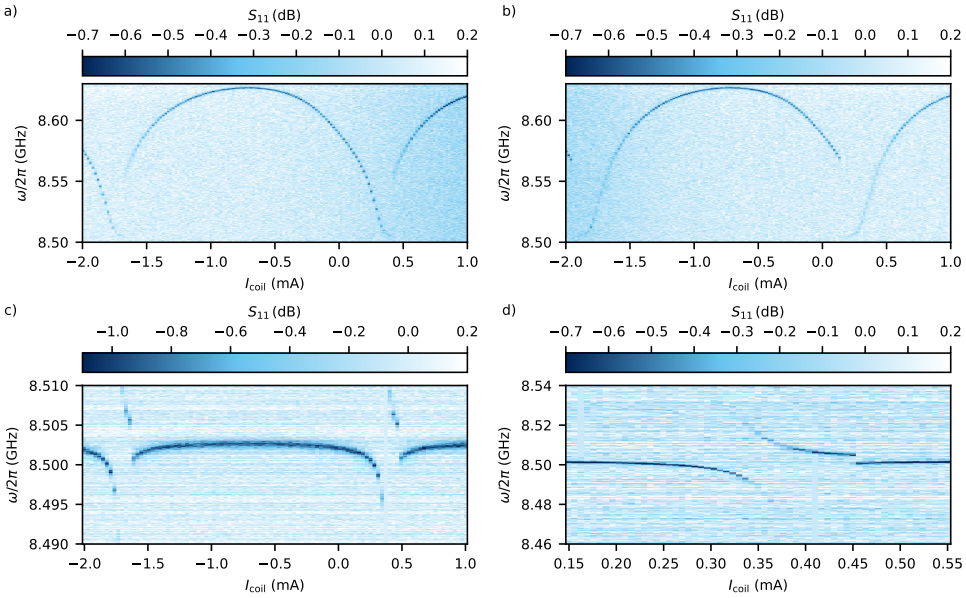

Fig. 6.5 Flux tuning of the SQUID-cavity and measuring its response through the side-port for **a)** current up and **b)** down sweep. **c)** Response of the post-cavity for the same current up sweep as in **a)**. **d)** Zoom-in to the avoided crossing reading out the post-cavity response.

measurements are summarized in Fig. 6.6, comparing different configurations of the setup: a) the post-cavity alone, b) the post-cavity coupled to the SQUID-cavity, c) the post-cavity with SQUID-cavity and flux hose, and d) the complete configuration including the optomechanical setup and flux hose. For the bare post-cavity the system was strongly overcoupled $Q_l \approx Q_c \ll Q_{int}$, which prevents to precisely determine the interal quality factor [139]. With the SQUID-cavity mounted, we obtain still a high-Q characteristic of the post-cavity of $Q_{int} = 4.5(1) \cdot 10^6$, from which we estimate the bare post-cavity quality factor to be at least $Q_{int} > 4 \cdot 10^6$. Regardless, the influence of the SQUID-cavity on the post-cavity is visible by the frequency shift from its bare mode due to the additional silicon in the high field region of the post-cavity mode. Contrary to the SQUID-cavity, adding the flux hose and the cantilever chip both result in a significant decrease of the qualitify factor of the post-cavity. This leads to the conlusion that due to the alignment restrictions of the SQUID-loop, the flux hose is positioned to close to the post-cavity mode. Thus, significant field contributions remain in lossy regions of the flux hose, such as the coil and the Stycast used for fixation. Furthermore, the silicon substrate of the stripline cavity appears to funnel a substantial fraction of the field towards the cantilever body. To avoid static charging, the cantilevers are fabricated from doped silicon, which is associated with high microwave losses, thereby accounting for the observed drop in quality factor.

As our u-shaped microstrip cavities restrict us to the chosen design, the post cavity approach is not suitable to realize the auxiliary setup due to the additional losses of the cantilever and flux hose in proximity to the high-Q mode. However, this only holds if one tries to realize the resolved sideband approach of the hybridization scheme making these high couplings J necessary. As a lower intracavity coupling J is needed for the Fano-like approach, we could move the fluxhose and SQUID-cavity deeper into the resonator tunnel, which would significantly reduce

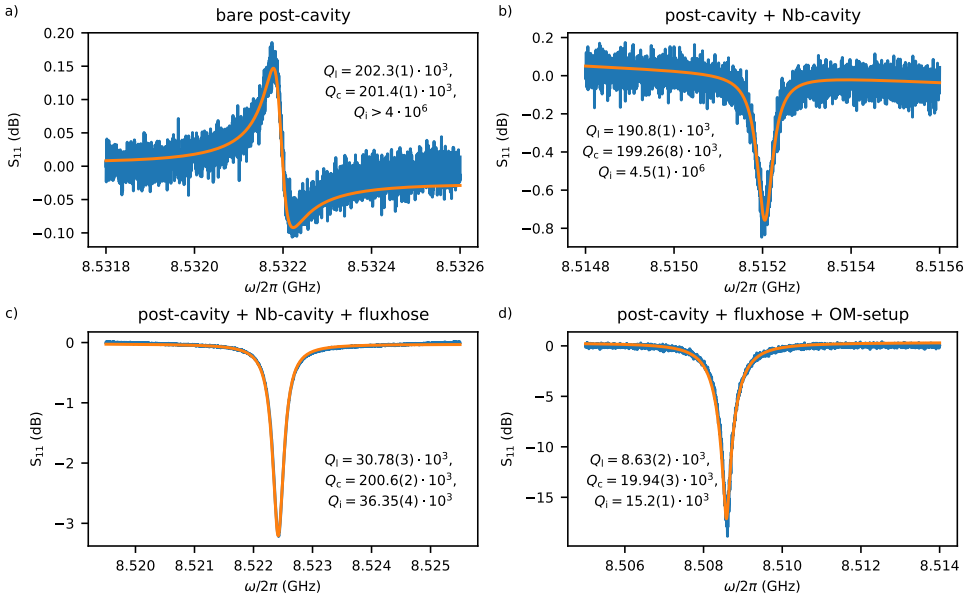

Fig. 6.6 Quality factor of the post-cavity measured for **a)** the bare post-cavity, **b)** with the SQUID-cavity added, **c)** with SQUID-cavity and flux hose, and **d)** for the full optomechanical setup.

their participation to the post cavity losses. To realize this would require the fabrication of a new post cavity, which was beyond the timeframe of this work.

6.3 Future of the Auxiliary Approach

Since the use of a flux hose both restricts the tunability of the achievable coupling strength after fabrication and increases the losses of the post-cavity, together with the cantilever chip, we chose to return to the waveguide setting. As demonstrated by the proof-of-principle measurement in Fig.6.2, sufficient coupling strength can be obtained by positioning two u-shaped cavities next to each other within the waveguide. Therefore, we rely on a bare cavity as the auxiliary system within the waveguide setting, as illustrated in Fig. 6.7a).

This approach offers several practical advantages over the post-cavity design. On one hand, we can fabricate our own auxiliary cavities based on a u-shaped Nb-stripline design in our clean-room (done by my coworker B. Thyagarajan). Even though Q_{int} for these samples is typically less compared to a post-cavity, the fabrication process is less time-consuming, allowing for a fast adaptation of system parameters if necessary. In addition, the u-shaped design of our stripline cavities confines the auxiliary cavity field to the end of its legs. Hence, the overall field remains weak at the lossy cantilever substrate, thereby preserving its high-Q character.
On the other hand, we can achieve a high flexibility in the coupling strength with only minor modifications to the standard waveguide setup. By enabling adjustment of the distance between the cavities during placement, we achieve a high flexibility in J. However, to maintain the required high-Q characteristic of the auxiliary cavity, it is necessary to ensure a low external coupling to the waveguide mode. Therefore, it must be placed near the waveguide center. With

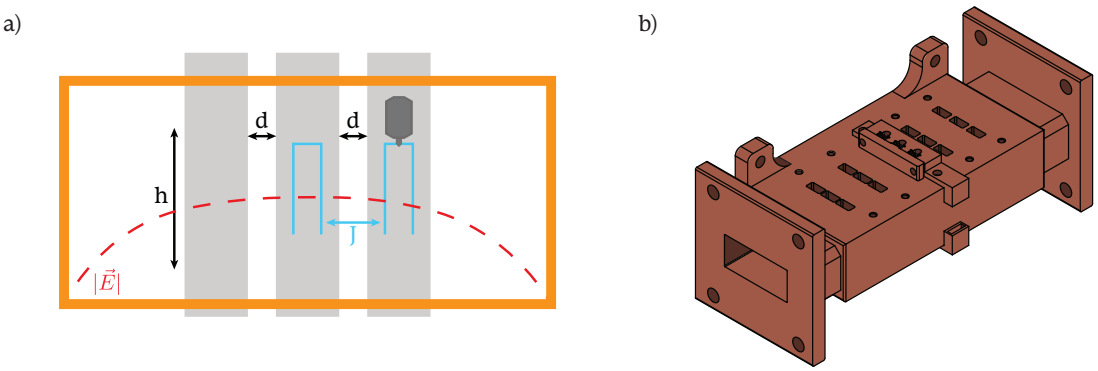

Fig. 6.7 **a)** Schematic cross-section of the rectangular waveguide, perpendicular to its propagation direction. The red dashed line represents the electric field of the fundamental TE_{10} mode. Placing the om. system and the auxiliary cavity next to each other leads to a capacitive coupling J between the two cavities. The coupling J can be tuned by adjusting the distance between the cavities, d, and the height, h. To ensure a low external coupling rate of the auxiliary cavity to the waveguide mode, it is placed at the center, with a bare chip opposite the om. system to symmetrize the electric field. **b)** *SolidWorks* drawing of a waveguide built to realize the auxiliary approach. Each row of 3 slots has a different chip distance d, allowing for different coupling strength J. To allow for a flexible mounting process, chips can also be placed from the bottom.

the asymmetrical distribution of the silicon substrate, the distorted waveguide mode would still result in a substantial waveguide coupling of the auxiliary cavity. Hence, we follow the findings in the supplementary of [30] and symmetrize the electric field of the waveguide by placing a bare silicon chip opposite to the om. system.
The final design is shown in Fig. 6.7b). The waveguide features five rows with three slots for the bare silicon chip, the auxiliary cavity, and the om. system. For each row, the slots are further apart, allowing for a different intra-cavity coupling strength J. By moving the auxiliary cavity in the clamp along the h-direction, J can be further modified to meet the experimental requirements.

Due to time constraints of this thesis, I could not continue measurements on the new design for the hybridization approach. However, this work is being continued by my coworkers. They have already demonstrated, using the WG approach, that it is possible to maintain the high-Q characteristic of the auxiliary cavity and to achieve sufficient intracavity coupling strength J for the sideband resolved method. Furthermore, first measurements indicate that the mechanical mode can be detected through both modes when the cavities are tuned into hybridization. With this, backaction measurments and further system characterization – neccessary due to the intrinsic nonlinearity of SQUID-cavity – are on going.

CHAPTER 7

Conclusion

The foundation of the experimental platform upon which this work is built was laid by prior members of the group, Mathieu L. Juan, Christian Schneider [1], and David Zöpfl [2]. They demonstrated the initial results of the inductive coupling scheme and the benefits of using a nonlinear cavity on the backaction cooling of the mechanical mode in the unresolved sideband regime [3, 4]. From this, the goals of this thesis were to improve reproducibility of the sample preparation and to implemente a passive vibration isolation for increased system stability. With this we could operate the system at larger coupling strengths and drive powers than what had been explored so far. Moreover, to reach the mechanical ground state, I started with a modification of the existing setup by adding an auxiliary cavity based on a theoretical proposal [6].

Based on our theoretical work in Ref. [53], we derive the fundamental equations of nonlinear optomechanics to describe the interaction between the photon and phonon modes in Chapter 2. Focusing on the achievable sideband cooling, we explain that the enhanced cooling capability of a nonlinear cavity in the sideband unresolved regime is based on the non-Lorentzian, skewed photon number noise spectral density as compared to an identical but linear cavity. After outlining the main backaction features arising from the nonlinear cavity, we discuss the limitation imposed by backaction heating, which prevents systems like ours operating in the unresolved sideband regime, from reaching the mechanical ground state.

In Chapter 3, we introduce microwave cavities and the fundamental toolbox of superconducting circuits. Using the Josephson junction as a basis, we explain the working principle of a SQUID as a flux-sensitive element and present a simulation routine to predict the tuning behavior of SQUID-cavities under externally applied flux and DC drive, following an approach similar to [81]. We further extend this model to include the magnetically modified cantilever with the aim of capturing its effect on the tuning dynamics. Depending on its alignment relative to the SQUID, the magnetic cantilever leads to a reduced hysteresis factor of the SQUID-cavity, introduces a current asymmetry and further alters the flux tuning behavior for the SQUID due to a periodic displacement of its resting position.

Within the experimental setup, Chapter 4, we emphasize the necessity of a vibration isolation setup for the experiment, during our discussion of the working principle of a dilution cryostat. We present a simple suspension approach based on an elastic pendulum, which allows us to achieve a noise reduction up to 20 dB for frequencies below 1 kHz, as verified by an accelerometer measurement. Since the increased isolation comes at the cost of reduced thermalization of the experiment, we describe the measures implemented that shorten the cooldown time by 2.5 days; ultimately limited by the thermal surface resistance [80]. After introducing the microwave building blocks of the experiment, we present a fitting routine adapted from [83] to characterize cavity parameters, including the nonlinear Kerr parameter. Besides a newly designed mounting stage that enables more precise and reliable sample preparation, the chapter ends by providing results of magnetometer measurements on our magnetic particles done by Prof. A. Ney (University of Linz). These allow us to estimate – depending on the actual particle size – a magnetic moment of typical particles of approximately $7\,\mathrm{nA\,m^2}$.

The main experimental results on the magnetomechanical system are presented in Chapter 5 and split into three parts: characterization of the microwave cavity (sec. 5.1), detection of the mechanical mode in the absence of backaction (sec. 5.2), and backaction measurements on the mechanics (sec. 5.3). By measuring the flux tuning before and after mounting the cantilever for different lateral and transverse positions with respect to the SQUID loop, we found that the change in tuning behavior – reduction in the shielding and participation parameter – is qualitatively in good agreement with predictions based on the simulations introduced in Chapter 3. Furthermore, the simulations reproduce the frequency shift of the mechanical mode – presented in the detection of the mechanical mode (sec. 3.4.4) – observed when flux tuning the cavity away from its sweet spot. This consistency confirms that the simulated model successfully captures the main features of our system. Using the modified circle fit routine and the shift of the resonance frequency [102] for different drive powers, we find good agreement and a nonlinearity of $\mathcal{K} = 12(3)\,\mathrm{kHz}$ and $\mathcal{K} = 13(3)\,\mathrm{kHz}$, respectively. However, the origin of the Kerr anomaly, which appears as an effective positive Kerr nonlinearity for a range of detunings from the sweet spot, remains unclear. Simulations predict a shift toward positive Kerr values for SQUIDs with junction asymmetry towards their lower sweet spot – consistent with observations from samples exhibiting corresponding flux-tuning behavior. Interestingly, the anomaly only emerges when a cantilever is mounted, suggesting a possible correlation with the induced deflection of the cantilever. Additionally, as soon as a cantilever is mounted, we observe a resonance frequency shift on timescales of the order of $\sim 1\,\mathrm{s}$ as we populate the cavity mode. We have been unable to explain this, as it is neither captured by our simulations nor by a radiation pressure model. We could show that the time scale of the shift decreases with increasing temperature of the base plate, matching the temperature broadening of the mechanical linewidth. The amplitude of the shift scales with intra-cavity photon number, and the direction of the shift depends on the sign of the fluxmap slope. Even though further investigations have to be made to grasp the origin of the observed slow frequency shift of our cavity, we could show how the intra-cavity photon number dependence can be used to distinguish the low and high photon number branches after bifurcation of the cavity.

By probing the mechanical mode in the absence of backaction, we verified the effective decoupling achieved by the suspension setup from the vibrational environment of the cryostat. Independent of the pulse-tube state – representing the main source of vibrations – we were able to measure a thermalized mechanical mode. Before implementing the suspension, this was only possible with the pulse tube turned off. On the one hand, this improvement significantly increases the data acquisition rate, as measurements are no longer restricted to pulse tube off intervals. On

the other hand, it reduces the flux noise, part of which originates from vibrations upconverted by the cantilever, thereby allowing operation of the system at more flux-sensitive bias points. We could further support this by determining the optomechanical coupling strength across different cooldowns, again observing good agreement between pulse tube on and off. However, the data also reveal setup limitations, such as variations in the achieved level of decoupling across multiple cooldowns and an inability to thermalize the mechanical mode below $\sim 200\,\mathrm{mK}$, likely due to the reduced thermal contact of the experiment to the cryostat base.

Taking advantage of the increased system stability, we were able to perform detailed cooling measurements across a range of coupling strengths, limiting the drive amplitude to the onset of bifurcation of the cavity. At low couplings $g_0/2\pi = 102.5\,\mathrm{Hz}$, the suspension setup enabled taking high-resolution cooling traces close to bifurcation. Resolving a distinct cooling feature at these drive powers, we observe excellent agreement between the data and a fit based on the developed theory in Ref. [53]. Operating at intermediate couplings $g_0/2\pi = 850\,\mathrm{Hz}$, we still observe indications of residual mechanical noise, similar to the data for the low-coupling regime. Nevertheless, under these conditions, the mechanical mode could be cooled from ~ 8000 down to an average phonon occupation of ~ 90 and ~ 50 with the pulse tube on and off, respectively. By tuning the sample to a large coupling of $g_0/2\pi = 3.52\,\mathrm{kHz}$, we push towards the cooling limits achievable in this setup. There, we achieved an average mode occupation of ~ 30 phonons, which we further back up with an independent estimate calculated from the broadening of the mechanical linewidth. This estimate allows for a comparison to the previously achieved minimum of 14 phonons at a lower bath temperature [4], suggesting that at these temperatures the suspension setup could enable cooling to below 10 phonons.

Having characterized the cooling behavior for different couplings before bifurcation, we turned to measurements entering the bistability regime. For a low coupling strength of $g_0/2\pi = 99\,\mathrm{Hz}$, we demonstrated that our system can be operated even beyond the cavity bifurcation, extending the observations of backaction cooling in nonlinear systems reported in Ref. [4]. As we can unambiguously distinguish the selected branches in this regime based on the observed slow frequency shift of the cavity, we achieved good agreement with the underlying theoretical model. By extrapolating the fitting results from a low power cooling trace over nearly an order of magnitude (a factor of six) in input power, we could accurately predict the observed cooling behavior, confirming a solid understanding of the processes at play. However, the cooling achieved in the bistable regime is limited by flux noise in the system, which prevents access to the narrow frequency range where optimal cooling is expected.

Despite the large coupling strengths achieved in our setup and the beneficial cooling effects demonstrated from the intrinsic nonlinearity of the cavity, residing in the sideband unresolved regime imposes a fundamental limit preventing us from reaching the mechanical ground state – a requirement for quantum state creation of the mechanical mode. A straightforward approach to overcome this limitation would be to operate the system in the sideband resolved regime by increasing the cavity's quality factor. However, as shown in [80], the large offset magnetic field generated by the permanent magnet, together with the inherently lossy cantilever material in close proximity to the cavity, significantly limits the quality factors we can achieve. This constraint could be mitigated by increasing the distance between the cantilever and the cavity by using a flux transformer to mediate the coupling. Here, we would place the cantilever over the pick up loop on one side of the flux transformer and align the actuator loop with the SQUID on the other side. The motion of the magnetic particle induces a current in the flux transformer, which couples only the small changes in magnetic field associated with the cantilever motion to the SQUID-cavity. With the larger distance between cantilever and cavity, the detrimental

effects of the static magnetic bias field and lossy cantilever dielectric on the cavity quality factors would be drastically reduced, which might allow to reach the sideband resolved regime. However, the parasitic inductance of the flux transformer itself leads to a reduction in the effective coupling strength between the cavity and cantilever mode, which can, in principle, be counteracted by using a stronger permanent magnet.

Another approach would be to hybridize the low-quality optomechanical system with a high-quality auxiliary cavity, as highlighted in Chapter 6. The working principle relies on the hybridization between the two cavities, through which the auxiliary cavity inherits the coupling to the mechanical mode – even though with a reduced strength compared to the original system – while largely preserving its high-quality characteristics, which technically puts it into the resolved sideband regime. After providing a proof of principle approach, we could show that a setup based on a 3D post cavity and our optomechanics platform still suffers from the lossy materials, such as the cantilever. Therefore, we propose another realization based on the hybridization with a high-quality u-shaped stripline resonator in a waveguide environment.

Another potential solution involves the use of an externally generated squeezed drive to allow for ground state cooling in the unresolved regime, as demonstrated in [140]. Our theory in Ref. [53] even shows that harnessing the cavity's intrinsic nonlinearity makes this protocol more efficient, reducing the amount of external squeezing required to reach the mechanical ground state.

Looking ahead, inductively coupled electromechanics remains a highly interesting field to follow for the creation of macroscopic quantum states due to the large coupling strength g_0 already demonstrated [3, 48–50]. The continuous advances in superconducting circuit fabrication – leading to qubits reaching relaxation times of $\sim 1\,\mathrm{ms}$ [32, 33, 141] and cavities with quality factors exceeding $Q > 10^6$ [29–31] – will benefit inductively coupled systems. Moreover, new circuit designs – increasing the magnetic field resilience by e.g. vortex pinning holes [142] or the mentioned flux transformer – might enable to further boost the coupling strength g_0 by using larger magnetic fields. These developments should allow to cool to the mechanical ground state, which remains to be demonstrated in inductively coupled systems. With further improvements, these systems are a prime candidate to enter the regime of high cooperativity. There, the photon enhanced coupling strength exceeds the decay rate of the photon mode and the mechanical coupling to the bath $C = 4\bar{n}_\mathrm{c} g_0^2/\kappa_\mathrm{l}\Gamma_\mathrm{m}\bar{n}_\mathrm{m}^\mathrm{th} \gg 1$. This allows to coherently transfer a quantum state into the mechanics [143, 144]. Lastly, further improving the inductively coupled platform would allow access to the single-photon strong-coupling regime $g_0 > \kappa_\mathrm{l}, \Gamma_\mathrm{m}$, where direct nonclassical quantum state generation in the mechanics due to the optomechanical interaction becomes possible [145]. Gaining quantum control over massive resonators opens a variety of possibilities for inductively coupled systems to study fundamental physics questions and a broad range of applications – e.g. testing the interplay between quantum mechanics and gravity as well as building quantum memory devices and quantum enhanced sensors.

Bibliography

1. Schneider, C. M. F. *Magnetic coupling between superconducting circuits and a cantilever* PhD thesis (Unversität Innsbruck, 2021). https://diglib.uibk.ac.at/urn:nbn:at:at-ubi:1-85331.
2. Zöpfl, D. *Demonstration of nonlinear enhanced backaction cooling in microwave magnetomechanics* PhD thesis (University of Innsbruck, Sept. 2022). https://diglib.uibk.ac.at/urn/urn:nbn:at:at-ubi:1-116886.
3. Zoepfl, D., Juan, M. L., Schneider, C. M. F. & Kirchmair, G. Single-Photon Cooling in Microwave Magnetomechanics. *Physical Review Letters* **125,** 023601 (July 2020).
4. Zoepfl, D. *et al.* Kerr Enhanced Backaction Cooling in Magnetomechanics. *Phys. Rev. Lett.* **130,** 033601. https://link.aps.org/doi/10.1103/PhysRevLett.130.033601 (3 2023).
5. Deeg, L. F. *et al.* Optomechanical backaction in the bistable regime. *Physical Review Applied* **23,** 014082. https://www.doi.org/10.1103/PhysRevApplied.23.014082 (2025) (Jan. 2025).
6. Liu, Y.-C., Xiao, Y.-F., Luan, X., Gong, Q. & Wong, C. W. Coupled cavities for motional ground-state cooling and strong optomechanical coupling. *Phys. Rev. A* **91,** 033818. https://link.aps.org/doi/10.1103/PhysRevA.91.033818 (3 2015).
7. Schrödinger, E. Quantisierung als Eigenwertproblem (Erste Mitteilung). *Annalen der Physik* **384,** 361–376. https://doi.org/10.1002/andp.19263840404 (1926).
8. Heisenberg, W. Über den anschaulichen Inhalt der quantentheoretischen Kinematik und Mechanik. *Zeitschrift für Physik* **43,** 172–198. https://doi.org/10.1007/BF01397280 (1927).
9. Davisson, C. & Germer, L. H. The Scattering of Electrons by a Single Crystal of Nickel. *Nature* **119,** 558–560. https://doi.org/10.1038/119558a0 (1927).
10. Estermann, I. & Stern, O. Beugung von Molekularstrahlen. *Zeitschrift für Physik* **61,** 95–125. https://doi.org/10.1007/BF01340293 (1930).
11. Arndt, M. *et al.* Wave–particle duality of C_{60} molecules. *Nature* **401,** 680–682. https://doi.org/10.1038/44348 (1999).
12. Fein, Y. Y. *et al.* Quantum superposition of molecules beyond 25 kDa. *Nature Physics* **15,** 1242–1245. https://doi.org/10.1038/s41567-019-0663-9 (2019).
13. Devoret, M. H., Martinis, J. M., Esteve, D. & Clarke, J. Resonant Activation from the Zero-Voltage State of a Current-Biased Josephson Junction. *Phys. Rev. Lett.* **53,** 1260–1263. https://link.aps.org/doi/10.1103/PhysRevLett.53.1260 (13 1984).

14. Devoret, M. H., Martinis, J. M. & Clarke, J. Measurements of Macroscopic Quantum Tunneling out of the Zero-Voltage State of a Current-Biased Josephson Junction. *Phys. Rev. Lett.* **55,** 1908–1911. https://link.aps.org/doi/10.1103/PhysRevLett.55.1908 (18 1985).

15. Martinis, J. M., Devoret, M. H. & Clarke, J. Energy-Level Quantization in the Zero-Voltage State of a Current-Biased Josephson Junction. *Phys. Rev. Lett.* **55,** 1543–1546. https://link.aps.org/doi/10.1103/PhysRevLett.55.1543 (15 1985).

16. Clarke, J., Cleland, A. N., Devoret, M. H., Esteve, D. & Martinis, J. M. Quantum Mechanics of a Macroscopic Variable: The Phase Difference of a Josephson Junction. *Science* **239,** 992–997. eprint: https://www.science.org/doi/pdf/10.1126/science.239.4843.992. https://www.science.org/doi/abs/10.1126/science.239.4843.992 (1988).

17. Schlosshauer, M. Decoherence, the measurement problem, and interpretations of quantum mechanics. *Rev. Mod. Phys.* **76,** 1267–1305. https://link.aps.org/doi/10.1103/RevModPhys.76.1267 (4 2005).

18. Romero-Isart, O. Quantum Superposition of Massive Objects and Collapse Models. *Physical Review A* **84,** 052121 (Nov. 2011).

19. Ghirardi, G., Grassi, R. & Rimini, A. Continuous-spontaneous-reduction model involving gravity. *Phys. Rev. A* **42,** 1057–1064. https://link.aps.org/doi/10.1103/PhysRevA.42.1057 (3 1990).

20. Bassi, A., Lochan, K., Satin, S., Singh, T. P. & Ulbricht, H. Models of wave-function collapse, underlying theories, and experimental tests. *Rev. Mod. Phys.* **85,** 471–527. https://link.aps.org/doi/10.1103/RevModPhys.85.471 (2 2013).

21. Penrose, R. On Gravity's Role in Quantum State Reduction. *General Relativity and Gravitation* **28,** 581–600. https://doi.org/10.1007/BF02105068 (1996).

22. Pikovski, I., Vanner, M. R., Aspelmeyer, M., Kim, M. S. & Brukner, C. Probing Planck-scale Physics with Quantum Optics. *Nature Physics* **8,** 393–397. ISSN: 1745-2481 (May 2012).

23. Aspelmeyer, M., Kippenberg, T. J. & Marquardt, F. Cavity Optomechanics. *Reviews of Modern Physics* **86,** 1391–1452 (Dec. 2014).

24. Teufel, J. D. *et al.* Circuit cavity electromechanics in the strong-coupling regime. *Nature* **471,** 204–208. https://doi.org/10.1038/nature09898 (2011).

25. Chu, Y. *et al.* Quantum acoustics with superconducting qubits. *Science* **358,** 199–202. eprint: https://www.science.org/doi/pdf/10.1126/science.aao1511. https://www.science.org/doi/abs/10.1126/science.aao1511 (2017).

26. Guo, J., Chang, J., Yao, X. & Gröblacher, S. Active-feedback quantum control of an integrated low-frequency mechanical resonator. *Nature Communications* **14,** 4721. https://doi.org/10.1038/s41467-023-40442-3 (2023).

27. Engelsen, N. J., Beccari, A. & Kippenberg, T. J. Ultrahigh-quality-factor micro- and nanomechanical resonators using dissipation dilution. *Nature Nanotechnology* **19,** 725–737. https://doi.org/10.1038/s41565-023-01597-8 (2024).

28. Seis, Y. *et al.* Ground state cooling of an ultracoherent electromechanical system. *Nature Communications* **13,** 1507. ISSN: 2041-1723. https://www.doi.org/10.1038/s41467-022-29115-9 (2025) (Mar. 2022).

29. Megrant, A. *et al.* Planar superconducting resonators with internal quality factors above one million. *Applied Physics Letters* **100,** 113510. ISSN: 0003-6951. eprint: https://pubs.aip.org/aip/apl/article-pdf/doi/10.1063/1.3693409/13262211/113510_1_online.pdf. https://doi.org/10.1063/1.3693409 (Mar. 2012).

30. Zoepfl, D. *et al.* Characterization of Low Loss Microstrip Resonators as a Building Block for Circuit QED in a 3D Waveguide. *AIP Advances* **7,** 085118 (Aug. 2017).

31. Zikiy, E. V. *et al. Investigation of tantalum films growth for coplanar resonators with internal quality factors above ten million* 2025. arXiv: 2509.04917 [quant-ph]. https://arxiv.org/abs/2509.04917.

32. Tuokkola, M. *et al.* Methods to achieve near-millisecond energy relaxation and dephasing times for a superconducting transmon qubit. *Nature Communications* **16,** 5421. https://doi.org/10.1038/s41467-025-61126-0 (2025).

33. Somoroff, A. *et al.* Millisecond Coherence in a Superconducting Qubit. *Phys. Rev. Lett.* **130,** 267001. https://link.aps.org/doi/10.1103/PhysRevLett.130.267001 (26 2023).

34. McGee, S. A., Meiser, D., Regal, C. A., Lehnert, K. W. & Holland, M. J. Mechanical resonators for storage and transfer of electrical and optical quantum states. *Phys. Rev. A* **87,** 053818. https://link.aps.org/doi/10.1103/PhysRevA.87.053818 (5 2013).

35. Arnold, G. *et al.* Converting microwave and telecom photons with a silicon photonic nanomechanical interface. *Nature Communications* **11,** 4460. https://doi.org/10.1038/s41467-020-18269-z (2020).

36. Lauk, N. *et al.* Perspectives on quantum transduction. *Quantum Science and Technology* **5,** 020501. https://doi.org/10.1088/2058-9565/ab788a (2020).

37. Clerk, A. A., Lehnert, K. W., Bertet, P., Petta, J. R. & Nakamura, Y. Hybrid quantum systems with circuit quantum electrodynamics. *Nature Physics* **16,** 257–267. https://doi.org/10.1038/s41567-020-0797-9 (2020).

38. Krause, A. G., Winger, M., Blasius, T. D., Lin, Q. & Painter, O. A High-Resolution Microchip Optomechanical Accelerometer. *Nature Photonics* **6,** 768–772. ISSN: 1749-4885, 1749-4893 (Nov. 2012).

39. Gerberding, O, Guzmán Cervantes, F, Melcher, J, Pratt, J. R. & Taylor, J. M. Optomechanical reference accelerometer. *Metrologia* **52,** 654. https://doi.org/10.1088/0026-1394/52/5/654 (2015).

40. Degen, C. L., Reinhard, F. & Cappellaro, P. Quantum sensing. *Rev. Mod. Phys.* **89,** 035002. https://link.aps.org/doi/10.1103/RevModPhys.89.035002 (3 2017).

41. Teufel, J. D., Harlow, J. W., Regal, C. A. & Lehnert, K. W. Dynamical Backaction of Microwave Fields on a Nanomechanical Oscillator. *Phys. Rev. Lett.* **101,** 197203. https://link.aps.org/doi/10.1103/PhysRevLett.101.197203 (19 2008).

42. Teufel, J. D. *et al.* Sideband Cooling of Micromechanical Motion to the Quantum Ground State. *Nature* **475,** 359–363. ISSN: 0028-0836, 1476-4687 (July 2011).

43. Peterson, G. A. *et al.* Ultrastrong Parametric Coupling between a Superconducting Cavity and a Mechanical Resonator. *Phys. Rev. Lett.* **123,** 247701. https://link.aps.org/doi/10.1103/PhysRevLett.123.247701 (24 2019).

44. Kotler, S. *et al.* Direct observation of deterministic macroscopic entanglement. *Science* **372,** 622–625. eprint: https://www.science.org/doi/pdf/10.1126/science.abf2998. https://www.science.org/doi/abs/10.1126/science.abf2998 (2021).

45. Chu, Y. *et al.* Creation and control of multi-phonon Fock states in a bulk acoustic-wave resonator. *Nature* **563,** 666–670. https://doi.org/10.1038/s41586-018-0717-7 (2018).

46. Ma, X., Viennot, J. J., Kotler, S., Teufel, J. D. & Lehnert, K. W. Non-classical energy squeezing of a macroscopic mechanical oscillator. *Nature Physics* **17,** 322–326. https://doi.org/10.1038/s41567-020-01102-1 (2021).

47. De Jong, M. H. J., Korkmazgil, E., Banniard, L., Sillanpää, M. A. & de Lépinay, L. M. *Measurement of the Casimir force between superconductors* 2025. arXiv: 2501.13759 [cond-mat.mes-hall]. https://arxiv.org/abs/2501.13759.

48. Luschmann, T. *et al.* Mechanical Frequency Control in Inductively Coupled Electromechanical Systems. *Scientific Reports* **12,** 1608. ISSN: 2045-2322 (Jan. 2022).

49. Bothner, D., Rodrigues, I. C. & Steele, G. A. Four-Wave-Cooling to the Single Phonon Level in Kerr Optomechanics. *Communications Physics* **5,** 33. ISSN: 2399-3650 (Dec. 2022).

50. Vinante, A. *et al.* High sensitivity SQUID-detection and feedback-cooling of an ultrasoft microcantilever. *Applied Physics Letters* **101,** 123101. ISSN: 0003-6951. eprint: https://pubs.aip.org/aip/apl/article-pdf/doi/10.1063/1.4752766/14254401/123101_1_online.pdf. https://doi.org/10.1063/1.4752766 (Sept. 2012).

51. Dhiman, S. *et al.* Self-Sustained Oscillations of a Nonlinear Optomechanical System in the Low-Excitation Regime. arXiv: 2510.01775 [quant-ph]. https://arxiv.org/abs/2510.01775 (2025).

52. Via, G., Kirchmair, G. & Romero-Isart, O. Strong Single-Photon Coupling in Superconducting Quantum Magnetomechanics. *Phys. Rev. Lett.* **114,** 143602. https://link.aps.org/doi/10.1103/PhysRevLett.114.143602 (14 2015).

53. Diaz-Naufal, N. *et al.* Kerr-enhanced optomechanical cooling in the unresolved-sideband regime. *Phys. Rev. A* **111,** 053505. https://link.aps.org/doi/10.1103/PhysRevA.111.053505 (5 2025).

54. Latorre, M. G., Paradkar, A., Hambraeus, D., Higgins, G. & Wieczorek, W. A Chip-Based Superconducting Magnetic Trap for Levitating Superconducting Microparticles. *IEEE Transactions on Applied Superconductivity* **32,** 1–5 (2022).

55. Bild, M. *et al.* Schrödinger cat states of a 16-microgram mechanical oscillator. *Science* **380,** 274–278. eprint: https://www.science.org/doi/pdf/10.1126/science.adf7553. https://www.science.org/doi/abs/10.1126/science.adf7553 (2023).

56. Yang, Y. *et al.* A mechanical qubit. *Science* **386,** 783–788. eprint: https://www.science.org/doi/pdf/10.1126/science.adr2464. https://www.science.org/doi/abs/10.1126/science.adr2464 (2024).

57. Gargiulo, O., Oleschko, S., Prat-Camps, J., Zanner, M. & Kirchmair, G. Fast flux control of 3D transmon qubits using a magnetic hose. *Applied Physics Letters* **118,** 012601. ISSN: 0003-6951. eprint: https://pubs.aip.org/aip/apl/article-pdf/doi/10.1063/5.0032615/14077188/012601_1_online.pdf. https://doi.org/10.1063/5.0032615 (Jan. 2021).

58. Schmidt, P. *et al.* Sideband-resolved resonator electromechanics based on a nonlinear Josephson inductance probed on the single-photon level. *Communications Physics* **3,** 233. https://doi.org/10.1038/s42005-020-00501-3 (2020).

59. Gardiner, C. W. & Collett, M. J. Input and Output in Damped Quantum Systems: Quantum Stochastic Differential Equations and the Master Equation. *Physical Review A* **31,** 3761–3774. ISSN: 0556-2791 (June 1985).

60. Mancini, S., Vitali, D. & Tombesi, P. Optomechanical Cooling of a Macroscopic Oscillator by Homodyne Feedback. *Physical Review Letters* **80,** 688–691 (Jan. 1998).

61. Rossi, M., Mason, D., Chen, J., Tsaturyan, Y. & Schliesser, A. Measurement-Based Quantum Control of Mechanical Motion. *Nature* **563,** 53–58. ISSN: 1476-4687 (Nov. 2018).

62. Tebbenjohanns, F., Frimmer, M., Jain, V., Windey, D. & Novotny, L. Motional Sideband Asymmetry of a Nanoparticle Optically Levitated in Free Space. *Physical Review Letters* **124,** 013603 (Jan. 2020).

63. Chan, J. *et al.* Laser Cooling of a Nanomechanical Oscillator into Its Quantum Ground State. *Nature* **478,** 89–92. ISSN: 0028-0836, 1476-4687 (Oct. 2011).

64. Delić, U. *et al.* Cooling of a levitated nanoparticle to the motional quantum ground state. *Science* **367,** 892–895. https://www.doi.org/10.1126/science.aba3993 (2025) (Feb. 2020).

65. Chan, J. *et al.* Laser cooling of a nanomechanical oscillator into its quantum ground state. *Nature* **478,** 89–92. ISSN: 1476-4687. https://www.doi.org/10.1038/nature10461 (2025) (Oct. 2011).

66. Vool, U. & Devoret, M. Introduction to quantum electromagnetic circuits. *International Journal of Circuit Theory and Applications* **45,** 897–934. eprint: https://onlinelibrary.wiley.com/doi/pdf/10.1002/cta.2359. https://onlinelibrary.wiley.com/doi/abs/10.1002/cta.2359 (2017).

67. Blais, A., Grimsmo, A. L., Girvin, S. M. & Wallraff, A. Circuit quantum electrodynamics. *Rev. Mod. Phys.* **93,** 025005. https://link.aps.org/doi/10.1103/RevModPhys.93.025005 (2 2021).

68. Saito, K. Temperature Dependence of the Surface Resistance of Niobium at 1300 MHz - Comparison to BCS Theory - (1999).

69. McRae, C. R. H. *et al.* Materials loss measurements using superconducting microwave resonators. *Review of Scientific Instruments* **91,** 091101. ISSN: 0034-6748, 1089-7623. https://www.doi.org/10.1063/5.0017378 (Sept. 2020).

70. Goetz, J. *et al.* Loss mechanisms in superconducting thin film microwave resonators. *Journal of Applied Physics* **119,** 015304. ISSN: 0021-8979. https://www.doi.org/10.1063/1.4939299 (2025) (Jan. 2016).

71. Earnest, C. T. *et al.* Substrate surface engineering for high-quality silicon/aluminum superconducting resonators. *Superconductor Science and Technology* **31,** 125013. https://dx.doi.org/10.1088/1361-6668/aae548 (2018).

72. Müller, C., Cole, J. H. & Lisenfeld, J. Towards understanding two-level-systems in amorphous solids: insights from quantum circuits. *Reports on Progress in Physics* **82,** 124501. ISSN: 0034-4885. https://www.doi.org/10.1088/1361-6633/ab3a7e (Oct. 2019).

73. Lisenfeld, J. *et al.* Electric field spectroscopy of material defects in transmon qubits. *npj Quantum Information* **5,** 105. ISSN: 2056-6387. https://www.doi.org/10.1038/s41534-019-0224-1 (2025) (Nov. 2019).

74. Martinis, J. M. *et al.* Decoherence in Josephson Qubits from Dielectric Loss. *Physical Review Letters* **95,** 210503. https://www.doi.org/10.1103/PhysRevLett.95.210503 (Nov. 2005).

75. Clarke, J. & Braginski, A. I. *The SQUID Handbook: Fundamentals and Technology of SQUIDs and SQUID Systems* (Wiley-VCH, Weinheim, 2006).

76. Gross, R. & Marx, A. *Festkörperphysik* ISBN: 978-3-11-035870-4. https://doi.org/10.1524/9783110358704 (De Gruyter Oldenbourg, Oct. 2014).

77. Song, C. *et al.* Microwave response of vortices in superconducting thin films of Re and Al. *Phys. Rev. B* **79,** 174512. https://link.aps.org/doi/10.1103/PhysRevB.79.174512 (17 2009).

78. Josephson, B. Possible new effects in superconductive tunnelling. *Physics Letters* **1,** 251–253. ISSN: 0031-9163. https://www.sciencedirect.com/science/article/pii/0031916362913690 (1962).

79. Devoret, M. H. Does Brian Josephson's Gauge–Invariant Phase Difference Live on a Line or a Circle? *Journal of Superconductivity and Novel Magnetism* **34,** 1633–1642 (2021).

80. Dejaco, C. *Preparation and characterisation of a magnetomechanical system* Master's thesis, supervised by Prof. Dr. Gerhard Kirchmair. MA thesis (Institute of Experimental Physics, Innsbruck, Austria, 2025). https://ulb-dok.uibk.ac.at/ulbtirolhs/content/titleinfo/12.

81. Pogorzalek, S. *et al.* Hysteretic Flux Response and Nondegenerate Gain of Flux-Driven Josephson Parametric Amplifiers. *Phys. Rev. Appl.* **8,** 024012. https://link.aps.org/doi/10.1103/PhysRevApplied.8.024012 (2 2017).

82. Sivak, V. *et al.* Kerr-Free Three-Wave Mixing in Superconducting Quantum Circuits. *Phys. Rev. Appl.* **11,** 054060. https://link.aps.org/doi/10.1103/PhysRevApplied.11.054060 (5 2019).

83. Probst, S., Song, F. B., Bushev, P. A., Ustinov, A. V. & Weides, M. Efficient and Robust Analysis of Complex Scattering Data under Noise in Microwave Resonators. *Review of Scientific Instruments* **86,** 024706. ISSN: 0034-6748, 1089-7623 (Feb. 2015).

84. Gorodetksy, M. L., Schliesser, A., Anetsberger, G., Deleglise, S. & Kippenberg, T. J. Determination of the Vacuum Optomechanical Coupling Rate Using Frequency Noise Calibration. *Optics Express* **18,** 23236–23246. ISSN: 1094-4087 (Oct. 2010).

85. Balshaw, N. H, Oxford Instruments Group & Scientific Research Division. *Practical cryogenics: an introduction to laboratory cryogenics* ISBN: 978-0-9527594-0-9 (Oxford Instruments, Scientific Research Division, Eynsham, 1996).

86. Batey, G. & Teleberg, G. *Principles of dilution refrigeration* 2015. https://nanoscience.oxinst.com/assets/uploads/NanoScience/Brochures/Principles%20of%20dilution%20refrigeration_Sept15.pdf (2025).

87. Dhuley, R. C., Ruschman, M., Link, J. T. & Eyre, J. Thermal conductance characterization of a pressed copper rope strap between 0.13 K and 10 K. *Cryogenics* **86,** 17–21. ISSN: 0011-2275. https://www.doi.org/10.1016/j.cryogenics.2017.07.001 (2025) (Sept. 2017).

88. Kalra, R. *et al.* Vibration-induced electrical noise in a cryogen-free dilution refrigerator: Characterization, mitigation, and impact on qubit coherence. *Review of Scientific Instruments* **87,** 073905. ISSN: 0034-6748. eprint: https://pubs.aip.org/aip/rsi/article-pdf/doi/10.1063/1.4959153/14734769/073905_1_online.pdf. https://doi.org/10.1063/1.4959153 (July 2016).

89. Maisonobe, R. *et al.* Vibration decoupling system for massive bolometers in dry cryostats. *Journal of Instrumentation* **13,** T08009. https://dx.doi.org/10.1088/1748-0221/13/08/T08009 (2018).

90. J., P. D. H. *Mechanical Vibrations* reprint. Dover Civil and Mechanical Engineering series. ISBN: 978-0486131856 (Courier Corporation, New York, 2013).

91. Votyakov, E. V. & Thess, A. *Interaction of a magnetic dipole with a slowly moving electrically conducting plate* 2011. arXiv: 1103.2245 [physics.flu-dyn]. https://arxiv.org/abs/1103.2245.

92. Ekin, J. *Experimental Techniques for Low-Temperature Measurements: Cryostat Design, Material Properties and Superconductor Critical-Current Testing* ISBN: 978-0-19-857054-7. https://doi.org/10.1093/acprof:oso/9780198570547.001.0001 (2025) (Oxford University Press, Oct. 2006).

93. Calatroni, S. *Materials & Properties: Thermal & Electrical Characteristics* June 2020. https://www.doi.org/10.48550/arXiv.2006.02842 (2025).

94. Valois, J. J., Nellis, G. F. & Pfotenhauer, J. M. Characterization of the thermal properties of OFHC copper at cryogenic temperature. *IOP Conference Series: Materials Science and Engineering* **1301,** 012167. ISSN: 1757-899X. https://www.doi.org/10.1088/1757-899X/1301/1/012167 (2025) (May 2024).

95. Tariq, A. & Asif, M. Experimental investigation of thermal contact conductance for nominally flat metallic contact. *Heat and Mass Transfer* **52,** 291–307. ISSN: 1432-1181. https://www.doi.org/10.1007/s00231-015-1551-1 (2025) (Feb. 2016).

96. Dhuley, R. C. Pressed copper and gold-plated copper contacts at low temperatures – A review of thermal contact resistance. *Cryogenics* **101,** 111–124. ISSN: 0011-2275. https://www.doi.org/10.1016/j.cryogenics.2019.06.008 (2025) (July 2019).

97. Gmelin, E., Asen-Palmer, M., Reuther, M. & Villar, R. Thermal boundary resistance of mechanical contacts between solids at sub-ambient temperatures. *Journal of Physics D: Applied Physics* **32,** R19. ISSN: 0022-3727. https://www.doi.org/10.1088/0022-3727/32/6/004 (2025) (Mar. 1999).

98. Dillon, A, McCusker, K, Van Dyke, J, Isler, B & Christiansen, M. Thermal interface material characterization for cryogenic electronic packaging solutions. *IOP Conference Series: Materials Science and Engineering* **278,** 012054. ISSN: 1757-899X. https://www.doi.org/10.1088/1757-899X/278/1/012054 (2025) (Dec. 2017).

99. Buzea, C. & Robbie, K. Assembling the puzzle of superconducting elements: a review. *Superconductor Science and Technology* **18,** R1. ISSN: 0953-2048. https://www.doi.org/10.1088/0953-2048/18/1/R01 (2025) (Nov. 2004).

100. Pozar, D. M. *Microwave engineering* 4th ed. ISBN: 978-0-470-63155-3 (Wiley, Hoboken, NJ, 2012).

101. Khalil, M. S., Stoutimore, M. J. A., Wellstood, F. C. & Osborn, K. D. An analysis method for asymmetric resonator transmission applied to superconducting devices. *Journal of Applied Physics* **111,** 054510. ISSN: 0021-8979. https://www.doi.org/10.1063/1.3692073 (Mar. 2012).

102. Brock, B. *et al.* Nonlinear Charge- and Flux-Tunable Cavity Derived From an Embedded Cooper-Pair Transistor. *Phys. Rev. Appl.* **15,** 044009. https://link.aps.org/doi/10.1103/PhysRevApplied.15.044009 (4 2021).

103. Cleland, A. N. *Foundations of Nanomechanics: From Solid-State Theory to Device Applications* ISBN: 978-3-540-43661-4. https://link.springer.com/book/10.1007/978-3-662-05287-7 (Springer Berlin, 2003).

104. Wu, J.-S. & Lin, T.-L. Free vibration analysis of a uniform cantilever beam with point masses by an analytical-and-numerical-combined method. *Journal of Sound and Vibration* **136,** 201–213. ISSN: 0022-460X. https://www.sciencedirect.com/science/article/pii/0022460X9090851P (1990).

105. Henins, I. Precision density measurement of silicon. *Journal of Research of the National Bureau of Standards Section A: Physics and Chemistry* **68A,** 529. ISSN: 0022-4332. https://www.doi.org/10.6028/jres.068A.050 (2025) (Sept. 1964).

106. Bowen, W. P. & Milburn, G. J. *Quantum Optomechanics* 1st. ISBN: 9780429159312 (CRC Press, Boca Raton, FL, 2015).

107. Kubo, R. The fluctuation-dissipation theorem. *Reports on Progress in Physics* **29,** 255. https://dx.doi.org/10.1088/0034-4885/29/1/306 (1966).

108. Callen, H. B. & Welton, T. A. Irreversibility and Generalized Noise. *Phys. Rev.* **83,** 34–40. https://link.aps.org/doi/10.1103/PhysRev.83.34 (1 1951).

109. Potticary, J., Avery, M. P., Mills, D. & Hall, S. R. DONALD: A 2.5 T wide sample space permanent magnet. *HardwareX* **3,** 39–48. ISSN: 2468-0672. https://www.doi.org/10.1016/j.ohx.2018.01.002 (2025) (Apr. 2018).

110. Imboden, M. & Mohanty, P. Dissipation in nanoelectromechanical systems. *Physics Reports. Dissipation in nano-electromechanical systems* **534,** 89–146. ISSN: 0370-1573. https://www.doi.org/10.1016/j.physrep.2013.09.003 (2025) (Jan. 2014).

111. Yasumura, K. *et al.* Quality factors in micron- and submicron-thick cantilevers. *Journal of Microelectromechanical Systems* **9,** 117–125. ISSN: 1941-0158. https://www.doi.org/10.1109/84.825786 (2025) (Mar. 2000).

112. *Custom Rare Earth Magnets* https://www.advancedmagnets.com/custom-magnets/ (2025).

113. Liu, Z. Temperature-Dependent Elastic Constants and Young's Modulus of Silicon Single Crystal. *Proceedings of the 11th Mechanical Engineering Design of Synchrotron Radiation Equipment and Instrumentation* **MEDSI2020.** ISSN: 2673-5520. https://www.doi.org/10.18429/JACOW-MEDSI2020-WEPC09 (2025) (2021).

114. Bing Rong, C., Poudyal, N. & Liu, J. P. Size-dependent spin-reorientation transition in Nd2Fe14B nanoparticles. *Physics Letters A* **374,** 3967–3970. ISSN: 0375-9601. https://www.sciencedirect.com/science/article/pii/S0375960110009485 (2010).

115. Hu, J., Kou, X. C. & Kronmüller, H. The low-temperature dependence of coercivity in NdFeB magnets. *physica status solidi (b)* **188,** 807–811. eprint: https://onlinelibrary.wiley.com/doi/pdf/10.1002/pssb.2221880224. https://onlinelibrary.wiley.com/doi/abs/10.1002/pssb.2221880224 (1995).

116. Herzer, G. Modern soft magnets: Amorphous and nanocrystalline materials. *Acta Materialia* **61.** The Diamond Jubilee Issue, 718–734. ISSN: 1359-6454. https://www.sciencedirect.com/science/article/pii/S1359645412007872 (2013).

117. Givord, D., Tenaud, P. & Viadieu, T. Analysis of hysteresis loops in Nd-Fe-B sintered magnets. *Journal of Applied Physics* **60,** 3263–3265. ISSN: 0021-8979. eprint: https://pubs.aip.org/aip/jap/article-pdf/60/9/3263/18607188/3263_1_online.pdf. https://doi.org/10.1063/1.337715 (Nov. 1986).

118. Magnets, E. *Neodymium (NdFeB) Characteristics* https://www.euromag-magnets.com/en/neodymium-characteristics/. Accessed: 2025-10-31. 2025.

119. Mironov, S. *et al.* Anomalous Josephson effect controlled by an Abrikosov vortex. *Phys. Rev. B* **96,** 214515. https://link.aps.org/doi/10.1103/PhysRevB.96.214515 (21 2017).

120. Krantz, P. *et al.* Investigation of nonlinear effects in Josephson parametric oscillators used in circuit quantum electrodynamics. *New Journal of Physics* **15,** 105002. ISSN: 1367-2630. http://dx.doi.org/10.1088/1367-2630/15/10/105002 (Oct. 2013).

121. Hoehne, F. *et al.* Damping in high-frequency metallic nanomechanical resonators. *Phys. Rev. B* **81,** 184112. https://link.aps.org/doi/10.1103/PhysRevB.81.184112 (18 2010).

122. Kamppinen, T., Mäkinen, J. T. & Eltsov, V. B. Dimensional control of tunneling two-level systems in nanoelectromechanical resonators. *Phys. Rev. B* **105,** 035409. https://link.aps.org/doi/10.1103/PhysRevB.105.035409 (3 2022).

123. Lulla, K. J., Defoort, M., Blanc, C., Bourgeois, O. & Collin, E. Evidence for the Role of Normal-State Electrons in Nanoelectromechanical Damping Mechanisms at Very Low Temperatures. *Phys. Rev. Lett.* **110,** 177206. https://link.aps.org/doi/10.1103/PhysRevLett.110.177206 (17 2013).

124. Seoánez, C., Guinea, F. & Castro Neto, A. H. Surface dissipation in nanoelectromechanical systems: Unified description with the standard tunneling model and effects of metallic electrodes. *Phys. Rev. B* **77,** 125107. https://link.aps.org/doi/10.1103/PhysRevB.77.125107 (12 2008).

125. Bourgeois, O., Fournier, T. & Chaussy, J. Measurement of the thermal conductance of silicon nanowires at low temperature. *Journal of Applied Physics* **101.** ISSN: 1089-7550. http://dx.doi.org/10.1063/1.2400093 (Jan. 2007).

126. Rocheleau, T. *et al.* Preparation and detection of a mechanical resonator near the ground state of motion. *Nature* **463,** 72–75. ISSN: 1476-4687. https://www.doi.org/10.1038/nature08681 (2025) (Jan. 2010).

127. Scikit-learn developers. *scikit-learn: Machine Learning in Python* https://scikit-learn.org/stable/.

128. Fani Sani, F., Rodrigues, I. C., Bothner, D. & Steele, G. A. Level attraction and idler resonance in a strongly driven Josephson cavity. *Phys. Rev. Res.* **3,** 043111. https://link.aps.org/doi/10.1103/PhysRevResearch.3.043111 (4 2021).

129. Reagor, M. *et al.* Quantum memory with millisecond coherence in circuit QED. *Phys. Rev. B* **94,** 014506. https://link.aps.org/doi/10.1103/PhysRevB.94.014506 (1 2016).

130. Heidler, P. *et al.* Non-Markovian Effects of Two-Level Systems in a Niobium Coaxial Resonator with a Single-Photon Lifetime of 10 milliseconds. *Phys. Rev. Appl.* **16,** 034024. https://link.aps.org/doi/10.1103/PhysRevApplied.16.034024 (3 2021).

131. Qu, K. & Agarwal, G. S. Fano resonances and their control in optomechanics. *Phys. Rev. A* **87,** 063813. https://link.aps.org/doi/10.1103/PhysRevA.87.063813 (6 2013).

132. Limonov, M., Rybin, M., Poddubny, A. & Kivshar, Y. Fano resonances in photonics. English. *Nature Photonics* **11,** 543–554. ISSN: 1749-4885 (Sept. 2017).

133. Jaynes, E. & Cummings, F. Comparison of quantum and semiclassical radiation theories with application to the beam maser. *Proceedings of the IEEE* **51,** 89–109 (1963).

134. Atanasova, D. *et al.* In Situ Tunable Interaction with an Invertible Sign between a Fluxonium and a Post Cavity. *PRX Quantum* **6,** 020318. https://link.aps.org/doi/10.1103/PRXQuantum.6.020318 (2 2025).

135. Yang, I., Agrenius, T., Usova, V., Romero-Isart, O. & Kirchmair, G. Hot Schrödinger cat states. *Science Advances* **11,** eadr4492. eprint: https://www.science.org/doi/pdf/10.1126/sciadv.adr4492. https://www.science.org/doi/abs/10.1126/sciadv.adr4492 (2025).

136. Heidler, P. *Improving the Quality Factor of Coaxial Quarterwave Resonators* Master's thesis, supervised by Prof. Dr. Gerhard Kirchmair. MA thesis (Institute of Experimental Physics, Innsbruck, Austria, 2019). https://ulb-dok.uibk.ac.at/ulbtirolhs/content/titleinfo/4556080?query=Paul%20Heidler.

137. Yang, I. Y. W. *Quantum Information Processing with Superconducting Circuits and High Q Cavities* PhD thesis in the group of Prof. Dr. Gerhard Kirchmair. PhD thesis (Institute for Quantum Optics and Quantum Information (IQOQI), Innsbruck, Austria, 2024). https://ulb-dok.uibk.ac.at/ulbtirolhs/content/titleinfo/9581425?query=Ian%20Yang.

138. Sanchez, A. & Bort-Soldevila, N. Shaping magnetic fields with zero-magnetic-permeability media. *Journal of Applied Physics* **130,** 163901. ISSN: 0021-8979. eprint: https://pubs.aip.org/aip/jap/article-pdf/doi/10.1063/5.0063263/15269816/163901_1_online.pdf. https://doi.org/10.1063/5.0063263 (Oct. 2021).

139. Rieger, D. *et al.* Fano Interference in Microwave Resonator Measurements. *Phys. Rev. Appl.* **20,** 014059. https://link.aps.org/doi/10.1103/PhysRevApplied.20.014059 (1 2023).

140. Clark, J. B., Lecocq, F., Simmonds, R. W., Aumentado, J. & Teufel, J. D. Sideband Cooling beyond the Quantum Backaction Limit with Squeezed Light. *Nature* **541,** 191–195. ISSN: 1476-4687 (Jan. 2017).

141. Place, A. P. M. *et al.* New material platform for superconducting transmon qubits with coherence times exceeding 0.3 milliseconds. *Nature Communications* **12,** 1779. https://doi.org/10.1038/s41467-021-22030-5 (2021).

142. Kroll, J. *et al.* Magnetic-Field-Resilient Superconducting Coplanar-Waveguide Resonators for Hybrid Circuit Quantum Electrodynamics Experiments. *Phys. Rev. Appl.* **11,** 064053. https://link.aps.org/doi/10.1103/PhysRevApplied.11.064053 (6 2019).

143. Wang, Y.-D. & Clerk, A. A. Using Interference for High Fidelity Quantum State Transfer in Optomechanics. *Phys. Rev. Lett.* **108,** 153603. https://link.aps.org/doi/10.1103/PhysRevLett.108.153603 (15 2012).

144. Palomaki, T. A., Harlow, J. W., Teufel, J. D., Simmonds, R. W. & Lehnert, K. W. Coherent state transfer between itinerant microwave fields and a mechanical oscillator. *Nature* **495,** 210–214. https://doi.org/10.1038/nature11915 (2013).

145. Nunnenkamp, A., Børkje, K. & Girvin, S. M. Single-Photon Optomechanics. *Phys. Rev. Lett.* **107,** 063602. https://link.aps.org/doi/10.1103/PhysRevLett.107.063602 (6 2011).

CHAPTER 8

Acknowledgment

Without the help of a bunch of people, I wouldn't have made it through these past years with a finished PhD-thesis. I'd like to take a moment to thank those who made this adventure possible.

First and foremost, I want to thank you, Prof. Gerhard Kirchmair, for giving me the opportunity to start my PhD in your group. I truly admire the dedication with which you follow each and every project in your group and the fun you have while discussing any new ideas. Despite your busy schedule, you always find the time to talk about the experiments hinting towards the last missing measurement or to share your ideas how to solve one of the many problems we encountered. I am very grateful for the many insightful – and often long – discussions we have had. Thank you for your comments on this manuscript and for being such a supportive group leader, I really enjoyed working as part of your group!

Next, I would like to thank the people who made my PhD-project possible in the first place by implementing our experiment platform: the previous mechanics team – some might call them the "old batch" – including **David Zöpfl** , **Christian Schneider** and **Prof. Mathieu Juan**. Thank you, **David**, for introducing me to the experiment and showing me every trick to know in your relaxed and down-to-earth way. I really enjoyed working together with including all the night shifts to close the fridge and I'm looking forward to each of your occasional IBK visits as they always include a bike ride. But most importantly, thank you for your friendship. Thank you, **Christian**, for all the discussions we had (even after you left Innsbruck) contributing with your broad knowledge – especially on SQUIDs – and your passion for science in general. Thanks for letting me crash at your place for the Beatstakes concert! Even though we finally met in person for the first time this year, thank you, **Mathieu**, for joining our weekly mechanics meetings over Zoom and all the creative input and ideas you contributed.

With that I turn to the "new batch" of the mechanics team. Introducing you, **Christian Dejaco**, to the project was a great pleasure. I really appreciate the teamwork we developed, discussing about the right way to turn circles, unconventional ways to excite our mechanics, or our occasionally fast-and-efficient workshop rounds to make the cooldowns work. **Raamamurthy Sathyanarayanan**, I want to thank you for all the simulations you ran in the past years, as well

as your perfect role as GM for any TTRPGs you host. Thank you, **Bhargava Thyagarajan**, for all the new insights you brought with you by joining our group as well as your tireless efforts to get our hybrid setup to work. Thank you three for the detailed correction of my thesis and the endless discussions we had about the system. As David said before, I'm glad to know that the experiment is in excellent hands. "Towards the Groundstate, guys!".

A large contribution of this thesis relied on the constant theory support provided by **Prof. Anja Metelmann** and **Nicolás Díaz Naufal**. Thank you, both, for your patience explaining the theory behind the nonlinear cooling and the effort you put in to understand our experimental side of view. Especially thanks to you, **Nico**, for all the time we spent together on various conferences sharing a room and your endless theory support in form of our weekly Zoom meetings or by proofreading the theory part of this work. Looking forward to visit you in Berlin, amigo! Thanks **Gustavo**, our new theory support on the hybrid project, for putting so much work on the theory description so I could use it in chapter 6.

Furthermore, I want to thank all current members and alumni of the Kirchmair group, especially **Desi**, **Julian**, **Teresa**, **Vasilisa**, **Lucien**, **Ian**, **Christian S.**, **Tanmoy** and **Niklas**. Working together in the lab and the necessary lunch/coffee breaks that go with it were always a great fun with you. Thanks for all the non-work related time we spent and all the delicious dinners and drinks we shared! It was blast getting to know all of you and I really think Gerhard has a great team of superb physicists!

I want to thank **Andreas Strasser** and **Bernhard Öttl** for their great work in the IQOQI mechanics workshop always offering a helping hand if needed. Especially you, **Andreas**, always took your time to understand my designs and without your help most of the experiments wouldn't have been possible.

Of course, a huge thank you to all the administrative staff that helped me navigate through my PhD. Thank you, **Elke Wölflmaier**, **Elizabeth Huck** and **Klaus Falschlunger**, for taking care of all the orders I placed and helping with the problems that they sporadically caused. Thank you, **David Jordan**, for the excellent IT support and fixing my laptop whenever it was broken. It surely wasn't my fault!

I'm also grateful for my time in the Doktoratskolleg DK-Alm and want to thank the whole team and the FWF for funding it. Thank you, **Dr. Heide Streicher**, for all the help getting started in Innsbruck as a new PhD student and your support organizing my stays abroad. They – and the many summer schools you organized – were definitely among the highlights of my PhD.

I would like to say a big thank you to **my parents**, whose support and encouragement has helped me throughout all my life and studies. Thanks to my two **older brothers** for all the adventures, bike rides, and memories I will never forget!

Lastly, thanks to you, **Flora**. You're the kindest person I know, and I'm forever grateful for your patience with me. Whenever I came home late, you waited for me with a smile – which means more to me than you can imaging – and every so often, with a dinner ready to eat. Thank you for always being there for me, supporting me in every way and venturing through the world by my side.